Nuclear Star Clusters in the Virgo Cluster of Galaxies

by

Chelsea Spengler
Bachelor of Science, Case Western Reserve University, 2012

A Dissertation Submitted in Partial Fulfillment of the
Requirements for the Degree of

DOCTOR OF PHILOSOPHY

in the Department of Physics and Astronomy

Nuclear Star Clusters in the Virgo Cluster of Galaxies

by

Chelsea Spengler
Bachelor of Science, Case Western Reserve University, 2012

Supervisory Committee

Dr. Patrick Côté, Co-Supervisor
(Department of Physics & Astronomy)

Dr. Jon Willis, Co-Supervisor
(Department of Physics & Astronomy)

Dr. Matthew Moffitt, External Member
(Department of Chemistry)

ABSTRACT

It is readily accepted that many galaxies are inhabited by dense, compact objects deep in their centres, manifesting as supermassive black holes (SMBHs) and/or nuclear star clusters (NSCs). Their widespread presence and apparent similar scaling relations with properties of their hosts implies that SMBHs and NSCs are two related flavours of central massive object (CMO) that play essential roles in their hosts' evolution. However, the formation conditions required for CMOs, the exact behaviour of these scaling relations, and the interplay among CMOs, their hosts, and the environment remain open questions, and are particularly poorly understood in lower-mass galaxies where NSCs are the dominant CMO. This thesis contributes to the answers to these questions through a study of ultraviolet, optical, and near-infrared imaging of NSCs and galaxies provided by three recent surveys of the Virgo Cluster: the ACS Virgo Cluster Survey (ACSVCS), Virgo Redux, and the Next Generation Virgo Cluster Survey (NGVS).

The analysis of the masses, ages and metallicities for a choice sample of 39 nucleated early-type galaxies with the complete wavelength coverage provided from all three surveys supports complex formation scenarios for the NSCs, involving a stochastic mix of dissipative and dissipationless processes. However, trends in the structural parameters of the NSCs show that the brightest NSCs tend to be flattened, suggesting that NSC formation may be dominated by dissipative processes in more massive systems, compared to dissipationless star cluster infall dominating in less massive galaxies. A comparison of these photometrically-derived stellar population parameters with those from available high quality optical spectra shows that estimated metallicities from the two samples are consistent, which is encouraging for using broadband photometry to derive stellar population parameters when spectroscopy is not feasible.

Probing the effects of environment with the unprecedented sample available in the NGVS first requires a method to identify distinct environments through the detection of substructures in an objective, self-consistent way. I introduce a novel clustering algorithm and validate its performance using NGVS and 12 Virgo analogues from the `Illustris` simulations. This validation also permits a test of the lambda cold dark matter (ΛCDM) model's ability to replicate observed structures on cluster-sized spatial scales. The algorithm successfully recovers already-known Virgo substructures along with multiple intriguing new substructure discoveries, verified using available

recessional velocities and distances from surface brightness fluctuations. Additional tests tentatively suggest that ΛCDM does not reproduce the level of substructure in Virgo; however, an expanded sample of observed clusters is necessary for a statistically robust conclusion.

Lastly, I expand the analysis of structural and photometric parameters to encompass all NSCs and galaxies with measured parameters in the NGVS, and combine this with the substructure identifications to explore how the properties and relationships of NSCs, nucleated galaxies, and non-nucleated galaxies change throughout the environments of the Virgo Cluster. I detect a clear dependence on environmental density for the NSC occupation fraction, but, interestingly, the sizes, shapes, masses, colours, and scaling relations of NSCs and their hosts appear unaffected by environment. I also reaffirm that nucleated galaxies are consistently more concentrated and rounder than their non-nucleated counterparts, as well as redder in the luminosity ranges where NSCs are most abundant. These relationships also remain constant throughout different environments. One possible interpretation of these results is that environment is important only for the initial creation of an NSC; alternatively, all NSC growth mechanisms may be influenced equally by the environment.

Contents

List of Tables

List of Figures

Acknowledgments

My sincere thanks to my supervisor, Pat Côté, for his abundance of knowledge, encouragement, and, above all, patience, during my graduate studies. I'd also like to thank the other members of my supervisory committee, Jon Willis and Matt Moffitt, for the time and effort they have invested over the years. This work was completed with the help of many wonderful collaborators — working with the NGVS team as well as the astronomers at UVic and the institute formerly known as HIA has been an absolute pleasure. Special thanks to Laura Ferrarese, Joel Roediger, Ruben Sánchez-Janssen, Nicholas McConnell, Jon Willis, and Sara Ellison for well-timed advice and encouragement when I needed it. Thanks also to Megan Nell and the other staff in the department office for all their assistance and expertise.

Of course I must offer my heartfelt thanks to my fellow graduate students, past and present, for being such valuable friends and resources. Thank you especially to Trystyn Berg, Alison Elliot, Sam Lloyd, Kyle Oman, Charli Sakari, Jon Sharman and Steve Mairs for your various roles in getting me out of the office, listening to me, and bestowing me with Python and academic wisdom.

To Ed Arellano, Emily Vojt Baum, and other dear friends who were subjected to my tedious GALFIT rants, moments of panic, and other unpleasantries, yet never stopped encouraging me — thank you.

Though they will never read this, I would be remiss if I did not acknowledge the unconditional support offered by my feline companions over the years. To Pixie, Mocha, Moses, and Dante — I wish you could know how much you've helped me.

Thanks also to Franz Ferdinand and Muse for recording so many bangers to keep me motivated (especially the album *Black Holes and Revelations*, for obvious reasons).

Last, but not least, I would like to thank my parents, Pam and Jon, who started this whole astronomy thing when they insisted on purchasing that copy of *Exploring the Night Sky* by Terrence Dickinson nearly 20 years ago. Look what you've done (is this gentle scolding or praise? you decide).

We do not ask for what useful purpose the birds do sing, for song is their pleasure since they were created for singing. Similarly, we ought not to ask why the human mind troubles to fathom the secrets of the heavens. The diversity of the phenomena of nature is so great and the treasures hidden in the heavens so rich precisely in order that the human mind shall never be lacking in fresh nourishment.

— Johannes Kepler

To Mom and Dad, for your unquestioning and steadfast embrace of my own heavenly fathoming.

Chapter 1

Introduction

Thanks largely to expansive galaxy surveys collectively spanning large volumes of the Universe, and to our current cosmological paradigm, the Λ cold dark matter (ΛCDM) model, we have a general outline of how galaxies form and evolve as a population. However, the detailed mechanisms driving growth within collapsing dark matter halos remain unclear. While predictions from ΛCDM are suitable for replicating the overall large-scale structure of the Universe, astronomers are still working to reconcile simulations and observations on smaller scales, ranging from galaxy clusters to within individual galaxies. Early evidence suggests that observed galaxy clusters may not resemble those predicted in simulations in terms of the spatial or mass distributions of galaxies. Within individual galaxies, regulatory processes known as feedback must be adjusted in simulations to replicate observed properties of galaxies; however, the exact nature of these feedback processes remain unclear.

One intriguing way to address these outstanding questions in galaxy evolution is through the study of the innermost central regions of galaxies. Virtually every high- and intermediate-mass galaxy hosts a massive, compact object at its centre. Their unique placement deep in the potential wells of their galaxies means that these objects have been subjected to a variety of events throughout their entire galactic history and thus serve as tracers of the many physical processes that shape each galaxy's evolutionary path, including effects due to the galaxy's surrounding neighbours and environment. By uncovering the origins of these central objects, and the processes that dominate their growth, it is possible to better understand the physics involved in galaxy evolution that produced the mass distribution and chemical content of the Universe today.

1.1 Seeds of structure in the Universe

The sizes and distribution of galaxies that we see in the present-day Universe are the products of billion of years of evolution driven by the initial conditions in the early Universe. Observations of the cosmic microwave background (CMB), the earliest radiation emitted in the Universe, indicate that these present-day structures somehow grew out of a remarkably smooth and isotropic matter distribution.

Our standard cosmological model explains the conditions necessary in the Universe to generate these observed properties: roughly 13.8 Gyr ago, the Universe originated in the "Big Bang" as an infinitely dense and hot singularity containing all matter and energy in the Universe. Within the first 10^{-36} to 10^{-32} seconds of the Universe's existence, it exponentially inflated, and has continued to expand throughout its existence (albeit at a lesser rate). For the past few Gyr, this expansion has been driven by the vacuum energy of the Universe. This vacuum energy is represented by the cosmological constant Λ and must comprise $\sim$70% of the total mass-energy budget of the Universe (Planck Collaboration et al., 2016).

The initial rapid inflation of the Universe smoothed out most of the perturbations in the matter density, leaving only small over- and under-densities in a Universe that was still so hot that matter and radiation were coupled, preventing the matter from cooling and gravitationally collapsing around the overdensities, and ultimately forming the first structures. In order to form the observed structures rapidly enough, they must begin forming before matter could decouple from the radiation. Therefore, a mysterious form of matter — something that does not interact with radiation and is kinematically cold[1] — must exist to form the seeds of structure. This cold dark matter makes up nearly 84% of all matter in the Universe and roughly 25% of the total mass-energy content (Planck Collaboration et al., 2016). This cosmological framework is known as the Λ cold dark matter (ΛCDM) model. With the initial dark matter structures in place, ordinary matter (known as baryons) could eventually cool and collapse onto these structures and form stars. The density perturbations of the Universe continued to increase as more matter was gravitationally accreted into structures, forming voids and filaments of halo structures. Over time, galaxies, groups of galaxies, and eventually larger associations like galaxy clusters formed via hierarchical assembly of smaller structures that are drawn into the deepest potential wells (Searle & Zinn, 1978; White & Rees, 1978). This process is illustrated in Figure 1.1, which

[1] In kinematic terms, cold systems are moving at slow, non-relativistic speeds.

shows the amount of structure present at different stages in the `Illustris` ΛCDM simulation.

1.2 The growth of galaxies

Galaxies are shaped by numerous physical processes throughout their lifetimes (e.g., gravitational interactions and collisions, and the inflow and outflow of star-forming gas), resulting in a myriad of different appearances. This diverse galaxy population can be quantified based on a number of observed properties, which are briefly summarized here. This summary is focused mainly on the overall features from galaxy imaging in broad wavelength bands, but more specific properties of the kinematics, gas, and stellar content can be achieved with spectroscopy.

1.2.1 Classical morphologies

Early attempts at galaxy classification were laid out by Hubble (1926) and later refined by de Vaucouleurs (1959). These classifications are based on the overall visual appearance of the galaxies, as shown in Figure 1.2. The broad galaxy classifications include elliptical and spiral galaxies. Ellipticals (class E) appear as smooth, featureless orbs that are further categorized with numbers 0-7 according to their roundness. They are often yellowish or red in colour, with minimal evidence of gas or dust. In contrast, spiral galaxies are thin disks, often blue in colour, with a central round bulge of stars that resembles a miniature elliptical galaxy. Their disks often contain clouds of gas and dark lanes of dust. Spirals are separated into those with (class SB) and without (class S) central bar-like structures. They have varying degrees of prominence of their bulges and spiral structures, transitioning from those with larger bulges and subtle spiral features (class Sa/SBa) to those with smaller bulges and more obvious spiral arms (class Sc/SBc).

Originally, Hubble (1926) proposed that galaxies *evolved* from ellipticals to spirals, so that ellipticals were thought to be "early-type" galaxy morphologies and spirals were "late-types." We now know that galaxies do not grow in this way, but the nomenclature has persisted (and is used in this thesis). *Early-type* galaxies refer to those with typical elliptical-type characteristics: red colours, minimal gas content, and a smooth elliptical shape, while *late-types* refer to galaxies that are more disk-shaped and blue in colour. Late-types also include irregular galaxies, defined by

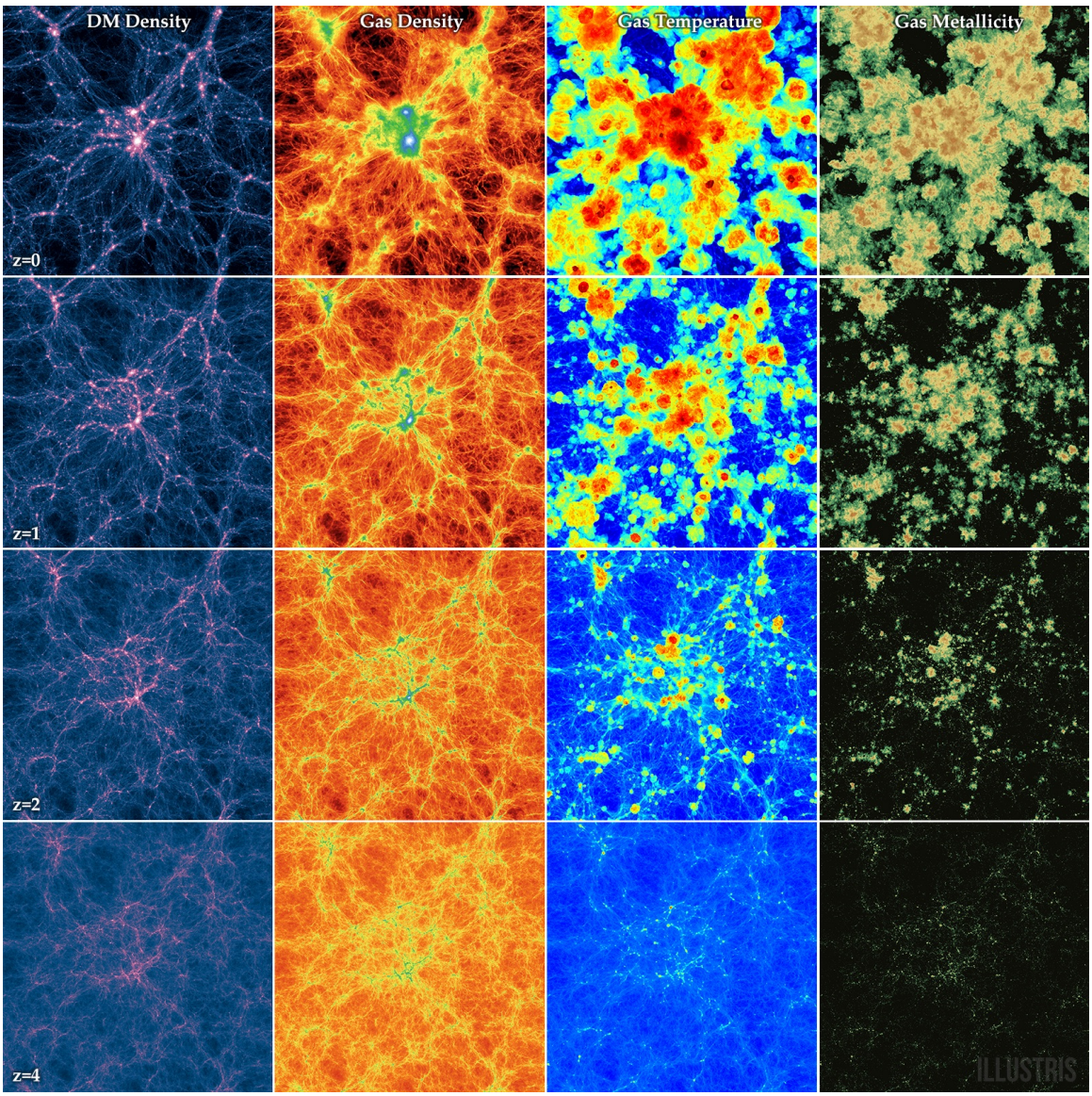

Figure 1.1 Distributions of (from left to right) dark matter, gas, gas temperature, and gas metallicity at four different snapshots in the `Illustris` simulation. The snapshots correspond to approximate Universe ages of (from top to bottom) 13.8, 6, 3, and 1.5 Gyr. Focusing on the first two columns, it can be seen that as the Universe ages, dark matter and gas become more structured, accreting onto the filamentary structures and becoming more concentrated on the nodes where filaments intersect. (Image credit: `Illustris` collaboration)

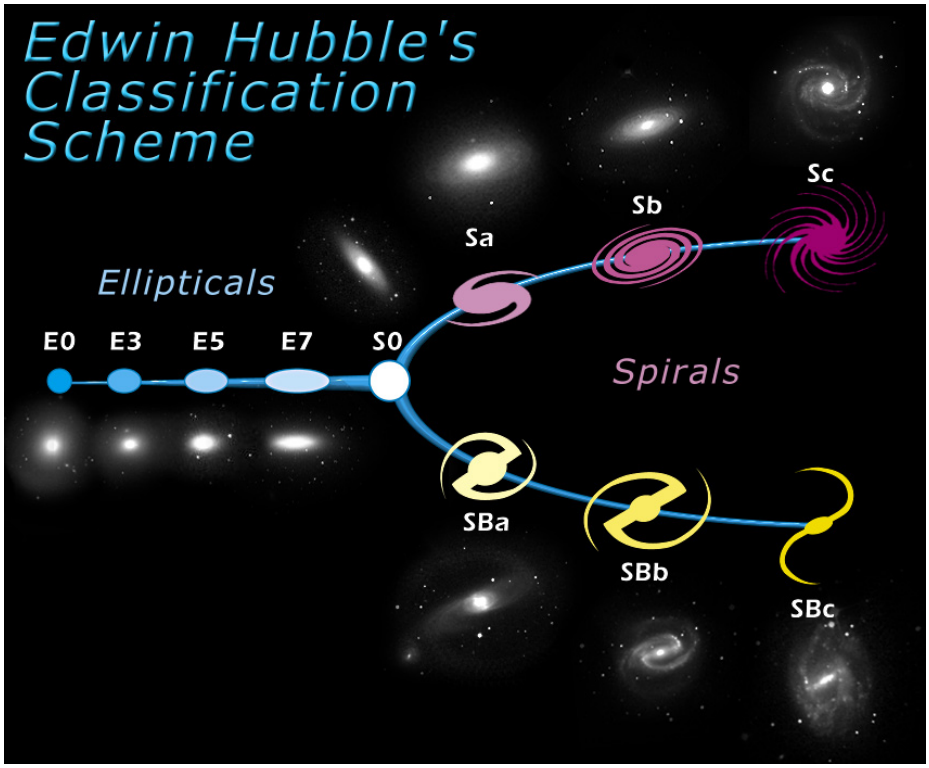

Figure 1.2 Representative galaxies for each classification in Hubble (1926). The galaxies are arranged in a "tuning fork" because of the idea that galaxies evolved from elliptical morphologies on the left to one of the two paths of spiral morphologies on the right. Although now known to be incorrect, this concept still persists in galaxy nomenclature, with red or elliptical galaxies often referred to as "early-types" and blue or spiral galaxies known as "late-types." (Image credit: NASA & ESA)

their amorphous shape and rich gas content, that do not fit into the original Hubble scheme. Additionally, this scheme focuses on high-luminosity galaxies, and does not include low-mass *dwarf* galaxies that dominate populations by overall number.

1.2.2 Luminosities and colours

The brightnesses of astronomical objects span many orders of magnitude, so they are commonly expressed on a logarithmic scale. This log-scaled brightness is simply called a magnitude and is defined as $m = -2.5 \log_{10}(f/f_0)$, where f is the flux of the object of interest, and f_0 is a reference flux to normalize the magnitude m on a standard scale. Note the negative sign in the equation, which means that the value of the magnitude *decreases* as luminosity increases. This equation specifically is for the *apparent magnitude* of an object. The absolute magnitudes[2] of galaxies in optical wavelengths range from ∼-25 mag for the largest ellipticals to ∼-2 mag for the faintest galaxies, known as dwarfs (McConnachie, 2012; Misgeld & Hilker, 2011).

Magnitudes are often measured for the flux within particular wavelength ranges that are isolated by using specific filters in the optical systems of telescopes. By comparing magnitudes measured in different filters, the colour index of an object can be defined. Conventionally, the magnitude at longer wavelengths is subtracted from the magnitude at shorter wavelengths, such that a redder object has a larger colour than a bluer one. For galaxies, these colours are mostly influenced by the properties of their stellar populations. Younger populations, dominated by luminous, hot stars with strong UV emission, appear bluer than older populations in which those bright blue stars have evolved into red giants. Another effect on colour is from the chemical composition, or metallicity, of these stellar populations. The metallicity is simply a ratio of the abundance of metals[3] to the abundance of hydrogen. Because it is challenging to observe and measure every single metal present in a stellar population, iron is used as a proxy for the total metal content and the metallicity is quantified by the ratio of iron (Fe) to hydrogen (H) using the equation

$$[\mathrm{Fe/H}] = \log_{10}\left(\frac{N_{\mathrm{Fe}}}{N_{\mathrm{H}}}\right) - \log_{10}\left(\frac{N_{\mathrm{Fe},\odot}}{N_{\mathrm{H},\odot}}\right),$$

[2]An object's brightness decreases proportional to its distance squared, so absolute magnitudes are normalized magnitudes that would be observed if the object was exactly 10 pc away from the observer.

[3]For astronomers, these are all elements that are not hydrogen or helium.

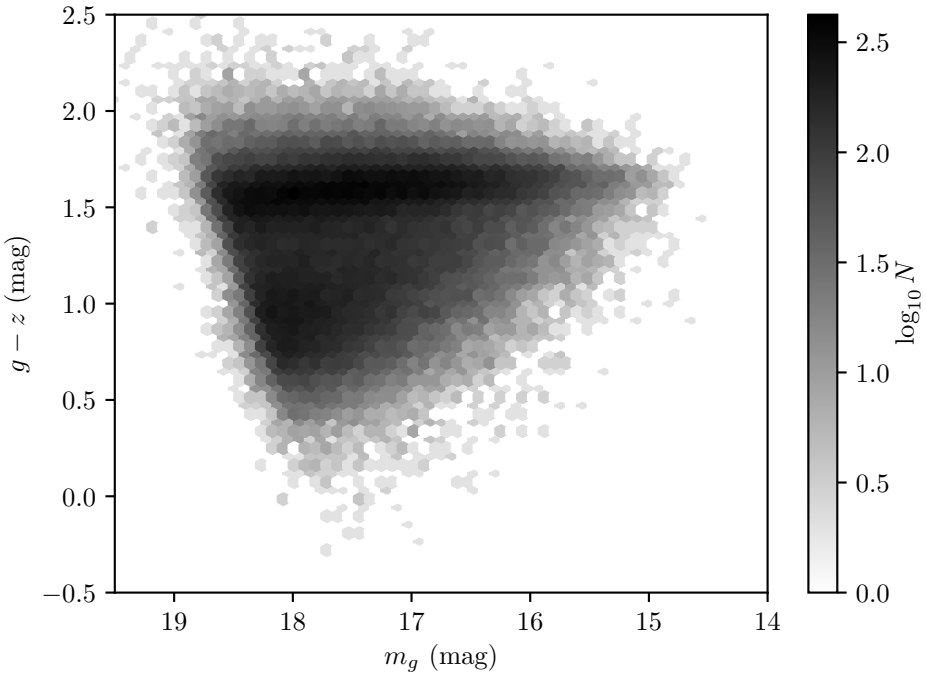

Figure 1.3 Galaxy $g - z$ colour as a function of apparent g band galaxy magnitude m_g for local galaxies (within ∼300 Mpc) in the Sloan Digital Sky Survey. The binned distribution of galaxies in the colour-magnitude space is shown, colour-coded according to the logarithm of the number of galaxies in each bin. A prominent red sequence can be seen spanning a broad range of magnitudes at a roughly constant colour of ∼1.6. Below this sequence is a more extended collection of bluer galaxies referred to as the blue cloud.

where [Fe/H] is the metallicity (as a logarithmic value relative to the solar value), N_{Fe} and N_{H} are the numbers of iron and hydrogen atoms, respectively, and $N_{\mathrm{Fe},\odot}$ and $N_{\mathrm{H},\odot}$ are the same quantities for our Sun. Objects with higher metallicity tend to have redder colours — metals preferentially absorb energy from higher-wavelength (bluer) regions of the object's spectrum and re-emit some of this energy at longer infrared wavelengths through a process known as line blanketing (Milne, 1928).

Galaxy colours and magnitudes are correlated, and can provide insight into their evolution. This colour-magnitude relation is shown in Figure 1.3 for galaxies in the nearby Universe (within ∼300 Mpc) from the Sloan Digital Sky Survey Data Release 14 (Abolfathi et al., 2018; Eisenstein et al., 2011; Doi et al., 2010; Gunn et al., 2006, 1998). The brightest galaxies are the reddest, indicating that they contain primarily old and/or metal-rich stellar populations. Galaxies that become this bright and red are thought to require growth through the merging of smaller, but similarly red early-

type galaxies (e.g. Naab et al., 2006; Cox et al., 2006). At fainter luminosities, there is a bimodal colour distribution, with some galaxies tightly grouped around redder colours (in what is known as the red sequence), and a less concentrated group with bluer colours (referred to as the blue cloud). Galaxies are thought to transition from the blue cloud to the red sequence as they stop forming stars and their existing stellar populations grow older. Schawinski et al. (2014) introduce two evolutionary paths that can halt star formation: the galaxy merges with another, which ejects the galaxy's gas and/or triggers a rapid bust of star formation that consumes all gas; or the galaxy may simply gradually convert all its gas reservoirs to stars and fail to retain or acquire gas for continued star formation. In summary, the colours and morphologies of galaxies are one set of present-day indicators of their varied evolutionary histories.

1.2.3 Sizes and shapes

Elliptical and disky galaxies have very different distributions of light — in ellipticals, much of the galaxy light is centrally concentrated and gradually tapers off with no well-defined boundary to the galaxy, while disky galaxies have a more uniform light distribution that truncates sharply at the edge of the disk. Despite these very different behaviours, both light distributions can be described by a common parameterization: the Sérsic profile (Sersic, 1968). In a Sérsic profile, the galaxy surface brightness μ[4] depends on radius r following the equation

$$\mu(r) = \mu_e \exp\Big[-b_n \Big\{(r/r_e)^{1/n} - 1\Big\}\Big],$$

where n is a measure of how concentrated the light is, r_e is the effective radius, or the radius that encloses half the total light of the galaxy, and μ_e is the surface brightness at r_e. The constant b_n is defined by the complete and incomplete gamma functions, $\Gamma(n)$ and $\gamma(n, x)$, respectively, such that $\Gamma(2n) = 2\gamma(2n, b_n)$. When fitting the 2D profile of a galaxy that is not perfectly round, the radius r can be expressed by a semi-major axis a and semi-minor axis b such that $r = \sqrt{ab}$, and then the galaxy's roundness can be quantified by the ellipticity $e = 1 - b/a$ (Graham & Driver, 2005). For ideal disky galaxies, the light follows an exponential profile with $n = 1$. In the largest elliptical galaxies, the light distribution is well represented by a Sérsic profile

[4]Surface brightness is the magnitude per unit area, in units of mag arcsec^{-2}.

with $n = 4$, which is a special case known as the de Vaucouleurs profile[5].

Figure 1.4 shows sizes as a function of luminosity for a variety of stellar systems. Note the sharp boundary in the distribution of systems along the lower right side of the figure: this "zone of avoidance" is where the densities produced by those sizes and luminosities are too high for stellar systems to survive without collapsing. In contrast, the lack of data populating the upper left region of the plot is largely driven by the sensitivity limits of current telescopes, as any objects inhabiting this size-luminosity space would be remarkably diffuse with very low surface brightness. The biggest, brightest galaxies are early-types and are found just outside the zone of avoidance, indicating they are as dense as possible for stellar systems of that size. At intermediate magnitudes, the galaxy population includes slightly more diffuse small ellipticals and late-type systems. The galaxy size-luminosity relation is well separated by the small star clusters that are concentrated around effective radii of a few pc and absolute magnitudes $-12 \leq M_V \leq -5$. However, a few unusual, very dense objects appear in the region connecting these star clusters to the larger elliptical galaxies. These include nuclear star clusters (NSCs; discussed in greater detail throughout the rest of this thesis) and ultra compact dwarf galaxies (UCDs), both of which have unclear origins, but may serve as an important link between galaxies and the star clusters that inhabit them.

1.3 A fundamental galaxy component: the central massive object (CMO)

Despite the diversity among galaxies, they all seem to share a common feature: in their centres lurk objects that, although spatially small, are remarkably dense. These central massive objects (CMOs) come in two flavours: supermassive black holes (SMBHs) and nuclear star clusters (NSCs, also known as compact stellar nuclei). SMBHs are found in the most massive galaxies (above $\sim 10^{10} M_{\odot}$), while NSCs are preferentially found in galaxies with masses between $\sim 10^{7}$ and $\sim 10^{10} M_{\odot}$. At intermediate masses, some galaxies, including our own Milky Way, contain both an SMBH and NSC (Neumayer & Walcher, 2012; Ghez et al., 2008; Schödel et al., 2007). Figure 1.5 shows examples of the many types of galaxies that all host some form of CMO.

[5]This $n = 4$ profile was actually defined in de Vaucouleurs (1948), before the more general Sérsic profile.

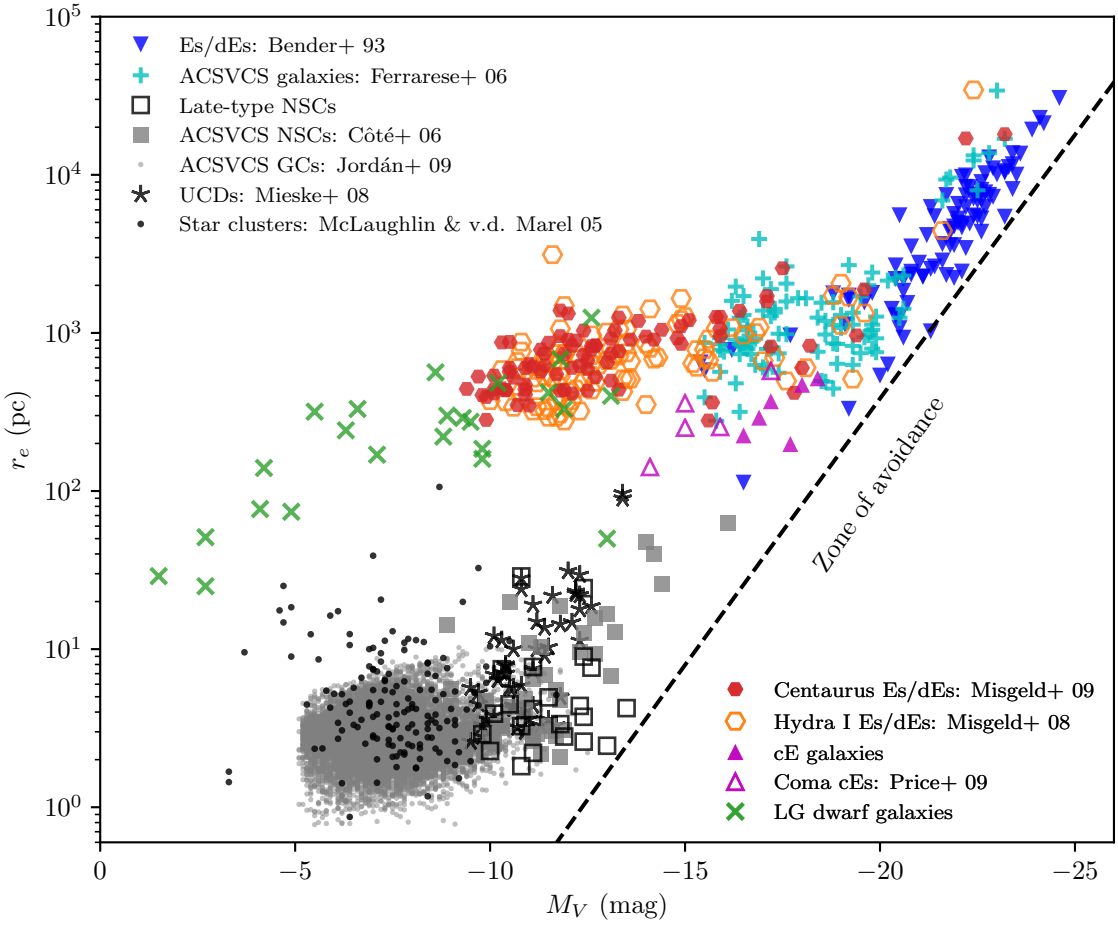

Figure 1.4 Size-luminosity relations for a variety of stellar systems, created using the data compiled in Misgeld & Hilker (2011). Effective radius r_e is shown as a function of absolute V band magnitude M_V. Different colours and shapes of the data points indicate different object morphologies, ranging from the largest elliptical galaxies to small stellar clusters. The black dashed line indicates the approximate boundary of the zone of avoidance where no stellar systems exist, calculated using Equation 8 from Misgeld & Hilker (2011) and approximate stellar mass-to-light-ratios for the luminosity range of interest.

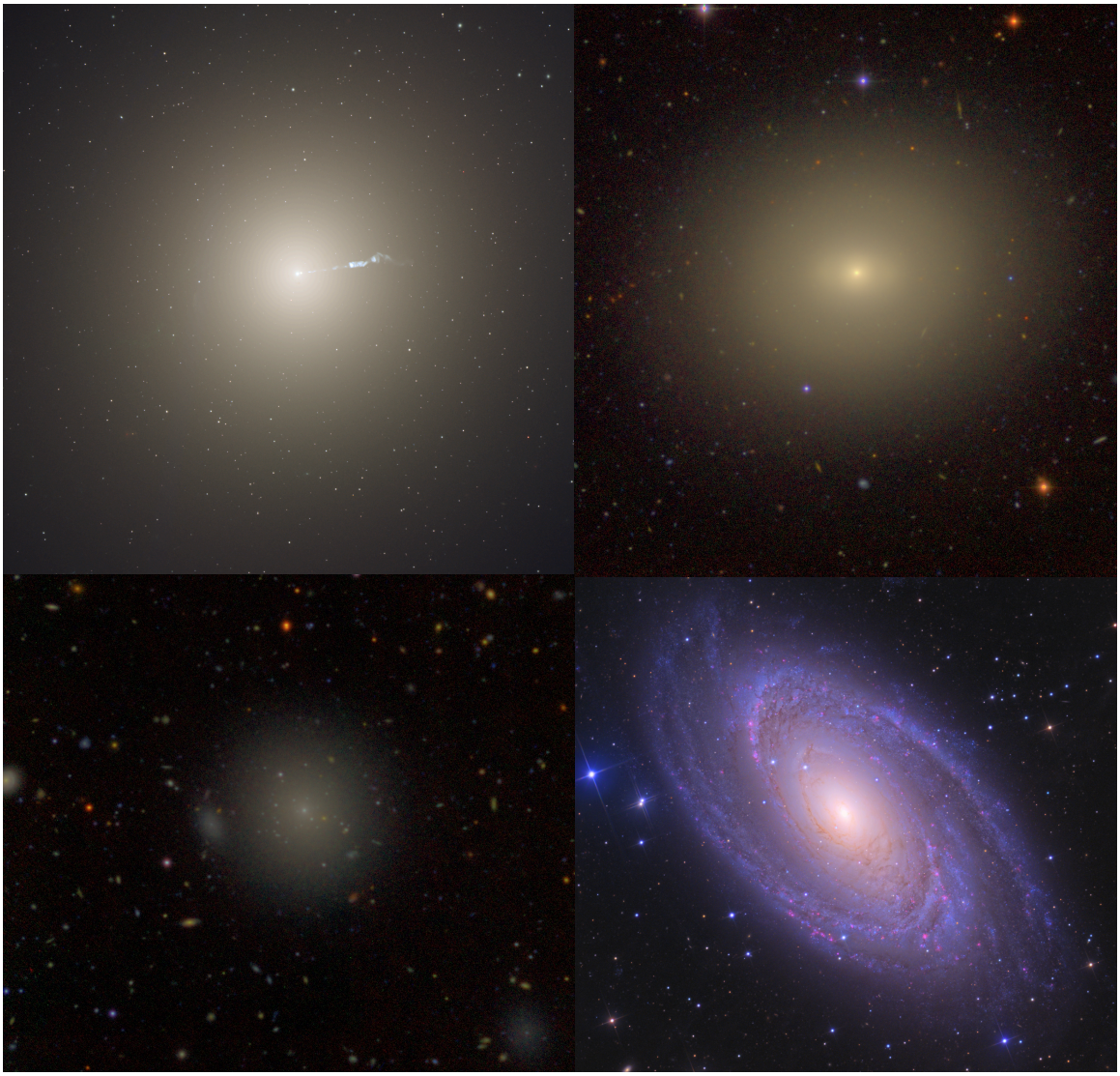

Figure 1.5 Examples of galaxies that host different types of CMOs. Note that the images are not to scale, although the apparent size differences among the galaxies are broadly consistent with their true scales. *(top left)* The giant elliptical M87, known to harbour a SMBH. (Image credit: NASA, ESA and the Hubble Heritage Team (STScI/AURA)) *(top right)* VCC 784, one of the nucleated galaxies studied in this thesis. Recent velocity measurements support the presence of an SMBH in this galaxy in addition to the NSC. *(bottom right)* The spiral galaxy M81, which is a confirmed host of an SMBH but likely contains an NSC as well. (Image credit: Ken Crawford) *(bottom left)* VCC 1539, another nucleated galaxy in this thesis. Its CMO appears to consist solely of an NSC.

SMBHs are the most massive black holes, with masses of at least $10^6 M_\odot$ up to $\sim 10^{10} M_\odot$ and gravitational force so strong that not even light can escape them. They can only be detected indirectly, such as through their gravitational influence on velocities of gas and stars in the innermost regions of galaxies, or from the intense radiation of heated material accreting onto the SMBH. NSCs, on the other hand, are small stellar systems, with typical half-light radii of 2–5 pc (Böker et al., 2004; Côté et al., 2004, 2006), and some as large as tens of parsecs (Geha et al., 2002; Georgiev & Böker, 2014). These small radii, coupled with their typical masses ($\sim 10^5 - 10^8 M_\odot$), make NSCs some of the densest stellar systems ever observed (Böker et al., 2004; Walcher et al., 2005).

CMOs appear to be ubiquitous, essential components of galaxy evolution. For SMBHs, multiple studies over the past few decades have detected not only the SMBHs themselves (in virtually every large galaxy observed with sufficient resolution), but also tight correlations between their masses and the velocity dispersions, masses, or luminosities of their host galaxies (e.g., Kormendy & Richstone, 1995; Magorrian et al., 1998; Ferrarese & Merritt, 2000; Gebhardt et al., 2000; Tremaine et al., 2002; McConnell & Ma, 2013; van den Bosch, 2016; Saglia et al., 2016). These SMBHs can potentially have far-reaching effects on the growth of their host galaxies via feedback that halts or regulates star formation throughout the galaxy (King, 2003; McQuillin & McLaughlin, 2012; Terrazas et al., 2016).

NSCs are found preferentially in less massive galaxies than SMBHs, but appear just as common at galaxy luminosities $-19.5 \lesssim M_B \lesssim -11$. Early imaging surveys with the Hubble Space Telescope (HST) found NSCs in ∼50–60% of spiral galaxies, with slightly higher nucleation fractions among the later morphologies (Phillips et al., 1996; Carollo et al., 1997, 1998). More recent surveys have increased that fraction to 65–80% (Böker et al., 2002; Seth et al., 2006; Georgiev & Böker, 2014). For early-type galaxies, the nucleation fraction is similar, at 70–80%(Côté et al., 2006; Turner et al., 2012; den Brok et al., 2014; Muñoz et al., 2015; Eigenthaler et al., 2018). Intriguingly, NSC masses also appear to be related to their host galaxy masses, following roughly the same relation that exists for SMBHs (Côté et al., 2006; Wehner & Harris, 2006; Rossa et al., 2006; Turner et al., 2012). The existence of similar mass relationships involving NSCs and SMBHs implies that these CMOs may share similar formation processes, with a gradual transition from SMBH- to NSC-dominated CMOs as galaxy profiles transition smoothly from central light deficits to excesses (Glass et al., 2011). However, recent work suggests that the NSC-galaxy mass relation can vary with

galaxy morphology, with late-type galaxies having a shallower mass relation than early-types (Georgiev et al., 2016) and more concentrated galaxies having brighter — and presumably more massive — NSCs (den Brok et al., 2014). Other studies have found that SMBHs and NSCs follow relations with different slopes (Balcells et al., 2007; Scott & Graham, 2013; Leigh et al., 2012; Graham, 2012), so the exact nature of CMOs remains unclear.

Because SMBHs can only be detected indirectly, their observed properties are generally limited to mass estimates. However, as stellar systems, NSCs can be quantified with a number of other observed properties, which further indicate a connection between NSCs and evolution of their hosts. For example, NSCs and galaxy colours seem to be loosely connected. While NSCs display a broad range of colours, they are usually somewhat bluer than their hosts (Lotz et al., 2004; Côté et al., 2006), suggesting that their stellar populations are younger than the underlying galaxy[6]. Detailed investigations of NSC ages, however, have yielded mixed results. Some NSCs show evidence of multiple stellar populations (Rossa et al., 2006; Walcher et al., 2006; Carson et al., 2015), although this can only be determined for resolved objects. Spectroscopic studies have measured ages ranging from 10 Myr to 12 Gyr, although, with a few exceptions, the NSCs ages are usually found to be younger than their host galaxies (Butler & Martínez-Delgado, 2005; Seth et al., 2006; Chilingarian et al., 2007; Chilingarian, 2009; Paudel et al., 2011; Guérou et al., 2015).

The relationship between NSCs and other compact stellar systems (such as globular clusters and ultra compact dwarf galaxies; GCs and UCDs) is also a matter of interest. NSCs are quite similar in size to most GCs, but tend to be brighter by $\sim$4 magnitudes (Böker et al., 2004; Georgiev & Böker, 2014). In contrast, UCDs are somewhat larger than NSCs, with half-light radii of 10–100 pc (Drinkwater et al., 2003; Mieske et al., 2008), and yet have similar masses ($2 \times 10^6 \leq M_\star \leq 10^8 M_\odot$). The optical colours of NSCs, GCs and UCDs in the central region of the Virgo Cluster are remarkably similar (Roediger et al., 2017). A number of groups have proposed that GCs could be the progenitors of NSCs (see below), and at least some UCDs are thought to be the stripped NSCs of disrupted nucleated dwarf galaxies (Goerdt et al., 2008; Pfeffer & Baumgardt, 2013).

How CMOs form is still not well understood. SMBHs are found even in the early Universe (Fan et al., 2001), meaning they must have built up their masses

[6]Although, this can also be attributed to a steeper initial mass function (Goudfrooij & Kruijssen, 2014).

very rapidly from some initial seed black hole. There are currently two ideas as to the nature of these seeds: they may be solar-mass black holes that grow via the accretion of matter, or intermediate-mass black holes formed via giant gas clouds that collapse directly into black holes without ejecting any mass in a supernova explosion (Volonteri, 2010; Greene, 2012). These two theories of SMBH seeds predict different numbers of SMBHs, particularly in galaxies with masses below $10^{10} M_{\odot}$. Therefore, the study of CMOs in low-mass galaxies is essential to constrain their origins.

For NSCs, there are also two broad scenarios for their formation: star cluster infall or *in situ* formation. In the cluster infall scenario, GCs spiral into the galaxy's core via dynamical friction and then merge to form a massive central star cluster (e.g., Tremaine et al., 1975; Oh & Lin, 2000; Lotz et al., 2001; Capuzzo-Dolcetta & Miocchi, 2008; Antonini et al., 2012; Gnedin et al., 2014). The alternative scenario is that the NSCs develop from gas funneled into the galactic centre, possibly as the result of a merger (e.g., Mihos & Hernquist, 1994; Milosavljević, 2004; Schinnerer et al., 2008; Bekki, 2015). In this picture, stellar feedback can regulate the growth of the nucleus, potentially producing multiple stellar populations and leading to the $M - \sigma$ relation, involving the galaxy stellar mass M and velocity dispersion σ, via the same mechanisms proposed for the growth of SMBHs (McLaughlin et al., 2006; Bourne & Power, 2016). Recently, Guillard et al. (2016) proposed a *wet migration* model in which massive clusters form outside the galaxy center, but retain gas reservoirs to continue forming stars as they fall to the center, merging with other clusters in the process. In reality, NSC formation is likely more complex that idealized models suggest, and some studies have indicated that NSCs form probably through a mixture of scenarios (den Brok et al., 2014; Antonini et al., 2015; Cole et al., 2016). It is also possible that NSCs form and grow together with an SMBH, with one object eventually becoming the dominant CMO due to mechanisms involved in that particular galaxy's evolution (e.g., Nayakshin et al., 2009). These various formation mechanisms can imprint different signatures on the stellar populations and structures of NSCs, so an understanding of the present-day properties of NSCs can provide insight into which formation mechanisms are most prevalent in galaxy evolution.

1.4 The Virgo Cluster: an ideal case for the study of NSCs and structure

At a distance of 16.5 Mpc (Mei et al., 2007; Blakeslee et al., 2009), the Virgo Cluster is a convenient target for studying NSCs and their parent galaxies. It is near enough for NSCs, with typical angular sizes of $\sim 0\farcs05$ (4 pc at the distance of Virgo; Côté et al., 2006), to be marginally resolved by HST. The cluster is a rich environment that contains a vast collection of nucleated galaxies spanning a broad range of luminosities and structural parameters. It is also a dynamically young cluster, with multiple subclusters still in the process of accreting into the primary cluster halo (Binggeli et al., 1987; Gavazzi et al., 1999; Boselli et al., 2014). This means that it is possible to study how NSCs and galaxies have been shaped by their environment, by sampling objects deep in the cluster core (which therefore have spent a longer time in the cluster) as well as those farther from the centre in the still-merging substructures (which have entered the cluster environment more recently).

As our nearest galaxy cluster, Virgo has been the target of numerous observing programs. Three recent or ongoing surveys of Virgo Cluster galaxies can provide both high-resolution, space-based imaging and deep, ground-based imaging in broadband filters that span the ultraviolet (UV) to near-infrared (IR) wavelength region. The first of these studies used the Advanced Camera for Surveys (ACS) instrument on HST to carry out the *ACS Virgo Cluster Survey* (ACSVCS, Côté et al., 2004, 2006; Ferrarese et al., 2006a,b). A follow-up HST program, *Virgo Redux*, expanded the ACSVCS dataset by adding UV and IR imaging. The latest, and most extensive, program is the *Next Generation Virgo Cluster Survey* (NGVS, Ferrarese et al., 2012) which used the MegaCam instrument on the 3.6m Canada France Hawaii Telescope (CFHT) to acquire deep, wide-field u^*giz imaging over 104 deg^2 of the Virgo Cluster. Using the NGVS, it is possible to identify and study NSCs belonging to galaxies of unprecedented faintness (R. Sánchez-Janssen et al. 2018, submitted). The NGVS also makes it possible to study the structural and photometric properties of not just NSCs, but also GCs and UCDs (Durrell et al., 2014; Liu et al., 2015; Zhang et al., 2015).

With these state-of-the-art surveys and its rich, diverse galaxy population, the Virgo Cluster presents a unique opportunity to investigate the structural and photometric properties of NSCs, and their relationship to their host galaxies, GCs, and UCDs, within a complete mass- and volume-limited sample.

1.5 Overview of thesis

The overarching goal of this thesis is to use extensive high resolution and wide field imaging of nucleated galaxies in the Virgo cluster to refine our understanding of the nature of CMOs throughout different environments and their role in galaxy evolution. To accomplish this, I focus on a few key research questions: What can the stellar populations of NSCs tell us about their origins and how they grow? What do NSCs and their host galaxies look like in different environments? Can the physical processes implemented in ΛCDM cosmological simulations replicate the observed distribution of galaxies throughout these environments? These questions are addressed through the work in this thesis as follows:

Chapter 2 presents a comprehensive analysis of NSC stellar populations in early-type galaxies and their connections to the host galaxy populations as well as other compact stellar systems to gain insight into the most important formation scenarios for these NSCs. This analysis uses the most extensive sample of UV, optical and near-IR imaging for NSCs to date, which provides firmer constraints on the ages, masses, and chemical compositions of NSCs — properties that are least understood in these early-type NSCs, which are particularly challenging to observe.

Chapter 3 presents a new identification of the substructures within the Virgo Cluster, a critical component of understanding the role of environment in shaping NSCs and their galaxies throughout the cluster. The unprecedented depth of the NGVS and its expanded catalogue of Virgo Cluster galaxies provides better sampling of the cluster structure, leading to the detection of potential new substructures in Virgo. With no single established method in the literature for identifying substructures, the novel substructure classification technique presented in this chapter satisfies the need for an objective, homogeneous comparison of substructure in the Virgo Cluster and simulated Virgo analogues from the `Illustris` simulation, which is used to explore whether ΛCDM can successfully explain the growth of structure on these spatial scales.

Chapter 4 expands upon the goals of the previous two chapters, examining the properties of NSCs and their galaxies throughout these substructures to determine the role of environment in forming and shaping NSCs, as well as their relationship to their hosts. This analysis capitalizes on the extensive dataset available in the NGVS. With 3,490 Virgo galaxies — over 700 of which are nucleated — with measured structural and photometric parameters, this is the first study of NSCs and their environments

with a single, self-consistent, homogeneous dataset.

Finally, Chapter 5 summarizes the updated interpretation of how NSCs and galaxies form and evolve together, and how environment influences this co-evolution, as informed by the results of this thesis. An outline of potential future analysis and observations to address outstanding questions is also presented.

Chapter 2

Virgo Redux: The Masses and Stellar Content of Nuclei in Early-Type Galaxies from Multi-Band Photometry and Spectroscopy

This chapter is a lightly modified version of Spengler et al. (2017) and presents an analysis of 39 NSCs and their early-type hosts in the Virgo Cluster using ten broad-band filters: F300W, F475W, F850LP, F160W, u^*griz, and K_s. I describe the *Virgo Redux* program, which provides high-resolution UV and NIR imaging. Combining this data with optical and NIR imaging from the *ACS Virgo Cluster Survey* and the *Next Generation Virgo Cluster Survey*, I estimate masses, metallicities and ages using simple stellar population (SSP) models. For 19 NSC, I also compare to SSP parameters derived from Keck and Gemini spectra to validate the photometrically-derived parameters. The sample galaxies in this chapter were selected based on the nucleation classifications produced in Côté et al. (2006). The analysis benefits from unpublished spectra provided by P. Côté and the spectra from Liu et al. (2016) and Toloba et al. (2016). The 1D surface brightness profiles were created by P. Côté and L. Ferrarese. Parametric fits to the final composite profiles were produced by P. Côté, although I was responsible for producing the composite profiles themselves.

2.1 Introduction

Over the past few decades, numerous studies of galaxies with a variety of morphologies have established nuclear star clusters (NSCs) as a widespread feature in 70–80% of intermediate- and low-mass galaxies (Phillips et al., 1996; Carollo et al., 1997, 1998; Böker et al., 2002; Seth et al., 2006; Côté et al., 2006; Turner et al., 2012; Georgiev & Böker, 2014; den Brok et al., 2014; Muñoz et al., 2015). Their prevalence, and the observed correlation between their properties and those of their host galaxies, indicate that NSCs play an essential role in galaxy evolution. Intriguingly, the NSC-galaxy mass relation follows roughly the same relation that exists for supermassive black holes (SMBHs; Côté et al., 2006; Wehner & Harris, 2006; Rossa et al., 2006; Turner et al., 2012), suggesting that NSCs and SMBHs are collectively a population of central massive objects (CMOs) that are formed by similar processes. However, other studies have found that SMBHs and NSCs follow different relations (Balcells et al., 2007; Scott & Graham, 2013; Leigh et al., 2012; Graham, 2012), so the exact nature of CMOs remains unclear. To better understand these CMOs and their role in the growth of their host galaxies, it is necessary to expand and improve the current sample of mass estimates so that these mass scaling relations can be robustly quantified.

There are two scenarios commonly invoked to form NSCs: star cluster infall or *in situ* formation. In the cluster infall scenario, GCs spiral into the galaxy's core via dynamical friction and then merge to form a massive central star cluster (e.g., Tremaine et al., 1975; Oh & Lin, 2000; Lotz et al., 2001; Capuzzo-Dolcetta & Miocchi, 2008; Antonini et al., 2012; Gnedin et al., 2014). The alternative scenario is that the NSCs form directly in the galactic centre from gas that is accreted there, possibly as the result of a merger (e.g., Mihos & Hernquist, 1994; Milosavljević, 2004; Schinnerer et al., 2008; Bekki, 2015). In simulations of this scenario, stellar feedback can regulate the growth of the nucleus by periodically heating gas and preventing its collapse into stars, potentially producing multiple stellar populations. It also leads to the $M - \sigma$ relation, which relates CMO mass (M) with the galaxy's velocity dispersion (σ), via the same mechanisms thought to drive the growth of SMBHs (McLaughlin et al., 2006; Bourne & Power, 2016). Recently, Guillard et al. (2016) proposed a *wet migration* model in which massive clusters form outside the galaxy center, but retain gas reservoirs to continue forming stars as they fall to the center, merging with other clusters in the process. In reality, NSC formation is likely more complex than idealized models suggest, with NSC samples displaying properties consistent with

formation via a mix of processes (den Brok et al., 2014; Antonini et al., 2015; Cole et al., 2016). Ultimately, each of these scenarios leaves a different signature on the observed sizes, shapes, and stellar content of NSCs, so quantifying these properties in observed NSCs is the key to understanding their formation.

While refinements to the simulations are always welcome, a robust test of any formation model is impossible until we have a large database of NSCs with accurately measured parameters based on high-quality, homogenous data. Unfortunately, such studies are observationally challenging. Given their compact sizes, NSCs are only marginally resolved, even with HST, in all but the nearest galaxies. Bright galaxies present an additional challenge, as their NSCs must be separated from the high underlying surface brightness of their hosts. In addition, large sample sizes are required for a meaningful statistical analysis of NSC properties. While it is possible to acquire spectroscopic observations with sufficient signal to noise ratio (SNR) for age and metallicity measurements, most spectroscopic studies of NSCs have concentrated on small samples of nearby galaxies (e.g., Seth et al., 2006) or limited surveys of more distant systems (Paudel et al., 2011). Multi-band imaging is thus an attractive alternative since it avoids the long observation times needed for spectroscopy, making it possible to efficiently characterize statically meaningful samples of NSCs.

Fortunately, multiple recent surveys of the Virgo Cluster provide an extensive set of this multi-band imaging for nucleated galaxies. The first of these studies used the Advanced Camera for Surveys (ACS) instrument on HST to carry out the *ACS Virgo Cluster Survey* (ACSVCS, Côté et al., 2004, 2006; Ferrarese et al., 2006a,b). A follow-up HST program, *Virgo Redux*, expanded the ACSVCS dataset by adding UV and IR imaging. The latest, and most extensive, program is the *Next Generation Virgo Cluster Survey* (NGVS, Ferrarese et al., 2012) which used the MegaCam instrument on the 3.6m Canada France Hawaii Telescope (CFHT) to acquire deep, wide-field u^*giz imaging over 104 deg^2 of the Virgo Cluster. The Virgo Cluster's relative proximity (16.5 Mpc Mei et al., 2007; Blakeslee et al., 2009), means that it is near enough for NSCs, with typical sizes of $\sim 0\farcs05$ (4 pc Côté et al., 2006), to be marginally resolved by HST and have their structural properties estimated. Additionally, by using the NGVS, it is possible to identify and study NSCs belonging to galaxies of unprecedented faintness (R. Sánchez-Janssen et al. 2018, submitted). The NGVS also makes it possible to study the structural and photometric properties of not just NSCs, but also GCs and UCDs (Durrell et al., 2014; Liu et al., 2015; Zhang et al., 2015). The NGVS also includes deep r-band and infrared (K_s) imaging for a subset of the NGVS

fields (Muñoz et al., 2014), which provide additional measurements to reduce the uncertainty in the stellar population estimates.

These multi-band data provide a measure of an object's energy output in various broad wavelength passbands, serving as a rough outline of its spectral energy distribution (SED). The SED of a stellar population is dictated by a host of properties, including its initial mass function (IMF), chemical composition, dust content, and detailed star formation history. The method of SED fitting aims to recover these properties by comparing observed SEDs to model spectra with known parameters. While a detailed knowledge of the full spectrum is necessary for a complete understanding of an object and its evolutionary history, even a coarse sampling of the SED with broadband photometry can provide useful constraints on important properties such as stellar mass (e.g., Taylor et al., 2011; Mendel et al., 2014), age, and metallicity (e.g., Li et al., 2007; Salim et al., 2007; Crockett et al., 2011; Kaviraj et al., 2012; Fan & de Grijs, 2014). The inclusion of UV or IR wavelengths are especially useful for improved age and metallicity measurements (e.g., Anders et al., 2004; Kaviraj et al., 2007a; Georgiev et al., 2012; de Meulenaer et al., 2014), or estimates of the star formation history (e.g., Yi et al., 2005; Kaviraj et al., 2007b). No matter what data are used to sample the SED, the precise choice of comparison model — and some assumptions applied during the SED fitting procedure — may introduce ambiguities in the derived parameters (Conroy & Gunn, 2010; Fan & de Grijs, 2012; Powalka et al., 2016). Nevertheless, SED fitting using broadband photometry can be a powerful method of characterizing the stellar populations of stellar systems, particularly in situations where spectroscopic measurements are challenging or impractical.

In this chapter, I combine all available data from the ACSVCS, Virgo Redux, and NGVS (including NGVS-IR) for 39 nucleated early-type galaxies observed in the various surveys. The combined dataset consists of observations in up to 10 filters spanning the UV, optical, and near-IR regions. With high-resolution imaging from HST, and deep, wide-field imaging from CFHT, I am able to estimate masses, ages and metallicities for the NSCs and their host galaxies in a systematic and homogeneous way. Additionally, for a subset of the targets, I use high quality optical spectra acquired with the 10m Keck and 8m Gemini telescopes to validate the photometrically derived parameters.

This chapter is organized as follows. §2.2 summarizes the sample and observations, while §2.3 describes the isophotal and 2D decomposition methods for measuring structural and photometric parameters. In §2.4, I describe the reduction and analysis

Table 2.1 Summary of Imaging

Telescope	Instrument	Field of View	Filters	Scale (arcsec px^{-1})	FWHM ($''$)	N_{gal}
HST	ACS-WFC	$202'' \times 202''$	F475W, F850LP	0.05	0.1	39
HST	WFPC2-PC	$35'' \times 35''$	F255W, F300W	0.05	0.08	37
HST	NICMOS-NIC1	$11'' \times 11''$	F160W	0.03	0.095	38
CFHT	MegaCam	$0.^{\circ}96 \times 0.^{\circ}94$	u^*griz	0.187	≤ 1	39
CFHT	WIRCam	$21' \times 21'$	K_s	0.186	≤ 0.7	6

Summary of telescopes and instruments used to collect the images analyzed in this paper. All MegaCam images have seeing better than $1''$ but FWHM varies with filter; the median seeing ranges from $0''.54$ in i to $0''.88$ in u^*. Note that two galaxies (VCC 1185 and VCC 1627) are missing WFPC2 observations due to a loss of guiding during the observation; similarly, VCC 1627 is missing NICMOS data due to a guiding failure. Only six objects have K_s-band imaging because WIRCam observations are available for only the central 4 deg^2 of the Virgo cluster (Muñoz et al., 2014).

of various ground-based spectroscopic observations available for a subset of the NSCs. In §2.5, I describe my SED-fitting process and present results on NSC properties measured from photometry and spectroscopy. These results are discussed in greater detail in §2.6. I summarize my findings in §2.7 and conclude with some directions for future work.

2.2 Data and Observations

2.2.1 Sample Selection and Properties

The 39 program galaxies were selected from three imaging surveys of the Virgo cluster that together span the UV, optical and IR regions (i.e., wavelength in the range 0.3–2.2 μm). Figure 2.1 shows giz colour images created from NGVS data with the different HST instrument footprints overlaid. The wide spectral coverage of the data enables more precise determination of stellar population properties, particularly ages and metallicities, which have a well-known degeneracy for old or intermediate-age populations, such as those expected for many NSCs. Figure 2.2 demonstrates the sensitivity of our filter set to differences in theoretical spectra for simple stellar populations (SSPs) of various ages and metallicities. The observational details of each program are explained in the following subsections, with some general information summarized in Table 2.1.

Here I focus on the target selection, which is largely determined by the ACSVCS

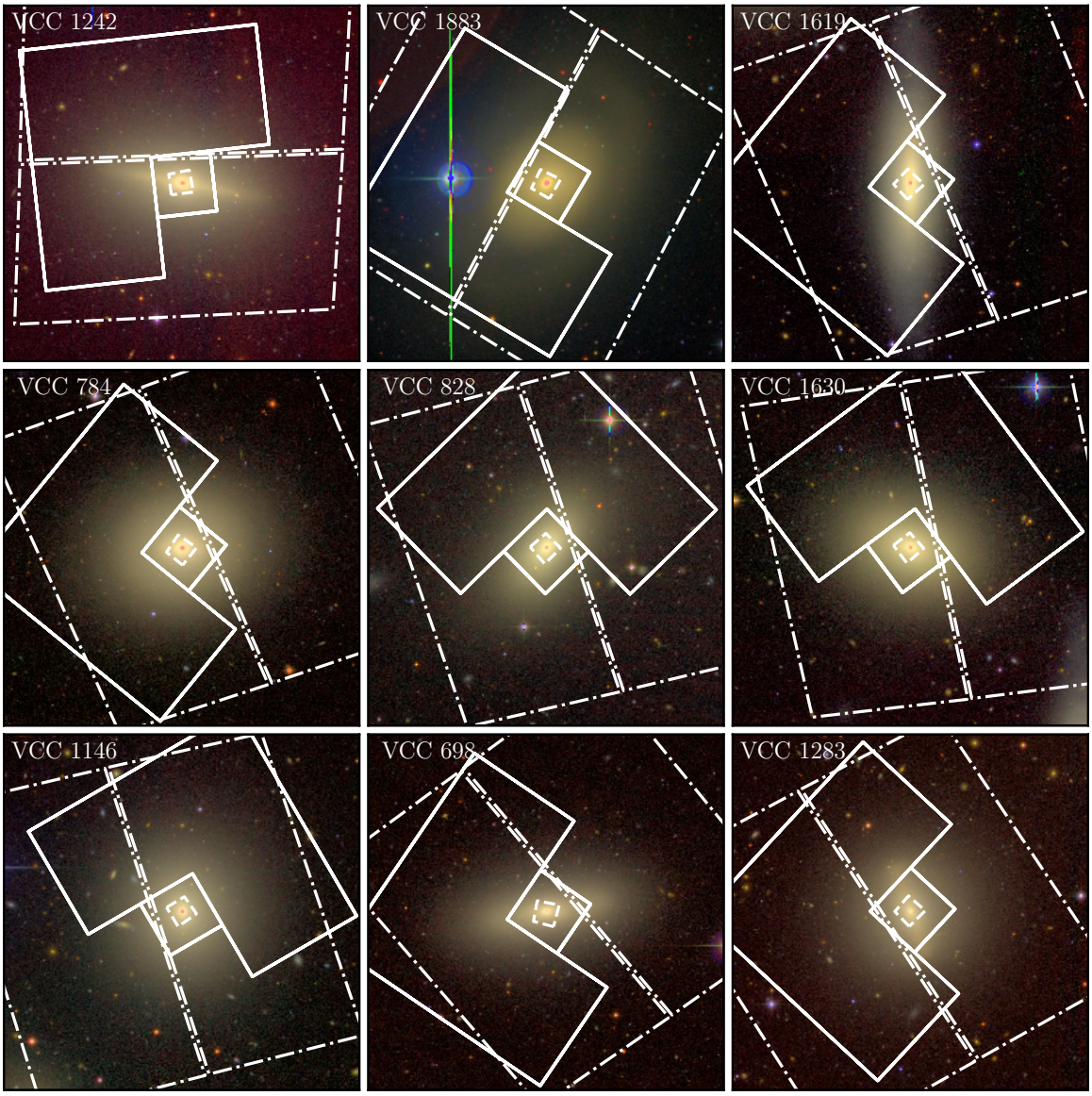

Figure 2.1 CFHT/MegaCam *giz* colour images with HST instrument footprints overlaid. Galaxies are shown in order of decreasing luminosity in the F475W filter (from left to right and top to bottom). Note that the colourmap scaling is not absolute across all panels. Each image measures $3\farcm75 \times 3\farcm75$ (18×18 kpc) and thus covers only a small fraction of the MegaCam 1 deg^2 field. ACS/WFC footprints are shown as dashed-dotted lines, NICMOS footprints are show as dashed lines, and WFPC2 footprints are shown as solid lines. In all cases, north is up and east is to the left.

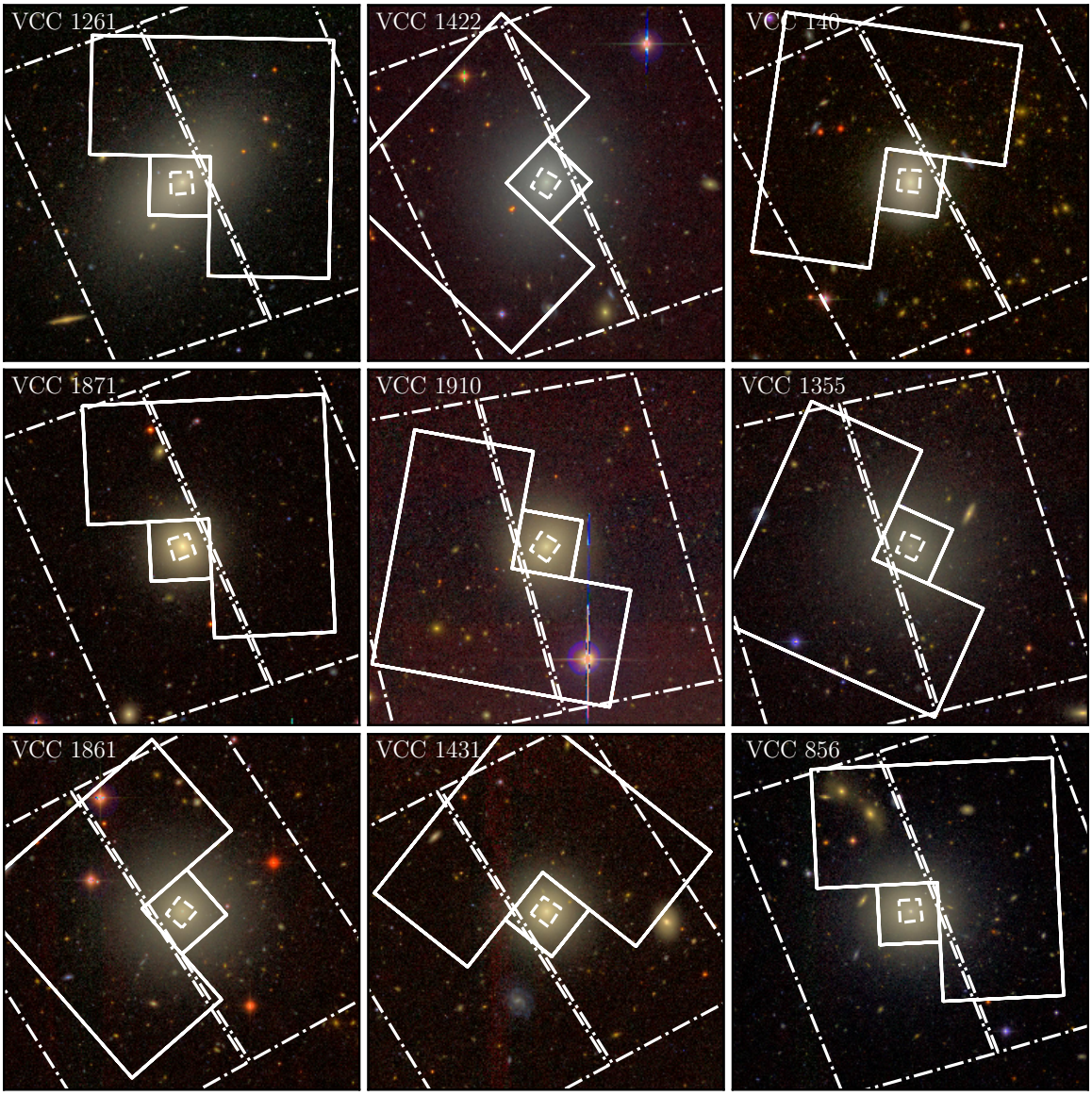

Figure 2.1 *Continued.*

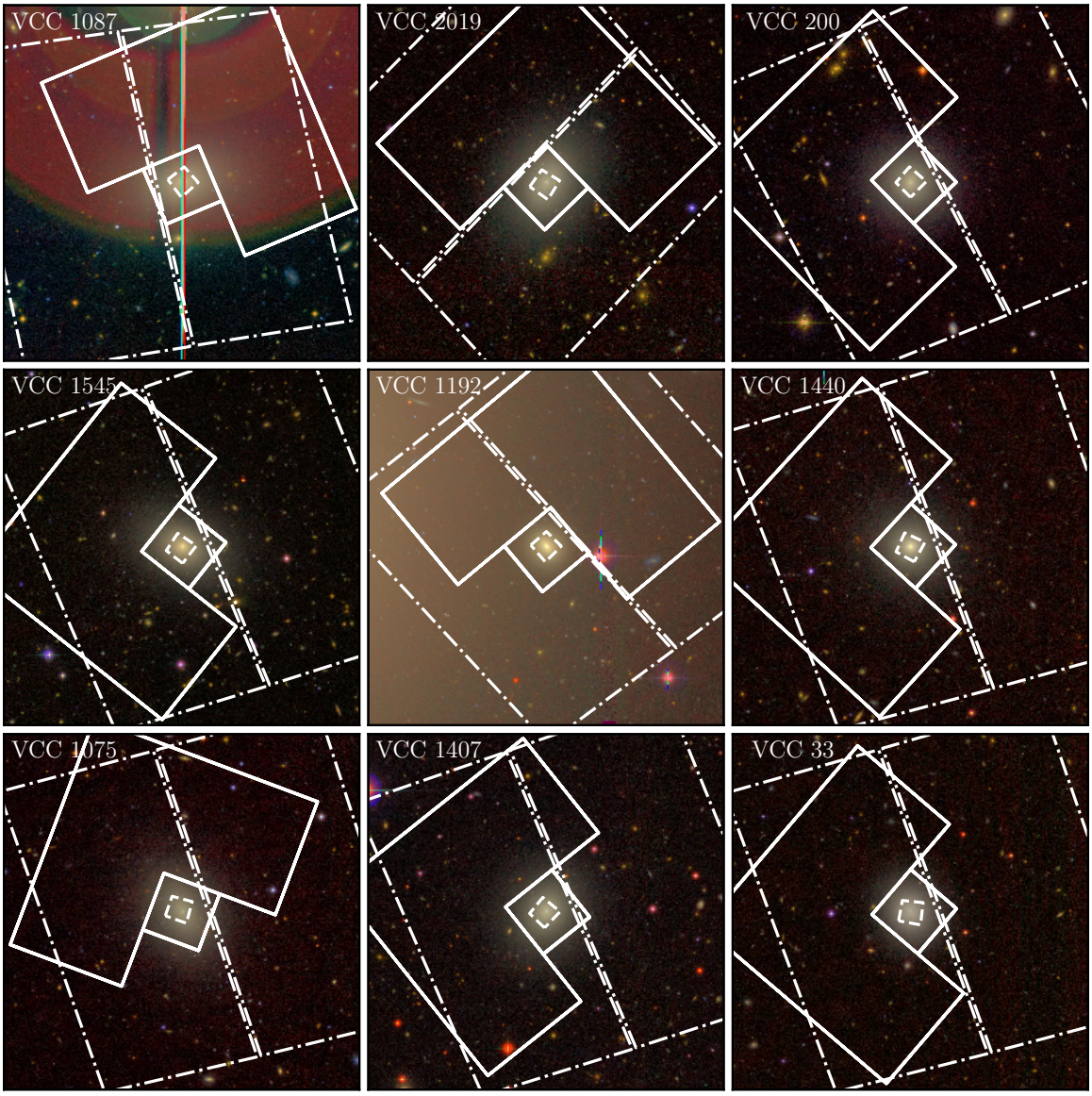

Figure 2.1 *Continued.*

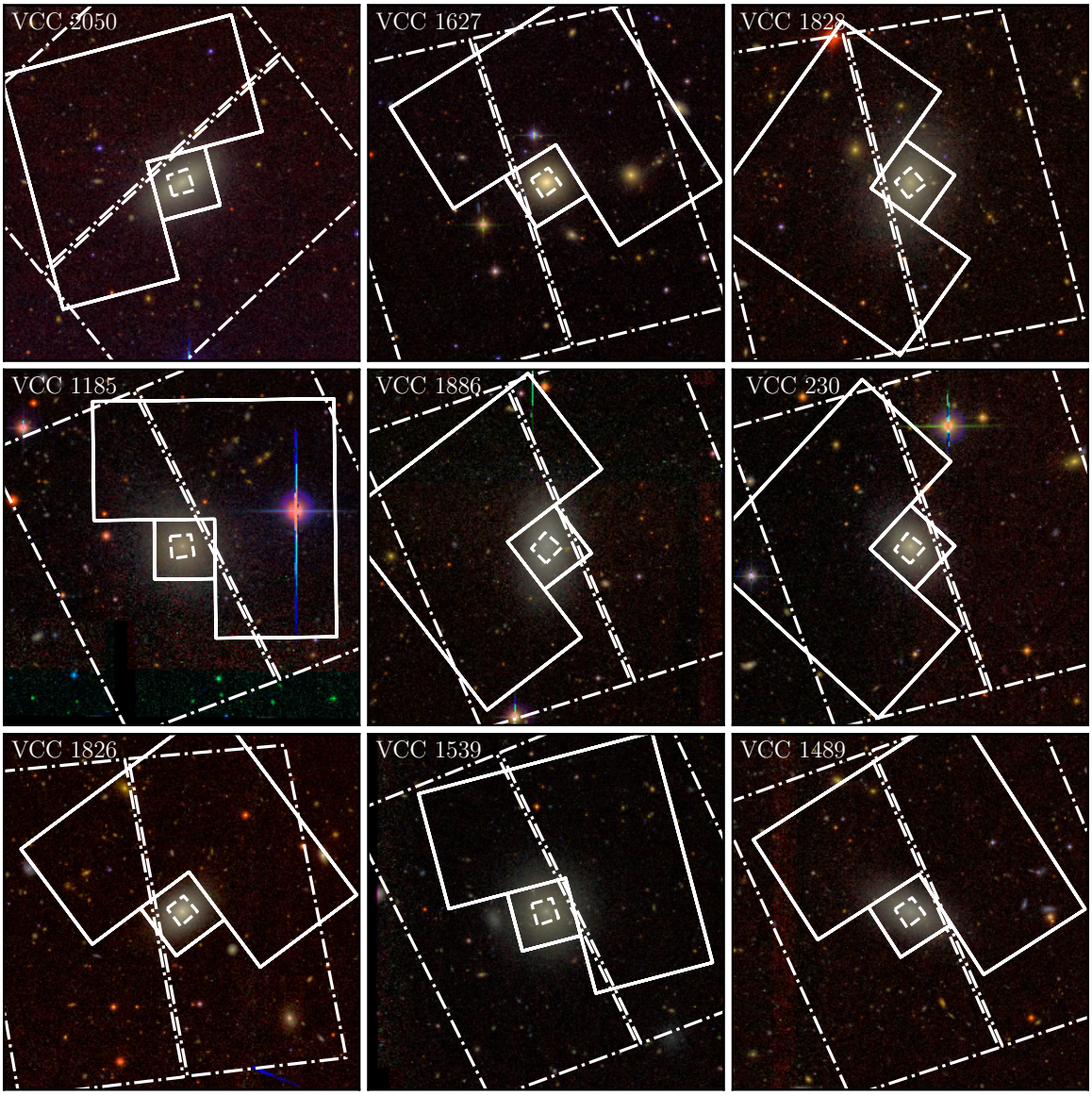

Figure 2.1 *Continued.*

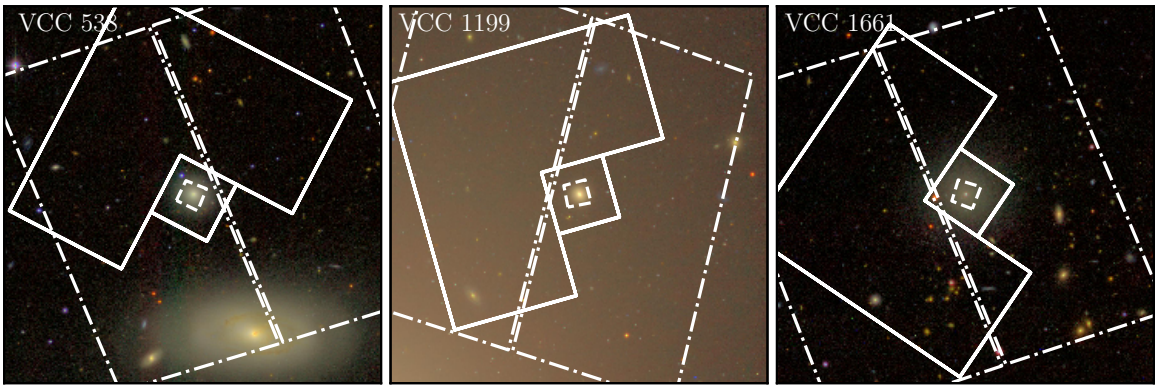

Figure 2.1 *Continued.*

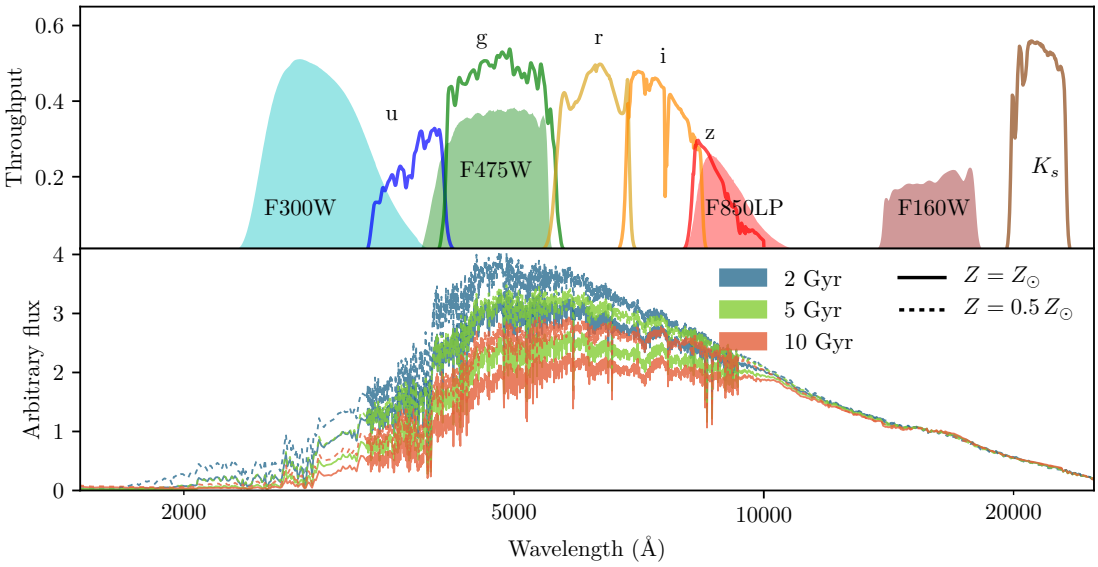

Figure 2.2 *(Top panel).* Passbands for the different filters used in this chapter. Filled curves show the HST filters while open curves show the CFHT filters. Note that the K_s filter is only available for the six galaxies that fall inside the 2 deg $\times$ 2 deg region around M87. *(Bottom panel).* Model spectra for selected SSPs using the Bruzual & Charlot (2003) models with a Chabrier IMF. Three different ages are shown: 2, 5, and 10 Gyr (as the blue, green, and red lines, respectively). Solid lines denote SSPs with solar metallicity, while dotted lines correspond to populations with half solar metallicity. The spectra have been normalized at 1.6 μm in the F160W filter.

sample and classifications. The ACSVCS imaged 100 early-type galaxies in the Virgo Cluster in the F475W ($\sim g$) and F850LP ($\sim z$) filters (Côté et al., 2004), covering a range of early-type morphologies (E, S0, dE, dE,N, dS0, dS0,N) with magnitudes $9.3 \lesssim B_T \lesssim 15.7$. The survey is 44% complete down to its limiting magnitude of $M_B = -15.2$.

The sample originates from the 51 galaxies in ACSVCS that were classified as clearly nucleated (`Type Ia`) in Côté et al. (2006), meaning that a King model profile (King, 1966) was successfully fitted to the galaxy's nuclear component. While other ACSVCS galaxies were classified as likely, or possibly, nucleated, I opted to focus only on the unambiguously nucleated galaxies, as these NSCs can be most easily modeled and separated from their host galaxies. The sample was further reduced by restricting ourselves to galaxies within the ~ 100 deg^2 NGVS survey footprint — a total of 39 galaxies. Some basic information for these galaxies, including coordinates, velocities from the NASA/IPAC Extragalactic Database (NED), and morphologies from Binggeli et al. (1985, hereafter BST85), NED and Kim et al. (2014) is given in Table 2.2. The more recent numerical classifications from Kim et al. (2014), which are based on SDSS imaging, confirm that these are predominantly early-type systems: 21 are dwarf ellipticals (classifications in the form 4XX), while another eight are considered ellipticals (1XX). The remaining nine galaxies classified by Kim et al. (2014) are disk galaxies (2XX), or lenticulars in the other classifications listed here. The sample galaxies are distributed throughout the cluster, as shown in Figure 2.3. Figure 2.4 shows the magnitude distribution of the galaxies selected for this analysis compared to the full set of `Type 1a` galaxies, the rest of the ACSVCS, and the general population of early-type galaxies in Virgo. The 39 selected galaxies span the full magnitude range of nucleated galaxies detected in the ACSVCS and are well distributed across this range.

2.2.2 HST/ACS Imaging

The ACSVCS carried out imaging with the ACS instrument (Ford et al., 1998) in its Wide Field Channel (WFC) mode (Program ID = 9401). ACS/WFC provides high resolution (FWHM $\approx 0\farcs1$) imaging across a $202'' \times 202''$ field of view with a pixel scale of $0\farcs049$ px^{-1}, although the final data products have been drizzled to a scale of $0\farcs05$ px^{-1}. Each galaxy was observed for a single orbit with two exposures per filter, plus an additional 90 s exposure in F850LP to correct any central saturation. Total

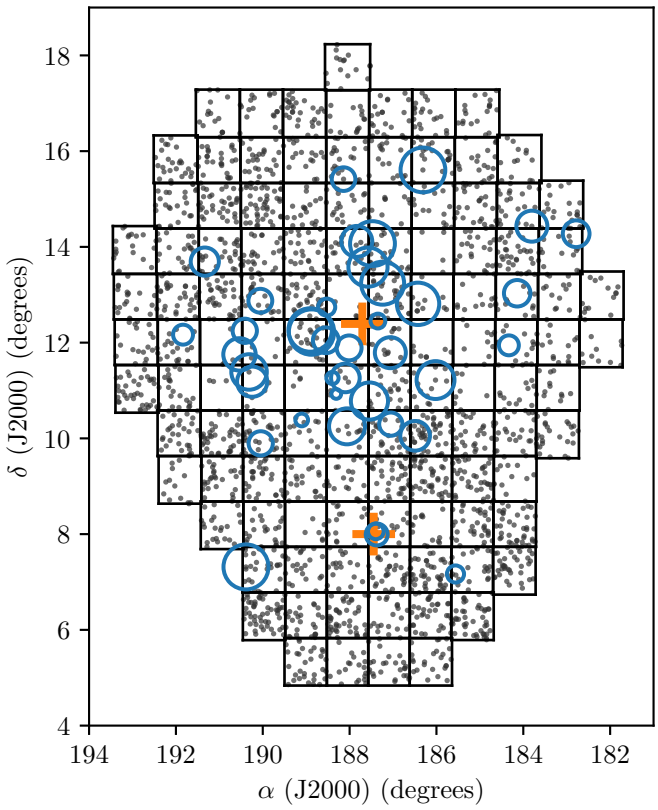

Figure 2.3 Distribution of the 39 galaxies selected for this analysis overlaid on the NGVS fields. Open blue circles indicate each sample galaxy. The size of the circles corresponds to galaxy brightness. M87 (VCC 1316) and M49 (VCC 1226) are labeled with orange crosses. Gray points show NGVS galaxies brighter than $M_g \simeq -14.5$.

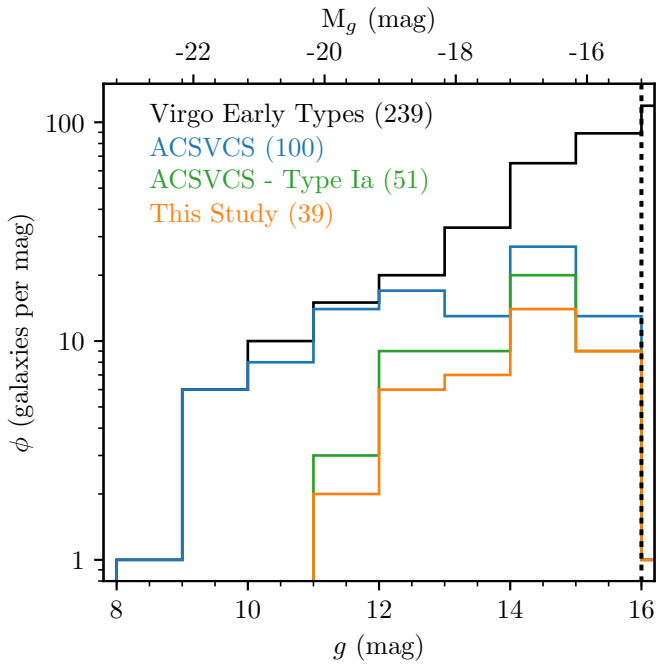

Figure 2.4 Magnitude distribution for the full ACSVCS sample, 51 nucleated galaxies (`Type Ia`) and 39 `Type Ia` galaxies analyzed in this work. For comparison, I also show the complete sample of Virgo early-type galaxies from Janz & Lisker (2008, 2009).

Table 2.2 Basic Data for Program Galaxies

VCC	Other	α(2000) (h:m:s)	δ(2000) $^\circ$:$'$:$''$)	B_T (mag)	$E(B-V)$ (mag)	V_r (km/s)	BST85	NED	EVCC
33	IC3032	12:11:07.8	+14:16:29.3	14.67	0.037	1186	d:E2,N:	E?	411
140	IC3065	12:15:12.6	+14:25:58.3	14.30	0.037	993	SO1/2(4)	S0?	200
200	...	12:16:33.7	+13:01:53.7	14.69	0.030	16	dE2,N	dE2,N	411
230	IC3101	12:17:19.7	+11:56:36.5	15.20	0.028	1429	dE4:,N:	dE4:,N:	401
538	NGC4309A	12:22:14.7	+07:10:01.7	15.40	0.020	750	E0	E0	100
698	NGC4352	12:24:05.0	+11:13:05.1	13.60	0.026	2070	S01(8)	SA0: sp	200
784	NGC4379	12:25:14.7	+15:36:26.7	12.67	0.024	1074	S01(2)	S0- pec:	200
828	NGC4387	12:25:41.7	+12:48:37.9	12.84	0.033	565	E5	E5	100
856	IC3328	12:25:57.9	+10:03:13.5	14.25	0.024	1025	dE1,N	dE,N	411
1075	IC3383	12:28:12.3	+10:17:51.5	15.08	0.027	1844	dE4,N	dE4,N	401
1087	IC3381	12:28:14.9	+11:47:23.3	14.31	0.027	675	dE3,N	dE,N	401
1146	NGC4458	12:28:57.6	+13:14:30.9	12.93	0.023	677	E0-1	E0-1	100
1185	...	12:29:23.5	+12:27:02.9	15.68	0.023	500	dE1,N	dE1	401
1192	NGC4467	12:29:30.3	+07:59:34.3	15.04	0.023	1423	E3[a]	E2	200
1199	...	12:29:35.0	+08:03:28.8	15.50	0.022	1401	E2[a]	E2	100
1242	NGC4474	12:29:53.6	+14:04:06.9	12.60	0.042	1611	S01(8)	S0 pec:	200
1261	NGC4482	12:30:10.3	+10:46:46.1	13.56	0.029	1871	d:E5,N	dE,N	400
1283	NGC4479	12:30:18.4	+13:34:39.4	13.45	0.029	876	SB02(2)	SB(s)0!0!:?	210
1355	IC3442	12:31:20.2	+14:06:54.7	14.31	0.034	6210	dE2,N	E0:	...
1407	IC3461	12:32:02.7	+11:53:24.3	15.49	0.032	1019	dE2,N	dE,N	401
1422	IC3468	12:32:14.2	+10:15:05.2	13.64	0.031	1288	E1,N:	E1,N:	210
1431	IC3470	12:32:23.4	+11:15:46.7	14.51	0.051	1505	E?	E?	401
1440	IC798	12:32:33.4	+15:24:55.5	15.20	0.028	382	E0[a]	E0	100
1489	IC3490	12:33:13.9	+10:55:42.5	15.89	0.034	80	dE5,N?	E?	401
1539	...	12:34:06.7	+12:44:29.7	15.68	0.032	1491	dE0,N	dE0,N	401
1545	IC3509	12:34:11.5	+12:02:56.2	14.96	0.042	2000	E4[a]	E4	401
1619	NGC4550	12:35:30.6	+12:13:15.0	12.50	0.040	459	E7/S01(7)	SB0!0!:sp LINER	200
1627	...	12:35:37.3	+12:22:55.3	15.16	0.039	236	E0[a]	E0	100
1630	NGC4551	12:35:38.0	+12:15:50.4	12.91	0.039	1176	E2	E:	100
1661	...	12:36:24.8	+10:23:04.8	15.97	0.020	1457	dE0,N	dE0,N	401
1826	IC3633	12:40:11.3	+09:53:46.0	15.70	0.017	2033	dE2,N	dE2,N	401
1828	IC3635	12:40:13.4	+12:52:29.1	15.33	0.037	1569	dE2,N	dE,N	401
1861	IC3652	12:40:58.6	+11:11:04.2	14.37	0.029	629	dE0,N	E	401
1871	IC3653	12:41:15.7	+11:23:14.0	13.86	0.030	588	E3	E3	100
1883	NGC4612	12:41:32.8	+07:18:53.5	12.57	0.025	1775	S01(6)	(R)SAB0!0!	200
1886	...	12:41:39.4	+12:14:50.6	15.49	0.033	914	dE5,N	dE5,N	401
1910	IC809	12:42:08.7	+11:45:15.3	14.17	0.031	206	dE1,N	E	401
2019	IC3735	12:45:20.4	+13:41:33.6	14.55	0.022	1895	dE4,N	E?	411
2050	IC3779	12:47:20.6	+12:09:59.1	15.20	0.023	1156	dE5:,N	dE5:,N	400

Key to columns: (1) VCC identification number, (2) Alternate names in the NGC, IC or UGC catalogs, (3) right ascension, (4) declination, (5) total B magnitude from BST85, (6) extinction from Schlafly & Finkbeiner (2011), (7) recessional velocity from NED, (8) morphological classification from BST85, (9) morphological classification from NED, and (10) morphological classification from Kim et al. (2014).

[a] Compact, low-luminosity E (M32-type) galaxy from Table XIII of BST85.

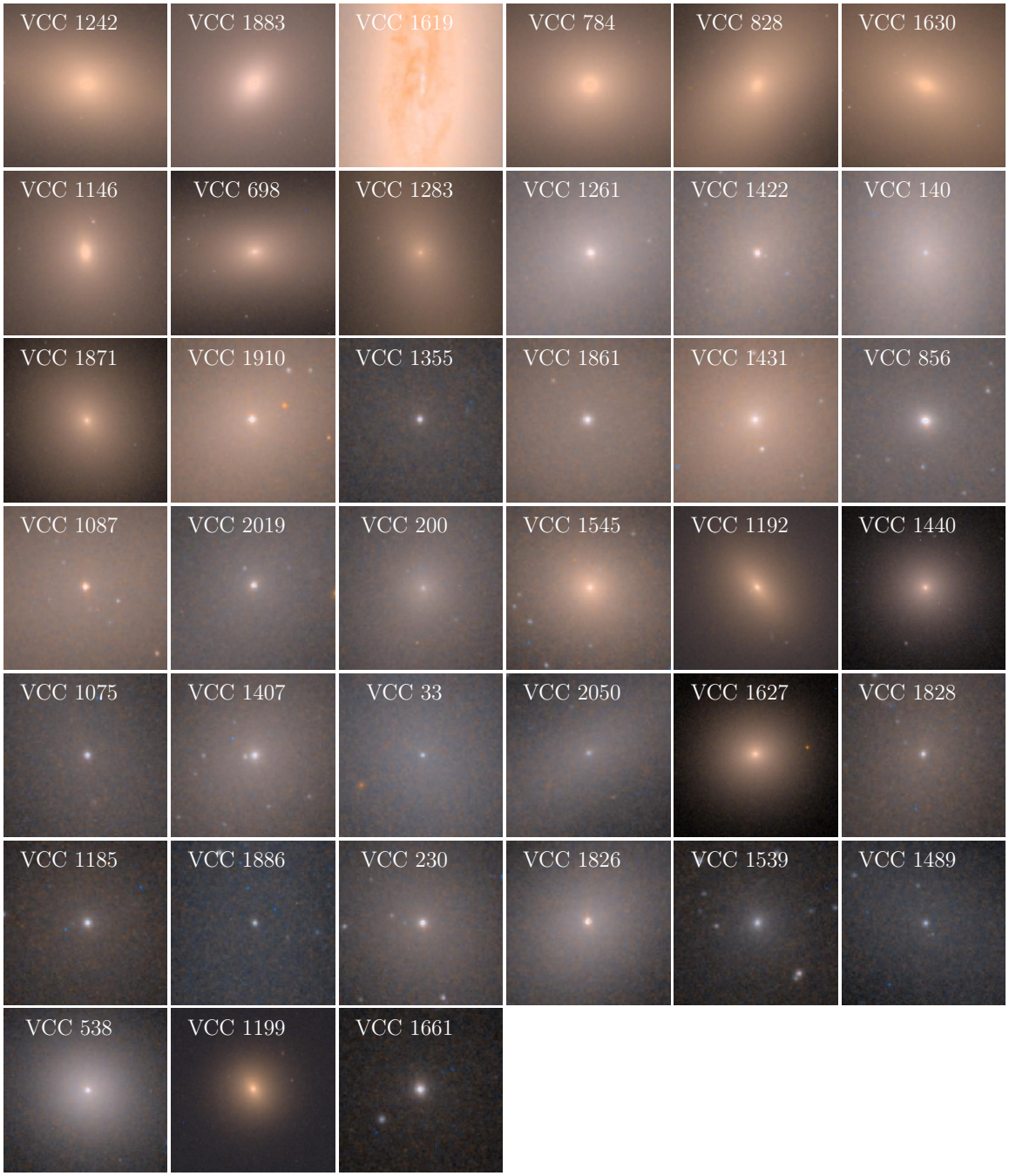

Figure 2.5 HST colour images focusing on the central $20'' \times 20''$ (1.6×1.6 kpc) region of each program galaxy, sorted by decreasing F475W luminosity. In all images, north is up and east is to the left.

exposure times were 750 s in F475W and 1210 s in F850LP. The centre of each object was initially positioned on the WFC1 detector, one of the WFC's two 2048 × 4096 detectors, roughly 15–20″ from the chip gap, depending on galaxy brightness.

After correcting for any small offsets ($\lesssim$ 0.2 px) between exposures, the images were drizzled and cosmic ray corrected using *multidrizzle* in `PyRAF`. Sky subtraction was omitted in the drizzling process because many target galaxies in the full ACSVCS sample dominate the field of view. The drizzling process also applies a kernel to the images when distributing flux onto the final science image. The ACSVCS reduction created science images with both the "Gaussian" and "Lanczos3" kernels. For this chapter, I use images created with the "Gaussian" kernel, which allows for more effective bad pixel repair and therefore better estimates of the light profile in the central galaxy regions where the nucleus dominates. Point spread functions (PSFs) were generated using DAOPHOT II (Stetson, 1987, 1993) and archival observations of the globular cluster 47 Tucanae, and were allowed to have second order variations across the field. For each galaxy a PSF was retrieved at the nucleus' position on the chip. Additional details of the observational techniques and data reduction are available in Jordán et al. (2004a).

With its excellent resolution, high signal-to-noise ratio (SNR) and comparatively wide field of view, the ACSVCS data are the clear choice for reference images in the 2D decompositions of our program galaxies. Figure 2.5 shows 20″ × 20″ (1.6×1.6 kpc) cutouts of the nuclear regions for the dataset. The NSCs are prominent and resolved in most of the galaxies, which aids in modeling and separating the nucleus and galaxy components. I therefore use the ACS F475W image to measure one set of structural parameters that are then applied to the full dataset. This procedure is described fully in §2.3.2.

2.2.3 CFHT Imaging: MegaCam and WIRCam

Full details on the NGVS observing strategy and data reduction procedures can be found in Ferrarese et al. (2012) and Muñoz et al. (2014). Here, I briefly explain the salient details of the observations.

NGVS was allocated ∼900 hours between 2008 and 2013 with the MegaCam (Boulade et al., 2003) instrument on CFHT. The survey was designed to cover 104 deg^2 of the Virgo Cluster in the u^*, g, r, i, and z bands — an area that fully covers the region within the virial radii of the Virgo A and B subclusters (which are cen-

tred on the galaxies M87 and M49, respectively; see Figure 2.3). Unfortunately, bad weather and dome shutter problems made it impossible to complete the r-band imaging; therefore, full-depth r-band exposures are available for only $\approx 9\,\mathrm{deg}^2$. Complete coverage of the survey region is available in the u^*giz bands.

Each MegaCam exposure covers $0.^\circ96 \times 0.^\circ94$ on the sky using a mosaic of 36 CCDs arranged in a 4×9 grid. With a pixel scale of $0.''187\,\mathrm{px}^{-1}$ and typical seeing $\sim 0.''7$, the PSF is well sampled. The data are of good quality, with a median seeing of $0.''88$, $0.''80$, $0.''54$, and $0.''75$ in the u^*, g, i and z bands, respectively. The long exposure data used in this work have exposure times between 2055 s in i and 6402 s in u^*, and reach limiting surface brightnesses of 29.3, 29.0, 27.4, and 26.0 AB mag arcsec^{-2} in the u^*, g, i and z bands, respectively.

All NGVS data were reduced using the *Elixir* pipeline which carries out bias subtraction, flat fielding, bad pixel masking, and applies a fringing correction to the i- and z-band images. A number of stacked science images were then produced using the *MegaPipe* pipeline (Gwyn, 2008). In this pipeline, all frames are matched to the Sloan Digital Sky Survey (SDSS) DR7 astrometric and photometric catalogs to produce astrometric corrections and photometric zeropoints. For this paper, we use the "global background subtraction" stacks. In these stacks, a background map, estimated from median-combined archival MegaCam imaging processed with *Elixir*, is scaled to each frame and then subtracted. While these stacks tend to have higher sky residuals (a few percent of the background level) compared to those created using *Elixir-LSB*, I nevertheless use them for this analysis because they are available for all filters — *Elixir-LSB* requires the input images to be acquired in a specific dither pattern, which was not possible for the r band. Despite the sky residuals, the chosen stacks have superior photometric accuracy compared to the other stacking techniques. PSFs were created using DAOPHOT and stars in each frame detected by both DAOPHOT and SExtractor. As with the ACS PSFs, second order variations were permitted, and a PSF in each filter was generated for the position of the nucleus.

The NGVS includes K_s-band imaging from the Wide-Field InfraRed Camera (WIRCam; Puget et al., 2004) over the $2^\circ \times 2^\circ$ region centred on M87 (Muñoz et al., 2014). WIRCam has a $21' \times 21'$ field of view covered by four detectors with a pixel scale of $0.''3\,\mathrm{px}^{-1}$. A total of 36 pointings were made between December 2009 and July 2010. Each pointing was built from a series of 25 s exposures observed in specific dither patterns designed to cover the $45''$ chip gap between detectors, ensure that each pixel covers a different sky region for each exposure, and enable precise sky subtrac-

tion. Total exposure times were 2700 s per pointing. The raw images were processed for dark subtraction, nonlinearity correction, flat fielding, and bad pixel masking using the `'I'iwi` 2.0 pipeline[1] . After removing cosmic rays and satellite trails, sky subtraction was performed in two steps. First a median sky for each science frame was calculated using designated sky pointings, and then subtracted from the target frames. The sky-subtracted frames were then stacked and all sources identified in the stacked image were masked in each sky frame. New median skies were created with the masked sky frames and subtracted from the stacked target images. Additional corrections for variations in the amplifiers of each detector and large-scale sky fluctuations were also applied. Astrometric and photometric calibrations were performed by comparing to 2MASS, resulting in an astrometric accuracy better than $0\farcs02$ and zeropoint uncertainty lower than 0.02 mag.

Images with seeing better than $0\farcs7$ were selected to create four stacked frames that mirror the NGVS MegaCam positions and field of view for the $2\,\mathrm{deg} \times 2\,\mathrm{deg}$ region around M87. These final images have a pixel scale $0\farcs186$ and median seeing $0\farcs54$. The limiting surface brightness is $\sim$24.0 AB mag arcsec^{-2} in K_s. PSFs were generated separately for each of these four fields using PSFex (Bertin, 2011). Spatial variations in the PSFs were modeled with a seventh-order polynomial. As with the other datasets, I extracted PSFs at the pixel position of each nucleus.

2.2.4 HST/WFPC2 and HST/NICMOS Imaging

A follow-up program to the ACSVCS, *Virgo Redux*, re-imaged the sample of ACSVCS galaxies at the UV and IR wavelengths (Program ID = 11083). UV observations were carried out using the F300W filter on the Wide Field Planetary Camera 2 (WFPC2). Galaxies were centred on the Planetary Camera (PC) chip, which has a finer pixel scale ($0\farcs046\,\mathrm{px}^{-1}$) than the adjacent Wide Field (WF) chips ($0\farcs1\,\mathrm{px}^{-1}$). Each galaxy was observed for one orbit; three exposures were collected in order to aid in cosmic ray rejection, for a total exposure times of 2100 s. My analysis uses only the PC chip, which measures $35'' \times 35''$, since it contains the nucleus and most of the galaxy signal for all our targets. The data were retrieved from the Hubble Legacy Archive, which provides PC exposures that have been combined and scaled to $0\farcs05\,\mathrm{px}^{-1}$ using *multidrizzle* in `PyRAF`. Flat-fielding, bias and dark subtraction, removal of saturated or bad pixels, and shutter shading corrections were performed

[1] `http://www.cfht.hawaii.edu/Instruments/Imaging/WIRCam/IiwiVersion2Doc.html`

using the *calwp2* software as part of the standard WFPC2 calibration pipeline. No sky subtraction was performed since the sky has a negligible contribution to the NSC counts.

Virgo Redux also includes IR imaging taken in the F160W filter ($\sim H$) with the Near-Infrared Camera and Multi-Object Spectrometer (NICMOS; Thompson, 1994). Images were acquired using the NIC1 detector which has a native pixel scale of $0\farcs043\,\mathrm{px}^{-1}$ and a field of view of $11'' \times 11''$. Each galaxy was observed in a series of 12 exposures, in a spiral dither pattern, for a total exposure time of 1920 s. One additional image was taken offset $2'$ from the galaxy centre to aid in background sky measurements. For some of the larger, brighter galaxies in the survey, this offset pointing is likely contaminated with galaxy light, so I excluded it from our background measurements. An additional 13 exposures, offset $\sim 5'$ from the galaxy centre, were taken in parallel with the WFPC2 imaging to serve as blank sky fields. Flat-fielding, bias and dark corrections and other reduction steps were performed using the *calnica* pipeline in `IRAF`. NICMOS images also have a pedestal effect, appearing as a residual flat-field signature that differs for each quadrant on the detector and varies with time. This effect was corrected using *pedsub*. The final science images were created using *multidrizzle* and have a pixel scale of $0\farcs03\,\mathrm{px}^{-1}$. Note that the drizzling task was run without sky subtraction. Instead, a sky level based on the mean sky measured from the 13 exposures with $5'$ offsets was subtracted later. I created PSFs for all Virgo Redux images using the Tiny Tim package[2].

2.2.5 Ground-Based Spectroscopy

For 19 of the NSCs in my sample, high-quality optical spectroscopy is available from three different ground-based instruments. While these data are only available for a subset of the objects, they provide an important point of comparison for the photometric results, allowing me to evaluate the robustness of the photometrically-determined masses, ages and metallicities (and vice versa). In a few cases, spectroscopy is available from multiple sources which allows me to assess the level of agreement among parameters derived from the different spectroscopic datasets.

Five NSCs were observed with the Integral Field Unit (IFU; Allington-Smith et al., 2002) within the Gemini Multi-Object Spectrograph (GMOS; Hook et al., 2004) on the Gemini South telescope during the 2008A and 2009A observing seasons. The

[2] `http://www.stsci.edu/hst/observatory/focus/TinyTim`

IFU's $7''\times\ 5''$ field of view, containing 1000 fibers, was centred on each object and rotated to align with the galaxy's semi-major axis. Another 500 fibers were configured in a $5''\times\ 3''$ field, offset by $1'$ from the centre of the science field. Observations were performed in the two-slit mode using the B600 grating ($600\,\mathrm{l\,mm^{-1}}$) and g' filter, although data from one slit were excluded because the key spectral features — H_β, Mgb, and Fe Lick indices — fell on a CCD with a number of bad columns and pattern noise. Four exposures for each nucleus were acquired, giving total exposure times between 1600 s and 8000 s. The final binned science spectra have a dispersion of $0.9\,\mathrm{\AA\,px^{-1}}$. Full details on the instrumental configuration and data reduction procedures are given in Liu et al. (2016).

Another 17 galaxies were observed with the Echellette Spectrograph and Imager (ESI; Sheinis et al., 2002) on the Keck II telescope during the 2003A and 2004A observing seasons. In its echelle mode, ESI offers 10 spectral orders, with complete wavelength coverage from 3900 to 10900 Å at a dispersion ranging from $0.15\,\mathrm{\AA\,px^{-1}}$ (for λ = 3900–4400 Å in order No. 15) to $0.39\,\mathrm{\AA\,px^{-1}}$ (for λ = 9500–11000 Å in order No. 6). The spectral dispersion, in units of velocity, is a nearly constant 11.5 km $\mathrm{s^{-1}}$ $\mathrm{px^{-1}}$. Object were observed with either a $0\farcs75\ \times\ 20''$ or a $1\farcs0\ \times\ 20''$ slit, giving an instrumental velocity resolution between 1.0 and 1.4 Å at ∼5200 Å. The processing of the raw data involved bias subtraction, finding and tracing the apertures, flat normalization, cosmic-ray removal, arc extraction, and spectral calibration. Reductions were carried out using the Mauna Kea Echelle Extraction package (MAKEE; Barlow & Sargent, 1997).

Lastly, seven NSCs were observed using the DEep Imaging Multi-Object Spectrograph (DEIMOS; Faber et al., 2003) on the Keck II telescope during the 2012A observing season. The observations, which were optimized for radial velocity and chemical abundance studies of star clusters in these galaxies, were carried out using the $600\,\mathrm{l\,mm^{-1}}$ grating centred at 7000 Å. When combined with the GG4455 filter, this set-up provided a wavelength coverage of 4800–9500 Å at a dispersion of $0.52\,\mathrm{\AA\,px^{-1}}$. Slit lengths were kept somewhat short, typically $\sim$4–$8''$, in order to place as many globular clusters, stars, and other point-like objects, including NSCs, as possible on each slit mask. A slit width of $0\farcs8$ was used in all cases. Exposure times varied between 3600 s and 4800 s, with the different exposure times meant to account for variations in the observing conditions (i.e., the seeing varied between $0\farcs6$ and $0\farcs9$). Additional observational details are presented in Toloba et al. (2016) and P. Guhatakurta et al. (2018, in preparation).

Table 2.3 Summary of Spectroscopic Observations

VCC	Telescope	Instrument	Grating	Dimenions (arcsec)	Θ (deg)	λ Range (Å)	Date (dd/mm/yyyy)	Exposure Time (sec)
33	Gemini-S	GMOS-IFU	g' filter + B600	$7''\times 5''$	115.0	3980 − 5520	22/2/2009	4400
33	Keck II	ESI	echelle	$1''\times 20''$	29.7	4020–7200	26/02/2003	1800
200	Keck II	ESI	echelle	$1''\times 20''$	165.0	4020–7200	17/03/2004	1800
230	Keck II	ESI	echelle	$1''\times 20''$	27.4	4020–7200	27/02/2003	2400
538	Keck II	ESI	echelle	$1''\times 20''$	60.6	4020–7200	26/02/2003	2100
1075	Keck II	DEIMOS	600ZD	$0\farcs8 \times 7\farcs2$	-1.9	4800–9500	23/4/2012	4500
1075	Keck II	ESI	echelle	$0\farcs75 \times 20''$	45.0	4020–7200	01/05/2000	1200
1185	Gemini-S	GMOS-IFU	g' filter + B600	$7''\times 5''$	77.0	3980 − 5520	25/2/2009	8400
1185	Keck II	ESI	echelle	$1''\times 20''$	28.2	4020–7200	26/02/2003	2700
1192	Keck II	ESI	echelle	$1''\times 20''$	37.6	4020–7200	26/02/2003	1800
1199	Keck II	ESI	echelle	$1''\times 20''$	45.0	4020–7200	26/02/2003	2100
1355	Gemini-S	GMOS-IFU	g' filter + B600	$7''\times 5''$	127.0	3980 − 5520	5/3/2009	8400
1407	Keck II	DEIMOS	600ZD	$0\farcs8 \times 4\farcs39$	-173.6	4800–9500	22/4/2012	3730
1407	Keck II	ESI	echelle	$0\farcs75 \times 20''$	68.0	4020–7200	01/05/2000	1800
1440	Keck II	ESI	echelle	$1''\times 20''$	28.9	4020–7200	26/02/2003	2100
1489	Keck II	ESI	echelle	$1''\times 20''$	60.5	4020–7200	27/02/2003	3600
1539	Gemini-S	GMOS-IFU	g' filter + B600	$7''\times 5''$	345.0	3980 − 5520	2/3/2009	8800
1539	Keck II	DEIMOS	600ZD	$0\farcs8 \times 4\farcs06$	119.2	4800–9500	21/4/2012	4800
1539	Keck II	ESI	echelle	$1''\times 20''$	46.0	4020–7200	17/03/2004	2100
1545	Gemini-S	GMOS-IFU	g' filter + B600	$7''\times 5''$	335.0	3980 − 5520	9/4/2008	3600
1545	Keck II	DEIMOS	600ZD	$0\farcs8 \times 5\farcs66$	-20.0	4800–9500	21/4/2012	3600
1545	Keck II	ESI	echelle	$1''\times 20''$	67.8	4020–7200	27/02/2003	2400
1627	Keck II	ESI	echelle	$1''\times 20''$	93.6	4020–7200	26/02/2003	2100
1826	Keck II	ESI	echelle	$1''\times 20''$	131.2	4020–7200	26/02/2003	2100
1828	Keck II	DEIMOS	600ZD	$0\farcs8 \times 6\farcs45$	-50.7	4800–9500	23/4/2012	4499
1828	Keck II	ESI	echelle	$0\farcs75 \times 20''$	75.0	4020–7200	30/04/2000	1800
1861	Keck II	DEIMOS	600ZD	$0\farcs8 \times 3\farcs86$	14.9	4800–9500	22/4/2012	3599
1871	Keck II	DEIMOS	600ZD	$0\farcs8 \times 4\farcs62$	14.9	4800–9500	22/4/2012	3599
2050	Keck II	ESI	echelle	$1''\times 20''$	127.0	4020–7200	26/02/2003	2400

Key to columns: (1) VCC identification number, (2) telescope, (3) spectrograph, (4) grating, (5) slit or IFU dimensions, (6) position angle, Θ, of the slit or major axis of the IFU, (7) wavelength range, (8) date of observation, and (9) total exposure time. For DEIMOS, slit lengths vary from galaxy to galaxy, with values in the range $\sim 4''$to $8''$..

A summary of the spectroscopic observations is provided in Table 2.3. In Figure 2.6, we show slit and IFU orientations for VCC 1545, one of two galaxies included in all three spectral datasets.

2.3 Photometric and Structural Measurements

There are a number of challenges involved in the measurement of photometric and structural parameters for NSCs, and, ultimately, in the characterization of their stellar populations. Nucleus-galaxy decompositions can be uncertain due to such factors as the number of components used in the modeling of the light distribution, the PSF used for the model convolution, and the presence of complex or nonparametric

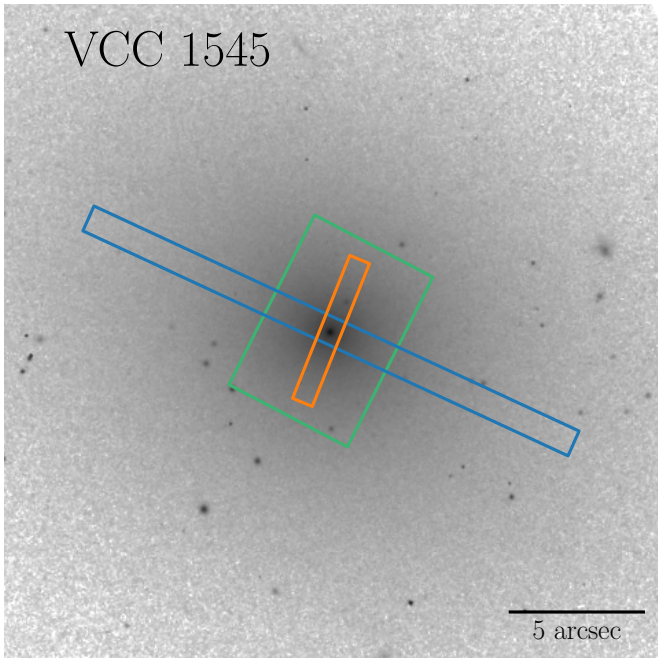

Figure 2.6 NGVS g-band image for VCC 1545 with the location of the Keck/ESI and Keck/DEIMOS slits shown in blue and red, respectively. The green rectangle indicates the location of the Gemini/GMOS IFU.

structures that may skew the model fit (see, e.g, Turner et al., 2012, for a discussion of these issues). When deriving stellar population properties, one familiar difficulty is the age-metallicity degeneracy — optical colours can be changed in similar ways by both age and metallicity (particularly for ages $t \gtrsim 2$ Gyr), such that an older, lower-metallicity population can appear indistinguishable from a younger, higher-metallicity population (Worthey et al., 1994). This is undoubtedly important for NSCs in early-type hosts, as both the galaxies and the NSCs are likely to contain old to intermediate age ($t > 5$ Gyr) populations. Age sensitivity can be improved by extending the photometric coverage into the UV and IR regions (Worthey et al., 1994; Puzia et al., 2002; Hempel et al., 2003; de Meulenaer et al., 2014) — a prime motivation for this analysis. Of course, the derived stellar population parameters can also vary with the choice of comparison models, which often rely on different isochrones, spectral libraries and stellar evolution treatments (Conroy & Gunn, 2010; Powalka et al., 2016).

To test the robustness of my results with these uncertainties in mind, I use multiple procedures to understand any possible systematics. This includes using different nucleus-galaxy decomposition techniques (described in §2.3.1 and §2.3.2) as well as deriving stellar population parameters from various population synthesis models.

2.3.1 `ELLIPSE`-Based Analysis

NSCs and galaxy parameters were derived from Sérsic component fits to radial profiles created using the `IRAF` task `ELLIPSE` which fits elliptical isophotes to each object using the method of Jedrzejewski (1987). The image intensity is sampled along each ellipse's path, creating an intensity distribution as a function of azimuthal angle, ϕ. If the ellipse's parameters are well matched to the galaxy's shape, then the intensity should be constant at all values of ϕ. Any deviations from the isophote can be expressed as higher order moments of a Fourier series:

$$I(\phi) = I_0 + \sum_k [A_k \sin(k\phi) + B_k \cos(k\phi)] \tag{2.1}$$

A_k and B_k represent the amplitude of each moment. A pure ellipse can be described by the first two moments of the series, while any deviations (e.g., a disky or boxy isophote) can be expressed with terms for $k \geq 3$. `ELLIPSE` determines the best-fit parameters by least-squares minimization of the residuals between the sampled image

intensity and Eq. 2.1. This isophotal fitting process is described in full in Ferrarese et al. (2006b) and Côté et al. (2006).

To capitalize simultaneously on HST's superior resolution and the depth of the wide-field NGVS imaging, composite surface brightness profiles were created by combining ACS F475W and MegaCam g-band profiles, as well as F850LP and z-band profiles. The two filter pairs are nearly identical, although a small ($\lesssim 0.01$ mag) zeropoint correction is required to transform each set to a common system. In addition, the HST profiles must have the sky removed. To accomplish both these tasks, the g and z profiles were first transformed to the SDSS photometric system using the colour transformations provided by the MegaPipe webpages[3]. Next, I estimated the zeropoint shifts and sky levels of the ACS images simultaneously. For the ACS profiles, a corrected surface brightness profile can be calculated using the equation

$$\mu_{AB}(r) = -2.5 \log_{10}(f(r) + f_{sky}) + z + \Delta z, \tag{2.2}$$

where $f(r)$ is the measured flux at each radial step, f_{sky} is the estimated sky level, z is the zeropoint for initial photometric system, and Δz is the zeropoint correction.

These corrections were determined on a galaxy-by-galaxy basis by matching the ACS profile produced by Eq. 2.2 to the CFHT profile using the orthogonal distance regression (ODR) package within SciPy. For the fit, only the profile regions beyond $4''$ were considered. This is roughly five times the seeing of the NGVS data, which should safely avoid any blurring of the nucleus and galaxy profiles (Schweizer, 1979). Figure 2.7 shows the matched profiles for galaxy VCC 1422 once the ACS component has been zeropoint-corrected and sky-subtracted. Residuals between the two original profiles in the fitted regions, unaffected by smearing, are shown as well.

Parametric fits to the composite profiles were produced following a method similar to that in Côté et al. (2006), Ferrarese et al. (2006a), and Turner et al. (2012). However, the approach here differs in a few ways, most notably in that I fitted the nucleus light using a Sérsic profile rather than a King profile (i.e., the entire profile nominally contains two Sérsic components). The intensity in a Sérsic profile is described by the equation

$$I(r) = I_e \exp\left\{-b_n\left[\left(\frac{r}{r_e}\right)^{1/n} - 1\right]\right\} \tag{2.3}$$

where the free parameters are I_e, the intensity at the effective radius r_e, and the Sérsic

[3] `http://www.cadc-ccda.hia-iha.nrc-cnrc.gc.ca/en/megapipe/docs/filt.html`

index n. The constant b_n is defined by complete and incomplete gamma functions, $\Gamma(n)$ and $\gamma(n, x)$, respectively, such that $\Gamma(2n) = 2\gamma(2n, b_n)$. For the nuclear component, n was fixed to $n = 2$ to diminish the likelihood of the nucleus component fitting non-nucleus light in galaxies with complex substructure.

The best-fit model was determined using χ^2 minimization with equal weight applied to all points in the profile after convolution with the appropriate PSF. Fits to the g and z profiles were performed both independently for each filter as well as simultaneously. I found that the structural parameters derived with independent and simultaneous fits were consistent, although small variations between the g and z parameters arose in the independent fits. However, each fit remained well-behaved. I adopt the results from the independent fits for the analysis.

2.3.2 GALFIT Analysis

Galaxy and nucleus magnitudes were measured simultaneously using GALFIT, an algorithm that fits two-dimensional (2D) parametric models to images (Peng et al., 2002, 2010). A galaxy model can be composed of an arbitrary number of components (e.g., exponential disk, Sérsic profile, point source) that are combined to best fit the 2D galaxy image. As inputs, GALFIT requires the original image, a PSF image to convolve with the model component(s), and either a sigma map containing the errors for each pixel, or the gain of the instrument in order to estimate errors from the Poisson noise.

Final magnitude measurements for the various components were obtained using an iterative process. Initially, each object was fitted with a basic model containing (1) a Sérsic component for the galaxy and (2) a Sérsic component for the nucleus. These components were defined by a single ellipticity and position angle (i.e., no isophote twisting), as well as an effective radius r_e, Sérsic index n, axis ratio b/a, and magnitude. Although GALFIT can estimate and fit the sky level, its brightness was fixed to a predetermined value because the fitted images are often object, not sky, dominated, and so GALFIT's sky level estimates were found to be consistently high. For the u^*griz, F300W and F160W images, sky subtraction had already been applied to the data, so sky levels were fixed to zero. For the ACS F475W and F850LP images, sky levels were determined from matching the F475W and F850LP one-dimensional (1D) profiles to the corresponding CFHT g and z profiles (see §2.3.1). The output parameters of the fit obtained with the basic model then were inspected for each

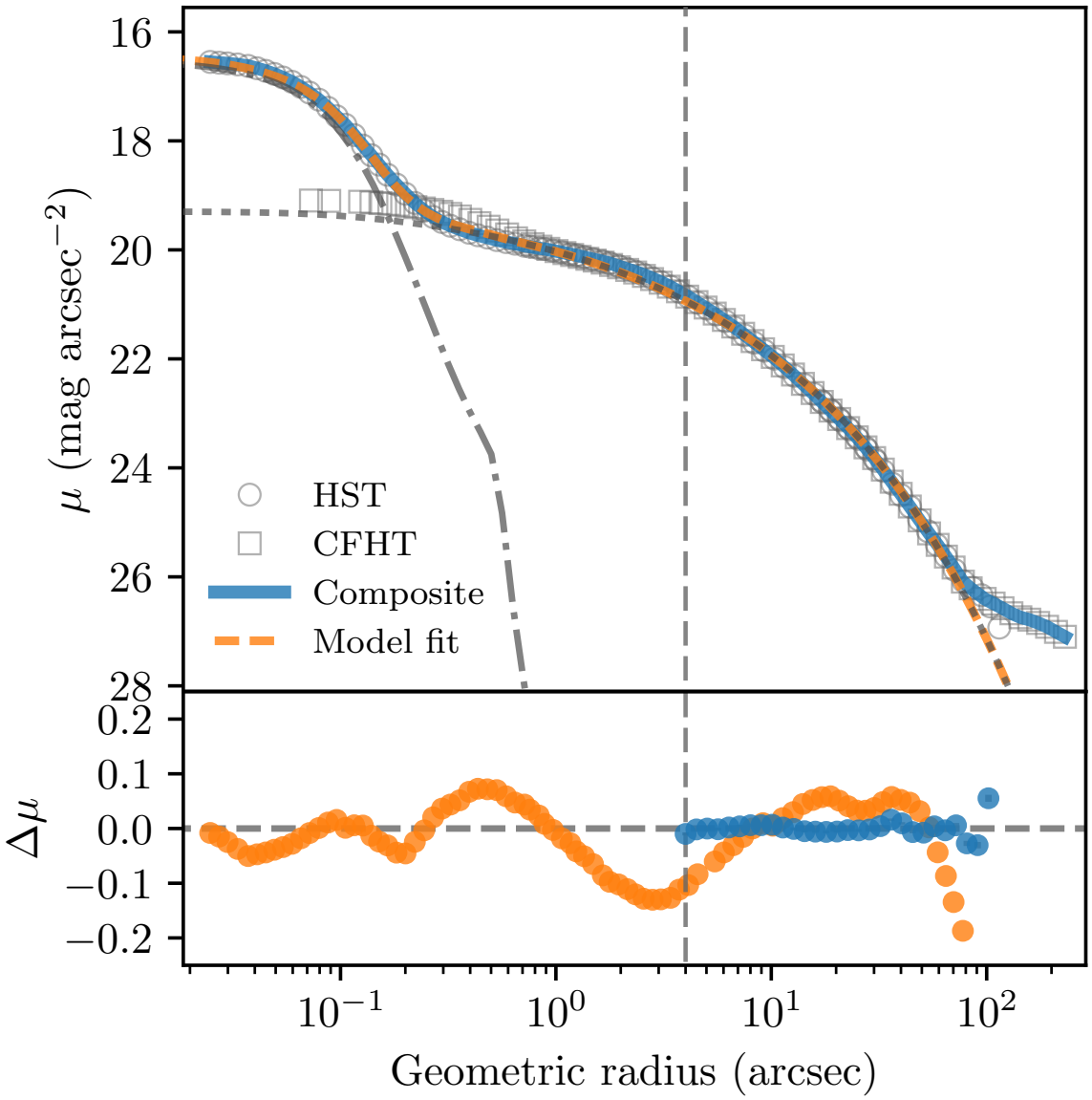

Figure 2.7 *(Top panel).* Matched HST/ACS (gray circles) and CFHT (gray squares) g-band surface brightness profiles for VCC 1422. The final composite profile is plotted in blue. The vertical dashed line indicates the inner boundary of the region used to match the space- and ground-based profiles. The dashed orange line shows a fit to the profile using two Sérsic components; the nucleus component is shown by the dot-dashed gray curve, and the galaxy component by the dotted gray curve. *(Bottom panel).* Blue points show the residuals between the HST and CFHT profiles in the region used to match the profiles. Orange points show the residuals between the composite profile and the best-fit model. Error bars are smaller than the data points.

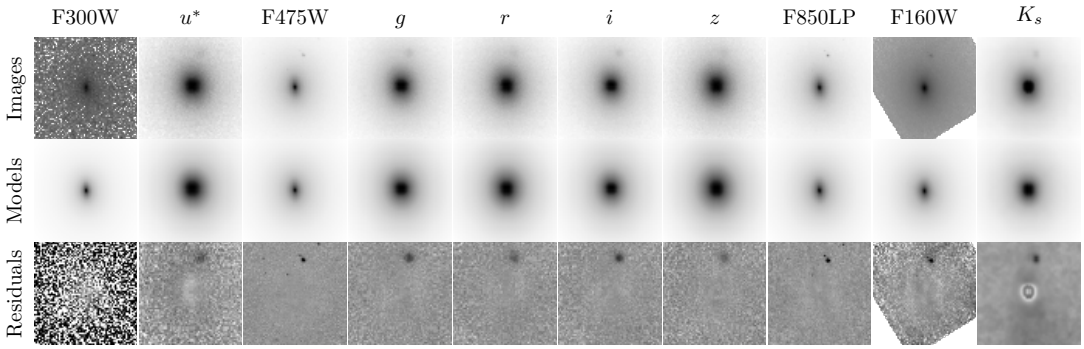

(a) VCC 1146.

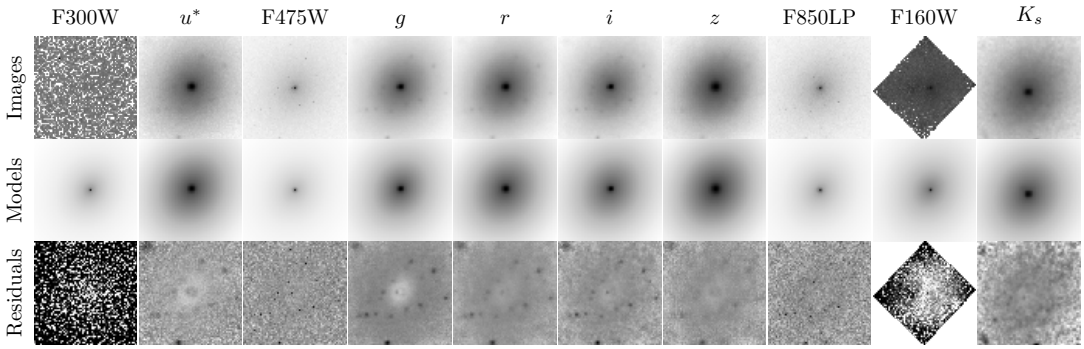

(b) VCC 1407.

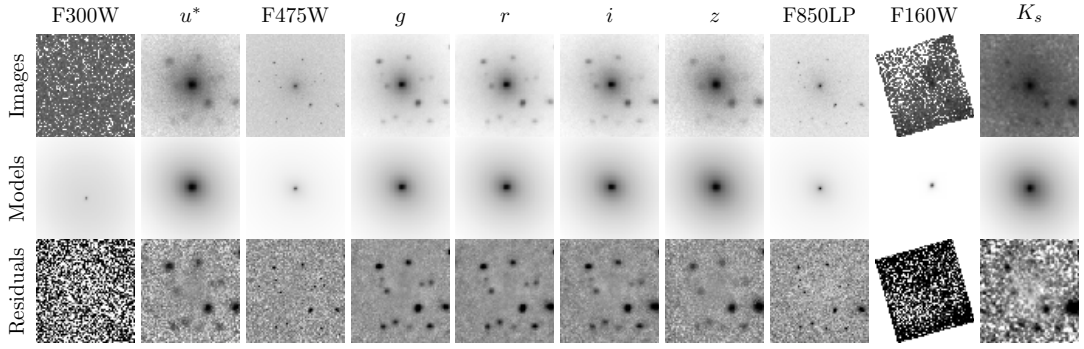

(c) VCC 1539.

Figure 2.8 Final images, best-fit GALFIT models, and model residuals for three of the program galaxies: VCC 1146 (a), VCC 1407 (b), and VCC 1539 (c).

object. The model was subsequently refined with additional Sérsic components for the galaxy if the fit met either, or both, of the following conditions: (1) n for any component was outside the range $0.5 < n < 4$; and (2) the nucleus' r_e was more than 10% of the galaxy's r_e. This second condition, a quite conservative criterion, was imposed to catch only the most obvious outliers: i.e., typically, the nucleus radius is $\sim$2% of the galaxy half-light radius. In all cases, a single component was used to fit the nucleus, resulting in an average $n = 1.57 \pm 0.64$, and average $r_e = 5.74 \pm 1.74$ pc. The models were also refined if a visual inspection of the fit residuals indicated an incomplete fit, even if the above conditions were not met. Even dwarf galaxies can display multiple structural components (see e.g., Janz et al., 2012, and references therein), so most of the galaxies in the sample have been modeled with more than one Sérsic component, typically requiring two or three. The maximum number of components required was seven for VCC 784, one of the brightest galaxies in the sample.

To ensure consistent measurements across all bands, the same physical parameters were held fixed and fitted to all images, with the only free parameters being the magnitudes of the model components (the sky level, however, was always held fixed). To determine the values of the fixed parameters, a completely free fit was performed on the F475W images. These are the obvious choice as reference images due to the combination of high SNR, high resolution and relatively wide field coverage. All NSCs in this sample were resolved in the HST data, enabling better measurement of NSC parameters. Once the fits to the F475W images were completed, the best-fit parameters for each object were extracted and fitted to the remaining images with only the magnitudes being allow to vary from their input values. Using this technique, I was able to measure component magnitudes in a homogeneous way. This is particularly important for the NICMOS and WFPC2 data, where a limited field of view, or marginal SNR, can present challenges in the fitting process. Figure 2.8 shows the GALFIT results for three program galaxies at a range of magnitudes and structural complexities. With the flexibility of adding multiple galaxy components, even a bright, complex galaxy such as VCC 1146 can be well-modeled. For the faintest galaxies in the sample, such as VCC 1539, the fixed structural parameters ensure consistent fits, even in filters where the detection is limited. Tables 2.4 and 2.5 list the extracted magnitudes for the NSCs and galaxies, respectively. Galaxy magnitudes are defined as the total magnitude of all components *excluding* the nucleus component.

Table 2.4: Photometric Measurements for Program Nuclei

VCC	F300W (AB mag)	u^* (AB mag)	F475W (AB mag)	g (AB mag)	r (AB mag)	i (AB mag)	z (AB mag)	F850LP (AB mag)	F160W (AB mag)	K_s (AB mag)
33	25.79 ± 0.30	23.43 ± 0.37	22.20 ± 0.37	22.27 ± 0.37	...	21.45 ± 0.37	22.06 ± 0.37	21.34 ± 0.37	21.04 ± 0.37	...
140	24.49 ± 0.30	23.72 ± 0.37	22.20 ± 0.37	21.87 ± 0.37	...	21.27 ± 0.37	21.61 ± 0.37	21.27 ± 0.37	20.53 ± 0.37	...
200	22.86 ± 0.30[a]	23.20 ± 0.35[a]	22.97 ± 0.35	23.18 ± 0.35	...	21.29 ± 0.35	21.12 ± 0.35	21.75 ± 0.35	20.76 ± 0.35	...
230	22.55 ± 0.30	21.31 ± 0.30	20.16 ± 0.30	19.95 ± 0.30	...	19.14 ± 0.30	19.01 ± 0.30	19.13 ± 0.30	19.06 ± 0.30	...
538	23.50 ± 0.30	21.84 ± 0.27	20.84 ± 0.27	20.96 ± 0.27	...	19.80 ± 0.27	19.36 ± 0.27	19.75 ± 0.27	19.09 ± 0.27	...
698	22.43 ± 0.30	21.11 ± 0.29	20.05 ± 0.29	19.27 ± 0.29	...	18.95 ± 0.29	18.68 ± 0.29	18.78 ± 0.29	18.37 ± 0.29	...
784	21.92 ± 0.30	20.59 ± 0.21	18.75 ± 0.21	18.34 ± 0.21	...	17.21 ± 0.21	16.84 ± 0.21	17.26 ± 0.21	16.31 ± 0.21	...
828	21.77 ± 0.30	19.37 ± 0.20	18.54 ± 0.20	18.45 ± 0.20	...	17.10 ± 0.20	17.28 ± 0.20	16.96 ± 0.20	16.22 ± 0.20	...
856	22.02 ± 0.30	20.57 ± 0.32	19.56 ± 0.32	19.38 ± 0.32	...	18.51 ± 0.32	18.37 ± 0.32	18.49 ± 0.32	17.90 ± 0.32	...
1075	23.54 ± 0.30	22.16 ± 0.27	21.08 ± 0.27	21.13 ± 0.27	...	20.24 ± 0.27	20.20 ± 0.27	20.19 ± 0.27	19.76 ± 0.27	...
1087	23.23 ± 0.30	22.12 ± 0.30	20.16 ± 0.30	17.52 ± 0.30[a]	17.32 ± 0.30[a]	16.77 ± 0.30[a]	16.00 ± 0.30[a]	18.93 ± 0.30	18.30 ± 0.30	18.17 ± 0.30
1146	19.32 ± 0.30	17.49 ± 0.12	16.60 ± 0.12	16.58 ± 0.12	16.05 ± 0.12	15.42 ± 0.12	15.37 ± 0.12	15.10 ± 0.12	14.24 ± 0.12	15.67 ± 0.12
1185	...	21.88 ± 0.28	20.76 ± 0.28	20.67 ± 0.28	20.12 ± 0.28	19.81 ± 0.28	19.70 ± 0.28	19.80 ± 0.28	19.42 ± 0.28	19.43 ± 0.28
1192	21.12 ± 0.30	19.70 ± 0.20	18.47 ± 0.20	18.44 ± 0.20	17.73 ± 0.20	17.61 ± 0.20	17.14 ± 0.20	17.23 ± 0.20	16.43 ± 0.20	...
1199	22.41 ± 0.30	20.63 ± 0.32	19.43 ± 0.32	19.08 ± 0.32	18.35 ± 0.32	18.25 ± 0.32	17.82 ± 0.32	18.01 ± 0.32	17.09 ± 0.32	...
1242	20.32 ± 0.30	19.12 ± 0.11	17.61 ± 0.11	17.37 ± 0.11	16.63 ± 0.11	16.25 ± 0.11	16.03 ± 0.11	16.09 ± 0.11	15.33 ± 0.11	...
1261	22.55 ± 0.30	21.39 ± 0.29	19.87 ± 0.29	20.33 ± 0.29	...	18.96 ± 0.29	18.59 ± 0.29	18.69 ± 0.29	18.69 ± 0.29	...
1283	22.75 ± 0.30	20.88 ± 0.29	19.94 ± 0.29	19.50 ± 0.29	18.89 ± 0.29	18.61 ± 0.29	18.32 ± 0.29	18.47 ± 0.29	17.50 ± 0.29	...
1355	23.48 ± 0.30	22.39 ± 0.26	21.10 ± 0.26	21.23 ± 0.26	20.67 ± 0.26	20.20 ± 0.26	20.06 ± 0.26	20.12 ± 0.26	19.68 ± 0.26	...
1407	23.36 ± 0.30	21.48 ± 0.29	20.76 ± 0.29	20.37 ± 0.29	19.94 ± 0.29	19.67 ± 0.29	19.38 ± 0.29	19.78 ± 0.29	19.31 ± 0.29	18.83 ± 0.29
1422	22.86 ± 0.30	21.31 ± 0.29	20.09 ± 0.29	19.99 ± 0.29	...	18.98 ± 0.29	18.76 ± 0.29	18.87 ± 0.29	18.32 ± 0.29	...
1431	22.16 ± 0.30	21.05 ± 0.30	19.89 ± 0.30	19.62 ± 0.30	...	18.83 ± 0.30	18.61 ± 0.30	18.79 ± 0.30	18.32 ± 0.30	...
1440	22.75 ± 0.30	21.09 ± 0.31	20.24 ± 0.31	19.80 ± 0.31	...	19.39 ± 0.31	18.36 ± 0.31	19.01 ± 0.31	18.54 ± 0.31	...
1489	24.38 ± 0.30	23.51 ± 0.38	22.41 ± 0.38	22.29 ± 0.38	...	21.63 ± 0.38	21.66 ± 0.38	21.62 ± 0.38	21.25 ± 0.38	...
1539	23.67 ± 0.30[a]	22.02 ± 0.27	21.20 ± 0.27	21.01 ± 0.27	20.53 ± 0.27	20.34 ± 0.27	20.36 ± 0.27	20.38 ± 0.27	19.74 ± 0.27	20.21 ± 0.27
1545	24.22 ± 0.30	22.50 ± 0.28	21.81 ± 0.28	21.29 ± 0.28	20.20 ± 0.28	20.28 ± 0.28	20.10 ± 0.28	20.61 ± 0.28	21.36 ± 0.28	19.05 ± 0.28
1619	23.30 ± 0.30	21.58 ± 0.19	18.99 ± 0.19	19.06 ± 0.19	...	17.86 ± 0.19	17.35 ± 0.19	17.78 ± 0.19	16.33 ± 0.19	...
1627	...	21.37 ± 0.30	20.20 ± 0.30	19.56 ± 0.30	...	20.03 ± 0.30	18.26 ± 0.30	18.81 ± 0.30	...	...
1630	21.80 ± 0.30	19.93 ± 0.20	18.67 ± 0.20	18.45 ± 0.20	...	17.35 ± 0.20	16.65 ± 0.20	17.04 ± 0.20	16.04 ± 0.20	...
1661	24.01 ± 0.30	22.12 ± 0.27	20.87 ± 0.27	20.23 ± 0.27	...	19.92 ± 0.27	19.36 ± 0.27	21.27 ± 0.27	19.28 ± 0.27	...
1826	22.69 ± 0.30	21.13 ± 0.29	20.05 ± 0.29	19.97 ± 0.29	...	18.99 ± 0.29	18.84 ± 0.29	18.91 ± 0.29	18.67 ± 0.29	...
1828	23.59 ± 0.30	22.81 ± 0.25	21.49 ± 0.25	21.44 ± 0.25	...	20.54 ± 0.25	20.39 ± 0.25	20.48 ± 0.25	20.17 ± 0.25	...
1861	21.95 ± 0.30	21.09 ± 0.29	20.01 ± 0.29	19.84 ± 0.29	...	19.02 ± 0.29	18.93 ± 0.29	18.92 ± 0.29	18.43 ± 0.29	...

Table 2.4 – continued from previous page

VCC	F300W (AB mag)	u^* (AB mag)	F475W (AB mag)	g (AB mag)	r (AB mag)	i (AB mag)	z (AB mag)	F850LP (AB mag)	F160W (AB mag)	K_s (AB mag)
1871	21.86 ± 0.30	20.32 ± 0.19	19.04 ± 0.19	19.31 ± 0.19	...	18.42 ± 0.19	17.58 ± 0.19	17.77 ± 0.19	17.15 ± 0.19	...
1883	20.03 ± 0.30	18.30 ± 0.13	17.61 ± 0.13	17.74 ± 0.13	...	29.30 ± 0.13[a]	16.09 ± 0.13	17.42 ± 0.13	15.53 ± 0.13	...
1886	24.27 ± 0.30[a]	23.06 ± 0.37	22.11 ± 0.37	22.02 ± 0.37	...	21.24 ± 0.37	21.30 ± 0.37	21.20 ± 0.37	21.10 ± 0.37	...
1910	22.36 ± 0.30	20.84 ± 0.31	19.74 ± 0.31	19.62 ± 0.31	19.01 ± 0.31	18.69 ± 0.31	18.53 ± 0.31	18.62 ± 0.31	18.30 ± 0.31	...
2019	23.01 ± 0.30	21.45 ± 0.32	20.27 ± 0.32	20.25 ± 0.32	...	19.27 ± 0.32	19.07 ± 0.32	19.18 ± 0.32	18.61 ± 0.32	...
2050	21.92 ± 0.30[a]	29.35 ± 0.37[a]	22.47 ± 0.37	23.08 ± 0.37	...	21.46 ± 0.37	22.11 ± 0.37	21.39 ± 0.37	20.56 ± 0.37	...

Note. — Magnitudes have not been corrected for Milky Way foreground extinction.

[a]Magnitude excluded from analysis due to image artifacts, failure of GALFIT to converge on a model fit, or, in the F300W, a non-detection.

Table 2.5: Photometric Measurements for Program Galaxies

VCC	F300W (AB mag)	u^* (AB mag)	F475W (AB mag)	g (AB mag)	r (AB mag)	i (AB mag)	z (AB mag)	F850LP (AB mag)	F160W (AB mag)	K_s (AB mag)
33	16.76 ± 0.30	16.05 ± 0.02	14.98 ± 0.02	14.90 ± 0.02	...	14.08 ± 0.02	13.83 ± 0.02	13.91 ± 0.02	13.50 ± 0.02	...
140	16.68 ± 0.30	15.26 ± 0.03	14.01 ± 0.03	13.95 ± 0.03	...	13.05 ± 0.03	12.83 ± 0.03	12.83 ± 0.03	12.52 ± 0.03	...
200	15.96 ± 0.30[a]	15.87 ± 0.02	14.69 ± 0.02	14.59 ± 0.02	...	13.70 ± 0.02	13.46 ± 0.02	13.50 ± 0.02	13.23 ± 0.02	...
230	17.41 ± 0.30	16.59 ± 0.02	15.47 ± 0.02	15.39 ± 0.02	...	14.50 ± 0.02	14.27 ± 0.02	14.32 ± 0.02	14.09 ± 0.02	...
538	18.89 ± 0.30	16.97 ± 0.02	15.87 ± 0.02	15.81 ± 0.02	...	14.91 ± 0.02	14.75 ± 0.02	14.74 ± 0.02	14.55 ± 0.02	...
698	15.51 ± 0.30	14.16 ± 0.01	12.98 ± 0.01	12.85 ± 0.01	...	11.91 ± 0.01	11.64 ± 0.01	11.65 ± 0.01	10.83 ± 0.01	...
784	15.81 ± 0.30	13.45 ± 0.10	12.23 ± 0.10	12.12 ± 0.10	...	11.12 ± 0.10	10.83 ± 0.10	10.83 ± 0.10	10.17 ± 0.10	...
828	15.68 ± 0.30	13.24 ± 0.10	12.36 ± 0.10	12.15 ± 0.10	11.76 ± 0.10	11.12 ± 0.10	10.78 ± 0.10	10.92 ± 0.10	10.25 ± 0.10	...
856	16.22 ± 0.30	15.38 ± 0.03	14.28 ± 0.03	14.19 ± 0.03	...	13.30 ± 0.03	13.09 ± 0.03	13.08 ± 0.03	12.85 ± 0.03	...
1075	17.00 ± 0.30	16.04 ± 0.02	14.87 ± 0.02	14.83 ± 0.02	...	13.92 ± 0.02	13.67 ± 0.02	13.68 ± 0.02	13.44 ± 0.02	...
1087	15.69 ± 0.30	15.46 ± 0.02	14.41 ± 0.02	14.11 ± 0.02[a]	13.41 ± 0.02[a]	13.18 ± 0.02[a]	13.05 ± 0.02[a]	13.06 ± 0.02	12.57 ± 0.02	12.95 ± 0.02
1146	15.18 ± 0.30	13.60 ± 0.04	12.48 ± 0.04	12.36 ± 0.04	11.68 ± 0.04	11.35 ± 0.04	11.16 ± 0.04	11.14 ± 0.04	10.56 ± 0.04	10.82 ± 0.04
1185	...	16.31 ± 0.03	15.20 ± 0.03	15.12 ± 0.03	14.56 ± 0.03	14.26 ± 0.03	13.97 ± 0.03	14.02 ± 0.03	13.30 ± 0.03	14.43 ± 0.03
1192	17.60 ± 0.30	16.18 ± 0.02	14.76 ± 0.02	14.66 ± 0.02	14.00 ± 0.02	13.61 ± 0.02	13.34 ± 0.02	13.29 ± 0.02	12.57 ± 0.02	...
1199	18.97 ± 0.30	17.68 ± 0.01	16.13 ± 0.01	16.02 ± 0.01	15.31 ± 0.01	14.90 ± 0.01	14.64 ± 0.01	14.57 ± 0.01	13.91 ± 0.01	...
1242	15.55 ± 0.30	13.33 ± 0.11	12.11 ± 0.11	12.01 ± 0.11	11.35 ± 0.11	10.95 ± 0.11	10.73 ± 0.11	10.73 ± 0.11	10.14 ± 0.11	...
1261	15.64 ± 0.30	14.50 ± 0.02	13.42 ± 0.02	13.31 ± 0.02	...	12.45 ± 0.02	12.23 ± 0.02	12.22 ± 0.02	11.75 ± 0.02	...
1283	14.30 ± 0.30	14.24 ± 0.01	13.05 ± 0.01	12.92 ± 0.01	12.25 ± 0.01	11.92 ± 0.01	11.63 ± 0.01	11.65 ± 0.01	10.81 ± 0.01	...
1355	16.84 ± 0.30	15.27 ± 0.03	14.17 ± 0.03	14.09 ± 0.03	13.53 ± 0.03	13.22 ± 0.03	13.01 ± 0.03	13.00 ± 0.03	12.73 ± 0.03	...
1407	16.62 ± 0.30	15.97 ± 0.02	14.94 ± 0.02	14.82 ± 0.02	14.26 ± 0.02	13.91 ± 0.02	13.70 ± 0.02	13.73 ± 0.02	13.14 ± 0.02	13.65 ± 0.02
1422	15.79 ± 0.30	14.48 ± 0.02	13.43 ± 0.02	13.34 ± 0.02	...	12.45 ± 0.02	12.17 ± 0.02	12.24 ± 0.02	11.73 ± 0.02	...
1431	17.06 ± 0.30	15.49 ± 0.03	14.27 ± 0.03	14.19 ± 0.03	13.53 ± 0.03	13.17 ± 0.03	12.92 ± 0.03	12.91 ± 0.03	12.50 ± 0.03	...
1440	17.96 ± 0.30	15.75 ± 0.02	14.78 ± 0.02	14.67 ± 0.02	...	13.74 ± 0.02	13.53 ± 0.02	13.53 ± 0.02	12.91 ± 0.02	...
1489	17.45 ± 0.30	16.84 ± 0.02	15.80 ± 0.02	15.76 ± 0.02	15.22 ± 0.02	14.94 ± 0.02	14.73 ± 0.02	14.76 ± 0.02	14.65 ± 0.02	...
1539	14.68 ± 0.30[a]	16.81 ± 0.02	15.68 ± 0.02	15.62 ± 0.02	15.07 ± 0.02	14.74 ± 0.02	14.56 ± 0.02	14.47 ± 0.02	16.09 ± 0.02	14.52 ± 0.02
1545	18.30 ± 0.30	15.93 ± 0.02	14.82 ± 0.02	14.69 ± 0.02	14.09 ± 0.02	13.75 ± 0.02	13.56 ± 0.02	13.55 ± 0.02	...	13.53 ± 0.02
1619	15.14 ± 0.30	13.36 ± 0.10	12.10 ± 0.10	12.03 ± 0.10	...	11.02 ± 0.10	10.69 ± 0.10	10.71 ± 0.10	10.55 ± 0.10[a]	...
1627	...	16.33 ± 0.02	15.04 ± 0.02	14.94 ± 0.02	...	13.90 ± 0.02	13.65 ± 0.02	13.63 ± 0.02	...	...
1630	15.24 ± 0.30	13.77 ± 0.10	12.41 ± 0.10	12.30 ± 0.10	...	11.27 ± 0.10	10.91 ± 0.10	10.93 ± 0.10	10.36 ± 0.10	...
1661	17.56 ± 0.30	16.88 ± 0.13	16.78 ± 0.13	15.58 ± 0.13	...	14.62 ± 0.13	14.40 ± 0.13	...	14.90 ± 0.13	...
1826	18.30 ± 0.30	16.74 ± 0.02	15.52 ± 0.02	15.47 ± 0.02	...	14.59 ± 0.02	14.37 ± 0.02	14.38 ± 0.02	14.18 ± 0.02	...
1828	17.65 ± 0.30	16.17 ± 0.02	15.08 ± 0.02	14.99 ± 0.02	...	14.07 ± 0.02	13.83 ± 0.02	13.85 ± 0.02	13.27 ± 0.02	...

Table 2.5 – continued from previous page

VCC	F300W (AB mag)	u^* (AB mag)	F475W (AB mag)	g (AB mag)	r (AB mag)	i (AB mag)	z (AB mag)	F850LP (AB mag)	F160W (AB mag)	K_s (AB mag)
1861	16.10 ± 0.30	15.28 ± 0.03	14.17 ± 0.03	14.03 ± 0.03	...	13.09 ± 0.03	12.86 ± 0.03	12.87 ± 0.03	12.76 ± 0.03	...
1871	16.88 ± 0.30	15.41 ± 0.03	14.14 ± 0.03	14.02 ± 0.03	...	12.98 ± 0.03	12.72 ± 0.03	12.73 ± 0.03	12.21 ± 0.03	...
1883	14.53 ± 0.30	12.91 ± 0.10	12.06 ± 0.10	11.68 ± 0.10	...	17.99 ± 0.10[a]	10.71 ± 0.10	10.49 ± 0.10	10.19 ± 0.10	...
1886	15.71 ± 0.30[a]	16.24 ± 0.03	15.26 ± 0.03	15.19 ± 0.03	...	14.40 ± 0.03	14.23 ± 0.03	14.25 ± 0.03	13.51 ± 0.03	...
1910	16.93 ± 0.30	15.32 ± 0.03	14.15 ± 0.03	13.99 ± 0.03	13.35 ± 0.03	13.02 ± 0.03	12.74 ± 0.03	12.78 ± 0.03	12.05 ± 0.03	...
2019	16.43 ± 0.30	15.63 ± 0.02	14.46 ± 0.02	14.42 ± 0.02	...	13.51 ± 0.02	13.30 ± 0.02	13.29 ± 0.02	12.89 ± 0.02	...
2050	17.57 ± 0.30[a]	14.33 ± 0.02	14.95 ± 0.02	14.82 ± 0.02	...	14.01 ± 0.02	13.74 ± 0.02	13.83 ± 0.02	13.71 ± 0.02	...

Note. — Magnitudes have not been corrected for Milky Way foreground extinction.

[a]Magnitude excluded from analysis due to image artifacts, failure of GALFIT to converge on a model fit, or, in the F300W, a non-detection.

2.3.3 Comparison of Results

Before proceeding, I pause to consider the robustness of my magnitude measurements. For the F475W and F850LP images, it is possible to compare magnitudes derived using the two methods described in §2.3.1 and §2.3.2. I can also compare the space- and ground-based 2D magnitudes from §2.3.2 to investigate the effect of resolution on the resulting values. All GALFIT F475W, F850LP, g-band and z-band magnitudes were first transformed to the SDSS photometric system following the same procedure outlined in §2.3.1. Comparisons among the various methods in the g bandpass are shown in Figure 2.9. For the galaxies, I find that both ground- and space-based 2D magnitudes differ slightly from the 1D composite profile magnitudes, with a typical scatter of $\sim$0.1 mag. The 1D magnitudes tend to be systematically brighter in galaxies with $g \gtrsim 14$ mag. This is not surprising as the 1D and 2D models differ in complexity. I find excellent agreement between the space- and ground-based 2D galaxy magnitudes, with a typical scatter of just $\sim$0.02 mag.

For the NSCs, the scatter among all measurement methods is understandably larger. Adjusting the nucleus model, even dramatically, will generally have a negligible effect on the derived galaxy magnitude (or on the total magnitude of the system) and the overall quality of the fit. When comparing the 1D and 2D magnitudes, the scatter is largest for the brightest NSCs, which have $g \lesssim 19.5$ mag. In this regime, the NSCs are embedded in the brightest, and most structurally complex galaxies in the sample and are thus the most difficult to model well (see Turner et al., 2012). These objects are also expected to be most affected by the number of components used in the model fit, which is a factor when comparing the 1D profile measurements (made with two Sérsic components) to the 2D method (which may include as many components as needed). However, despite the fairly large scatter of 0.2–0.5 mag, I see no evidence of systematic offsets among the various measurement methods. The good overall agreement between the space- and ground-based 2D magnitudes is especially notable: the NSCs are unresolved in the CFHT imaging, but I am nevertheless able to measure consistent total magnitudes.

2.3.4 Adopted Errors

The uncertainties provided by GALFIT are purely statistical and do not account for systematic effects such as the deviation of real galaxies from parametric models. As a result, the errors on GALFIT parameters are unrealistically small and not well deter-

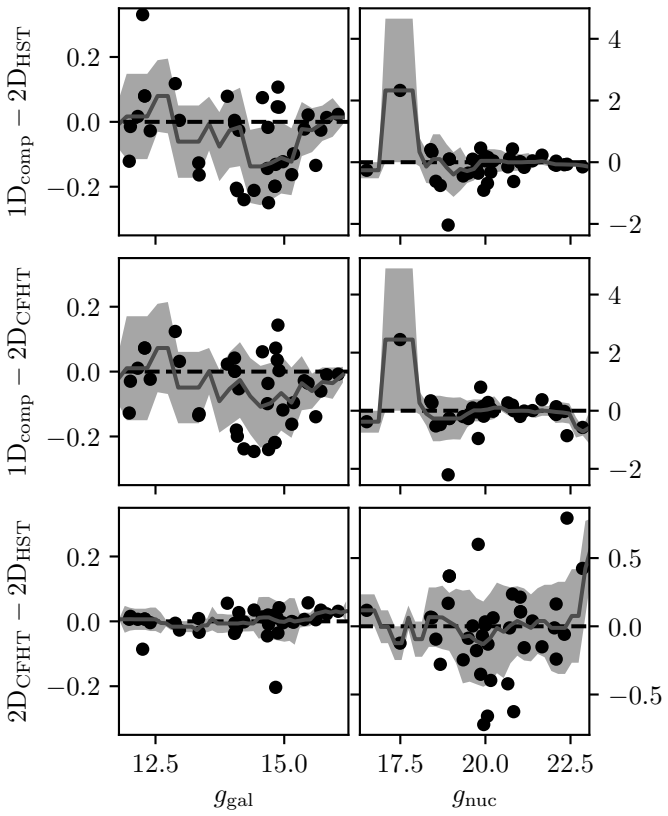

Figure 2.9 Differences in magnitudes measured, measured with different methods, plotted as a function of magnitude. The left column shows galaxy magnitudes, while the right shows nuclear magnitudes. The top row shows differences between the 1D HST+CFHT composite profile and 2D HST magnitudes. The middle row compares the 1D HST+CFHT composite profile and 2D CFHT magnitudes, while the bottom row compares the 2D CFHT and HST magnitudes. In each panel, the gray curve shows the average offset as a function of magnitude, with the shaded region showing the associated $1\,\sigma$ scatter.

mined (Häussler et al., 2007; Lange et al., 2016), so I do not apply these errors to my results. Instead I estimate the errors based on the comparisons in §2.3.3. The largest source of error for the NSCs is almost certainly due to the modeling process, as even subtle adjustments to the overall galaxy model may affect the distribution of light in its centre. As a result, the nucleus parameters can vary significantly. In addition, with only a few pixels in each image providing information on the nucleus, the χ^2 values calculated by GALFIT are dominated by the quality of the fit of the galaxy components, so determining the best-fit nucleus model can prove challenging. Comparing the results from multiple fitting methods can help quantify the uncertainties in my component magnitudes.

Magnitude differences in the g and z bands appear similar, so I do not expect a strong wavelength dependence on my estimated errors. In fact, the errors should be quite correlated, as all structural parameters have been held fixed at those measured from the F475W images. For the u^*griz, K_s, F475W, F850LP and F160W images, I adopt errors based on the typical scatter in the bottom left and right panels of Figure 2.9 at each object's g magnitude. However, other factors can contribute to the error budget in the case of the WFPC2 imaging: e.g., the low SNR and the limited field of view. In these images, I estimate errors directly from annuli on the images. I treat any signal outside 20 pixels of the nucleus to be noise that dominates the uncertainty on the nucleus measurement. I estimate this uncertainty from an annulus 5 pixels wide and with an inner radius of 20 pixels, centred on the nucleus.

2.4 Spectroscopic Analysis

The spectroscopic observations for my target NSCs are summarized in Table 2.3. For the spectroscopic analysis, I focus entirely on the NSC spectra because coverage of the galaxy is usually quite limited. For all three datasets (GMOS, ESI and DEIMOS), I have employed as homogeneous an analysis as possible in order to minimize any differences arising from different techniques.

2.4.1 Data Reduction and Calibration

Full details on the reduction of the GMOS spectra are given in Liu et al. (2016). In brief, cosmic rays were removed from the spectra before reducing them using the standard GMOS-IFU pipeline in `IRAF`, which performs bias subtraction, dark

correction, flat fielding, sky subtraction, and wavelength calibration. The spectra were then continuum normalized and stacked. For each galaxy, the galaxy light was modeled as a Sérsic profile using the signal outside one FWHM of the galaxy centre. This profile was then extrapolated into the central region and subtracted to isolate the nucleus spectrum.

The ESI spectra were reduced using the MAuna Kea Echelle Extraction (MAKEE) pipeline (Barlow & Sargent, 1997). MAKEE is designed to extract isolated and unresolved sources, subtract a sky spectrum from the source, and perform wavelength calibrations using a sixth order polynomial fit to each echelle order. While the NSCs are unresolved, they clearly are not isolated. Therefore, MAKEE was adapted to treat the adjacent galaxy spectrum as the "sky" component during the sky removal step of the pipeline. As before, the NSC spectra were continuum normalized and then shifted to rest-frame wavelengths.

The `spec2D` pipeline was used on the DEIMOS spectra to reduce 1D and 2D spectra corrected for flat fielding, sky subtraction, cosmic ray removal, and wavelength calibration. The nucleus light in each spectrum was extracted from the galaxy light by collapsing the 2D spectrum in the wavelength direction and fitting a Gaussian distribution to the resulting light profile. The width of this Gaussian defines an extraction window. Each pixel within this window is weighted by the value of the Gaussian distribution at that position before being added to the final 1D spectrum. Complete details of this reduction process are provided in Toloba et al. (2016). Once again, the NSC spectra were then continuum normalized and shifted to rest-frame wavelengths. As an illustration of the data quality, the final, wavelength-calibrated, continuum-normalized spectra for the nucleus of VCC 1545 are shown in Figure 2.10.

2.4.2 Line Index Measurements

Line indices were measured using the IDL script `Lick-EW`, provided as part of the `EZ-AGES` code package (Schiavon, 2007; Graves & Schiavon, 2008). `Lick-EW` measures equivalent widths on the Lick system by broadening the input spectra to Lick/IDS resolution and following the method described in Worthey et al. (1994). For this sample, I omit corrections for the velocity dispersion, as the low dispersions ($\sim$50 km s^{-1}) for dwarf early-type galaxies do not significantly affect the line widths (Kuntschner, 2004). While `Lick-EW` will measure every available Lick index, I selected only the H_β, Mgb, Fe5270 and Fe5335 lines to estimate ages, metallicities and α-element abun-

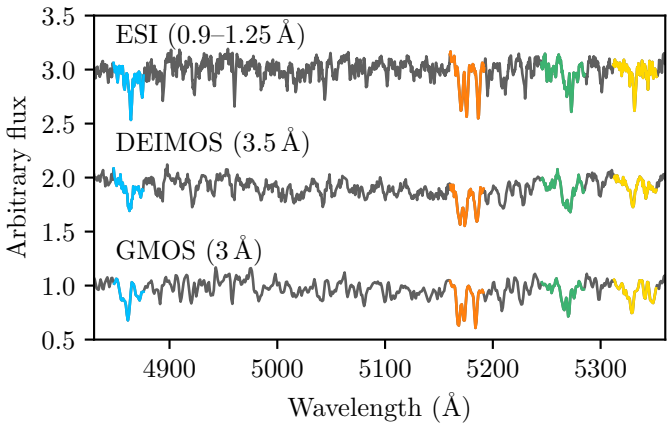

Figure 2.10 Wavelength-calibrated, continuum-normalized, rest-frame spectra for VCC 1545 obtained using the ESI, DEIMOS and GMOS instruments. Four indices used to measure ages, metallicities, and α-element abundances have been highlighted: H_β (light blue), Mgb (orange), Fe5270 (green), and Fe5335 (yellow). Values in parentheses after each instrument name indicate the spectral resolution at 5000 Å.

Table 2.6 Mean Measured Lick Indices

VCC	Instruments	H_β (Å)	Mgb (Å)	Fe5270 (Å)	Fe5335 (Å)
33	ESI,GMOS	3.13 ± 0.41	1.38 ± 0.42	1.91 ± 0.47	1.12 ± 0.57
200	ESI	2.09 ± 0.90	2.27 ± 0.70	2.38 ± 1.45	2.12 ± 0.81
230	ESI	2.30 ± 0.61	1.56 ± 0.79	1.91 ± 0.59	1.58 ± 0.86
538	ESI	2.22 ± 0.73	2.09 ± 0.82	2.19 ± 0.67	2.21 ± 1.03
1075	ESI,DEIMOS	2.26 ± 0.58	1.17 ± 0.48	1.69 ± 0.61	1.52 ± 0.61[a]
1185	ESI,GMOS	2.29 ± 0.42	1.70 ± 0.41	1.96 ± 0.54	1.71 ± 0.77
1192	ESI	1.76 ± 0.71	4.06 ± 0.97	2.75 ± 0.79	2.43 ± 0.97
1199	ESI	1.86 ± 0.83	4.05 ± 0.70	3.12 ± 0.81	3.17 ± 0.77
1355	GMOS	2.81 ± 0.42	1.42 ± 0.48	0.80 ± 0.58	0.63 ± 0.66
1407	ESI,DEIMOS	2.66 ± 0.84	2.04 ± 0.54	1.55 ± 0.63	1.22 ± 1.00
1440	ESI	1.90 ± 0.76	2.63 ± 0.92	2.49 ± 0.62	2.29 ± 0.96
1489	ESI	2.84 ± 0.39	0.71 ± 0.54	1.11 ± 0.85	1.86 ± 0.92
1539	ESI,DEIMOS,GMOS	1.98 ± 0.47	1.76 ± 0.43	1.33 ± 0.55[c]	0.91 ± 0.57
1545	ESI,DEIMOS,GMOS	2.09 ± 0.26	2.81 ± 0.32	2.66 ± 0.44	2.53 ± 0.31
1627	ESI	1.87 ± 0.72	3.24 ± 0.73	2.81 ± 0.86	2.82 ± 0.79
1826	ESI	2.26 ± 0.66	1.96 ± 0.71	2.25 ± 1.11	1.55 ± 1.15
1828	ESI,DEIMOS	2.32 ± 0.49[b]	1.94 ± 0.86	2.47 ± 0.71	1.48 ± 0.60
1861	DEIMOS	2.33 ± 0.83	1.22 ± 0.55	1.79 ± 0.57	1.60 ± 0.63
1871	DEIMOS	1.80 ± 0.45	3.61 ± 0.20	2.92 ± 0.21	2.73 ± 0.24
2050	ESI	2.33 ± 0.76	1.45 ± 1.06	2.37 ± 1.23	1.23 ± 0.97

[a] ESI data excluded from measurement due to non-detection.
[b] DEIMOS data excluded from measurement due to a gap in the spectrum.
[c] GMOS data excluded from measurement due to non-detection.

dances due to their strong features and presence in the wavelength coverage of all three datasets. The measured Lick indices for each nucleus are listed in Table 2.6. The tabulated values are the mean values of the measurements from each dataset when multiple observations are available.

To investigate the robustness of my line index measurements, I compare results from the three spectroscopic datasets for all NSCs that appear in more than one dataset. These comparisons are shown in Figure 2.11 for the H_β, Mgb, Fe5270 and Fe5335 indices. There is generally very good agreement among the index measurements, particularly for Fe5270. The H_β agreement for DEIMOS data is somewhat poorer for two objects; however, note that the H_β feature is at the extreme blue end of the DEIMOS wavelength range where the detector's efficiency drops quickly, leading to low SNR. Overall, the agreement among datasets suggests that my line index measurements are reliable.

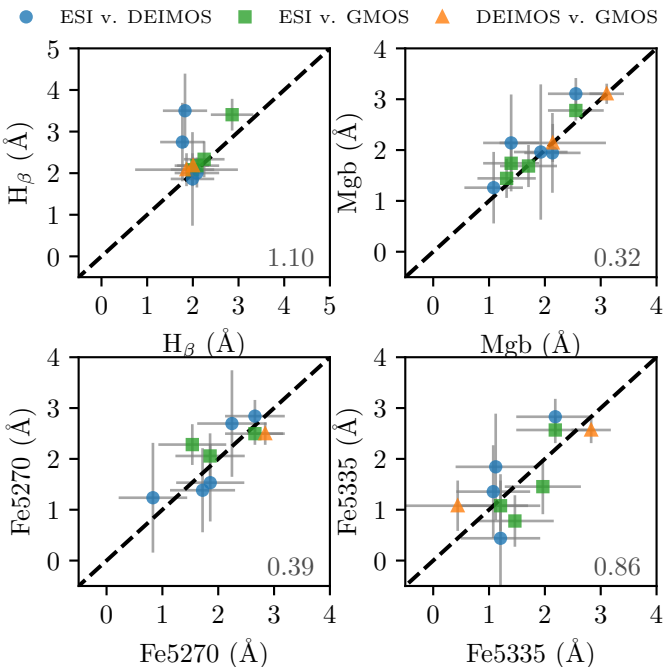

Figure 2.11 Comparison of Lick index measurements among the ESI, GMOS and DEIMOS datasets. The blue points show the value measured with ESI data compared to that measured with the DEIMOS data. Similarly, green squares show the ESI values against the GMOS values. In both cases, ESI measurements are plotted along the abscissa. The orange triangles are DEIMOS values compared to GMOS values for the two NSCs (VCC 1539 and VCC 1545) that appear in both datasets. The dashed line in each panel shows the one-to-one relation, while numbers in the bottom right corner show the RMS scatter in Å.

2.5 Results

2.5.1 Nucleus and Galaxy Colours

Many studies have noted that NSCs are typically bluer than their hosts in optical colours (e.g., Lotz et al., 2004; Côté et al., 2006; Turner et al., 2012). This is consistent with my findings here. In Figure 2.12 I present (F475W – F850LP) colours, as well as (F300W – g) and (z – F160W) colours. I confirm that NSCs are bluer than their hosts in optical colours — on average, NSCs are 0.12 ± 0.12 mag bluer than their hosts. This trend does not persist in infrared colours, with no clear colour offsets between NSCs and their host galaxies. Unfortunately, given the uncertainties in the UV data it is difficult to draw any strong conclusions about how NSCs compare to their hosts' UV colours. If the NSCs are truly bluer, this could be indicative of some fraction of the stellar content consisting of a young ($\lesssim 2$ Gyr) population. Alternatively, redder UV colours in the NSCs could be a sign of internal dust extinction. Although dwarf early-type galaxies are not expected to have a *substantial* dust content, any dust that is present tends to be more concentrated than the stellar content (di Serego Alighieri et al., 2013). In that case, NSCs may be more affected by centrally-concentrated galactic dust. Moreover, NSCs may well show larger dust fractions if they have recently formed stars. In this work I have assumed zero internal extinction for both galaxies and NSCs, which may present a bias in the derived population parameters. In the future, high-resolution UV and MIR data could be used to investigate the dust content and extinction in these objects. Further details on dust content and its effect on the results are included in §2.5.3.

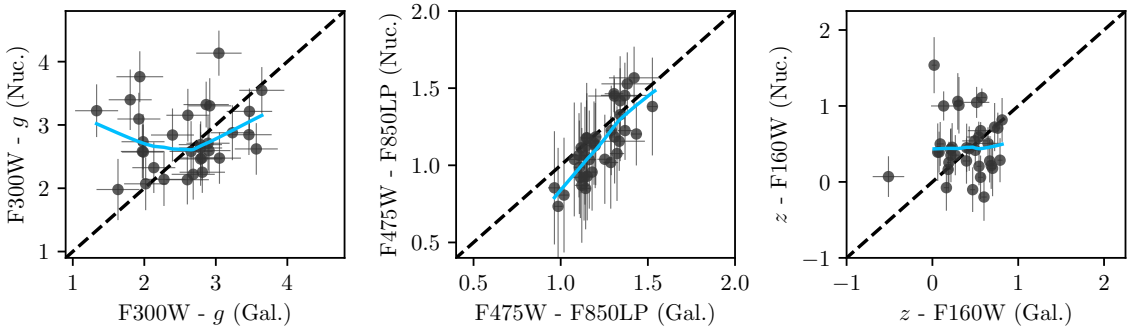

Figure 2.12 NSC UV-optical (left panel), optical (middle panel) and optical-IR (right panel) colours as a function of galaxy colour. In each panel, one to one lines are shown to guide the eye. The blue lines in each panel are LOWESS (Cleveland, 1979) curves for the data to illustrate the typical colour trend for the sample.

2.5.2 SED Fitting and Parameter Estimation

The results of §2.3.3 suggest that the 2D image decomposition technique yields the most homogeneous photometry for each nucleus and galaxy. I therefore use these UV, optical and IR measurements as the basis of my SED analysis for all objects.

The overarching goal of my SED analysis is to estimate the masses, ages and metallicities for each nucleus and its galaxy in a consistent way. To do this, I adopt a Markov Chain Monte Carlo (MCMC) approach. MCMC methods are designed to select N samples from the parameter space in a random walk such that, as N increases, the sample distribution approaches the true probability distribution. I constructed an SED fitting program in Python based on the `emcee` package (Foreman-Mackey et al., 2013). The `emcee` algorithm is the affine-invariant MCMC ensemble sampler, which has a few substantial differences from the more common Metropolis-Hastings algorithm. The Metropolis-Hastings method relies on a single Markov chain to probe the parameter space, and each time the chain attempts to jump to a new region of parameter space, the move is rejected or accepted based only on the likelihood of the proposed position relative to the likelihood of the current position. In contrast, the affine-invariant method uses multiple *walkers* to probe parameter space, and the proposed jump for each walker is based on the likelihood of that walker's current position as well as the likelihood of one other randomly selected walker's position. As a result, this method should require fewer tuning parameters and be less sensitive to the initial choices of model parameters.

Predicted stellar population properties can vary substantially based on the models used for comparison in the SED fit (Kannappan & Gawiser, 2007; Muzzin et al., 2009). When creating a model population, a number of components must be included, and the choices for these ingredients naturally will affect the resulting population. Such components include, for example: an initial mass function (IMF), spectral libraries, stellar isochrones, and the treatment of post-main sequence phases. The last point is especially important for poorly-understood evolutionary phases such as the thermally-pulsating asymptotic giant branch (TP-AGB). Depending on how TP-AGB stars are modeled, the population spectrum for ages $0.3 \leq t \leq 2$ Gyr can change dramatically (Maraston, 2005). A thorough overview of the uncertainties among models is given in Conroy & Gunn (2010).

To minimize the effect of model-specific features, I fit the data to an assortment of model SEDs and look for any results that remain consistent regardless of the adopted

Table 2.7 Properties of Population Synthesis Models

Model Set	Stellar Tracks	Spectral Libraries	IMF	Metallicities
BC03	Padova 1994	STELIB & BaSeL 3.1	Chabrier	$0.0001 \leq Z \leq 0.05$
M05	Cassisi and Geneva	BaSeL 3.1	Kroupa	$0.0004 \leq Z \leq 0.04$
PÉGASE.2	Padova 1994	BaSeL 2.2	Kroupa	$0.0001 \leq Z \leq 0.1$

model. I also have chosen similar or matching IMFs whenever possible: i.e., a Chabrier or Kroupa IMF, both of which are appropriate for dwarf, low-σ early-type galaxies (Cappellari et al., 2012; Mentz et al., 2016). I used simple stellar population (SSP) spectra from Bruzual & Charlot (2003, hereafter BC03), Fioc & Rocca-Volmerange (1997, 1999, PÉGASE.2), and Maraston (2005, hereafter M05). The features of each model set are summarized in Table 2.7.

In all cases, the model SEDs are purely stellar in nature: i.e., I assume zero dust content and no nebular emission. Therefore, only three free parameters are needed: stellar mass $M_\star$, metallicity Z, and age t. I assume a flat prior in the mass range $1 \leq M_\star \leq 10^{14}\,M_\odot$, and across the full metallicity range of each model set (see Table 2.7). I also apply flat priors to ages in the range $0 \leq t \leq 14$ Gyr, eliminating ages older than that of the universe. Model grids were created with 50 metallicity steps and 100 age steps, regularly spaced across the full space of $\log_{10} Z$ and $\log_{10} t$ covered by each model family. To evaluate how well the model reproduces the observed data, I use the log-likelihood equation:

$$\ln \mathcal{L} = -\frac{1}{2} \sum_{i=1}^{N} \left[\ln(2\pi\sigma_{obs,i}^2) + \frac{\left(\frac{M_\star}{m(t,Z)} F_i(t,Z) - F_{obs,i} \right)^2}{\sigma_{obs,i}^2} \right] \tag{2.4}$$

Here $F_{obs,i}$ is the observed flux in each filter, $\sigma_{obs,i}$ is the flux error, $m(t,Z)$ is the stellar mass of the model, and $F_i(t,Z)$ is the model flux in each filter. Because the model SEDs are normalized to one solar mass at $t = 0$, $M_\star/m(t,Z)$ is effectively a scale factor that is applied to best match the model to the observed flux.

Before fitting each object, I omitted any magnitudes that were obvious outliers based on visual inspection of the SED. These outliers represent cases in which the GALFIT model clearly failed to converge on a reasonable fit, and affected, at most, a single data point for each observed SED. These values were often at least an order of magnitude brighter or fainter than the surrounding measurements and could be

confidently excluded.

For each nucleus and galaxy, 500 walkers with 1000 steps through parameter space (after a burn-in period of 500 steps) provided a total of 500,000 samplings to generate posterior probability distributions for each parameter. Figure 2.13 shows an example of the joint and individual posteriors for the VCC 1422 nucleus and the selected best-fit parameters. I extracted the median of each distribution as the best-fit value, and use the 16^{th} and 84^{th} percentiles as $1\,\sigma$ uncertainties. The best-fit SED using these values is shown in Figure 2.14, again for the VCC 1422 nucleus. For comparison, I also calculate the χ^2 value for each parameter combination, and determine an additional set of best-fit parameters based on χ^2 minimization. This technique is more consistent with previous work, but produces systematically different values from the median best-fit parameters, which are generally older and less metal rich. I find that the χ^2 value changes very minimally due to the age-metallicity degeneracy, such that the χ^2 value of each set of median parameters is only marginally larger than the minimum χ^2. With this in mind, I adopt the median parameters as the final best-fit parameters, as I believe that the MCMC technique and error estimation better accounts for the degeneracy. The resulting masses, metallicities and ages estimated using the BC03 models for NSCs and galaxies are listed in Table 2.8.

By comparing results from different models, I can explore possible systematic differences among the calculated parameters. A comparison of the stellar population properties for galaxies and NSCs derived from the three models is shown in Figure 2.15. The BC03 values are adopted as a baseline on the abscissa, with the M05 or PÉGASE.2 value on the ordinate. There are no strong systematic differences among the derived parameters. All models produce masses and metallicities that are in very good agreement within the uncertainties. The BC03 and PÉGASE.2 results are quite consistent with each other, although the M05 models do tend to predict a different range of ages. While the BC03 and PÉGASE.2 models tend to produce ages between 5 and 12 Gyr, the M05 ages can be as young as 1 Gyr. This is likely an effect of the treatment of the TP-AGB population and other post-main sequence evolutionary stages. The unique fuel consumption model employed by M05 for these stages of stellar evolution means that the contribution of these red stars to the population's total becomes highly significant at ages $\sim$1–3 Gyr. As a result, the M05 models can match relatively redder observed colours with younger populations compared to the other models.

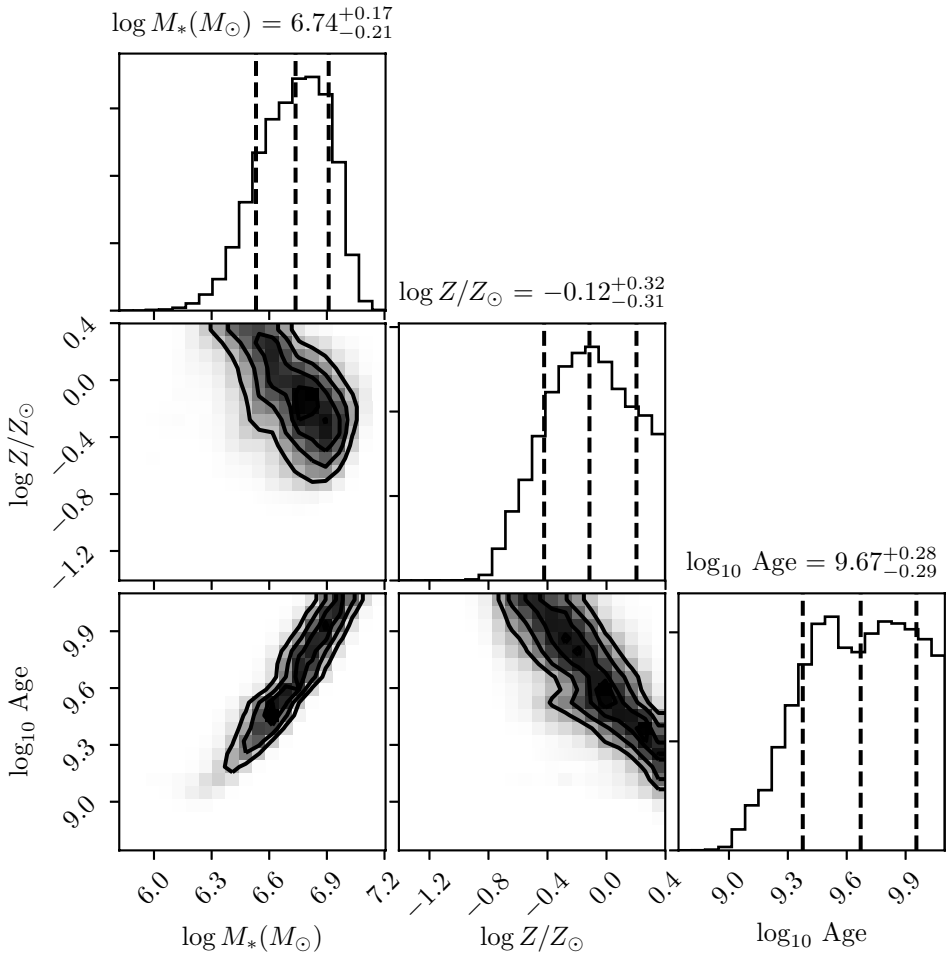

Figure 2.13 Stellar masses, metallicities, and ages derived using the BC03 models with a Chabrier IMF for the nucleus in VCC 1422. Plots along the diagonal show the collapsed individual posterior probability distributions for the mass (top left), metallicity (middle), and age (bottom right), while other panels show joint probability distributions. The median value for each parameter is quoted along the top of the diagonal, with error bars determined from the 16^{th} and 84^{th} percentiles.

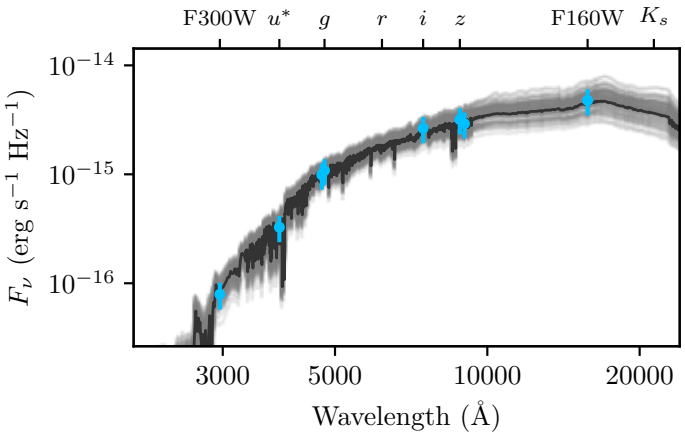

Figure 2.14 Best-fit model (in black) compared to the observed SED for the nucleus of VCC 1422 (blue points). The model SED has been generated using the best-fit parameters shown in Figure 2.13. 100 models have been randomly extracted from the posterior distribution and plotted in gray to demonstrate the uncertainty on the best-fit model.

Table 2.8 Masses, Metallicities and Ages Derived from SED Fitting Using BC03

VCC	$\log_{10} M_{\star,\mathrm{gal}}$ ($M_\odot$)	$\log_{10} M_{\star,\mathrm{nuc}}$ ($M_\odot$)	$\mathrm{T_{gal}}$ (Gyr)	$\mathrm{T_{nuc}}$ (Gyr)	$\log_{10} Z/Z_{\odot,\mathrm{gal}}$ (dex)	$\log_{10} Z/Z_{\odot,\mathrm{nuc}}$ (dex)
33	$8.44^{+0.19}_{-0.21}$	$5.56^{+0.20}_{-0.24}$	$1.82^{+2.12}_{-0.56}$	$4.06^{+4.52}_{-2.11}$	$-0.25^{+0.33}_{-0.32}$	$-0.12^{+0.35}_{-0.35}$
140	$9.10^{+0.12}_{-0.21}$	$5.56^{+0.24}_{-0.24}$	$4.38^{+3.86}_{-2.23}$	$2.80^{+4.24}_{-1.44}$	$-0.40^{+0.22}_{-0.23}$	$-0.40^{+0.48}_{-0.39}$
200	$8.85^{+0.10}_{-0.24}$	$5.45^{+0.28}_{-1.48}$	$5.19^{+3.27}_{-3.03}$	$3.49^{+4.88}_{-3.47}$	$-0.50^{+0.19}_{-0.19}$	$-0.22^{+0.48}_{-1.00}$
230	$8.51^{+0.14}_{-0.24}$	$6.42^{+0.25}_{-0.24}$	$5.24^{+4.32}_{-3.06}$	$3.17^{+5.17}_{-1.79}$	$-0.61^{+0.22}_{-0.16}$	$-0.53^{+0.48}_{-0.33}$
538	$8.38^{+0.13}_{-0.46}$	$6.35^{+0.19}_{-0.21}$	$7.15^{+3.73}_{-5.84}$	$3.98^{+4.32}_{-1.94}$	$-0.71^{+0.35}_{-0.06}$	$-0.16^{+0.35}_{-0.34}$
698	$9.40^{+0.06}_{-0.05}$	$6.68^{+0.20}_{-0.22}$	$1.86^{+0.47}_{-0.21}$	$3.73^{+4.38}_{-1.94}$	$0.34^{+0.04}_{-0.11}$	$-0.28^{+0.40}_{-0.32}$
784	$9.91^{+0.19}_{-0.09}$	$7.68^{+0.08}_{-0.13}$	$3.78^{+3.78}_{-1.06}$	$9.25^{+2.23}_{-3.12}$	$0.23^{+0.13}_{-0.22}$	$0.27^{+0.09}_{-0.15}$
828	$9.82^{+0.14}_{-0.08}$	$7.54^{+0.14}_{-0.17}$	$3.10^{+1.57}_{-0.83}$	$5.50^{+4.05}_{-2.26}$	$0.24^{+0.11}_{-0.17}$	$0.18^{+0.15}_{-0.22}$
856	$8.97^{+0.12}_{-0.22}$	$6.77^{+0.22}_{-0.23}$	$4.41^{+3.86}_{-2.39}$	$3.18^{+4.33}_{-1.67}$	$-0.52^{+0.30}_{-0.21}$	$-0.29^{+0.42}_{-0.36}$
1075	$8.76^{+0.10}_{-0.24}$	$5.99^{+0.26}_{-0.22}$	$5.18^{+3.37}_{-3.11}$	$2.54^{+4.74}_{-1.26}$	$-0.51^{+0.18}_{-0.19}$	$-0.46^{+0.51}_{-0.38}$
1087	$9.08^{+0.13}_{-0.21}$	$6.83^{+0.15}_{-0.21}$	$6.39^{+3.85}_{-3.38}$	$6.23^{+3.92}_{-2.93}$	$-0.35^{+0.19}_{-0.14}$	$0.12^{+0.18}_{-0.24}$
1146	$9.74^{+0.17}_{-0.11}$	$8.02^{+0.14}_{-0.09}$	$3.57^{+3.42}_{-1.25}$	$2.65^{+1.58}_{-0.67}$	$-0.08^{+0.23}_{-0.24}$	$0.11^{+0.15}_{-0.24}$
1185	$8.73^{+0.07}_{-0.13}$	$6.19^{+0.25}_{-0.22}$	$9.62^{+2.16}_{-3.53}$	$2.76^{+4.26}_{-1.42}$	$-0.81^{+0.08}_{-0.06}$	$-0.39^{+0.43}_{-0.33}$
1192	$8.86^{+0.10}_{-0.05}$	$7.31^{+0.18}_{-0.16}$	$3.11^{+1.22}_{-0.62}$	$3.60^{+3.92}_{-1.52}$	$0.30^{+0.08}_{-0.12}$	$-0.06^{+0.32}_{-0.32}$
1199	$8.50^{+0.10}_{-0.13}$	$7.21^{+0.14}_{-0.19}$	$5.06^{+2.60}_{-1.70}$	$6.38^{+3.81}_{-2.94}$	$0.25^{+0.10}_{-0.14}$	$0.12^{+0.18}_{-0.24}$
1242	$10.00^{+0.17}_{-0.14}$	$8.00^{+0.10}_{-0.15}$	$4.35^{+4.81}_{-1.60}$	$6.63^{+3.22}_{-2.66}$	$0.08^{+0.21}_{-0.26}$	$0.11^{+0.16}_{-0.17}$
1261	$9.15^{+0.09}_{-0.11}$	$6.66^{+0.18}_{-0.24}$	$2.05^{+1.23}_{-0.69}$	$4.60^{+4.39}_{-2.49}$	$-0.05^{+0.27}_{-0.30}$	$-0.33^{+0.36}_{-0.29}$
1283	$9.45^{+0.06}_{-0.07}$	$7.00^{+0.15}_{-0.18}$	$2.25^{+0.54}_{-0.45}$	$5.56^{+4.06}_{-2.48}$	$0.33^{+0.05}_{-0.12}$	$0.09^{+0.20}_{-0.27}$
1355	$8.95^{+0.16}_{-0.19}$	$6.08^{+0.23}_{-0.21}$	$3.71^{+3.50}_{-1.99}$	$3.07^{+4.27}_{-1.59}$	$-0.45^{+0.39}_{-0.24}$	$-0.36^{+0.43}_{-0.33}$
1407	$8.62^{+0.17}_{-0.11}$	$6.29^{+0.24}_{-0.21}$	$3.25^{+2.63}_{-1.36}$	$2.86^{+4.19}_{-1.50}$	$-0.39^{+0.20}_{-0.16}$	$-0.18^{+0.41}_{-0.36}$
1422	$9.15^{+0.07}_{-0.07}$	$6.74^{+0.17}_{-0.21}$	$2.05^{+0.78}_{-0.52}$	$4.69^{+4.33}_{-2.31}$	$0.01^{+0.19}_{-0.28}$	$-0.12^{+0.32}_{-0.31}$
1431	$9.10^{+0.12}_{-0.18}$	$6.63^{+0.23}_{-0.23}$	$4.73^{+3.57}_{-2.27}$	$2.99^{+4.36}_{-1.57}$	$-0.25^{+0.28}_{-0.22}$	$-0.40^{+0.44}_{-0.34}$
1440	$8.63^{+0.07}_{-0.06}$	$6.48^{+0.23}_{-0.25}$	$1.89^{+0.54}_{-0.37}$	$3.03^{+4.41}_{-1.61}$	$0.23^{+0.10}_{-0.18}$	$-0.28^{+0.42}_{-0.38}$
1489	$8.38^{+0.12}_{-0.59}$	$5.41^{+0.28}_{-0.27}$	$7.24^{+3.33}_{-5.90}$	$3.10^{+4.92}_{-1.97}$	$-0.86^{+0.20}_{-0.10}$	$-1.00^{+0.73}_{-0.71}$
1539	$8.50^{+0.09}_{-0.25}$	$6.05^{+0.25}_{-0.24}$	$8.06^{+2.66}_{-4.80}$	$3.31^{+5.11}_{-1.84}$	$-0.74^{+0.18}_{-0.05}$	$-0.58^{+0.42}_{-0.28}$
1545	$9.00^{+0.05}_{-0.09}$	$5.98^{+0.22}_{-0.21}$	$10.24^{+1.68}_{-2.61}$	$2.77^{+3.84}_{-1.26}$	$-0.63^{+0.10}_{-0.06}$	$-0.04^{+0.32}_{-0.42}$
1619	$10.04^{+0.08}_{-0.12}$	$7.60^{+0.05}_{-0.06}$	$7.94^{+3.01}_{-3.31}$	$11.43^{+0.83}_{-1.53}$	$-0.42^{+0.21}_{-0.14}$	$0.38^{+0.01}_{-0.04}$
1627	$8.83^{+0.11}_{-0.16}$	$6.58^{+0.27}_{-0.37}$	$5.58^{+2.91}_{-2.97}$	$3.93^{+4.68}_{-2.29}$	$-0.19^{+0.38}_{-0.22}$	$-0.31^{+0.46}_{-0.59}$
1630	$9.89^{+0.16}_{-0.13}$	$7.65^{+0.12}_{-0.16}$	$4.19^{+4.20}_{-1.40}$	$7.18^{+3.38}_{-2.98}$	$0.08^{+0.20}_{-0.25}$	$0.24^{+0.11}_{-0.18}$
1661	$8.21^{+0.12}_{-0.23}$	$6.47^{+0.15}_{-0.21}$	$6.58^{+3.66}_{-4.11}$	$6.06^{+4.20}_{-3.05}$	$-0.62^{+0.42}_{-0.26}$	$-0.06^{+0.26}_{-0.27}$
1826	$8.51^{+0.11}_{-0.24}$	$6.59^{+0.21}_{-0.24}$	$6.57^{+2.94}_{-4.00}$	$3.75^{+4.56}_{-2.05}$	$-0.58^{+0.23}_{-0.12}$	$-0.32^{+0.41}_{-0.31}$
1828	$8.51^{+0.07}_{-0.08}$	$5.92^{+0.23}_{-0.21}$	$1.94^{+0.63}_{-0.49}$	$3.11^{+4.39}_{-1.64}$	$0.12^{+0.16}_{-0.32}$	$-0.47^{+0.43}_{-0.29}$
1861	$9.10^{+0.12}_{-0.21}$	$6.51^{+0.25}_{-0.22}$	$6.34^{+3.61}_{-3.33}$	$2.79^{+4.58}_{-1.44}$	$-0.60^{+0.22}_{-0.14}$	$-0.49^{+0.49}_{-0.39}$
1871	$9.17^{+0.15}_{-0.13}$	$7.02^{+0.19}_{-0.15}$	$4.23^{+3.95}_{-1.51}$	$3.41^{+3.89}_{-1.38}$	$-0.03^{+0.24}_{-0.25}$	$-0.03^{+0.30}_{-0.34}$
1883	$9.90^{+0.19}_{-0.12}$	$6.95^{+0.05}_{-0.05}$	$3.40^{+3.71}_{-1.34}$	$0.61^{+0.13}_{-0.09}$	$-0.20^{+0.32}_{-0.27}$	$0.32^{+0.06}_{-0.22}$
1886	$8.21^{+0.12}_{-0.08}$	$5.58^{+0.27}_{-0.30}$	$1.27^{+0.49}_{-0.30}$	$3.65^{+5.22}_{-2.48}$	$0.14^{+0.23}_{-0.39}$	$-0.94^{+0.71}_{-0.67}$
1910	$9.03^{+0.10}_{-0.08}$	$6.75^{+0.20}_{-0.23}$	$2.56^{+1.21}_{-0.63}$	$3.82^{+4.51}_{-2.07}$	$0.24^{+0.11}_{-0.25}$	$-0.31^{+0.41}_{-0.32}$
2019	$8.77^{+0.17}_{-0.15}$	$6.57^{+0.19}_{-0.22}$	$2.88^{+2.06}_{-1.43}$	$4.14^{+4.39}_{-2.10}$	$-0.28^{+0.31}_{-0.16}$	$-0.17^{+0.36}_{-0.33}$
2050	$8.82^{+0.06}_{-0.13}$	$5.48^{+0.24}_{-0.32}$	$9.57^{+2.11}_{-3.40}$	$4.18^{+4.79}_{-2.55}$	$-1.18^{+0.18}_{-0.21}$	$-0.26^{+0.48}_{-0.84}$

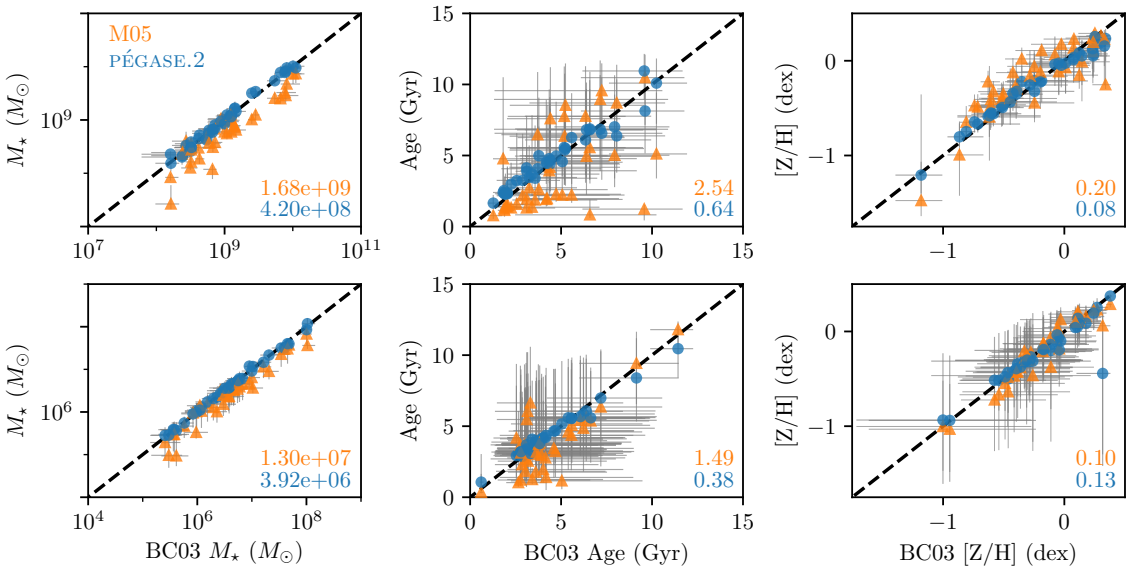

Figure 2.15 Comparison of stellar masses (left column), ages (middle column), and metallicities (right column) found using different SSP models in the SED fitting analysis. Values from the BC03 models (plotted along the abscissa, listed in Table 2.8, and adopted as my preferred values) are plotted against the M05 (Maraston, 2005) and PÉGASE.2 (Fioc & Rocca-Volmerange, 1997, 1999) values (orange triangles and blue circles, respectively). Results are shown for both the galaxies (top row) and NSCs (bottom row). The dashed line in each panel shows the one-to-one relation, while the numbers in the bottom right corner show the RMS scatter, in the same units as each panel, between M05 and BC03 (in orange) and PÉGASE.2 and BC03 (in blue).

2.5.3 A Note on Dust Effects

Given the potential impact of internal dust on the measured colours and population parameters, I have investigated the degree to which dust could alter the estimated stellar population parameters. I have done so by carrying out an independent set of SED fits with the addition of a free parameter, $E(B-V)$. The model fluxes were reddened according to the attenuation law in Calzetti et al. (2000). On average, the best-fit $E(B-V)$ for the NSCs is $\sim$0.3 mag, and $\sim$0.1 mag for the galaxies. There are, however, large uncertainties on these values, as well as substantial degeneracies with the best-fit ages. The galaxy results appear to be relatively unchanged compared to the dust-free models, with generally only slight decreases (1-2 Gyr) in age after including the reddening parameter. The galaxy metallicities remain roughly the same, around solar values, but lower metallicity objects become even more metal poor once reddening is included. The nucleus metallicities exhibit a similar change, while the shift in nucleus ages is more dramatic with reddening: i.e, the NSCs as a population become clustered around 0.5-1.5 Gyr. However, the uncertainties on these results do not rule out the possibility of older ages (3-6 Gyr) — consistent with the dust-free results.

In a parallel approach, I explored using FIR data as a means of constraining the range of plausible $E(B-V)$ values for the sample. In the Herschel Virgo Cluster Survey (HeViCS; di Serego Alighieri et al., 2013), only one of the sample galaxies, VCC 1619, had a dust detection, with an estimated dust mass $(25.5\pm5.5) \times 10^4\ M_\odot$ and dust temperature 21.7$\pm$1.0 K. For the remainder of the sample, I assume an upper limit on the dust mass of $2.44 \times 10^3\ M_\odot$, based on stacking the images of 227 early type dwarfs with non-detections in HeViCS (De Looze et al., 2010).

For the simple scenario of a foreground dust screen in front of a stellar point source (much like a nucleus with foreground galactic dust), the dust optical depth at a given wavelength, τ_λ, is proportional to the reddening $E(B-V)$, following the equation

$$\tau_\lambda = 0.921 E(B-V)\kappa(\lambda),$$

where $\kappa(\lambda)$ is value of the attenuation curve at a given wavelength. The optical depth depends on the dust mass density, ρ_d, the path length through the dust, L, and the dust absorption coefficient, k_λ, such that $\tau_\lambda = \rho_d L k_\lambda$. The dust mass density is determined by assuming various areas and values of L to create volumes in which the upper limit dust mass can be distributed. In the following calculations, I adopt the

extinction curve from Calzetti et al. (2000) and the absorption coefficients tabulated in Li & Draine (2001).

To estimate $E(B-V)$ in the program objects, I consider two cases. In the simplest scenario, I assume that all of the dust is evenly distributed in front of the galaxy in some sort of foreground screen. Assuming a typical dE effective radius of $\sim$1 kpc, and therefore a screen of 1 kpc $\times$ 1 kpc, this produces a negligibly small reddening of $E(B-V) = 0.0014$ mag. On the other hand, I find an (extreme) upper limit on $E(B-V)$ if I assume that all of the dust is contained in a foreground cylinder with a radius of $\sim$5 pc (i.e., the size of a typical nucleus). This leads to an upper limit of $E(B-V) = 18$ mag, which is obviously not a useful constraint on the plausible reddening values for these objects.

In a more realistic approach, I assume that the dust has uniform densities throughout the galaxy and nucleus. To estimate this density, I assume that 0.3% of the total dust mass is contained within a spherical volume with a nucleus-sized radius of 5 pc — in other words, the dust mass follows the same nucleus-galaxy stellar mass relation. The value of $E(B-V)$ can be calculated for various path lengths through a foreground screen with this density of dust. A dust screen 5 pc thick generates 0.04 mag of reddening, while a screen of 1 kpc (the typical r_e for early-type Virgo dwarfs) causes 8 mag of reddening. To produce $E(B-V) \sim 0.3$ mag, as suggested by the SED fits for the NSCs, the dust screen must be only 30-40 pc thick.

To summarize, I find that dust can produce non-negligible amounts of reddening, even in objects considered to contain minimal dust, like the program objects. The severity of the effect on the resulting stellar population parameters depends strongly on the distribution of this dust. Unfortunately, without high-resolution, deep imaging in FIR bands, I can only guess at the intrinsic dust distribution. Note, however, that the good agreement between the dust-free metallicity and the spectroscopic metallicities (see §2.5.6 for details) suggests that the assumption of minimal dust is reasonable for these objects, as the Lick indices — given the narrow wavelength coverage of each absorption feature — should be relatively unaffected by reddening.

2.5.4 Measurement of Spectroscopic Parameters

I use the Lick indices measured in §2.4.2 to estimate an age, [Fe/H] and [Mg/Fe] for each nucleus using the code `EZ-AGES` (Graves & Schiavon, 2008). This code uses the models from Schiavon (2007) which probe ages $0.1 \leq t \leq 15.8$ Gyr and metallicities

$-1.3 \leq$ [Fe/H] ≤ 0.2 for the solar-scaled isochrone that I chose for my analysis. `EZ-AGES` uses a sequential grid inversion technique to determine varied abundance ratios for Fe, Mg, C, N and Ca (with options to specify ratios for O, Na, Si, Ti and Cr); however, with the four Lick indices I have available, I can only determine [Fe/H] and [Mg/Fe]. Following the default settings of `EZ-AGES`, C, N, Ca, O and Cr are fixed to solar values ([X/Fe] = 0), and Na, Si and Ti are fixed to Mg ([X/Fe] = [Mg/Fe]).

In brief, `EZ-AGES` first calculates an initial guess for the population age and [Fe/H] using a model grid of H_β and $\langle$Fe$\rangle$, an average of Fe5270 and Fe5335. It then creates another model grid using $\langle$Fe$\rangle$ and Mgb to probe [Mg/Fe], and adjusts the [Mg/Fe] until this grid fits a model with age and [Fe/H] values sufficiently similar to the fiducial estimates. For my purposes, the code stops here because I provide no other indices to constrain other element ratios. Lastly, the code computes errors on age and [Fe/H] by shifting the H_β, Fe5270 and Fe5335 indices by their error bars and repeating the grid inversion. For other element abundances, errors are determined by uncertainties on the fiducial age and [Fe/H] as well as errors on the relevant Lick indices.

There are a few caveats to the results of this analysis. In some NSCs, low SNR can influence the pseudo-continuum estimates surrounding the Lick indices, introducing a bias to the measurements. Additional uncertainty arises due to smoothing the spectra to the Lick resolution, which may not be matched perfectly. Finally, even though there is evidence indicating these objects may be α-enhanced (Liu et al., 2016), I have used the solar-scaled isochrones in `EZ-AGES` rather than the α-enhanced versions because those have been found to predict ages that are too old (Weiss et al., 2006; Schiavon, 2007). The fitting process in `EZ-AGES` can still produce super-solar enhancements for *individual* elements such as Mg (and the other elements set to follow the [Mg/Fe] value); however, the abundances of the remaining elements will remain solar-scaled as I do not provide any index measurements for those elements. This may be a non-physical model for α-enhanced objects and introduces uncertainty in my estimates.

For consistency with the photometric results, I quote [Z/H] based on the estimated [Fe/H] and [Mg/Fe] values using the equation

$$[\mathrm{Z/H}] = [\mathrm{Fe/H}] + 0.94\,[\alpha/\mathrm{Fe}], \tag{2.5}$$

where I use [Mg/Fe] as a proxy for [α/Fe] (Thomas et al., 2003; Trager et al., 2000). Considering that most of the α-elements are set to match the Mg abundance, this

is a reasonable approximation. The resulting age, [Z/H] and [α/Fe] estimates are provided in Table 2.9. When multiple measurements are available for a nucleus, I quote the weighted median value.

Just as I did for the indices in §2.4.2, I now compare the age and abundance estimates for objects included in two or more of the spectroscopic datasets. These comparisons are shown in Figure 2.16. There are fewer data here compared to Figure 2.11 because `EZ-AGES` could not always converge on a fit to the provided index measurements. I find excellent agreement for [α/Fe] and [Z/H] among the datasets. Age estimates are less consistent and less certain than the abundance estimates, likely due to the inherent challenges of separating SSP ages for populations older than a few Gyr.

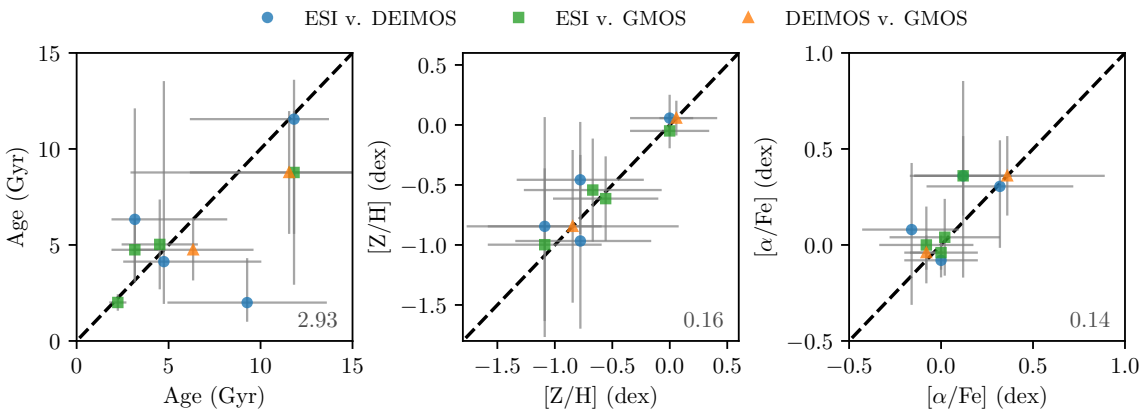

Figure 2.16 Comparison of age, [Z/H], and [α/Fe] estimates among the ESI, GMOS and DEIMOS datasets. Symbols are the same as in Figure 2.11. The dashed line in each panel shows the one-to-one relation, while numbers in the bottom right corner show the RMS scatter in the units of each panel.

2.5.5 Comparison to Previous Spectroscopic Studies

In Figure 2.17, I show published spectroscopic age and metallicity measurements for the sample galaxies along with my estimates from SED fitting of the photometry. In general, spectroscopic values are consistent within their uncertainties, although the average age differences among measurements are 4.3 ± 2.2 Gyr for ages and 0.48 ± 0.23 dex for metallicities. Some of these discrepancies can likely be explained by the use of different model sets when fitting the data, or by differences in the spatial coverage of the galaxies themselves. Consider, for example, the ATLAS3D

Table 2.9 Best-fit SSP Parameters from Spectroscopy

VCC	Instruments	T (Gyr)	[Z/H] (dex)	[α/Fe] (dex)
33	ESI,GMOS	$2.12^{+0.32}_{-0.75}$	$-0.61^{+0.37}_{-0.42}$	$0.03^{+0.18}_{-0.19}$
200	ESI	$3.40^{+1.29}_{-4.69}$	$-0.15^{+0.38}_{-0.43}$	$0.00^{+0.20}_{-0.20}$
230	ESI	$3.68^{+1.46}_{-4.01}$	$-0.56^{+0.47}_{-0.54}$	$0.00^{+0.28}_{-0.26}$
538	ESI	$3.26^{+1.18}_{-4.51}$	$-0.22^{+0.39}_{-0.43}$	$-0.04^{+0.20}_{-0.20}$
1075	ESI,DEIMOS	$4.44^{+1.56}_{-5.40}$	$-0.87^{+0.46}_{-0.47}$	$-0.04^{+0.24}_{-0.22}$
1185	ESI,GMOS	$4.77^{+1.56}_{-3.57}$	$-0.59^{+0.29}_{-0.32}$	$-0.04^{+0.16}_{-0.16}$
1192	ESI	$6.51^{+3.77}_{-6.60}$	$0.23^{+0.31}_{-0.39}$	$0.24^{+0.22}_{-0.20}$
1199	ESI	$3.78^{+1.89}_{-6.60}$	$0.20^{+0.33}_{-0.33}$	$0.04^{+0.14}_{-0.14}$
1407	ESI,DEIMOS	$5.63^{+2.22}_{-2.46}$	$-0.62^{+0.36}_{-0.37}$	$0.31^{+0.26}_{-0.23}$
1440	ESI	$5.59^{+2.89}_{-7.90}$	$-0.11^{+0.36}_{-0.41}$	$0.04^{+0.23}_{-0.23}$
1489	ESI	$3.67^{+1.46}_{-2.90}$	$-1.00^{+0.46}_{-0.47}$	$-0.22^{+0.14}_{-0.21}$
1539	ESI,DEIMOS,GMOS	$10.72^{+3.60}_{-2.27}$	$-0.98^{+0.41}_{-0.40}$	$0.28^{+0.21}_{-0.20}$
1545	ESI,DEIMOS,GMOS	$4.75^{+1.29}_{-2.66}$	$0.00^{+0.13}_{-0.16}$	$-0.04^{+0.08}_{-0.08}$
1627	ESI	$4.93^{+3.20}_{-7.95}$	$0.19^{+0.33}_{-0.32}$	$0.04^{+0.15}_{-0.12}$
1826	ESI	$3.73^{+1.53}_{-4.68}$	$-0.44^{+0.44}_{-0.51}$	$0.00^{+0.26}_{-0.26}$
1828	ESI	$5.20^{+2.59}_{-6.15}$	$-0.56^{+0.49}_{-0.57}$	$0.12^{+0.29}_{-0.29}$
1861	DEIMOS	$5.47^{+3.33}_{-5.33}$	$-0.80^{+0.43}_{-0.49}$	$-0.12^{+0.24}_{-0.26}$
1871	DEIMOS	$9.15^{+5.67}_{-4.40}$	$0.04^{+0.12}_{-0.14}$	$0.00^{+0.08}_{-0.09}$
2050	ESI	$3.31^{+1.20}_{-3.99}$	$-0.50^{+0.46}_{-0.51}$	$0.00^{+0.26}_{-0.26}$

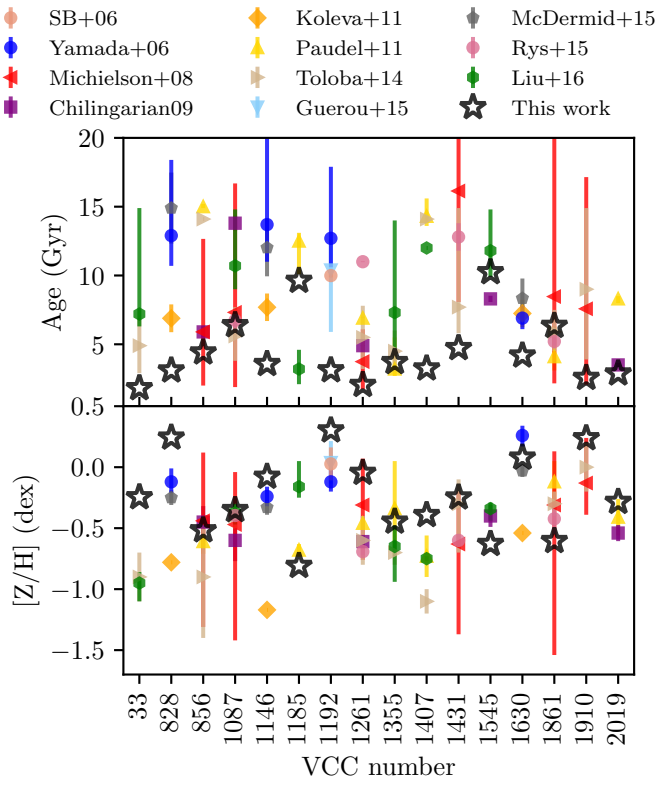

Figure 2.17 Comparison of my spectroscopic ages (upper panel) and metallicities (lower panel) with estimates from literature for the program galaxies. Only objects with more than one literature estimate are included. Estimates derived from my SED analysis are plotted as black stars.

measurements from McDermid et al. (2015), whose values are measured within one effective radius and use the Schiavon (2007) models for comparison to Lick index measurements. Their measurements often differ from those of Koleva et al. (2011) who relied on full spectral fitting and compared to the PÉGASE.HR models (although they too focused on the region inside one effective radius). Similarly, the discrepancies with Yamada et al. (2006) are likely due to model differences (i.e., they used SSP models from Vazdekis (1999)), the large number of spectral indices used in their analysis, and differences in spatial sampling (i.e., the latter study focused on the galaxy spectrum within $\sim 0.1\, R_e$). An additional hurdle in measuring ages is the difficulty in distinguishing between SSP models older than $\sim$6 Gyr (see, e.g, Powalka et al., 2016). Since most early-type galaxies contain a prominent old stellar population, it is clear that the estimation of accurate ages is quite challenging.

In Figure 2.18, I show a similar comparison for the NSCs. Parameter estimates for the NSCs have an additional source of uncertainty — possible contamination of the nucleus spectrum by the underlying galaxy which could affect the derived NSC parameters. A comparison of independent spectroscopic measurements may therefore help us understand the importance of such possible systematic errors. Unfortunately, such measurements are available in the literature for only four NSCs in my sample, from two studies: Chilingarian (2009) and Paudel et al. (2011). The ages are generally in good agreement, with only one nucleus, VCC 856, showing discrepant spectral age estimates from the literature. Three NSCs (VCC 856, VCC 1261 and VCC 2019) have conflicting metalllicity estimates from the literature. Note that Paudel et al. (2011) modeled the galaxy light profile and subtracted it from their NSC estimates, while Chilingarian (2009) did not. This is likely a key factor in the overall discrepancy between the two sets of measurements. It is also interesting to note that my photometric metallicities seem more consistent with those from Chilingarian (2009), even though my extraction methodology is more similar to that of Paudel et al. (2011). This is perhaps an effect of the different SSP models used in each analysis. Of course, it is difficult to draw firm conclusions with only four NSCs in common among the samples.

2.5.6 Comparison of Spectroscopic and Photometric Results

In this section, I compare the ages and metallicities derived for the NSCs using the ESI, GMOS and DEIMOS spectra to those found from SED fitting of the photometry.

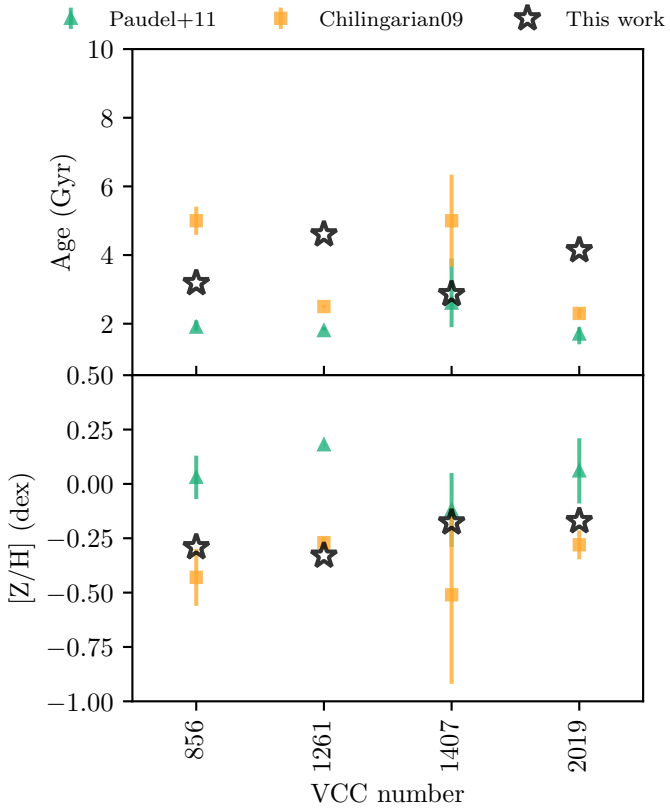

Figure 2.18 The same comparison as Figure 2.17, but for the NSCs.

It is worth emphasizing that spectra have all been reduced in similar ways, with the galaxy light modeled and removed from the nucleus in all cases (see §2.4.1. In addition, the spectra have been analyzed in an identical manner, using a single model set and methodology (as described in §2.4.2 and §2.5.4). This homogeneous analysis should reduce the possible sources of disagreement among the datasets, so that any scatter in the results should largely be attributable to the data.

Figure 2.19 compares my photometric age and metallicity estimates (calculated using the BC03 models) to the corresponding spectroscopic estimates. In general, there is good agreement within the uncertainties. In particular, the derived metallicities appear to be robust; the RMS scatter is 0.3 dex with a Spearman rank correlation coefficient $\rho = 0.79$. The ages seem to be more uncertain, five NSCs having fairly old (9–12 Gyr) spectroscopically derived ages but younger ($\sim$3 Gyr) photometric ages. This discrepancy can be attributed to the similar broadband features of populations older than a few Gyr. In addition, the spectroscopic data only include four optical lines, which also limits their ability to discriminate in age. Overall, this comparison illustrates, once again, the challenges inherent in distinguishing between old (≥ 5 Gyr) and intermediate-age populations. Based on these comparisons, I conclude that photometry alone can provide accurate metallicity estimates for galaxies and NSCs. The age estimates, while less tightly constrained, can at least eliminate the presence of prominent young ($\lesssim 2$ Gyr) stellar populations in either system.

2.6 Discussion

2.6.1 Masses and Relation to Host Galaxies

In the SED fitting process, I measure stellar masses for both NSCs and their host galaxies. The uncertainties in the derived masses range from $\sim$15% to $\sim$75%, with most masses having a precision of $\sim$35%. These uncertainties are dramatically improved over previous literature estimates (Ferrarese et al., 2006a; Leigh et al., 2012; Georgiev et al., 2016), even without imposing fixed values for the age, metallicity, or M/L. My mass uncertainties are dominated by the relatively large uncertainties on age: i.e., at a given metallicity, a 10 Gyr population will require $\sim$30% more mass to emit as much light as a 2 Gyr population.

In Figure 2.20, I show the nucleus-galaxy mass relation found using my median masses (which were computed using the BC03 SSP models and a Chabrier IMF). To

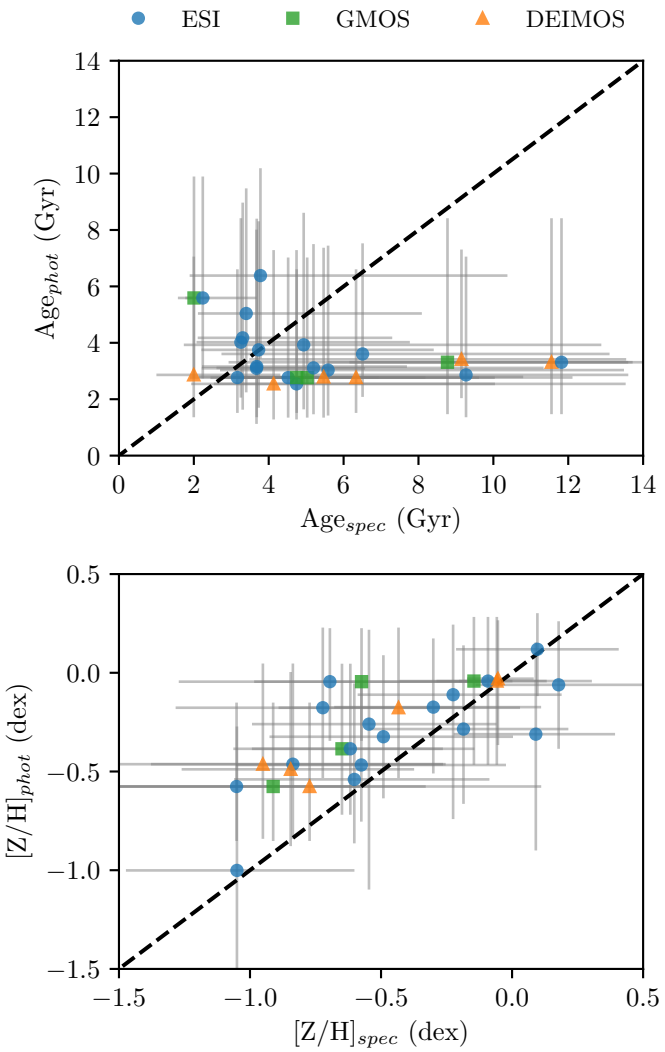

Figure 2.19 Comparison of NSC ages (top panel) and metallicities (bottom panel) derived from my photometric and spectroscopic analyses. The values from SED fitting have been calculated using the BC03 models. Typical uncertainties for the measurements are shown by the black errorbars in each panel. The dashed line in each panel shows the one-to-one relation.

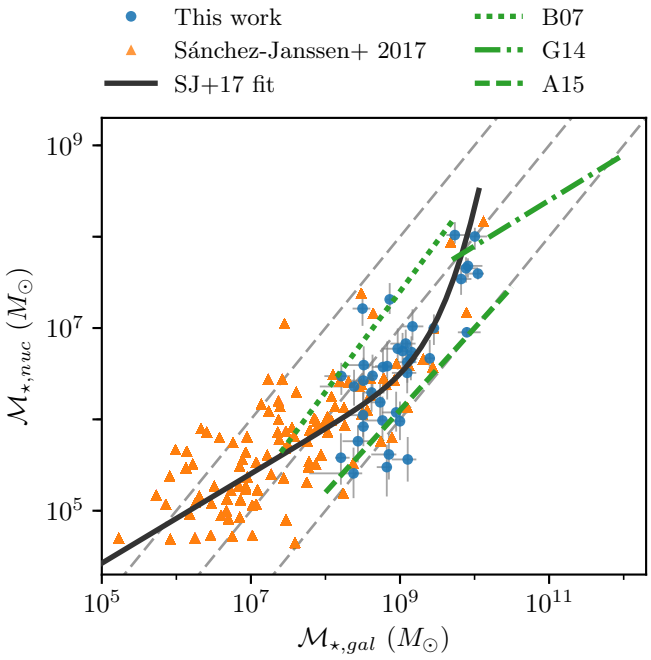

Figure 2.20 Nucleus stellar mass plotted as a function of galaxy stellar mass. Blue points show the 39 galaxies from this work, while green points are estimates based on NGVS u^*griz photometry from R. Sánchez-Janssen et al. (2018, submitted) for 107 nucleated galaxies in a 4 deg^2 region centred on M87. Dotted light gray lines indicate, from left to right, mass fractions of 10%, 1% and 0.1%. The solid dark gray curve shows the mass relation derived by R. Sánchez-Janssen et al. (2018, submitted). I also include comparison to three nucleus formation models: Antonini et al. (2015), Gnedin et al. (2014) and Bekki (2007). A description of these models is given in the text.

extend the nucleus-galaxy relation to lower masses, I have included masses for 107 nucleated galaxies from the NGVS located in the 4 deg^2 region surrounding M87 (R. Sánchez-Janssen et al. 2018, submitted). Note that these masses are approximate, being calculated from the observed i-band magnitudes and a mean M/L computed from the NGVS optical colours. The grey curve shows the best-fit relation of R. Sánchez-Janssen et al. (2018, submitted).

I overplot the observed data with predictions from three different simulations: Antonini et al. (2015, hereafter A15), Gnedin et al. (2014, hereafter G14) and Bekki (2007, hereafter B07). A15 provide an analytic mass relation for their model `CliN`. This is a simple model of GC infall within an isolated spheroid. A15 also use a more complex model (`GxeV`) that allows for *in situ* star formation as well as galaxy and black hole mergers in addition to GC infall. However, the resulting mass relations for both models look quite similar in the regime of these data, with `GxeV` producing a relation with larger scatter.

The G14 model is a numerical model based on pure cluster infall via dynamical friction. This model produces nucleus-to-galaxy mass fractions that are consistent with the observed fractions for Virgo NSCs (as well as other samples). However, these mass fractions are for more massive simulated galaxies (ranging from galaxies comparable to the Milky Way to M87-like systems). The results from G14 show that NSCs become slightly more prominent as galaxy mass decreases. Therefore, once their mass relation is extrapolated to the mass regime of this work, the predicted NSC masses are somewhat over-massive. However, it is important to note that G14 quote the total stellar mass within 10 pc of the galaxy centre as the nucleus mass; they also caution that their dynamical friction model might be too effective in migrating clusters to the galaxy centre. The G14 predicted mass relation differs significantly from the `CliN` relation; this is likely due to the absence of black hole disruption in the G14 scenario.

Lastly, there is the prediction from the B07 model, which is a pure dissipative formation model accounting for nucleus growth regulation from stellar feedback and a central black hole. The model galaxy is a spheroid (usually about 10^9 solar masses), within which is embedded a 1 kpc gas disk. Different iterations of the model assign between 2% and 50% of the mass to the gas disk. The models typically produce a nucleus with $\sim$4.6% of the spheroid mass, a larger mass fraction than observed in this sample. This efficient formation scenario may be appropriate for NSCs in lower mass galaxies considered in the model ($M_{\star,gal} \approx 10^8$), which tend to be more prominent

within the host galaxy.

The B07 and A15 mass relations have slopes that are roughly consistent with the trend among the most massive nucleated galaxies ($M_{\star,gal} \geq 10^8$), although the B07 relation produces overmassive NSCs, while the A15 relation produces undermassive NSCs. The observed mass relation is effectively bounded by these two cases, suggesting that variation in mass fraction can be produced by varying the contribution of dissipative and dissipationless formation processes. This is supported by the results shown in A15, in which the `GxeV` model produces a wide range of nucleus masses at fixed galaxy mass.

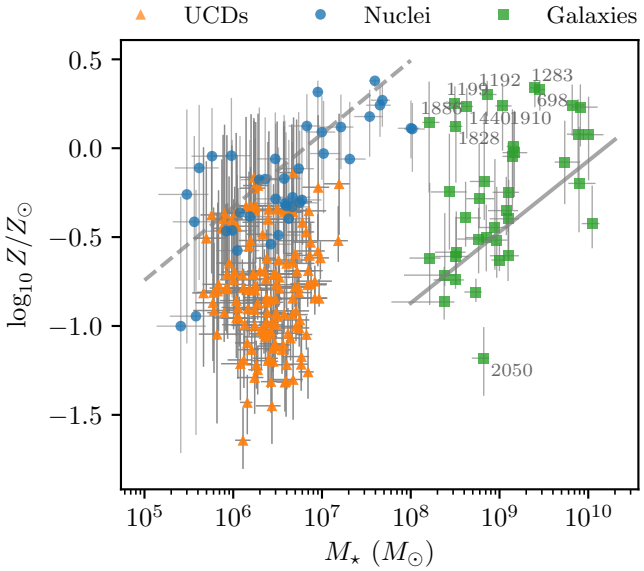

Figure 2.21 Mass-metallicity relations for my sample NSCs and galaxies (blue circles and green squares, respectively). For comparison, orange triangles show UCDs in the M87 region from Liu et al. (2015). Masses and metallicities for the three different types of stellar systems were derived homogeneously using the BC03 SSP models with a Chabrier IMF. Note, however, that F300W and F160W photometry is unavailable for the UCDs, and roughly a third of the sample also does not have r or K_s imaging. The dotted line shows the fitted relation for the NSCs, while the solid line shows the galaxy mass-metallicity relation from the simulations in Ma et al. (2016), shifted to higher metallicities by 0.3 dex. VCC numbers are labeled for galaxies that diverge from this mass-metallicity relation.

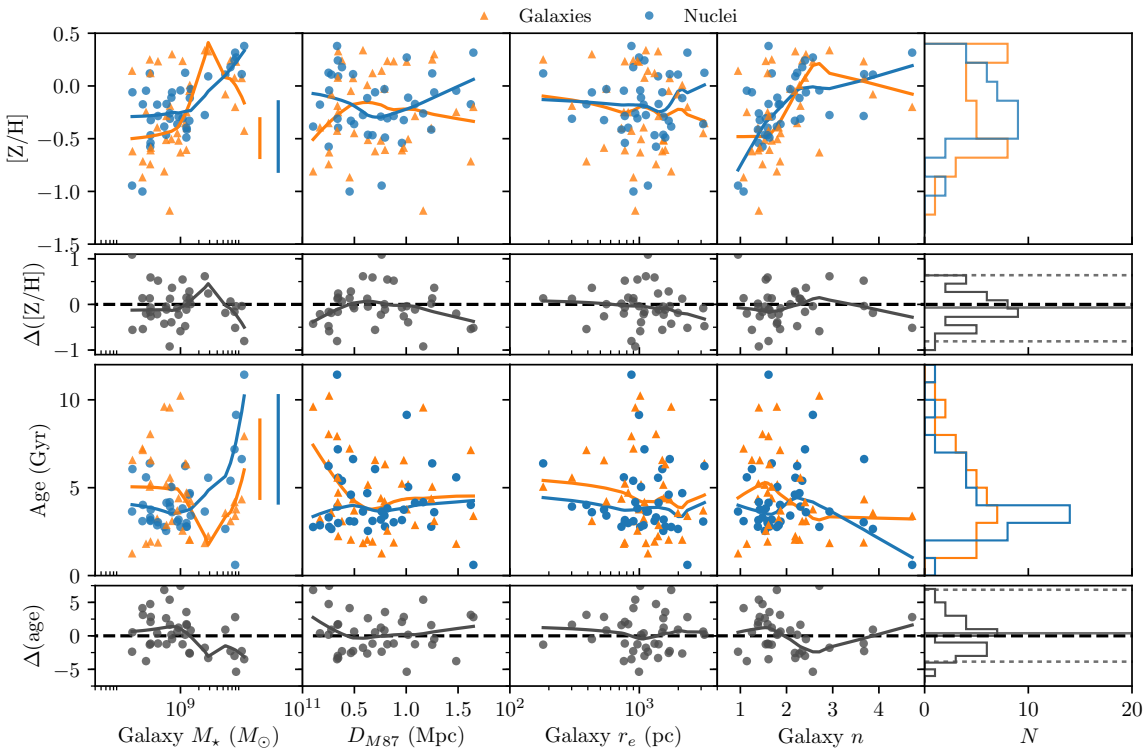

Figure 2.22 Metallicities (first row), metallicity differences (galaxy [Z/H] - nucleus [Z/H]; second row), ages (third row), and age differences (galaxy age - nucleus age; fourth row) for galaxies (orange triangles) and NSCs (blue circles). These parameters are plotted, from left to right, against galaxy stellar mass, distance from M87 (as a proxy for environment density), galaxy effective radius, and galaxy Sérsic index. LOWESS (Cleveland, 1979) fits are shown as solid lines in each panel. Typical error bars are shown in the first column in orange and blue for galaxies and NSCs, respectively. Distributions for each population are shown in the far right column, with the mean (solid line) and 2.5 and 97.5 percentiles (dotted lines) shown for the metallicity and age difference distributions. Metallicity and age values are derived using the BC03 models with a Chabrier IMF.

2.6.2 Abundances

In this section, I examine the photometrically derived SSP ages and metallicities, focusing mainly on the estimates found using a Chabrier IMF and the BC03 SSP models (Table 2.8).

A comparison of the masses and metallicities for galaxies and NSCs is shown in Figure 2.21. For comparison, I also show results for UCDs based on the sample of Liu et al. (2015). I used the published u^*giz photometry (and, when available, r and K_s photometry) to estimate mass, metallicity and age using the SED fitting procedure described in §2.5.2. This figure shows that a remarkably similar mass-metallicity relation holds for both the NSCs and galaxies. Fitting an equation of the form $\log_{10} Z/Z_\odot = \alpha \log_{10} M_\star + \beta$ yields $\alpha = 0.41 \pm 0.05$ and $\beta = -2.80 \pm 0.35$ for the NSCs. I compare the galaxies to the relation produced by the simulations of Ma et al. (2016). The slope of this relation fits the data well; however, a shift of $+0.3$ dex in metallicity is required to match the data. This offset may be explained by morphological or environmental differences — since I am looking exclusively at early-type galaxies in a cluster environment — or by different model assumptions. A few outliers are found to have metallicities even higher than the shifted relation. These include the compact ellipticals VCC 1192, VCC 1199, and VCC 1440, as well as the bright, structurally complex galaxies VCC 698 and VCC 1283.

NSCs and galaxies are found to occupy a similar, broad range in metallicity. It is interesting to note that, at fixed mass, the UCDs are systematically *less* metal rich (by 0.56 ± 0.12 dex) than the NSCs. UCDs are thought to be either the stripped remains of nucleated galaxies, or simply the high-mass tail of the globular cluster luminosity function (e.g., Janz et al., 2016; Pfeffer et al., 2014; Norris et al., 2014; Mieske et al., 2013). In the mass range $10^6 - 10^8 M_\odot$, Janz et al. (2016) find that the UCDs span a broad metallicity range $-1.1 \leq$ [Z/H] ≤ 0.2, consistent with a sample containing both stripped objects and GCs. I do not detect any solar or super-solar metallicity UCDs, which may suggest that the sample is predominantly high-mass GCs. However, a subset of the UCDs overlap with the nucleus sample, suggesting that these UCDs and NSCs are drawn from the same population. Perhaps the UCD hosts were stripped or disrupted at early times, removing the surrounding supply of gas and halting their chemical enrichment. However, firm conclusions regarding UCD metallicities would be premature because other factors may be at play. For instance, the sample of galaxies and NSCs examined in this paper are scattered throughout the

entire cluster (see Figure 2.3), whereas the UCDs of Liu et al. (2015) are drawn from the central ~ 4 deg^2 and, thus, may be among the oldest stellar systems in Virgo (e.g., Lisker et al., 2009).

In the top two rows of Figure 2.22, I plot the nucleus and galaxy metallicities, as well as the metallicity *differences*, as a function of galaxy stellar mass, distance from M87, galaxy effective radius, and galaxy Sérsic index. Both galaxies and NSCs trend toward higher metallicities as mass increases. On average, the NSCs in the sample have metallicities statistically indistinguishable from those of their host galaxies, with a mean metallicity 0.07 ± 0.3 dex higher than that of their hosts. However, if I exclude the galaxies (and their corresponding NSCs) that deviate from the mass-metallicity relation in Figure 2.21, then the NSCs are, on average, 0.20 ± 0.28 dex more metal rich than their hosts. This suggests that most NSCs are not formed primarily via GC infall, as GC systems typically have lower metallicities than their host galaxies (Jordán et al., 2004b; Puzia et al., 2005). It is also apparent that the metallicity distributions, shown in the top right panel of Figure 2.22, are shaped differently, with NSCs having a broad, single-peaked distribution, compared to a bimodal distribution for the galaxies.

The third column of Figure 2.22 suggests that the smallest galaxies in the sample exclusively have metallicities [Z/H] ≥ -0.5. Although this may seem counterintuitive, the relation is, in fact, driven by the small number of intrinsically rare, compact ellipticals in the sample: e.g., VCC 1192, VCC 1199, and VCC 1627. These galaxies, despite their low masses and compact sizes, have some of the oldest ages and highest metallicities in the sample. This would be consistent with the notion that they represent the tidally-stripped relics of initially much more massive galaxies (Guérou et al., 2015).

The relationship between metallicity and Sérsic index in the fourth column of Figure 2.22 is likely another manifestation of the mass-metallicity relation. Dwarf ellipticals tend to have lower indices than their more massive counterparts (e.g., Caon et al., 1993; Ferrarese et al., 2006a; Mahajan et al., 2015), so the Sérsic index effectively traces mass.

2.6.3 α-Element Abundances

The α-element abundance [α/Fe] is known to trace star formation timescales, with short timescales corresponding to higher [α/Fe] values. Type II supernovae from the

most massive, rapidly-evolving stars eject relatively large amounts of α elements. The [α/Fe] of the galaxy only begins to decrease after less α-enhanced ejecta from Type Ia supernovae begin to appear. Previous results for low-mass galaxies show that their star formation timescales are regulated by the density of their environment, with galaxies in the densest regions having both super-solar [α/Fe] and higher GC specific frequencies (Liu et al., 2016). In addition, GCs in early type galaxies are known to have super-solar [α/Fe] (Puzia et al., 2005). Therefore the [α/Fe] of NSCs may indicate the importance of environment and/or GC infall in nucleus formation.

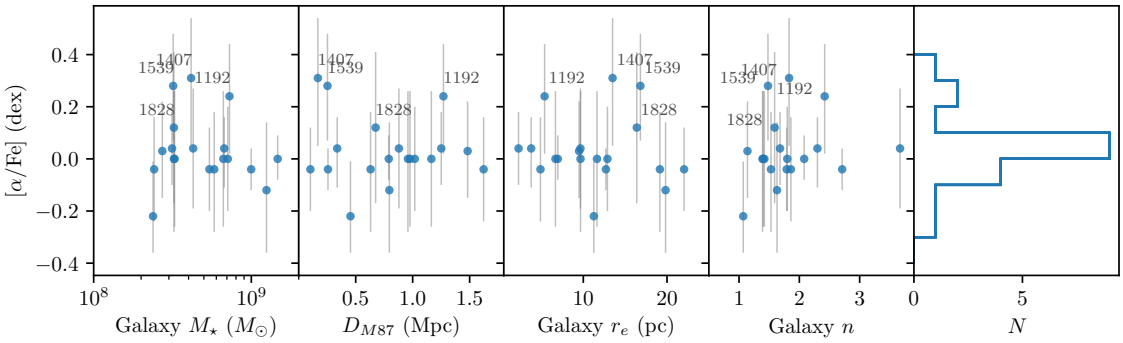

Figure 2.23 Nucleus [α/Fe] plotted as a function of, from left to right, galaxy stellar mass, distance from M87 (as a proxy for environmental density), galaxy effective radius, and galaxy Sérsic index. The far right panel shows the [α/Fe] histogram. NSCs with [α/Fe] > 0.1 have been labeled by VCC number.

While my spectroscopic analysis does not include the galaxies in the sample, I can still investigate any trends among the 19 NSCs for which I have measured [α/Fe]. I show [α/Fe] as a function of galaxy mass, distance to M87, galaxy r_e, and galaxy n in Figure 2.23. There are no clear trends, with most NSCs having roughly solar [α/Fe] regardless of environment or galaxy properties. However, it is interesting to note that the galaxies VCC 1407 and VCC 1539, which were found to have super-solar [α/Fe] and high GC specific frequency by Liu et al. (2016), have similar [α/Fe] in their NSCs. The VCC 1185 galaxy also has with a similarly high [α/Fe], but its nucleus has [α/Fe]$= -0.04$ and it has a low GC specific frequency for its [α/Fe]. In general, though, the lack of significant α enhancement suggests that NSCs have not formed through particularly brief star formation episodes. A more thorough investigation of the connections among NSCs, GC populations, and [α/Fe] is beyond the scope of this paper.

2.6.4 Ages

As discussed previously, measuring accurate ages for SSP populations older than a few Gyr can be challenging, given the similarities among the model spectra within one model family, and the differences between predictions from various codes (Powalka et al., 2016). Therefore, my age estimates are hampered by somewhat large uncertainties and any apparent trends should be considered with caution.

As can be seen in the left panel of the third row of Figure 2.22, there appear to be two populations, clustered distinctly in age, among the galaxies and the NSCs. The most massive objects ($M_{\star,gal} \geqslant 2 \times 10^9 M_\odot$) contain NSCs that are consistently older, with typical ages of $\sim$7 Gyr, than the lower-mass NSCs (which have ages scattered around 4 Gyr). The overall age distributions for galaxies and NSCs (shown in the far right panel of the third row) appear quite similar and there are no clear age offsets between the two types of object. However, the age differences in the bottom right panel do have a tail toward positive values in which the galaxy is older than the nucleus.

The density of the surrounding environment, as traced by distance from M87, does not appear to have a strong effect on the galaxies or the NSCs. There is perhaps some evidence that older objects tend to be found in higher density environments, as expected if the earliest objects to fall into the Virgo Cluster are now found close to the bottom of the cluster potential. Having been stripped of any gas upon infall, only old stellar populations would remain.

I reiterate that the derived ages are SSP-equivalent ages. The galaxies almost certainly host complex populations, and it is quite possible that NSCs consist of multiple stellar populations. As a result, fitting an SSP model introduces some bias and uncertainty. If the actual stellar content is primarily that of an old population, even a small contribution from a substantially younger population could skew the SSP-equivalent, luminosity-weighted age. Also, the results of this work do not consider the effect of dust extinction. Future analyses should consider stellar populations that are more complex than SSPs and explore the possibility of non-zero dust extinction.

2.6.5 Structural Parameters of NSCs

By fitting each nucleus with a Sérsic profile, I can measure not only its effective radius, r_e, but also its concentration index, n, axis ratio, b/a, and position angle, PA. However, for NSCs that are only marginally resolved, these structural parameters are

clearly not very meaningful — after convolving the model with the PSF, any intrinsic flattening would go unnoticed. Nevertheless, in this section, I look for possible trends in r_e, b/a, n, and the offset between nucleus and galaxy PA, ΔPA. Because most of the galaxies have been modeled with multiple components in the 2D decomposition, there is no single PA that I can provide for the galaxy. Therefore, I estimate a mean PA from the `ELLIPSE` isophotes between 1″ and 1 r_e, with r_e determined through curve of growth analysis (Ferrarese et al., 2016).

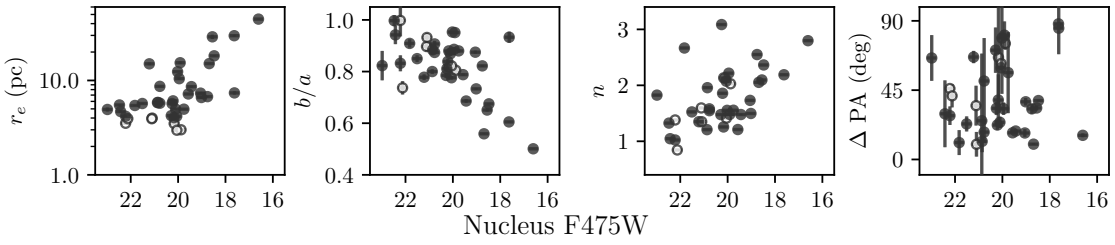

Figure 2.24 Trends in nucleus effective radius, axis ratio, Sérsic index and position angle offset between the nucleus and galaxy, plotted as a function of nucleus F475W magnitude. Open circles denote NSCs that I consider marginally resolved ($r_e < 4$ pc or 0.″05) and as such have less robust structural measurements. All parameters have been measured using a single Sérsic component fitted to the nucleus using GALFIT as described in §2.3.2 with the exception of the galaxy position angle (see text for details).

I have searched for trends in these structural parameters as a function of magnitude, environment, metallicity, and colour, finding that most parameters are tightly correlated with nucleus magnitude. In Figure 2.24, I show nucleus r_e, b/a, n, and ΔPA as a function of nucleus magnitude. Côté et al. (2006) determined the resolution limit for ACSVCS images to be 2 pc, so I consider NSCs with $r_e < 4$ pc (0.″05) to be marginally resolved. Seven NSCs meet this criterion and have been indicated with open circles in the figure. Overlooking these NSCs, some trends emerge. Unsurprisingly, the brightest NSCs tend to be larger (Côté et al., 2006) and have larger Sérsic indices compared to the fainter NSCs. Indeed, the trends in these nuclear parameters mimic what I observe for the galaxies. However, it is interesting to note that as nucleus luminosity increases, the NSCs become more flattened, and are weakly aligned with the semi-major axis of the host galaxy. If this flattening is indicative of rotation, then it is likely that these NSCs formed predominantly via dissipative processes when gas falls to the centre of the galaxy and forms a rotating disk. On the other hand, recent dissipationless models have been able to produce a rotating, flattened nucleus

as well (Tsatsi et al., 2017). Understanding the significance of the observed trends may shed light on the various formation scenarios, although it is already clear that kinematic information with high spatial and spectral resolution would be extremely useful in discriminating between the competing models. For now, I simply note that these results suggest that different formation mechanisms may dominate in different regimes of nucleus and galaxy mass (Turner et al., 2012).

2.6.6 Co-existence with Supermassive Black Holes

Many studies have established that both a nucleus and supermassive black hole (SMBH) exist in the Milky Way (e.g., Ghez et al., 2008; Schödel et al., 2007; Becklin & Neugebauer, 1968), a situation that is true of some other galaxies as well (Seth et al., 2008; Neumayer & Walcher, 2012). In this section, I investigate whether any NSCs in the sample might contain a supermassive black hole as well — a possibility that bears consideration following the recent discovery of a supermassive black hole in a Virgo UCD (Seth et al., 2014). In addition, the various proposed modes of SMBH formation produce different occupation fractions in this regime of galaxy mass, so SMBH detections can be a valuable constraint in our understanding of SMBH formation and galaxy evolution (Volonteri, 2010; Greene, 2012).

To test this possible co-existence, I adopt the black hole mass to galaxy mass relation from McConnell & Ma (2013),

$$\log_{10}(M_\bullet) = (8.46 \pm 0.08) + (1.05 \pm 0.11)\log_{10}(M_{\star,bulge}/10^{11}M_\odot), \tag{2.6}$$

where $M_\bullet$ is the mass of the SMBH and $M_{\star,bulge}$ is equal to galaxy stellar mass for early-type galaxies. For a simple, first-order approach, I assume that this relation applies for the total "compact massive object" (CMO) mass (Ferrarese et al., 2006b), noting that previous work suggests NSCs and SMBHs may follow separate mass relations (Balcells et al., 2007; Scott & Graham, 2013; Leigh et al., 2012; Graham, 2012). I then highlight any nucleus that deviates from the expected relation at the $3\,\sigma$ level or more.

The results of this exercise are shown in Figure 2.25, along with any confirmed SMBH masses based on X-ray detections in the AMUSE-Virgo survey (Gallo et al., 2010). VCC 140 is an under-massive outlier nucleus; a SMBH of $\sim 10^{6.4} M_\odot$ would be

necessary to match the relation from Eq 2.6. I also consider galaxies in the sample that may have over-massive NSCs. Significant outliers in this region include the compact ellipticals, VCC 1192 and VCC 1199, and the bright galaxies, VCC 1146 and VCC 1242, which have structurally complex inner regions. One might expect to find compact ellipticals in this region if they are indeed the tidally-stripped relics of more massive galaxies that hosted a similarly massive nucleus. Meanwhile, the NSCs of galaxies such as VCC 1146 and VCC 1242 seem to be markedly different morphologically from other NSCs (Turner et al., 2012), which may be evidence that these NSCs have experienced a different evolutionary path, perhaps leading to increased growth of the CMO.

Assuming the mass relation from massive galaxies holds at these slightly lower-mass regimes, one may expect that SMBHs may indeed co-exist with the NSCs in this sample, particularly in cases like VCC 140 in which the NSC has a lower mass than expected. The five already confirmed SMBHs in this sample also support the idea that more of these galaxies are likely harbouring SMBHs. However, it remains unclear if one would expect the same mass relation in this regime, considering the dramatic change in the mass relation for nucleated galaxies with masses below $\sim 10^9 M_\odot$.

2.7 Summary

I have carried out a comprehensive analysis of the stellar populations and masses of 39 NSCs belonging to early-type galaxies in the Virgo cluster. The UV, optical and infrared datasets that form the basis of my analysis — consisting of both imaging and spectroscopy — are the most extensive ever used to characterize the stellar content of NSCs in nearby, early-type galaxies. My photometric analysis rests on multi-band imaging from HST (ACS, WFPC2, and NICMOS) and CFHT (MegaCam and WIRCam) that was collected in the course of the *Virgo Redux* survey, *ACS Virgo Cluster Survey* (ACSVCS; Côté et al., 2004), and *Next Generation Virgo Cluster Survey* (NGVS; Ferrarese et al., 2012). For 19 of the program NSCs, I have also analyzed long-slit and/or IFU optical spectroscopy from the Keck II (DEIMOS and ESI) and Gemini South (GMOS) telescopes.

Nucleus and galaxy magnitudes were extracted through two methods: (1) a two-component (nucleus and galaxy) surface brightness profile decomposition, using composite profiles created from the high resolution HST data combined with deep, wide-field CFHT data; and (2) a multi-component image decomposition, allowing for more

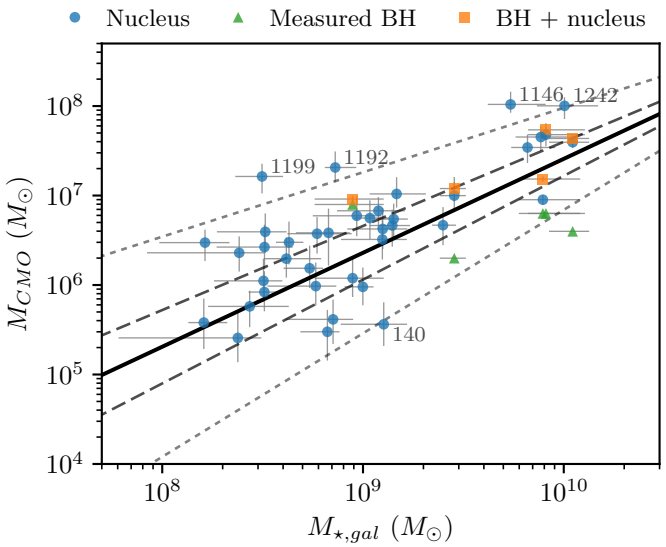

Figure 2.25 Relationship between galaxy stellar mass and the mass of the central massive object (CMO), including confirmed black holes within NSCs. The solid line shows the relation from McConnell & Ma (2013) with $1\,\sigma$ and $3\,\sigma$ uncertainties indicated by the dashed and dotted lines, respectively. The stellar masses of the NSCs are shown as blue circles. Green triangles indicate black hole detections from AMUSE-Virgo (Gallo et al., 2010), while orange squares show the total mass of these black holes and their corresponding NSCs. Objects that fall outside the $3\,\sigma$ region are labeled with their VCC numbers.

complex galaxy structure, using GALFIT. After a careful comparison of the two methods, the two-dimensional approach was used to produce my final photometric measurements for the extracted nucleus and its host. Through Markov Chain Monte Carlo fitting of the spectral energy distributions to various sets of SSP models, I have determined robust mass and metallicity measurements, as well as broad age estimates. Parameters obtained from my photometric analysis have been compared to the spectroscopic results, derived homogeneously using the `EZ-AGES` code (Schiavon, 2007; Graves & Schiavon, 2008).

The main results of this chapter can be summarized as follows:

- Regardless of the choice of SSP model, there are no strong systematic trends in the derived properties. The Maraston (2005) models can produce a broader, younger range of ages for the sample, likely due to their treatment of the TP-AGB stellar evolutionary phase. NSC stellar population parameters derived from the Keck-DEIMOS, Keck-ESI and Gemini-GMOS spectra show good internal agreement, despite the different instrumental setups.

- A comparison of spectroscopic age and metallicity estimates in the literature for NSCs and galaxies in the sample shows a significant level of scatter among the measured parameters. Some variation may be due to differences in model assumptions (i.e., adopted isochrones, spectral libraries and stellar evolution treatments) or data analysis methods (i.e., the radius selected for analysis or decomposition techniques). Although homogeneous datasets should still provide reliable *relative* age and metallicity estimates, this comparison suggests that conclusions on the stellar populations in the NSCs, and differences with respect to their host galaxies, should be viewed with caution.

- The photometric metallicities are in reasonable agreement with those derived from spectroscopy for the NSCs, with an RMS scatter of $\sim$0.3 dex. Photometric ages are scattered around 4 Gyr, although spectroscopic ages can be as old as 12 Gyr. This discrepancy may be caused by (1) loss of age sensitivity for old stellar populations in optical spectra; or (2) the possible presence of a small young stellar population that can enhance the blue-optical and UV fluxes in the NSCs. The limited age resolution at old and intermediate ages available from SED fitting is due, in part, to the modest SNR in the UV data, and the underlying assumption of pure SSP populations (which can display similar broadband features for most ages older than a few Gyr).

- My computed stellar masses (measured from SED fitting to six to ten photometric bands) are accurate to typical precisions of 35%. This is nearly a factor of two improvement over previous measurements that have usually been derived using just one or two photometric bands with assumed ages and/or metallicities (Georgiev et al., 2016; Leigh et al., 2012; Ferrarese et al., 2006a). Over the range of $10^{8.4}$ to $10^{10.3} M_{\odot}$ in galaxy stellar mass for my galaxies, the NSCs are found to contribute a fraction of $0.33^{+0.09}_{-0.07}$ percent of the total stellar mass, consistent with previous results for early-type galaxies based on less precise stellar masses for the NSCs and simpler nucleus-galaxy decompositions (Turner et al., 2012; Côté et al., 2006; Ferrarese et al., 2006a). The M_{nuc} vs. M_{gal} relation is also consistent with new results from R. Sánchez-Janssen (2018, submitted) which extend the relation to much lower masses (after combing the observed i-band luminosities with an assumed $M/L = 1$).

- The NSCs show evidence for a rather steep mass-metallicity relation of the form $\log_{10} Z/Z_{\odot} \propto \alpha \log_{10} M_{\star}$ with $\alpha = 0.41 \pm 0.05$. A similar trend is exhibited by UCDs (with masses $10^6 \leq M_{\star} \leq 10^{7.3} M_{\odot}$) in the Virgo core region, although the UCDs are more metal-poor, by 0.56 ± 0.12 dex, at fixed mass. The galaxies follow the slope of the relation measured in Ma et al. (2016), but systematically shifted to higher metallicities by $\sim$0.3 dex.

- NSC metallicities are statistically indistinguishable from those of their hosts, appearing 0.07 ± 0.3 dex more metal-rich on average. However, excluding outlier galaxies (i.e., compact ellipticals and morphologically unusual galaxies) that do not follow the mass-metallicity, NSCs are 0.20 ± 0.28 dex more metal-rich than their hosts, qualitatively consistent with conclusions from previous studies (Paudel et al., 2011; Chilingarian, 2009; Koleva et al., 2011). There is no clear age difference, with NSC ages showing a broad distribution between $\sim$3 and $\sim$12 Gyr.

- There is a clear trend for the brightest NSCs to be the most flattened; a far more tentative trend suggests that these bright NSCs may also be more closely aligned with the major axes of their hosts. Due to the barely-resolved sizes of the fainter NSCs, it is unclear how these trends manifest in the fainter regimes. However, this suggests that the largest NSCs — which belong to galaxies with stellar masses greater than $\sim 10^{9.5} M_{\odot}$ — may be formed predominantly through

dissipative processes that can induce flattening and rotation.

A number of questions regarding the stellar populations and the formation of NSCs remain unanswered. This work has adopted a fairly simple approach to the stellar populations of the NSCs. Future work should consider the effects of internal extinction as well as more complex stellar populations, which may provide a better understanding of the systematics of the age estimates. Given current predictions from formation scenarios, it is still difficult to determine how much each mechanism might contribute to the formation of a particular nucleus, or whether certain processes become more important in different regimes of mass, environment, or other properties. This could be addressed with model predictions for not only size, mass and velocity dispersion relations, but also ages and abundances, which would provide more points of comparison with observations. While some models have presented qualitative statements about the ages of NSCs relative to their hosts (Bekki, 2007), precise predictions for relative or absolute ages could prove useful. Simulations that include multiple processes of nucleus formation, such as those in Antonini et al. (2015), would be ideal for investigating the relative contributions of dissipative and dissipationless processes, and any differences these may produce in abundance and age distributions.

The present study has focused on a somewhat limited sample of NSCs — in the sense that I have explored a restricted morphological type and mass range for the host galaxies — so I do not yet have a complete picture of the nucleus population. Fortunately, many hundreds of nucleated galaxies are available in the NGVS survey area. By applying my methods to the full sample in NGVS, albeit with a smaller number of photometric bands, it should be possible to examine the nucleation fraction, stellar population parameters, and scaling relations for a greatly expanded number of NSCs. This will include exploring a new and important regime in galaxy mass (see, e.g., R. Sánchez-Janssen et al. 2018, in preparation, for first results). The large numbers of UCDs and GCs detected in the NGVS imaging should also enable a full comparison of the properties of compact stellar systems within a single, homogeneous dataset (Powalka et al., 2016; Liu et al., 2015).

Chapter 3

A Fresh Look at the Structure of the Virgo Cluster with the Next Generation Virgo Cluster Survey

The Next Generation Virgo Cluster Survey (NGVS) contains deep, optical imaging for nearly 3,700 galaxies in a a range of environmental conditions throughout the Virgo Cluster, so it seems natural to extend the analysis in the previous chapter to explore how the structural parameters and stellar populations of nucleated galaxies change in different environments. A first step in this extended analysis is to develop clear definitions of the various environments in Virgo by identifying distinct substructures within the cluster. This chapter introduces a novel clustering algorithm for this purpose. The analysis is aided by tables of galaxy properties for 12 Virgo Cluster analogues from the `Illustris` cosmological simulations, provided by L. Sales. The results presented in this chapter are currently being prepared for publication (C. Spengler et al., 2018, in preparation).

3.1 Introduction

Galaxy clusters are assembled though the hierarchical mergers of smaller groups of galaxies (White & Rees, 1978). The timescales of these merger events — as well as the scales of the groups involved and the properties of the resulting clusters — are governed by the number and distribution of filaments and halos of dark matter, which define the cosmic web and dominate the mass budget of the Universe. Eventually

these small, merging galaxy groups form a well-mixed, virialized cluster with a regular appearance, but many galaxy clusters still retain signatures of their hierarchical formation, such as residual structures in distribution of galaxies or hot x-ray gas. By studying these residual substructures, we can explore how galaxies are shaped by the changing environment as they enter a cluster (this is explored in greater detail in the following chapter). More fundamentally, by comparing observed cluster substructures to those created in cosmological simulations, we can test whether our current dark matter paradigm can correctly replicate the formation and growth of structure in the Universe.

Ideally, the cosmological paradigm should be able to reproduce the observed appearance and frequency of structures at all spatial scales — everything from the large-scale web of filaments and voids, to galaxy clusters and groups, down to individual galaxies and their satellite systems. The current ΛCDM paradigm has already encountered some challenges on the smallest scales: one is the missing satellites problem, which arose because the observed number of low-mass satellite galaxies is much lower than what simulations predict (Klypin et al., 1999; Bullock, 2010). However, it is possible to reduce or eliminate this discrepancy with some mechanism to suppress star formation at earlier times, such as reionization (Simon & Geha, 2007). Another issue is the "too big to fail" problem, in which simulations predict the existence of massive satellite halos that should have no problem forming stars. However, no observed satellites are consistent with residing in such massive halos — their observed velocities are too low, implying that additional physical processes must be incorporated into the simulations to limit star formation in those massive halos, and/or redistribute their mass (Boylan-Kolchin et al., 2011). The substructures within galaxy clusters provide another scale which can be used to evaluate ΛCDM models. Some initial studies have already suggested that observed galaxy clusters have too much substructure to be explained by the ΛCDM framework (Jauzac et al., 2016; Schwinn et al., 2017, 2018), so a detailed study of the Virgo Cluster and its substructure would be quite valuable for exploring this potential issue within our current paradigm.

There are a number of challenges involved in the analysis of these substructures, however. Most fundamentally, structures exist in a six-dimensional space — three dimensions of both position and velocity. However, we can only observe a portion of this space as two dimensions of position (projected coordinates on the sky), or three dimensions with the addition of recessional velocities and/or other properties that can be used to correlate distance from the observer, such as distances from

surface brightness fluctuations (SBF; Tonry & Schneider, 1988; Tonry, 1991; Blakeslee et al., 1999; Mei et al., 2007; Blakeslee et al., 2009). With the observables that are usually available, there is no foolproof method for identifying observed structures and a number of techniques have been used over the years, frequently involving some combination of projected separations with recessional velocities or distances from SBF to identify groups (e.g., Dressler & Shectman, 1988; Bird, 1994; Schindler et al., 1999; Mei et al., 2007; Blakeslee et al., 2009).

Additionally, substructures in observations and simulations are often identified using completely separate techniques. Because simulations contain far more information than simple sky coordinates and velocities of the galaxies, the methods discussed above are not used. Instead, substructures are typically identified based on the distributions of the underlying dark matter halos rather than the galaxies themselves, or based on considerations of which galaxies were bound together at earlier times in the simulation.

Arguably, the biggest challenge in this type of analysis is the choice of algorithm itself. Substructures can manifest at a range of densities and spatial scales depending on the overall mass and number of galaxies within a cluster, so algorithms that extract substructures in which members are linked within a fixed physical separation — such as the popular Friends-of-Friends (FoF) method (Davis et al., 1985) — may be insensitive to particular types of substructures.

Given the limitations of available datasets and the analysis methods themselves, the best way to minimize sources of error is through a homogeneous analysis of both observed and simulated datasets with an algorithm that can detect substructures across a range of densities and spatial scales. Such a homogeneous analysis is introduced in this chapter. I implement the use of a novel density-based hierarchical clustering algorithm to extract substructures and their member galaxies. In addition, I present a comparison of the identified substructures in NGVS with those from Virgo analogues in the `Illustris` cosmological simulation using similar measurements for both real and simulated clusters to test how well ΛCDM can reproduce observed structure within galaxy clusters.

3.2 Data and Observations

3.2.1 The Next Generation Virgo Cluster Survey (NGVS)

The optical imaging data in this chapter comes entirely from the Next Generation Virgo Cluster Survey (NGVS; Ferrarese et al., 2012), which comprised a substantial portion of the data used in Chapter 2. Details of the observations and data reduction can be found in Chapter 2 and Ferrarese et al. (2012). In brief, NGVS contains u^*griz imaging for 104 deg^2 of the Virgo Cluster to unprecedented depth, providing detections of galaxies down to stellar masses of $\sim 10^5 M_\odot$. Figure 3.1 shows the NGVS survey area as well as all confirmed or probable Virgo Cluster member galaxies relative to the surrounding area. The cluster environment is covered more extensively by the Extended Virgo Cluster Catalog (EVCC; Kim et al., 2014) as shown in the figure, but the sensitivity of NGVS to lower-mass galaxies provides an excellent probe of the Virgo Cluster substructure by enabling better sampling of the full galaxy distribution. With these NGVS data, the complex substructure within the Virgo Cluster is readily apparent, as shown in Figure 3.2. This figure is a "cleaned" version of the Virgo Cluster — it is not an actual on-sky image of the cluster, but instead represents the Virgo galaxies with their best-fit parametric surface brightness profiles, without contamination from foreground or background objects. Overlaid on the galaxy map are contours of the x-ray gas distribution from ROSAT (Böhringer et al., 1994). Like the galaxy distribution, the hot gas is concentrated on the bright central galaxy, M87, but asymmetric extensions of the gas can be seen to the south and east, following the same distribution as the galaxies. This indicates that Virgo is a dynamically young cluster with numerous substructures still in the process of being incorporated.

In the remainder of this section, I will focus on how the NGVS data was used to generate the catalogue of Virgo Cluster member galaxies and their structural properties used in this analysis. I will also introduce supplementary data provided by follow-up observations and related projects from the NGVS collaboration: recessional velocities from various spectroscopic observing programs, and distances from surface brightness fluctuations estimated using the NGVS imaging. These supplementary data are used to validate substructure candidates derived using the NGVS galaxy catalogue.

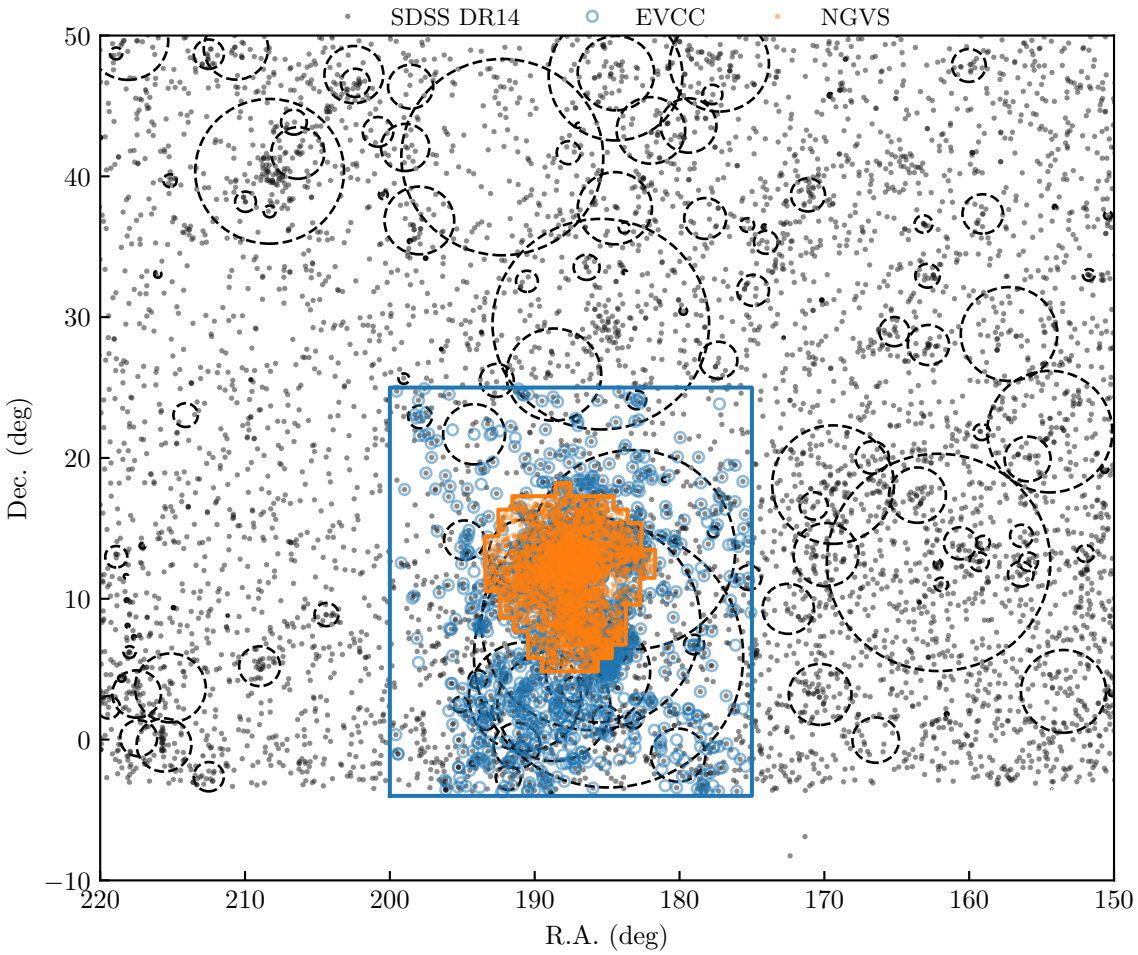

Figure 3.1 Sky coordinates of all 3,687 confirmed or probable Virgo galaxies in the NGVS (orange points), all Virgo galaxies from the EVCC (blue squares), and all galaxies from the most recent SDSS data release with recessional velocities below 3000 km s^{-1}. The survey areas of the NGVS and EVCC are shown in orange and blue lines, respectively. Dashed circles indicate any nearby galaxy groups recessional velocities below 3000 km s^{-1}, as identified by Kourkchi & Tully (2017).

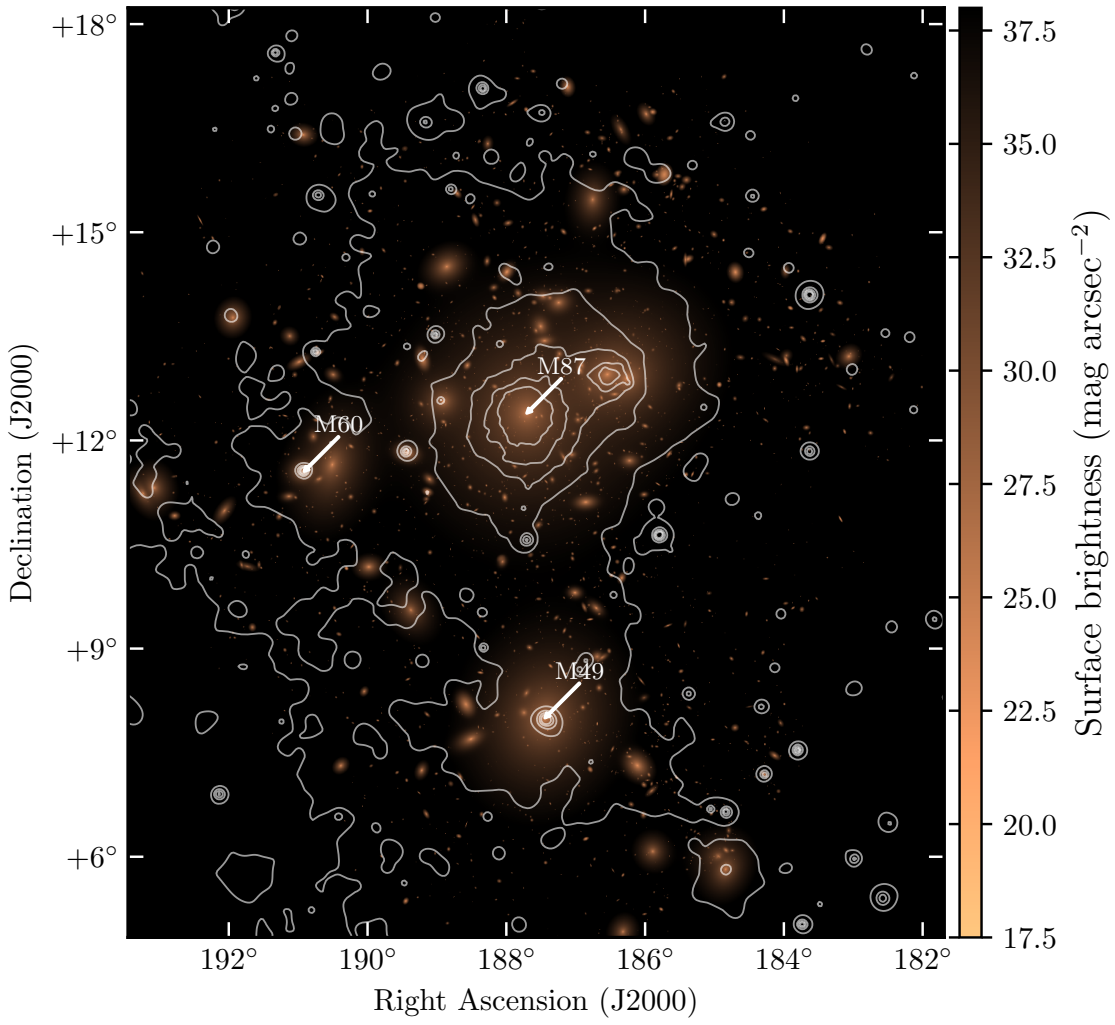

Figure 3.2 Surface brightness map for the Virgo Cluster generated using best-fit Sérsic models for the 3,687 NGVS galaxies included in this analysis. Contours from the ROSAT x-ray observations of Böhringer et al. (1994) are overlaid in white. The distributions of both hot gas (traced by the x-rays) and stars (traced by the optical imaging) are well matched.

Catalogue of galaxy properties

The full set of detections in the NGVS footprint includes not only Virgo galaxies, but also foreground stars, foreground and background galaxies, and any other contaminants, such as image artifacts or even Solar System transients (Chen et al., 2013). These detected sources have been excluded when creating the final catalogue of Virgo galaxies using the following procedure. Photometric redshifts, sizes, surface brightnesses, and morphologies are used to separate galaxies from stars and other compact objects, and then to further refine the galaxy sample to select only objects with redshifts and appearances consistent with belonging to the Virgo Cluster. A final visual inspection of the images was used to classify all objects in the galaxy sample as certain, likely, or possible members of Virgo. This visual inspection (coupled with the results of fitting each galaxy's light profile) was also used to further classify the galaxies as certainly or possibly nucleated or non-nucleated.

Magnitudes and structural parameters (effective radius, ellipticity, concentration, and position angle) were derived from both 1D azimuthally averaged brightness profiles as well as 2D fits to the imaging. Parameters from the 1D profiles were estimated from the growth curve, and 2D parameters were estimated using `ELLIPSE` (primarily for brighter galaxies) and GALFIT (for smaller, fainter systems). In `ELLIPSE`, each galaxy was fitted with both a single Sérsic (appropriate for simple, non-nucleated galaxies) and a double Sérsic model (more suitable for complex and/or nucleated objects). In GALFIT, the double Sérsic model was replaced with a Sérsic + point source model, as GALFIT could not reliably converge on a Sérsic fit to the unresolved, point-like stellar nuclei. These fits were performed with all images fixed to have the same structural parameters as measured in the g images (following a similar method as in Chapter 2) — however, only the fixed results were performed for the GALFIT, mainly to ensure consistent results for the faintest galaxies.

I extracted the structural parameters from the best available set of results from the above methods — `ELLIPSE` results were preferred over GALFIT, if available. I adopted the structural parameters measured from the g band, and estimated approximate masses for each galaxy using the g magnitude and assuming a mass-to-light ratio $M/L = 1$. For this analysis, I am primarily concerned only with the coordinates of the galaxies to detect substructures, although the masses are used later to investigate whether the identified substructures have mass functions that are reasonable for a true association.

Master spectroscopic catalogue

In addition to the imaging data, recessional velocities have been compiled for 862 objects with velocities below 3500 km s^{-1} in the NGVS field and used to validate any substructures detected using the imaging data — a plausible substructure should have a roughly Gaussian velocity distribution that is also narrower than that of the entire cluster. The distributions for Virgo galaxies with velocities are shown in the panels of Figure 3.3 for four ranges of velocity (which correlates roughly with depth in the cluster). From these panels, it is apparent that most of the field is covered by galaxies with velocities distributed around 1000 km s^{-1}, although there is a minor low velocity component in the northern half of the survey area, and high-velocity (likely background) streams in the southwest (Mei et al., 2007). The overall velocity distribution is shown in Figure 3.4, where multiple peaks in the distribution indicate the presence of multiple dynamically-distinct structures in the cluster. For comparison, bars indicating the velocity distribution of substructures produced in this analysis are overlaid on the distribution. These substructures are discussed in greater detail in §3.4.1.

These spectroscopic values are compiled from a variety of sources. The bulk of the measurements for bigger, brighter galaxies have been retrieved from public databases such as the SDSS or the NASA/IPAC Extragalactic Database (NED), when available. The master spectroscopic catalogue includes 524 SDSS velocities and 774 NED velocities, including a number of measurements from the Virgo Cluster Catalogue (Binggeli et al., 1987). A few targeted follow-up observations planned and executed by the NGVS team provide additional velocities, particularly for compact elliptical galaxies, ultra compact dwarf galaxies, and other compact stellar systems. Summaries of these observations are listed in Table 3.1. These follow-up spectra have been previously used to study the kinematics and GC systems of dwarf elliptical galaxies (Toloba et al., 2016) or the dynamical properties of UCDs and GCs (Zhang et al., 2015). These targets of these programs were predominantly star clusters within galaxies, but they still provide additional data for 12-20 galaxies (see Table 3.1).

Surface brightness fluctuation (SBF) distances

An additional confirmation of any substructure candidates would be a verification that galaxies associated with a given substructure are found at similar distances from the observer, rather than being chance superpositions along the line of sight. Recessional

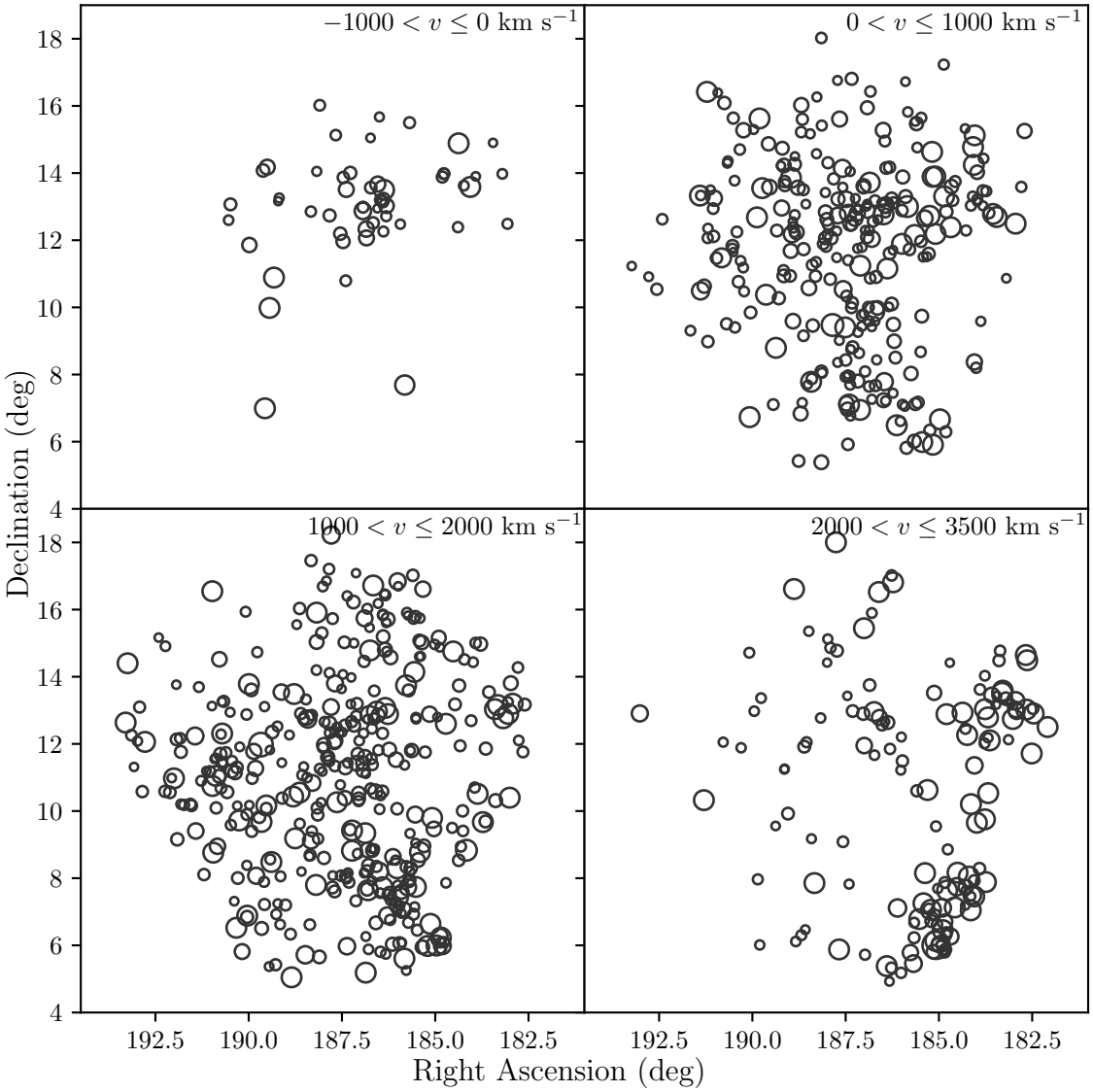

Figure 3.3 Coordinates for the 862 NGVS galaxies with measured recessional velocities below 3500 km s^{-1}. Galaxies are plotted in four panels showing different velocity ranges. The sizes of the markers scales with galaxy luminosity.

Table 3.1 Summary of NGVS spectroscopic follow-up observations

Telescope	Instrument	Date	Resolution	Wavelength (Å)	N_{gal}
MMT	Hectospec	2009–2010	1000	3650–9200	12
AAT	2dF/AAOmega	2012	1300	3700–8800	13
Keck II	DEIMOS	2012	2500	4800–9500	20

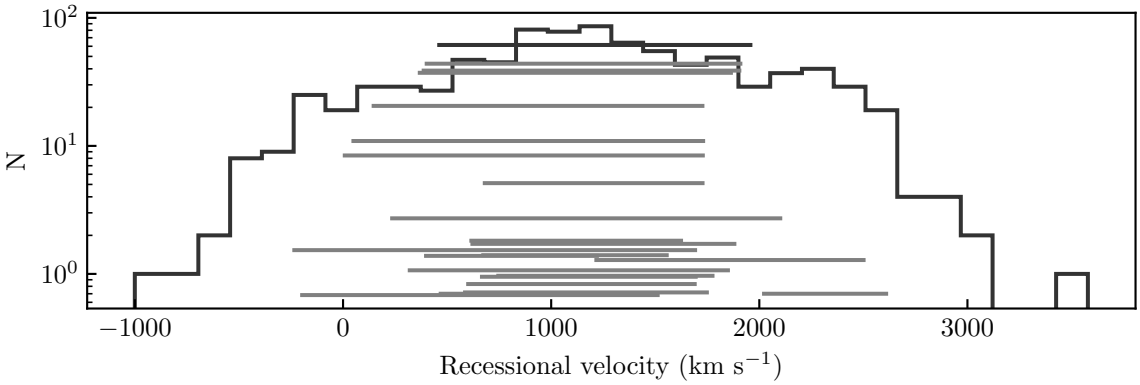

Figure 3.4 Distribution of all recessional velocities available for Virgo galaxies. Light grey horizontal bars indicate the velocity dispersions of substructures from this analysis. The ordinate of each bar is arbitrary but has been scaled such that the bars are ordered by most to least number of members from top to bottom. The darker grey horizontal line shows the dispersion for the full velocity sample.

velocities can, in theory, be used to approximate distances to remote objects. This is because the expansion of the Universe causes distant galaxies to appear to move away from us, with the magnitude of this recession increasing linearly with distance. However, this technique breaks down for such a large, nearby cluster as Virgo. In this case, the local cluster dynamics override the velocity due to expansion, such that the velocity dispersion of the cluster members is almost as large as the mean velocity itself (e.g., Ftaclas et al., 1984; Binggeli et al., 1987; Karachentsev & Nasonova, 2010). Fortunately, surface brightness fluctuations (SBFs) can be used for robust distance estimates, even in the Virgo Cluster, by calibrating the pixel-to-pixel variations in a galaxy's brightness — caused by discrete variations in the stellar distribution — with its distance from the observer (Tonry & Schneider, 1988; Tonry, 1991; Blakeslee et al., 1999; Mei et al., 2007; Blakeslee et al., 2009). Cantiello et al. (2018) have recently presented NGVS SBF distances and corresponding uncertainties for 260 galaxies in Virgo, so I use these state-of-the-art distances, when available, to investigate whether the substructure candidates are simply projected groups of galaxies. The overall SBF distribution and the ranges of the substructures produced in this analysis are shown in Figure 3.5.

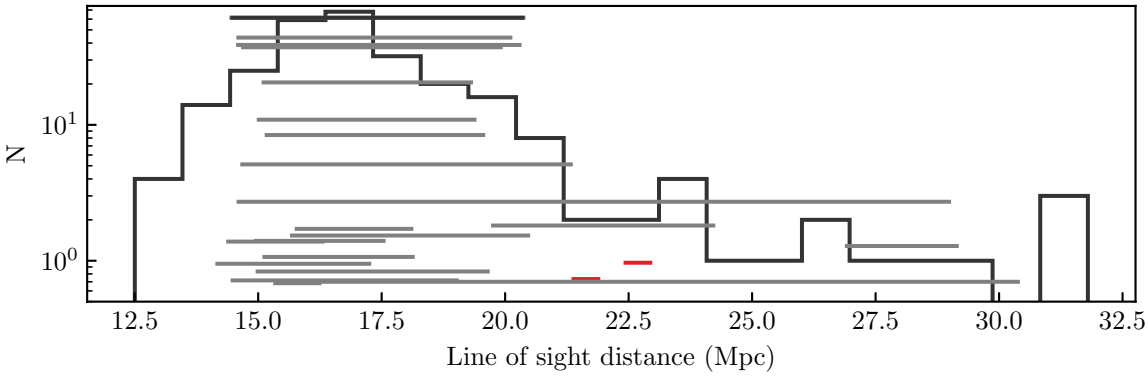

Figure 3.5 Same as Figure 3.4, but for SBF distances. The substructures highlighted in red do not include enough distance measurements to calculate dispersions, so the lengths of the bars are arbitrary.

3.2.2 Simulated galaxy clusters from the Illustris cosmological simulations

`Illustris` is a cosmological hydrodynamic simulation of dark matter, stars, and gas, including the interactions among these different forms of matter. It uses an

adaptive mesh refinement code to redistribute the simulation particles effectively and efficiently — regions with more interactions or activity can be simulated with a finer spatial grid and more particles to trace small-scale effects (the resolution is $\sim$50 pc at redshift $z = 0$), while cosmic voids or other less "active" regions can be quickly simulated with a lower resolution grid of fewer particles. With each dark matter and baryonic particle representing a mass of $6.3 \times 10^6 M_\odot$ and $1.3 \times 10^6 M_\odot$, respectively, the simulation can confidently resolve galaxies down to masses of $\sim 10^7 M_\odot$ throughout a cubic volume of 1.2×10^6 Mpc^3. Full details of the simulations can be found in Vogelsberger et al. (2014b,a) and Genel et al. (2014).

Twelve galaxy clusters have been extracted from `Illustris` as roughly equivalent to the observed Virgo Cluster in terms of dark matter halo mass. Virgo has an estimated gravitating mass of $\sim 1.4 - 8 \times 10^{14} M_\odot$ (e.g., Schindler et al., 1999; McLaughlin, 1999; Urban et al., 2011; Karachentsev et al., 2014), and the selected `Illustris` clusters have halo masses on the order of $10^{14} M_\odot$. Figure 3.6 shoes the `Illustris` clusters projected at the distance of Virgo, along with two visualizations of the NGVS dataset for comparison: the full sample, and the sample limited to the mass range resolved in `Illustris` ($M_\star \geq 10^7 M_\odot$).

3.3 Identification of substructures

3.3.1 The clustering algorithm: ordering points to identify the clustering structure (OPTICS)

Ordering Points To Identify Clustering Structure (OPTICS; Ankerst et al., 1999) is the basis of the method used to extract substructures in this analysis based on the density of points in a region. It is more of a sorting algorithm which generates results that can then be used to extract groups — it does not, strictly speaking, assign cluster membership to each point in the sample. Instead, it sorts points by proximity, with each point being added to a sorted list as the nearest unsorted neighbour of the last point in the list. Its strength comes from calculating the distance to the nth nearest neighbour for each point, which probes the local density around that point. This, when coupled with the sorting, enables a visualization of the data that can be quite powerful when identifying clusters of points at a range of densities.

OPTICS only requires the user to define one parameter, n, that is used to specify the nth nearest neighbour for each point. This is, to some extent, a subjective choice

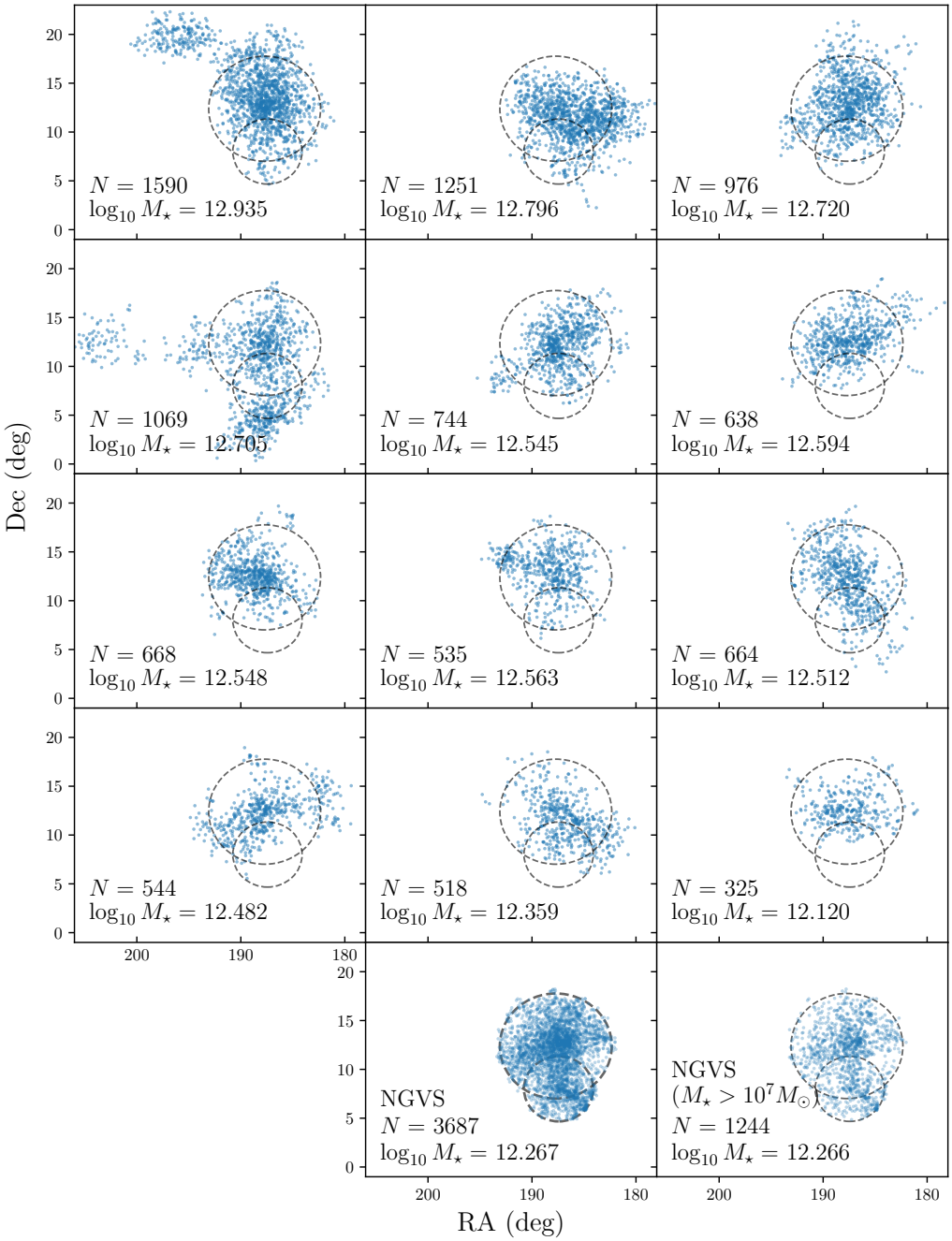

Figure 3.6 Snapshots of each `Illustris` sample in projected coordinates, shown with a common scaling for all panels. Dashed circles in each panel indicate the virial radii of the Virgo A and B substructures. To aid in comparison to the NGVS data, galaxy positions have been shifted such that the reference position (the most massive galaxy in the cluster) corresponds to the sky coordinates of M87 at the mean distance of the Virgo Cluster (16.5 Mpc). The panels in the bottom row show the full NGVS dataset (left) and the subset of galaxies with stellar masses above the mass resolution limit of `Illustris`, $10^7 M_\odot$ (right).

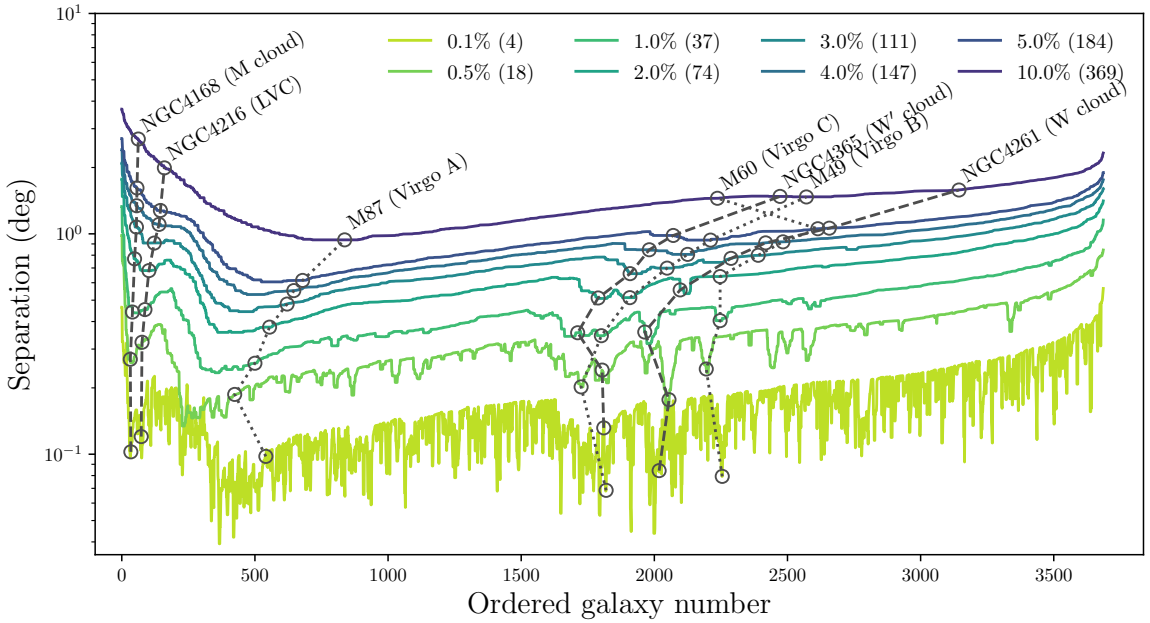

Figure 3.7 Reachability plots for the NGVS dataset, produced by the OPTICS algorithm, for a variety of values for the n number of points required to form a substructure. For each galaxy, the core distance, or distance to the n-th nearest neighbour, is calculated. The algorithm proceeds through the sample by selecting the nearest *unprocessed* neighbour of the current galaxy to be processed next, and builds a sorted list by appending each of these neighbours (and its corresponding reachability) one by one. The resulting reachability plot, then, shows each substructure of galaxies as "valleys" of smaller reachabilities. Small valleys can be superimposed on larger valleys, revealing the hierarchical structure of the sample. In this example, the locations of the primary galaxies of previously-identified Virgo substructures are overlaid on each reachability curve. For suitable values of n, each of these galaxies should reside at the centre of some valley. In this case, $n \approx 1\%$ of the sample size recovers these structures without being dominated by noise (for $n < 0.5\%$) or losing sensitivity to structures of those scales or densities ($n \geq 3\%$).

based on the sizes of structures that are of interest to the user. The choice of n can be informed by the sample size and spatial extent of the dataset, as well as the available coordinate information (i.e., only projected positions, or projected positions with recessional velocities, or full spatial and kinematic knowledge). An optional second parameter, ϵ, defines the maximum separation used to search for neighbours of a point. This can be applied to optimize processing times for larger datasets by reducing the number of potential neighbours considered for each point. Setting ϵ effectively defines a minimum density for structures of interest — each potential structure must have at least n neighbours within ϵ in order for OPTICS to process it. In this work, I have not used ϵ, setting it as larger than the maximum separation possible within the dataset. I also apply OPTICS to the full NGVS dataset, using only projected coordinates to classify structures initially. Although velocity information is available for $\sim$800 galaxies in the sample, this approach enables us to take advantage of the increased sampling of the full dataset. This is particularly important given that many of the galaxies without velocities are faint dwarfs, which, as the most abundant satellites and group members, are useful for highlighting the clustering structure around brighter galaxies. However, the velocities (and SBF distances) provide crucial validation of the OPTICS results, so, when available, I use them to determine if the candidate structures from OPTICS are kinematically and spatially consistent.

The algorithm iteratively builds an ordered set of points from the original, unordered sample. For each unprocessed point, the algorithm goes through the following steps:

1. The point is marked as processed, which appends it to the ordered list and removes it from the unordered list (the input dataset).

2. It is assigned a core distance, defined as the distance to the nth nearest neighbour (if ϵ is specified, the core distance would remain undefined unless the nth neighbour is within ϵ from the point of interest).

3. If the core distance is defined, then a reachability distance is calculated for each unprocessed neighbour of the point (within ϵ separation, if applicable). This reachability is the larger value of either the core distance or the actual separation between the neighbour and the point.

4. Each unprocessed neighbour, is assigned its reachability distance if its reachability is currently undefined, or if the previous reachability is larger than the

current value. In other words, for points that fall within the neighbourhoods of multiple structures, they are assigned a reachability for their nearest core point.

5. The algorithm selects the next point to be processed, which is the nearest neighbour to the point that was just processed.

The ordered reachability distances produced by OPTICS are used to produce a reachability diagram. Figure 3.7 shows how the reachability diagram for the NGVS dataset changes for different choices of n. In this visualization of the data, any "valleys" in the data correspond to points within one structure. The valleys indicate regions where the density of points changes noticeably relative to the rest of the neighbourhood. Structure at a range of spatial scales can be detected: narrow valleys are superimposed on broader valleys, indicating substructures within larger structures. For reference, Figure 3.7 also shows the locations of the prominent galaxies in each established Virgo substructure.

3.3.2 Extraction of potential structures

To reiterate, OPTICS is primarily a sorting and visualization tool. Additional steps are required to extract any potential substructures using the OPTICS reachability data. I follow a modified version of the method outlined by Ankerst et al. (1999) and similar to the approach in McConnachie et al (2018, in preparation). A valid substructure candidate must have a density significantly different from its neighbourhood — that is, the sides of the valley must be sufficiently steep, indicating this notable change in density. I set a threshold such that each valid cluster must be bounded by points on the left and right that are at least 2% lower and higher, respectively, than their immediate neighbours deeper in the valley. Within these bounds, the cluster candidate must also contain at least n members to ensure that it is a meaningful substructure, rather than a chance fluctuation in the reachability plot.

We concluded, after some experimentation, that the two conditions are sufficient to identify single clusters on the smallest scales. However, with OPTICS it is possible to identify nested substructures. For "parent" substructures that encompass smaller substructures, I have additional qualifiers. Each parent must contain at least two distinct substructures; otherwise, it is simply a larger version of a previously-identified substructure and so I replace that substructure with its larger counterpart.

The results of this analysis can be seen in Figure 3.8, which shows the reachability plot for the NGVS dataset using our adopted 1% value for n and the above criteria

to select substructures. All detected substructures are bounded by horizontal bars, with any regions falling below a given bar being associated with that substructure. It is possible to detect, for example, small valleys indicating substructures around M49 and NGC 4365 (associated with Virgo B and W′ substructures, respectively), but both can be associated in the same larger substructure, which in turn can be joined with Virgo A in an even larger substructure. The bottom panel displays these relationships in a more traditional tree diagram. These substructure candidates are discussed in greater detail in §3.4.1.

After each substructure is extracted, I estimate a best-fit ellipse to the positions of the substructure members on the sky and use the properties of this ellipse (central coordinates, radius, and ellipticity) as representative, first-order properties of the substructure. The ellipses were derived by performing a linear regression on the substructure member coordinates. The resulting slope of the best-fit line is the inverse tangent of the position angle of the semi-major axis. This angle is used to transform the coordinates such that the semi-major and semi-minor axes are aligned with the abcissa and ordinate, respectively. The centre coordinate and lengths of the semi-major and semi-minor axes are measured using the maximum separation between members along each axis. Finally, these values are transformed back to the native coordinate system. All but the largest four substructures can be well-represented by an ellipse, as shown in the maps of each substructure in Appendix A.

3.3.3 Validation of OPTICS with Illustris

Given the complete spatial and kinematic information available for simulated data, I can use `Illustris` to explore how OPTICS performs with different sets of positions and/or velocities as input. Additionally, substructure identifications using FoF are already available for the `Illustris` clusters, enabling a quick comparison between OPTICS and established structure-detection algorithms. In this section I compare the substructures detected by FoF (hereafter referred to as "`Illustris`-detected") and those extracted using OPTICS with a variety of input datasets: full position-velocity information, projected coordinates with a recessional velocity, and projected coordinates only.

The `Illustris`-detected substructures can be as small as pairs of galaxies, probing much smaller structures than I intend to explore currently with OPTICS. Therefore I only consider groups with membership numbers above the detection threshold for

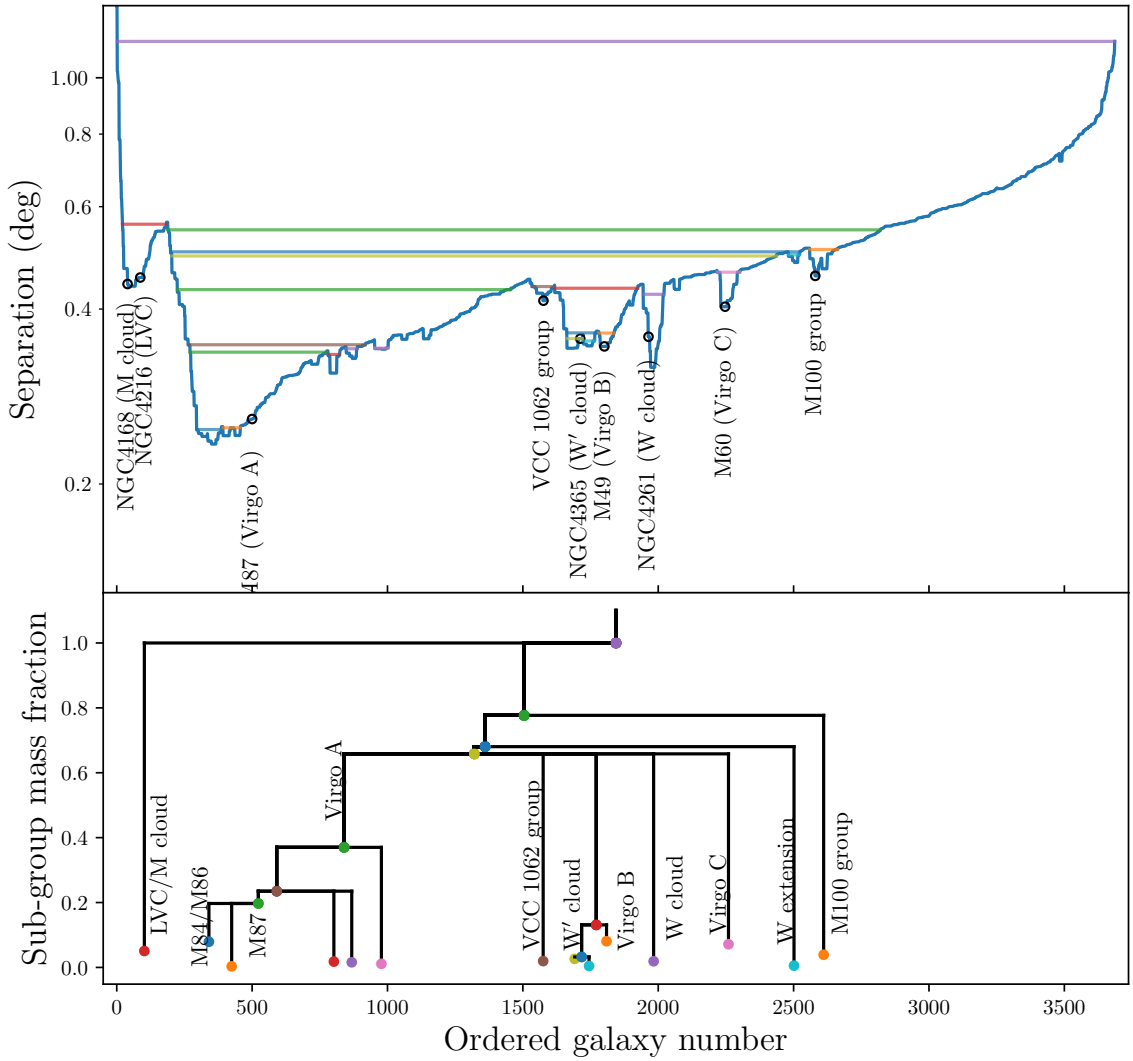

Figure 3.8 Final reachability plot with detected substructure valleys bounded by the horizontal bars (top panel) and corresponding dendrogram (bottom panel) for the Virgo Cluster. Potential substructures were extracted by running OPTICS with the minimum points set to 1% of the sample size (roughly 35 galaxies). The primary galaxies for all previously established substructures, as well as a few new candidates, are labeled in the reachability plot. Coloured vertical bars indicate the breadth of each valley used to define a substructure, and coloured points of the same colours show each valley's place in the dendrogram.

OPTICS (1% of the total sample size). The `Illustris`-detected groups can have nested substructures, like OPTICS — although, again, some of these substructures are smaller than what I have currently programmed OPTICS to detect. Any substructures below the OPTICS threshold are simply merged with their parent substructures and are not recognized as separate substructures. The vast majority of bound `Illustris`-detected substructures are small pairs or trios of galaxies. In the sample halo shown in Figure 3.9, only seven substructures (out of 226 bound groups detected using the `Illustris`-detected classifications) remain above the OPTICS threshold. In contrast, using OPTICS, I find 12 substructures when using the full 6D information, 15 substructures when limited to projected coordinates and recessional velocities, and 31 substructures when using only projected coordinates. Clearly, OPTICS recovers a very different set of substructures compared to FoF — there are multiple levels of nested substructures, as well as a greater number of substructures overall.

A more appropriate test for OPTICS is to evaluate how the extracted substructures change as the amount of input information is changed. The results using full 6D information can be thought of as the "true" substructures, as they are identified with the most complete spatial and kinematic information. With the limited information provided by projected coordinates and recessional velocities, or by projected coordinates only, a few differences appear. Most notably, it is very difficult to recover similar or identical sets of individual galaxies within one substructure across the various OPTICS results. I matched the true OPTICS substructures to substructures recovered in other results by finding the smallest substructure that contained at least 50% of the same galaxy IDs as the true substructure. I recovered zero exact matches, and in roughly half the cases, the smallest true substructures (with < 100 members) have no similar counterpart in other runs, such that the best match becomes the parent structure containing the entire sample. The limited knowledge of line-of-sight position and/or tangential motion is the likely culprit here.

Despite the challenges of correctly recovering individual member galaxies, the overall structural properties of the substructures remain well matched across the OPTICS results. For example, the bottom-left concentration of galaxies shown in Figure 3.9 is consistently separated into two or three smaller substructures within a larger substructure encompassing the entire clump. Aside from the smallest substructures near the dense centre of the cluster, rough counterparts that are similar in shape and location can be found throughout the different OPTICS results.

In addition to the Illustris-detected FoF substructures, I also compare OPTICS to

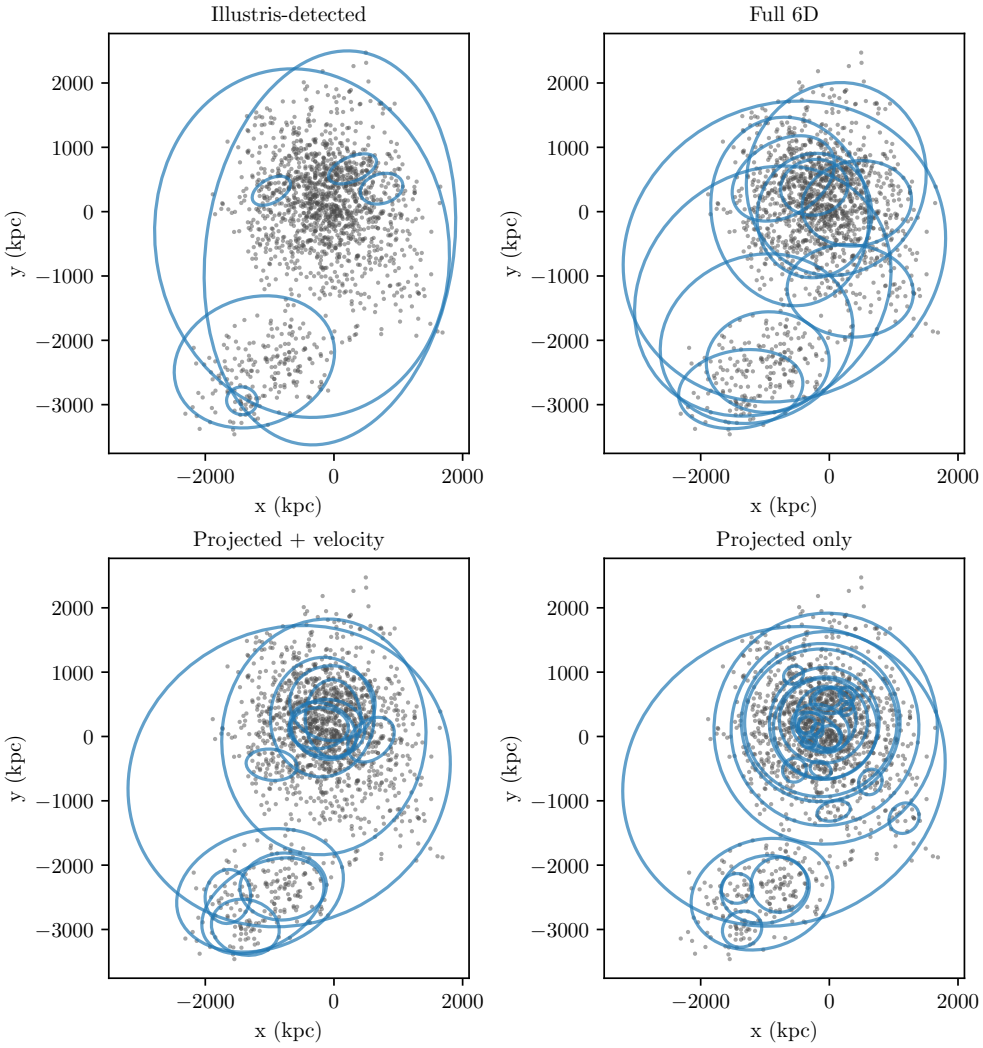

Figure 3.9 Maps of one sample `Illustris` halo and ellipses indicating substructures detected using the `Illustris` method, SUBFIND (*top left panel*), and a selection of OPTICS-detected substructures for various inputs: the 6D position-velocity information (*top right panel*), projected positions with a recessional velocity (*bottom left panel*), and projected positions only (*bottom right panel*).

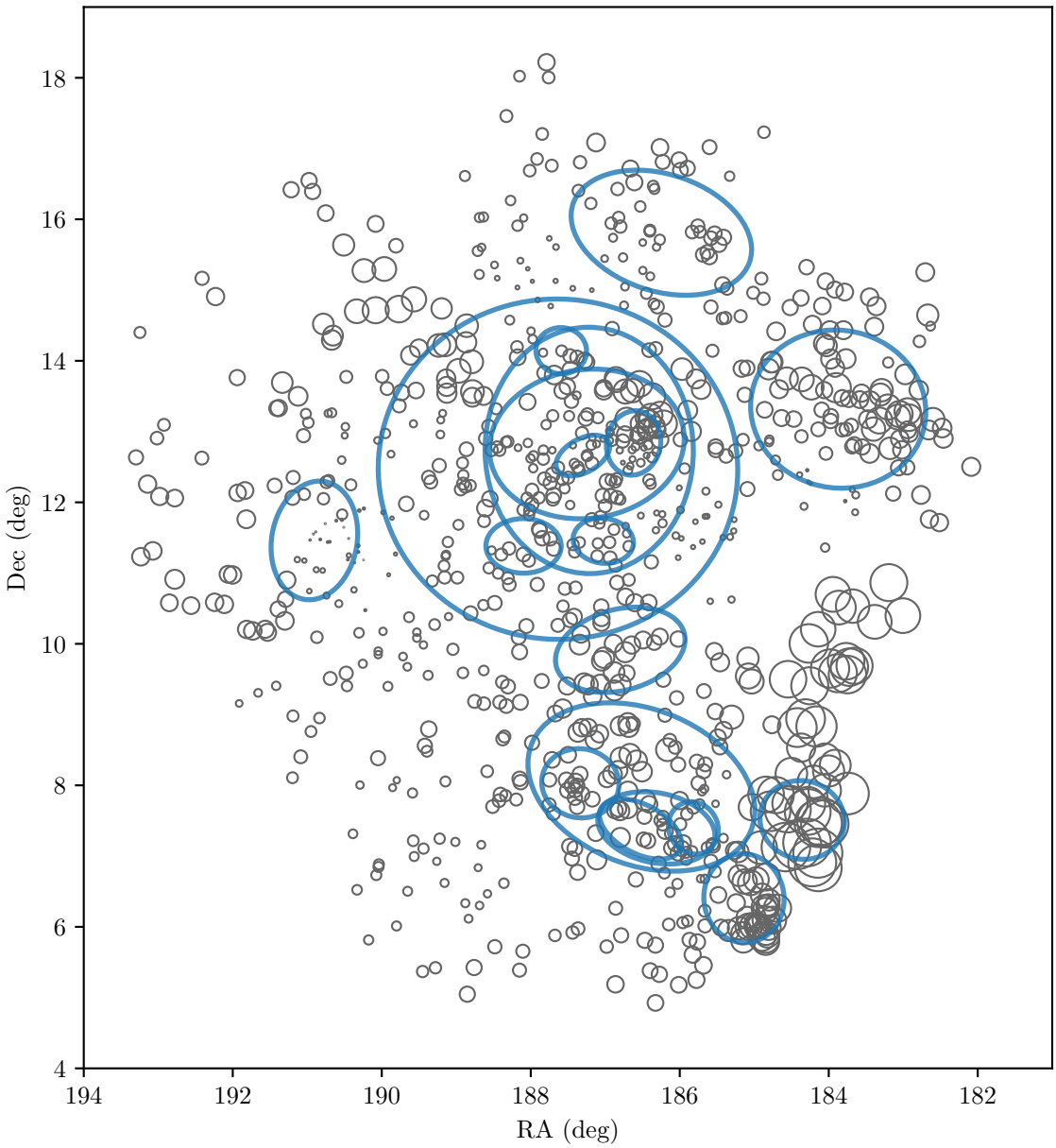

Figure 3.10 Results of the substructure detection method presented in Dressler & Shectman (1988). The velocity distribution of each galaxy and its ten nearest neighbours is compared to the global velocity distribution for the cluster, with the size of each galaxy's circle corresponding to its level of deviation from the global distribution. Concentrations of similar-sized circles indicate likely substructures. For comparison, ellipses denoting the Virgo substructures detected with OPTICS are plotted as well. The four largest substructures, which are superstructures containing nearly every other structure, have been omitted for clarity.

results from the method of Dressler & Shectman (1988), which uses velocity anomalies relative to the mean cluster velocity to detect substructures. These results, as well as the OPTICS results, are shown in Figure 3.10. The size of the plotted circles are scaled according to each galaxy's level of deviation from the mean. Concentrations of similarly-sized circles, then, indicate groups of galaxies that are similar in both projected position and velocity. Most of the OPTICS substructures, overlaid as blue ellipses, encompass these concentrations, lending credence to the OPTICS results.

Ultimately, any clustering algorithm will have its own limitations and biases, and observational data will always provide an incomplete picture of the true cluster structure. Despite these caveats, OPTICS can provide a robust *relative* comparison of substructure among multiple datasets when given homogeneous input information. It thus represents an attractive way to capitalize on the uniform and homogeneous galaxy catalogue that is available from the NGVS.

3.4 Results

3.4.1 Structure of the Virgo Cluster

This section presents the most recent understanding of the various subcomponents of the Virgo Cluster. It includes a review of previous substructures discussed in the literature as well as a revised map of Virgo using the OPTICS results. These OPTICS results are shown in Figure 3.8 which presents both the reachability plot and dendrogram of Virgo, and in Figure 3.11, which shows the boundaries of each substructure as they appear on the sky.

Previous studies

The substructure of the Virgo Cluster has been readily apparent since the earliest studies of the cluster, beginning primarily with the studies of Shapley & Ames (1929a,b,c,d) and Hubble & Humason (1931). Subsequent surveys established the richness and complexity of the cluster by revealing the presence of numerous, low-mass galaxies (Reaves, 1962, 1983), and it is now known that the bulk of the cluster lies at a distance of $\approx$16.5 Mpc (Mei et al., 2007; Blakeslee et al., 2009). However, the cluster is quite extended along the line of sight, with two wedges or tails of galaxies extending out to 40 Mpc (Solanes et al., 2002; Gavazzi et al., 1999). This complexity renders classification difficult, leading to a variety of definitions for cluster

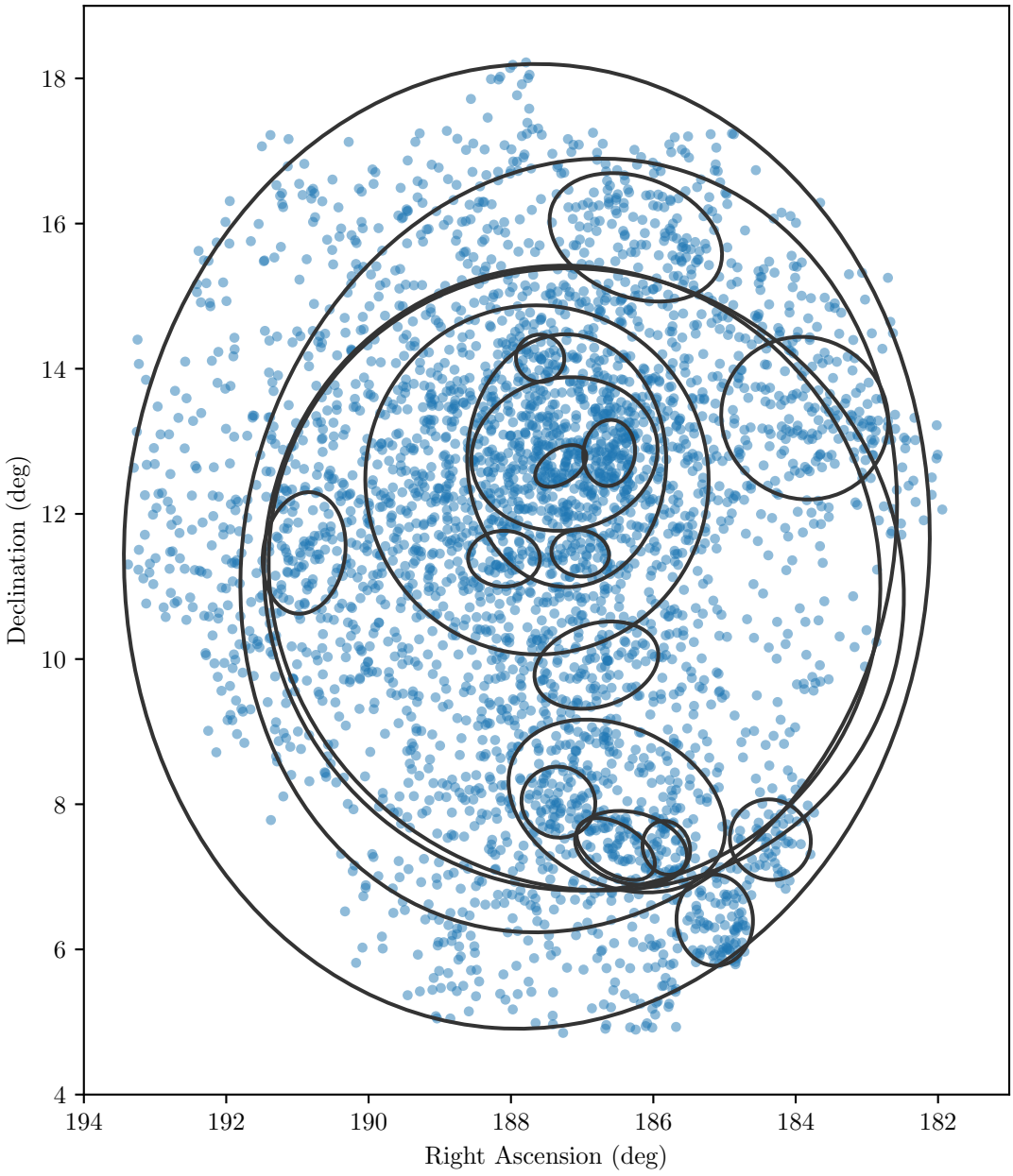

Figure 3.11 Representative ellipses denoting the Virgo substructures detected with OPTICS. Blue points show the positions of every galaxy in the NGVS dataset.

and subcluster boundaries. Many boundaries are defined by eye simply based on apparent overdensities of galaxies, or informed by morphology distributions, surface brightness arguments, radial velocities, or the x-ray gas distribution. In some cases, parametric decomposition of the various substructures has been used to separate the structures and assign probabilities of membership for each galaxy (Schindler et al., 1999). In this section, I summarize the current generally accepted substructures and the development of these designations throughout the last century. I follow the substructure naming convention that is primarily from Binggeli et al. (1987), but note newer, alternate and historical designations when applicable.

Virgo A The Virgo A substructure is generally considered the dominant structure of the Virgo Cluster, containing the majority of the stellar mass and the strongest source of x-ray emission (Böhringer et al., 1994). As the brightest and most massive galaxy in the region, M87 is often labelled as the centre of this substructure; however, the centre of the galaxy distribution is notably offset from M87, highlighting the dynamically young state of Virgo (Binggeli et al., 1987). Nearly all galaxies in this region appear to be associated with the main Virgo body at 16.5 Mpc; however, there appears to be a small substructure, located to the northwest of M87, still merging into Virgo A — M86 and its associated galaxies are slightly behind the main cluster and have negative velocities (Mei et al., 2007; Schindler et al., 1999; Binggeli et al., 1993, 1987). The earliest classifications of substructure defined Virgo A as a superposition of primarily early-type galaxies known as the E cloud as well as a more distant, elongated cloud of late-types called the S_i cloud (de Vaucouleurs, 1961).

Virgo B Located $\simeq 4^\circ$ to the south of Virgo A, this is the second most prominent substructure in Virgo, but contains only 20% of the cluster virial mass (Ferrarese et al., 2012). Virgo B contains a relatively higher fraction of late-type galaxies compared to Virgo (Binggeli et al., 1987). Earlier, it was proposed that Virgo B may be falling toward Virgo A from the background (Gavazzi et al., 1999; Binggeli et al., 1987; de Vaucouleurs & Corwin, 1986), or an entirely separate, more distant structure altogether (de Vaucouleurs, 1961, originally called the S′ cloud). More recent studies have firmly established that Virgo A and B lie at similar distances (Mei et al., 2007; Cantiello et al., 2018).

Virgo C This substructure is associated with M60 and a prominent x-ray point source (Böhringer et al., 1994), located to the east of Virgo A. It lies at similar distance as the Virgo A and B substructures (Cantiello et al., 2018), serving to define the principal axis of the cluster (West & Blakeslee, 2000; Mei et al., 2007).

Southern extension Initially identified as Cloud X in de Vaucouleurs (1961), this very extended substructure may be part of a larger-scale sheet connected to the W and M clouds and also falling into the Virgo Cluster (Binggeli et al., 1987, 1993).

W cloud This is one of the more distant, high velocity substructures found primarily in the southwest of the Virgo Cluster region. This was initially split into the W-a and W-b groups by de Vaucouleurs (1961), although subsequent studies combined these into the W cloud. I note that OPTICS detects two substructures in the W cloud region, which coincide well with the original W-a and W-b designations — however, these OPTICS substructures are also clearly associated in a single parent substructure.

W′ cloud This cloud is part of a proposed filament of galaxies extending along the line of sight, connecting Virgo B to the W cloud (Binggeli et al., 1993). However, distance estimates suggest that this might in fact be a very clumped structure, rather than a filament (Mei et al., 2007).

M cloud This background substructure was named and confirmed with velocity measurements by Ftaclas et al. (1984), but was initially noted by Shapley & Ames (1929) as a structure more distant than the core of Virgo. Velocities are consistent with the Hubble flow, suggesting that this is not a component of the main Virgo cluster (Ftaclas et al., 1984), although Gavazzi et al. (1999) state that the M cloud is actually falling into Virgo A. It has also been suggested that the M cloud is potentially a northern extension of the W cloud, as both are at similar large distances (Paturel, 1979). Ftaclas et al. (1984) also identified a less clumped, related substructure to the north, dubbed the N cloud. This is another substructure that Ftaclas et al. (1984) thought to be more distant that Virgo itself. However, its projected location includes M100, which, with an estimated distance of $17.2 \pm 1.7\,\mathrm{Mpc}$, is at odds with this statement (Cantiello et al., 2018).

Low Velocity Cloud (LVC) This cloud includes NGC 4216, the bombarded spiral from Paudel et al. (2013), as well as other associated galaxies that are all moving at high velocities relative to the mean Virgo velocity. The LVC overlaps almost completely with the M cloud, so the two clouds can only be separated with velocities.

Virgo structures identified with OPTICS

This section briefly summarizes all substructures extracted from the OPTICS analysis, including justifications for whether these substructures are accepted or ignored for subsequent analysis and discussion. These justifications are based on the velocity and SBF distance distributions of substructure members as well as overlap with substructures previously adopted in the literature. I also consider each substructure's usefulness for exploring distinct environments and densities, which is one of the primary intended applications of these results (see Chapter 4). Even if a (parent) substructure meets the criteria outlined in §3.3.2, it may contain so many smaller, distinct substructures spanning a range of densities that it, as a whole, does not represent any particular local environment. An extreme case that can be seen in the top panel of Figure 3.8 is the largest substructure, which includes all galaxies with reachabilities smaller than $\sim$1 deg, which encompasses effectively the entire NGVS dataset and all other detected substructures. Detailed figures for each substructure, including its position on the sky and velocity, SBF distance, and mass distributions, are provided in Appendix A. Substructures are referenced according to their IDs in Table 3.2.

OPTICS 0-3 These four largest substructures span effectively the entire sample with only minor differences among them as smaller substructures on the outskirts become associated with the parent supercluster at each density threshold. For the purposes of this work, these are not considered as particularly relevant or meaningful substructures.

OPTICS 4 The next largest substructure corresponds well with previous definitions of the Virgo A subcluster (e.g., Mei et al., 2007; Boselli et al., 2014). Velocities and SBF distances confirm that this is a single structure at the mean Virgo distance.

OPTICS 5-6 These two substructures are major components of Virgo A, and form the bulk of that substructure with the addition of a few much smaller groups. Both

demonstrate a slightly bimodal distribution in their velocities, indicating that these substructures include some substantial component that overlaps in projected space — this is likely the galaxies associated with M86, which has a negative velocity ($cz \approx -224$ km s^{-1}) and is falling "forward" into the Virgo core from the back side of Virgo A.

OPTICS 7 This is a small parent substructure containing galaxies around M49 (in the core of Virgo B) and a counterpart to the W$'$ cloud. The velocity distribution is narrower than the overall Virgo distribution, consistent with this smaller group of galaxies. However, the distances indicate that this substructure may be extended along the line of sight, or contain groups at multiple distances.

OPTICS 8 This substructure matches quite well with the position and extent of the LVC and M clouds. Velocities show that this is clearly two superimposed groups with very different kinematic signatures, and limited distance information confirms that the member galaxies are in both the background and slight foreground of Virgo. While there are confirmed substructures here, projection effects prevent this substructure from being meaningful.

OPTICS 9 This substructure is an obvious counterpart to the W$'$ cloud, but very little distance information is available to investigate any projection effects or extension along the line of sight. However, velocities are consistent with this being a tightly bound group.

OPTICS 10 There is no previous counterpart to this substructure, except for perhaps the N cloud of Ftaclas et al. (1984). Both are in the vicinity of M100; however, distances suggest that this substructure is consistent with the mean Virgo distance and is not in the background. The velocity distribution is at slightly higher velocities than the overall cluster distribution, so this substructure may be falling through Virgo from front to back. With only eight distance measurements, this is an intriguing candidate that should be observed in greater detail.

OPTICS 11 The position of this substructure overlaps with M84 and M86, but velocities do not indicate a distinct kinematic group here. The low-velocity infalling

group around M86 cannot be separated from other densely clustered galaxies in the core of Virgo, so this substructure candidate is not considered a robust detection.

OPTICS 12 This is a very clear detection of the Virgo C substructure, centred on M60, and is validated by both velocity and distance measurements.

OPTICS 13 Here is the second OPTICS substructure with no previously-named counterpart. This appears to be a valid substructure with a consistent velocity distribution and a location slightly in front of the main body of Virgo. The most notable galaxy here is VCC 1062 or NGC 4442.

OPTICS 14 This substructure is very consistent with the position and distance of the W cloud. A slight low-velocity tail to the velocity distribution indicates that there may be some contamination from projection in this substructure, or this may be a group that is extended along the line of sight. In any case, this is a convincing detection from OPTICS.

OPTICS 15 This small substructure is concentrated on M87 and may perhaps be its satellite galaxies. However, such a small group superimposed on the densest region of the Virgo Cluster is difficult to confirm as a distinct substructure. The velocity distribution is broad and bimodal, indicated that this may simply be a cone of galaxies through the cluster core.

OPTICS 16 OPTICS detects two substructures within the W′ cloud, including this one. With a single distance measurement, it's difficult to understand how much this substructure truly differs from its sibling or parent substructures. This may be a more distant half of the W′ cloud, but with the current information, this does not stand out clearly as a physically meaningful substructure.

OPTICS 17 Concentrated on M49, this substructure matches the coordinates, but not the typical extent, of Virgo B. The concentration of galaxies in this substructure is clearly higher than the surrounding area — so this is perhaps the central core of the traditional Virgo B substructure.

OPTICS 18-19 These two substructures have reasonable velocity and distance distributions, consistent with being very centrally located in Virgo's position and velocity space. However, given their small numbers of members and proximity to the cluster core, is it difficult to determine if these are significant detections or chance projected overdensities within Virgo A.

OPTICS 20 This is the counterpart to the first substructure of the W′ cloud, OPTICS 16. Again, the meagre distance measurements prevent any investigation into the significance of this group. Its velocities and (two) distances are very similar to those for OPTICS 16, so these two substructures may best be represented as only the parent substructure W′ (OPTICS 9).

OPTICS 21 Tentatively dubbed the W cloud extension, this substructure corresponds to the Wb group identified by de Vaucouleurs (1961) and lies just to the north of the typical W cloud (OPTICS 14). This is clearly a group with high velocities, suggesting that it is in the background of Virgo (as expected for the W cloud). A few distances suggest that this substructure may be extended along the line of sight, but it is unclear if this is a clump or a stream, and how exactly it is related to the rest of the W cloud.

OPTICS 22 This substructure is very similar to OPTICS 18 and 19. Even with only seven velocity measurements, this group shows a broad spread, so this is almost certainly a simple projected overdensity and not a distinct, physical substructure.

3.4.2 Substructure properties

Table 3.2 presents a summary of membership numbers and structural parameters of all OPTICS clusters. These values have been derived based on the best-fit ellipses described in §3.3.2, masses estimated from g-band luminosities, and the available velocity and SBF distance measurements. For reference, I have indicated any notable primary galaxies or corresponding previous substructures, when applicable.

Table 3.2 General properties of OPTICS substructures

Name	Notes	Right Ascension (deg)	Declination (deg)	N	$\log_{10} M_\star$ ($M_\odot$)	$\bar{v}$ (km s^{-1})	$\bar{D}_{SBF}$ (Mpc)	r (deg)	e	$\log_{10} \Sigma$ ($M_\odot$ deg^{-2})
OPTICS 0	Full sample	187.775 ± 0.039	11.552 ± 0.008	3685	12.27 ± 0.30	1215 ± 499	16.7 ± 1.1	6.650 ± 0.015	0.150 ± 0.003	9.894 ± 0.090
OPTICS 1	. . .	187.184 ± 0.074	11.566 ± 0.016	2632	12.16 ± 0.01	1134 ± 470	16.7 ± 1.1	5.401 ± 0.055	0.162 ± 0.012	9.971 ± 0.005
OPTICS 2	. . .	186.942 ± 0.039	11.098 ± 0.003	2324	12.10 ± 0.02	1138 ± 478	16.8 ± 1.1	4.522 ± 0.011	0.066 ± 0.014	10.021 ± 0.006
OPTICS 3	. . .	187.137 ± 0.065	11.116 ± 0.005	2234	12.09 ± 0.02	1108 ± 449	16.7 ± 1.1	4.375 ± 0.029	0.027 ± 0.017	10.017 ± 0.006
OPTICS 4	Virgo A	187.635 ± 0.007	12.468 ± 0.001	1232	11.84 ± 0.02	937 ± 574	16.9 ± 1.0	2.415 ± 0.016	0.006 ± 0.004	10.274 ± 0.004
OPTICS 5	. . .	187.216 ± 0.004	12.733 ± 0.003	655	11.64 ± 0.04	920 ± 683	16.9 ± 1.0	1.741 ± 0.008	0.197 ± 0.004	10.454 ± 0.004
OPTICS 6	. . .	187.247 ± 0.008	12.825 ± 0.008	505	11.56 ± 0.05	849 ± 706	17.0 ± 0.8	1.314 ± 0.005	0.200 ± 0.005	10.624 ± 0.005
OPTICS 7	. . .	186.514 ± 0.016	7.976 ± 0.011	307	11.39 ± 0.04	1201 ± 233	17.1 ± 2.0	1.595 ± 0.004	0.315 ± 0.012	10.346 ± 0.008
OPTICS 8	LVC/M cloud	183.874 ± 0.028	13.317 ± 0.012	163	10.97 ± 0.01	1349 ± 864	18.1 ± 2.9	1.183 ± 0.023	0.061 ± 0.031	10.055 ± 0.010
OPTICS 9	W′ cloud	186.313 ± 0.002	7.400 ± 0.012	109	10.78 ± 0.00	1125 ± 154	22.7 ± 1.1	0.799 ± 0.009	0.383 ± 0.009	10.383 ± 0.009
OPTICS 10	M100 group	186.246 ± 0.015	15.810 ± 0.014	103	10.86 ± 0.02	1337 ± 378	16.5 ± 0.6	1.254 ± 0.001	0.343 ± 0.034	10.047 ± 0.023
OPTICS 11	M84/M86	186.622 ± 0.014	12.838 ± 0.013	92	11.17 ± 0.09	634 ± 680	17.5 ± 1.1	0.457 ± 0.004	0.214 ± 0.050	11.152 ± 0.038
OPTICS 12	Virgo C	190.904 ± 0.025	11.462 ± 0.011	84	11.12 ± 0.01	1110 ± 199	16.3 ± 0.7	0.845 ± 0.020	0.320 ± 0.036	10.638 ± 0.016
OPTICS 13	VCC 1062	186.800 ± 0.016	9.915 ± 0.017	83	10.56 ± 0.01	861 ± 271	15.8 ± 0.5	0.890 ± 0.004	0.360 ± 0.021	10.055 ± 0.015
OPTICS 14	W cloud	185.137 ± 0.010	6.403 ± 0.015	77	10.54 ± 0.05	1941 ± 373	28.3 ± 0.7	0.629 ± 0.007	0.141 ± 0.036	10.215 ± 0.025
OPTICS 15	M87	187.300 ± 0.008	12.660 ± 0.002	64	9.79 ± 0.10	1094 ± 629	16.9 ± 0.7	0.398 ± 0.005	0.414 ± 0.037	10.026 ± 0.032
OPTICS 16	. . .	186.528 ± 0.005	7.382 ± 0.005	58	10.69 ± 0.00	1238 ± 245	(22.7)	0.606 ± 0.009	0.436 ± 0.041	10.575 ± 0.025
OPTICS 17	M49	187.332 ± 0.022	8.029 ± 0.005	57	11.17 ± 0.07	1245 ± 329	15.5 ± 1.3	0.522 ± 0.013	0.066 ± 0.047	10.971 ± 0.025
OPTICS 18	. . .	188.097 ± 0.017	11.384 ± 0.013	50	10.31 ± 0.00	1296 ± 341	16.5 ± 1.2	0.505 ± 0.004	0.237 ± 0.029	10.224 ± 0.020
OPTICS 19	. . .	187.027 ± 0.005	11.455 ± 0.016	43	10.52 ± 0.02	1313 ± 214	16.7 ± 1.7	0.406 ± 0.012	0.215 ± 0.042	10.611 ± 0.017
OPTICS 20	. . .	185.816 ± 0.013	7.398 ± 0.012	42	9.91 ± 0.02	1043 ± 162	21.6 ± 2.1	0.377 ± 0.012	0.133 ± 0.095	10.023 ± 0.039
OPTICS 21	W cloud ext.	184.357 ± 0.013	7.511 ± 0.030	42	10.00 ± 0.01	2337 ± 150	21.5 ± 4.4	0.575 ± 0.012	0.045 ± 0.033	9.703 ± 0.013
OPTICS 22	. . .	187.591 ± 0.013	14.143 ± 0.010	41	10.47 ± 0.01	902 ± 343	15.8 ± 0.4	0.340 ± 0.010	0.044 ± 0.039	10.624 ± 0.029

Key to columns: (1) ID assigned to each cluster; (2) unique notes for each substructure, such as a previously-defined structure that it matches well, or the Messier or NGC designation of the central galaxy, if available; (3-4) sky coordinates for the centre of the substructure; (5) number of galaxies belonging to the substructure; (6) total stellar mass of the substructure based on its galaxy content; (7) median recessional velocity and uncertainty; (8) median distance from SBF and uncertainty; (9) radius of the substructure; (10) ellipticity of the substructure; (11) projected stellar mass surface density based on the total stellar mass and the area of the best-fit ellipse.

3.4.3 Comparison of substructure in real and simulated galaxy clusters

The amount of residual substructure in galaxy clusters is driven largely by gravitational interaction with the dark matter, which provides most of a galaxy cluster's mass. Thus, a comparison of substructure in real and simulated clusters provides a test for current ΛCDM cosmologies and dark matter distributions. Previous results have indicated tension between observed and simulated clusters, but also noted that the use of heterogeneous methods for detecting substructure in the two regimes may contribute to this tension (Schwinn et al., 2017; Jauzac et al., 2016). In this work, I apply the OPTICS algorithm equally to the NGVS and `Illustris` datasets. By creating projections of the `Illustris` clusters along a variety of sight-lines, I can create a dataset of simulated projected coordinates for a homogeneous comparison with the real Virgo Cluster.

The `Illustris` clusters chosen for this analysis were selected to have dark matter halo masses similar to that of the real Virgo Cluster, so their galaxy populations and distributions should also match that of Virgo. However, `Illustris` galaxies are only resolved down to stellar masses of $\sim 10^7 M_\odot$, while the NGVS sample includes galaxies 100 times less massive. The abundance of galaxies changes sharply with mass — low-mass galaxies are far more common than more massive ones, so the inclusion of these lower-mass galaxies in the observed dataset could drastically change the level of detected substructure. To enable a matched sampling of the cluster area, it is reasonable to limit both samples to the same mass range. However, it is already established that the `Illustris` mass function does not reproduce the observed function below $\sim 10^{10} M_\odot$ and above $\sim 10^{11.5} M_\odot$ (Genel et al., 2014, see also Figure 3.12), and so restricting both datasets to identical masses might not actually produce a matched galaxy distribution. The masses of the simulated galaxies are affected by the behavior of baryonic processes in the simulations (i.e. nuclear and stellar feedback, star formation rates), which do not have a strong effect on the overall clustering of galaxies. Therefore, it may be reasonable to compare `Illustris` to the full NGVS sample despite the fact that the galaxy properties themselves are not consistent. With these factors in mind, I compare both the full and mass-limited NGVS samples to `Illustris`.

To aid in the comparison of real and simulated substructures, I introduce a parameter to quantify the size and depth of substructures on the reachability plot. This

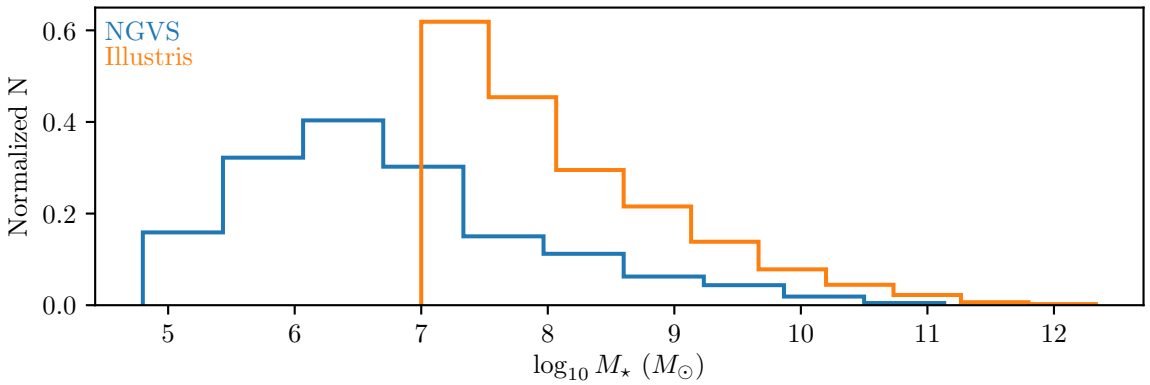

Figure 3.12 Observed and simulated normalized galaxy mass distributions from NGVS (in blue) and `Illustris` (in orange). Galaxies above the $10^7 M_\odot$ resolution limit of `llustris` are overabundant relative to galaxies of similar masses in the Virgo Cluster.

parameter is a rough counterpart to the equivalent width used to express the strength of absorption lines in spectra and was motived by the reachability plot's resemblance to a spectrum. Like the spectral equivalent width, this "equivalent width" defines the width of a rectangle with an area equal to the area contained between the spectrum continuum and the curve of the absorption feature. However, in this case, the "continuum" is the value on the reachability plot at the top of the valley defining the substructure, and the width is expressed as a *unitless* fraction of the total area enclosed by the reachability curve (such that a substructure containing the entire sample has an "equivalent width" of unity. This parameter can be expressed by the equation

$$\frac{1}{EW_{max}} \int \Big(1 - \frac{R(N)}{R_0}\Big) dN \tag{3.1}$$

where $R(N)$ is the reachability of each galaxy N within the substructure, R_0 is the peak reachability of the substructure valley, and EW_{max} is the "equivalent width" of the largest substructure in the sample.

Analysis with the full NGVS sample recovers fewer substructures than with the mass-limited sample — 23 and 35, respectively. This may seem counterintuitive at first, as including low-mass satellites should enable better sampling and detection of substructures, particularly on small scales. Indeed, relatively larger amounts of substructures with small equivalent widths can be found in the results from the full sample (see Figure 3.13). The increased substructuring in the mass-limited sample is actually due to larger abundances of the largest substructures, particularly the parent structures made of multiple distinct substructures. Because the mass-limited sample produces a more "fragmented" distribution of galaxies, the reachability plot has steeper features — that is, every substructure valley is defined more sharply relative to surrounding regions of the reachability plot. Because part of the substructure detection criteria involves checking that the valleys are sufficiently steep, the mass-limited results provide a larger number of sufficiently steep areas that can be used to select substructures, particularly larger, parent substructures. In contrast, the inclusion of lower-mass galaxies creates an overall shallower shape to the reachability plot, and many potential parent structures are discarded because they are not bounded by such steep curves. This fragmentation of the galaxy distribution in the mass-limited sample also increases the equivalent widths of most, if not all, substructures because each substructure is more distinctly separated from the others, causing each

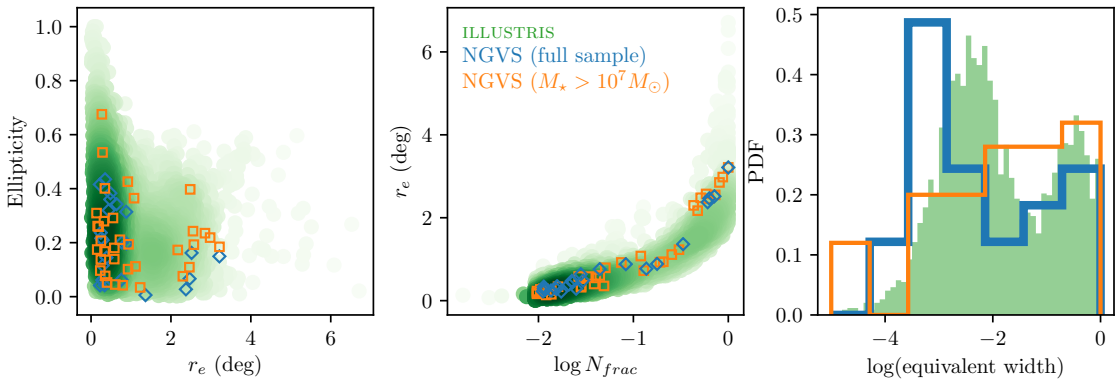

Figure 3.13 *(left panel)* Substructure ellipticity as a function of effective radius. Due to the large number of substructures, results for `Illustris` are shown as a density map (in green), with darker shades corresponding to regions of higher density. Blue diamonds indicate substructures extracted from the full NGVS dataset, while orange squares show substructures from a subset of the 1244 NGVS galaxies in the same mass range as the `Illustris` simulated galaxies. *(centre panel)* Effective radii of all extracted substructures as a function of number of members in each substructure (expressed as a fraction of the total number of members in each cluster). Colours and symbols are the same as the left panel. *(right panel)* Comparison of substructure equivalent widths for the projections of `Illustris` (in green), the full NGVS (blue), and the mass-limited NGVS subset (in orange). The Anderson-Darling test between Illustris and the full NGVS, and between `Illustris` and the mass-limited NGVS, rejects the null hypothesis (that each pair of equivalent width samples are drawn from the same distribution) at the 5.37% and 23.98% level, respectively.

substructure's valley to be much deeper.

The level of substructure between the observed and simulated galaxy clusters is not clearly consistent. Although the relative number of members, sizes, and shapes are broadly similar (see the first two panels of Figure 3.13), the frequencies of different scales of substructure differ between the observations and simulations. This is true when comparing to results from both the full and mass-limited NGVS dataset. I use a two-sample Anderson-Darling test (Scholz & Stephens, 1987) on the distributions of equivalent widths to estimate the amount of similarity between the simulations and each of the observed results. For a test of the full NGVS and Illustris results, the p-value is $p = 0.0537$, meaning that two samples with this level of difference (or greater) can be selected 5.37% of the time. This indicates that reproducing the observed structure of Virgo (as determined by the full dataset) with `Illustris` is a relatively uncommon occurrence. When comparing to the results from the mass-limited NGVS sample, $p = 0.2398$, so such a substructure distribution is somewhat more consistent with the simulations. In either case, the null hypothesis — that both simulated and observed clusters have the same distribution of substructures — cannot be rejected. This suggests that our current cosmological paradigm is suitable to explain the formation of galaxy clusters like Virgo, although a larger sample of observed clusters should be included for a more thorough analysis, especially considering the relatively low probability of producing the substructure observed in the full NGVS sample. The Virgo Cluster may very well be an outlier galaxy cluster with an exceptional amount of substructure.

3.5 Summary

Using position and velocity information for the Virgo Cluster and twelve of its simulated counterparts, I have demonstrated the application of a novel clustering detection algorithm, OPTICS, to real and simulated data. This algorithm enables self-consistent detection of substructures across a broad range of densities and spatial scales with flexible amounts of input information. Using OPTICS and the unprecedented sample of Virgo galaxies from the NGVS, I have redefined the structure of the Virgo Cluster. I have also evaluated how well cosmological simulations can match the observed level of structure in Virgo with a homogeneous analysis of substructures in NGVS and Illustris using OPTICS. Based on these results, I conclude that:

- OPTICS can successfully recover most previously-identified Virgo substructures, with projection effects becoming a major issue only in the separation of the LVC and M cloud. In addition to these anticipated substructures, sixteen new substructure candidates are identified. Some of these are simply parent substructures containing multiple child substructures, while others might be local overdensities within Virgo A. However, three of these candidates appear to be distinct substructures based on limited velocities and SBF distances, and are worthy of follow-up observations for robust confirmations.

- The number of detected substructures and their appearances vary greatly depending on the clustering algorithm used, as shown by the dramatic differences in results from FoF and OPTICS. Fortunately, the results from OPTICS remain relatively consistent, even with varying amounts of spatial and kinematic information. The specific galaxies assigned to each substructure may change, but the overall positions, properties, and sizes of the substructures are often similar.

- Matching amounts of substructure in simulated and observed clusters are rejected at the 5.23% and 23.93% level when comparing to the full NGVS sample or the sample limited to the Illustris mass range, respectively. This tentatively suggests that the ΛCDM cosmology may need to be modified to better predict clustering at the scales within galaxy clusters. However, it is also quite feasible that the Virgo Cluster is a cluster with an unusually large amount of substructure, so this comparison should be revisited with a larger, representative sample of observed galaxy clusters.

Chapter 4

Nuclear Star Clusters and the Environment

Combining the substructures identified in Chapter 3 with measured photometry and structural parameters for 3,490 galaxies within the NGVS, this chapter expands upon the goals of Chapter 2 and explores the role of environment in shaping the properties of NSCs and their hosts, as well as their scaling relations. A wealth of photometry and structural parameter measurements were extracted and provided by L. Ferrarese, although I completed various quality checks to create the final catalogue of values used in this analysis. The results described in this chapter are currently being expanded and prepared for publication (C. Spengler et al., 2018, in preparation).

4.1 Introduction

NSC formation and growth appears to be a complex, stochastic process and is attributed to two primary mechanisms: a dissipationless process in which star clusters (such as GCs) migrate to the centre of the galaxy due to dynamical friction (e.g., Tremaine et al., 1975; Oh & Lin, 2000; Lotz et al., 2001; Capuzzo-Dolcetta & Miocchi, 2008; Antonini et al., 2012; Gnedin et al., 2014); and a dissipative process that funnels gas into the galactic centre to form the stellar content of an NSC *in situ* due to disk instabilities (e.g., Milosavljević, 2004; Bekki, 2007; Schinnerer et al., 2008) or mergers (Mihos & Hernquist, 1994; Bekki, 2015). Some observations of nucleated early-type galaxies in clusters indicate that GC infall may be the dominant mode of NSC growth at lower galaxy masses, although some gas infall is still required to

match the properties of the NSCs (Lotz et al., 2004; Turner et al., 2012; den Brok et al., 2014). Similarly, late-type NSCs show evidence of younger and multiple stellar populations, requiring episodes of dissipative formation (Rossa et al., 2006; Walcher et al., 2006; Carson et al., 2015), but may still require a contribution from GC infall (Hartmann et al., 2011).

While mass and morphology have been correlated with the growth mechanisms of NSCs, their contributions and efficiency may be influenced by environment as well. For example, in denser environments, galaxies host more massive GC systems (Peng et al., 2008), suggesting that compact star clusters like NSCs form more readily in higher densities (or that more GCs are available for the dissipationless formation scenario). Galaxy interactions are also more frequent in denser environments, so the NSC may experience additional periods of growth during galaxy mergers, which have been shown to trigger bursts of star formation in the galactic centre (Mihos & Hernquist, 1994; Bekki, 2015). Alternatively, the increased density of the intergalactic medium (IGM) in denser environments may prevent supernova outflows from escaping the galaxy, retaining star-forming gas for the NSC (Babul & Rees, 1992). Given these environmental aids to NSC growth mechanisms, one might expect to find that NSC properties — or even their very presence — could be dependent on environment.

This connection between NSCs and environment was previously noted by R. Sánchez-Janssen et al. (2018, submitted, hereafter SJ18) who used the NGVS to study the core of the Virgo Cluster. By comparing with literature samples for other environments, they found that, at fixed host galaxy mass, NSCs are most common in the Coma Cluster, less common in the Virgo and Fornax clusters, and least common in the Local Group. This was attributed to total halo mass of the environment, with the most massive systems having the highest fraction of NSC-hosting galaxies.

SJ18 also revisited the NSC-galaxy mass relation, and, with the addition of such a large sample of low-mass nucleated galaxies, were able to quantify the changing mass relation in this regime. NSC masses become substantially larger relative to their hosts (up to 0.3% of the host mass at $M_\star \sim 10^6 M_\odot$, compared to 0.03% at higher galaxy masses), even though NSC abundance tapers off below galaxy stellar masses of $\sim 10^9 M_\odot$. The shape of this relation mirrors the stellar mass-dark matter halo mass relation, suggesting that NSC masses are regulated by their dark matter halos. However, without similarly large datasets of low-mass galaxies in *other* environments, it is unclear if, or how, this mass relation is affected by environment.

The photometric and structural properties for all galaxies in the complete NGVS

dataset, combined with the substructure classifications from Chapter 3, allow for a thorough exploration of the relationship between NSCs and their environment: where in Virgo are they most common? Are their masses and colours, their relationship to their host galaxies, or the properties of the hosts themselves, influenced by the environment? In this chapter I examine how, if at all, the properties of the NSCs and their galaxies are shaped by the properties of their host substructures. This analysis provides additional observational constraints on the factors that are important for the formation of an NSC.

4.2 Data and Observations

The analysis in this chapter builds upon the data products from the Next Generation Virgo Cluster Survey (NGVS; Ferrarese et al., 2012) used in the previous chapter. The analysis in Chapter 3 made use of effectively every confirmed or probable Virgo Cluster member in NGVS, but for the purposes of this analysis it is important to refine the sample further, selecting objects with robust photometric and structural parameters. As described in Chapter 3, galaxy properties were extracted using either a 1D approach with `ELLIPSE` or a 2D method with GALFIT. All objects with positions and measured g magnitudes were included in the analysis of Chapter 3, but for this work, I select only those objects with magnitudes brighter than the point-source limits of the NGVS[1] in at least two bands. For objects with 1D results, I further refine the sample to include only those with magnitudes from curve-of-growth and Sérsic fits that are consistent within 0.5 mag. For structural parameters (effective radius r_e, Sérsic index n, and ellipticity e), I only include objects with $0 < n \leq 10$ and $0 < r_e \leq 250''$[2]. Out of the 3,689 confirmed or probable Virgo members in the NGVS catalogue, 3,490 meet these quality requirements, including 709 clearly nucleated systems.

I focus primarily on results from the g and i bands given their exceptional image quality ($0\farcs8$ and $0\farcs54$ average FWHM) and depth (limiting surface brightnesses of 29.0 and 27.4 mag arcsec^{-2}), which aid in the brightness profile fitting, particularly for nucleated galaxies. Additionally, these are the most widely available bands — much of the scheduled r observing was never completed due to weather, and the u and z fit

[1] from Ferrarese et al. (2012), the limiting magnitudes are $u^* = 26.3, g = 25.9, r = 25.3, i = 25.1$, and $z = 24.8$

[2] $250'' \approx 20$ kpc at the distance of Virgo

results for faint or complex objects are more likely to have converged on unrealistic values that are excluded from this analysis. The adopted structural parameters are measured in the g band. Lastly, stellar masses are estimated using the $g-i$ colours and g luminosity combined with the models of Bell et al. (2003), which correlate colour with an object's stellar mass-to-light ratio. For objects without a $g-i$ colour (due to lack of valid i band measurements), I adopted the average colour of all other objects with a g magnitude within 0.3 mag of the object of interest.

Lastly, to compare directly with the results of SJ18, I select all objects considered to be part of the NGVS Pilot Programme. This is a subset of the survey covering the core $4\,\mathrm{deg}^2$ of the Virgo Cluster around the galaxy M87. This Pilot Programme includes 401 galaxies that meet the quality criteria described above, with 91 of those hosting NSCs.

4.3 Selection of substructures and properties

The results of Chapter 3 include 23 detected substructures in Virgo and a discussion of how likely it is that each of these substructures is a *bona fide* association, based on a few factors: their overlap with substructures accepted in the literature; available velocities and SBF distances for the substructure member galaxies (see §3.4.1 and Appendix A); and the size and position of the substructure in Virgo. As an example of the last point, a large, extended parent substructure containing numerous smaller substructures may very well be a true, bound structure; however, it is so expansive that it is not an informative probe of any one particular environment. In contrast, a very small substructure superimposed on the core of Virgo is difficult to classify as a real substructure or a random overdensity of galaxies — it may have a plausible velocity or distance distribution, but only because it is sampling from the larger (valid) distribution of the core region.

With these considerations in mind, I have sorted the OPTICS substructures into three classes. The substructures most strongly supported by both velocity and SBF distances, literature definitions of Virgo, and the size/position argument, become the "best" substructures. Those with limited velocities or distances, but having reasonable sizes and locations, are classified as "plausible" substructures. Finally, any substructures that are less informative due to their sizes and positions, or have velocities or distances that indicate that they are not truly bound, are considered to be "uninformative."

Table 4.1 Structural properties of OPTICS substructures

ID	Flag	$\log_{10} M_\star$ ($M_\odot$)	$\log_{10} \Sigma_\star$ ($M_\odot$ deg^{-2})	f	f_{max}	$\log_{10} M_f$ ($M_\odot$)	N	N_{NSC}
0	Uninformative	12.557	10.592	0.192	0.805	9.85	3685	709
1	Uninformative	12.461	10.675	0.207	0.802	9.30	2632	546
2	Uninformative	12.416	10.732	0.211	0.854	10.50	2324	491
3	Uninformative	12.406	10.732	0.213	0.868	10.50	2234	476
4	Best	12.227	11.016	0.212	0.875	10.00	1232	261
5	Plausible	12.089	11.219	0.229	0.933	9.10	655	150
6	Plausible	12.028	11.380	0.242	0.941	8.80	505	122
7	Plausible	11.573	10.920	0.248	0.718	8.75	307	76
8	Uninformative	11.222	10.778	0.202	1.000	10.40	163	33
9	Best	11.173	11.178	0.183	0.889	8.55	109	20
10	Best	11.009	10.568	0.223	1.000	9.15	103	23
11	Uninformative	11.540	11.926	0.326	1.000	8.95	92	30
12	Best	11.204	11.417	0.274	1.000	10.50	84	23
13	Best	10.897	10.792	0.205	1.000	9.30	83	17
14	Best	10.957	11.035	0.195	1.000	9.05	77	15
15	Plausible	10.003	10.717	0.219	1.000	9.30	64	14
16	Plausible	11.084	11.361	0.207	0.875	8.65	58	12
17	Best	11.234	11.409	0.333	1.000	8.05	57	19
18	Plausible	10.651	10.987	0.280	1.000	9.80	50	14
19	Plausible	10.938	11.463	0.233	0.667	10.35	43	10
20	Plausible	10.213	10.778	0.190	1.000	8.60	42	8
21	Best	10.350	10.577	0.143	1.000	9.65	42	6
22	Uninformative	10.832	11.415	0.220	1.000	10.20	41	9

The final component for the analysis is estimating the properties of the substructures that are used to represent the environment. I derive total stellar masses as well as stellar mass surface densities for each substructure. The masses are summed from the stellar masses of all galaxies belonging to the substructure. Lastly, mass surface densities are calculated simply using this total stellar mass and the area of the best-fit representative ellipse for each substructure, which was fit in §3.3.2.

4.4 Results

Key properties of the OPTICS substructures (masses, densities, peak NSC occupation fraction, galaxy mass at which the peak occurs, and membership numbers — are summarized in Table 4.1. The classes determined in §4.3 are also included. In the following subsections I confirm whether these substructure properties have any influence on the nucleated galaxies within them.

4.4.1 NSC occupation fraction

It is now well known that the fraction of galaxies hosting NSCs depends strongly on galaxy mass (Grant et al., 2005; Côté et al., 2006; Lisker et al., 2007; Turner

et al., 2012; den Brok et al., 2014; Muñoz et al., 2015; Eigenthaler et al., 2018, SJ18). Recently, SJ18 hypothesized that the fraction of galaxies with NSCs, or the occupation fraction, also has a secondary effect from total halo mass. This was determined with heterogeneous samples from the Coma, Fornax and Virgo Clusters, as well as with limited information from our own Local Group. With the substructures detected in Chapter 3 spanning two orders of magnitude in stellar mass, it is now possible to investigate this proposed secondary effect on the NSC occupation fraction (assuming that the stellar mass is an effective tracer of total halo mass).

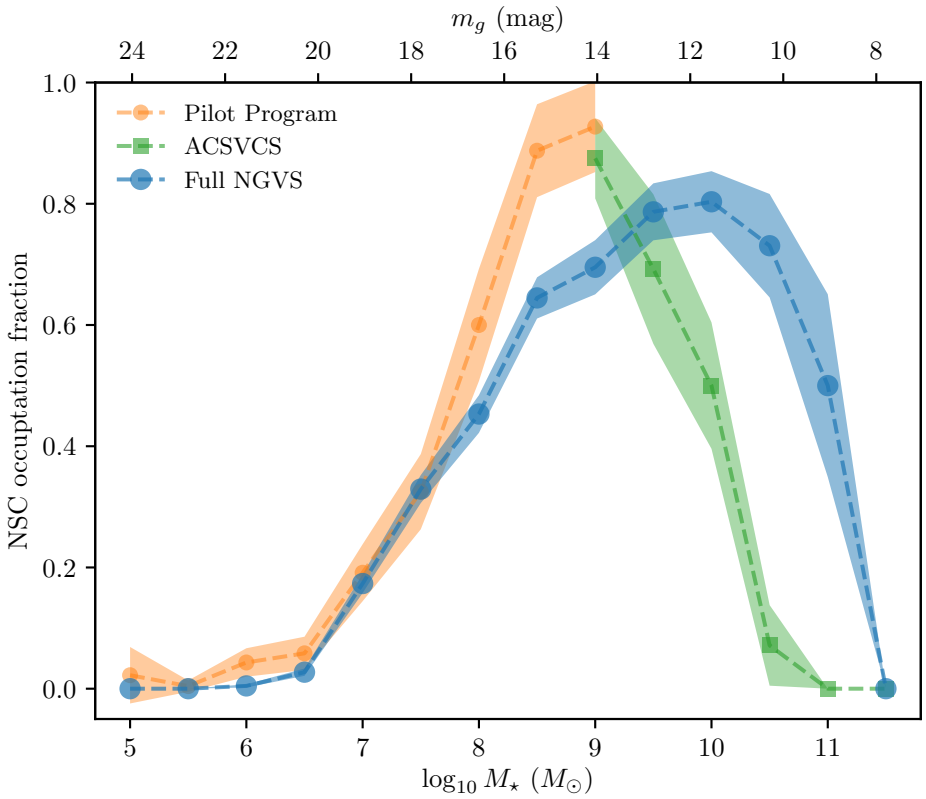

Figure 4.1 NSC occupation fraction (the fraction of galaxies with detected NSCs) as a function of galaxy stellar mass. The small orange circles and green squares indicate prior measurements based on the NGVS pilot program and the ACSVCS, respectively. Results from the full NGVS sample are shown by the large blue circles. Shaded regions around each curve show the 68% Bayesian credible interval for a binomial probability.

Figure 4.1 shows the NSC occuptation fraction as a function of galaxy mass for the entire NGVS sample, with results re-derived for the ACSVCS and the Pilot Programme for reference. The Pilot Programme and ACSVCS fractions are in good agreement, showing an overall nucleation fraction that peaks at galaxy masses of

$10^9 M_\odot$ and tapers off at higher and lower masses. The same overall trend is observed with the full NGVS; however, the peak fraction is ∼10% lower and occurs at galaxy masses ten times larger. This shift indicates immediately that there must be a secondary effect on the NSC occupation fraction. The Pilot Programme and ACSVCS samples are exclusively early-type galaxies, so the difference may be a morphological effect. Indeed, the early-type spirals analyzed by Carollo et al. (2002, 1998, 1997), have non-zero occupation fractions of NSCs up to galaxy masses of $10^{11} M_\odot$. However, morphology is inherently linked to environment, with early-type galaxies increasingly common in higher density environments (Dressler, 1980).

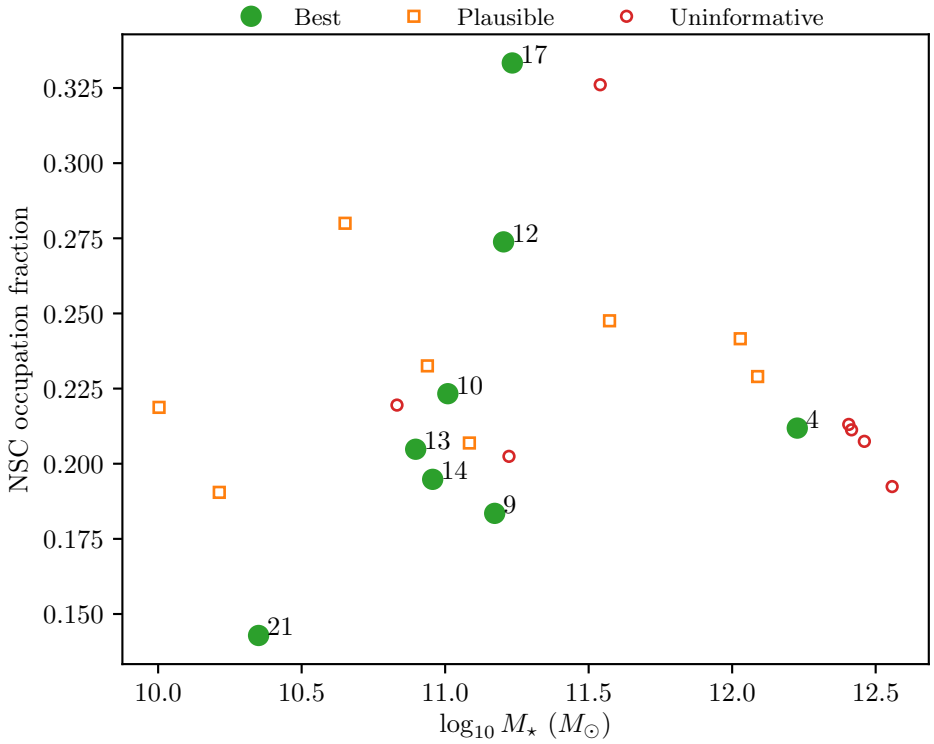

Figure 4.2 The overall NSC occupation fraction as a function of total stellar mass in each substructure. Using available positions/sizes, velocities and SBF distances from Chapter 3, substructures are grouped into three classes: those that are most certainly distinct, true substructures verified with sufficient velocity and/or distance estimates (green circles); likely substructures that are lacking velocities and/or distances for robust confirmation (open orange squares); and the least conclusive or informative substructures (open red circles), which includes "substructures" that may be chance projections on the sky, or true parent substructures that span too large a range of environments to be informative in this case. The OPTICS IDs are shown for the "best" detections (green circles).

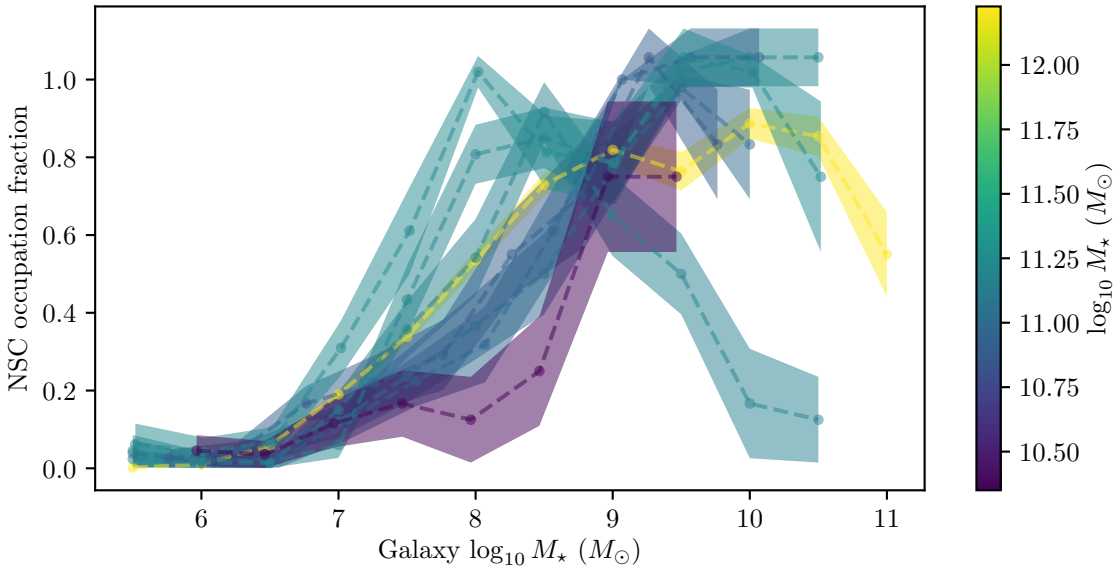

Figure 4.3 NSC occupation fraction as a function of stellar mass in each substructure, colour-coded by total stellar mass of the substructure. For clarity, only the eight most robust substructure detections are shown.

When looking at individual substructures within Virgo, again, halo mass does not appear to correlate with the NSC occupation fraction, as shown in Figure 4.2. The correlation coefficient is $r = -0.18$, indicating a tentative *anti*-correlation between NSC occupation fraction and mass. Even when focusing only on the most confident substructure identifications, no clear trend emerges ($r = 0.01$). At a fixed total stellar mass of $10^{11} - 10^{11.5} M_{\odot}$, the occupation fraction can vary from 18% to 33%. Even when looking at the occupation fraction as a function of galaxy mass, such as in Figure 4.3, there is no dependence on total substructure mass.

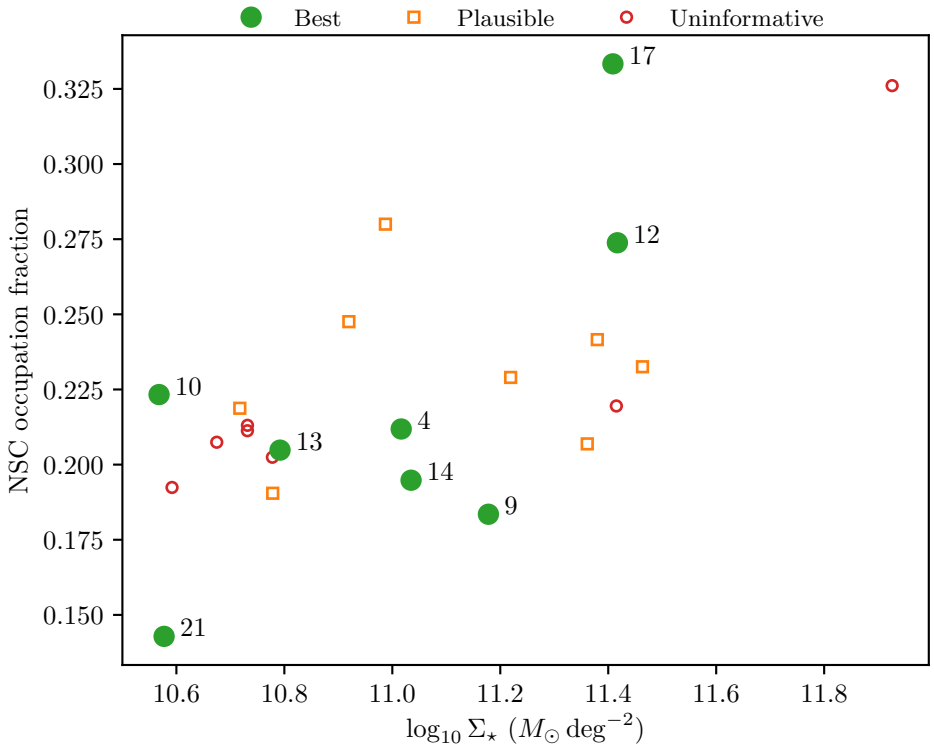

Figure 4.4 Same as Figure 4.2, but for substructure stellar mass surface density instead of total stellar mass.

Instead, the secondary factor driving NSC occupation fraction appears to be density. When Figure 4.2 is redisplayed in terms of substructure stellar mass surface density, as in Figure 4.4, a clear trend emerges: NSCs are more common in denser substructures. Here the correlation coefficients are $r = 0.65$ for all substructures and $r = 0.70$ for the "best" substructures. This trend is most pronounced in galaxies with stellar masses below $10^9 M_{\odot}$, as shown in Figure 4.5. Interestingly, many of the substructures flagged as plausible or uninformative are broadly consistent with the

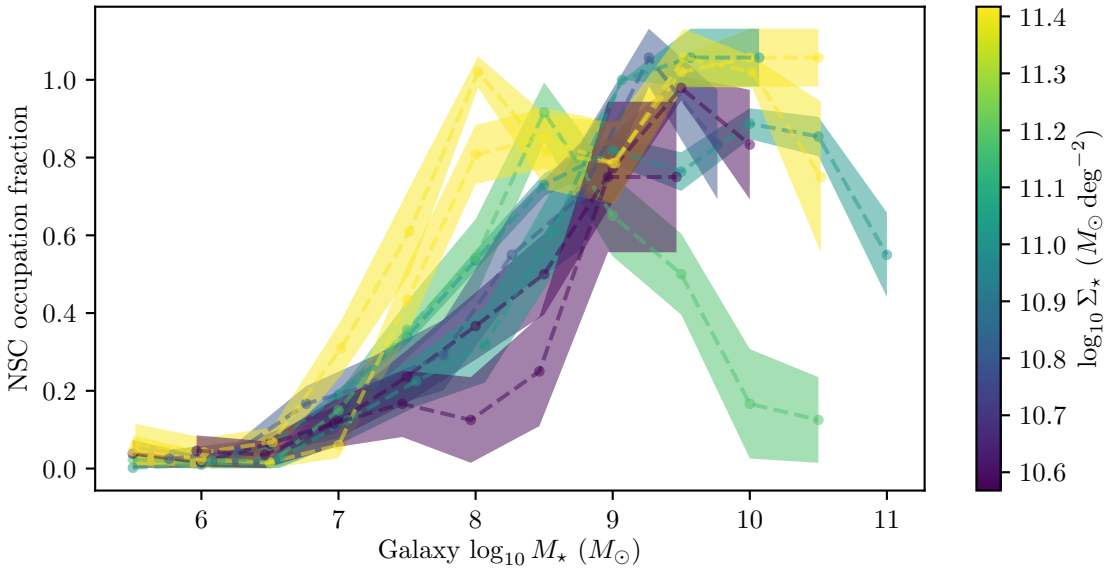

Figure 4.5 Same as Figure 4.3, but for substructure stellar mass surface density instead of total stellar mass.

occupation fraction-density trend set by the "best" substructures in Figure 4.4. This suggests that these are valid substructures, despite their classifications.

One substructure stands out in Figures 4.3 and 4.5 as having uncharacteristically low NSC occupation fractions above stellar masses of $10^9 M_\odot$. This substructure is OPTICS 9, which roughly corresponds to the literature definition of the W′ cloud. Despite this low fraction, its average occupation fraction is not unreasonable for its density (see Figure 4.4). Perhaps this is due to the substructure's proximity to M49 and OPTICS 17, or Virgo B — there may be some confusion between the boundaries of these structures and some (nucleated) galaxies have been erroneously assigned to OPTICS 17. This is supported by the fact that the NSC occupation fraction for OPTICS 17 is unusually high in Figure 4.5 at high masses, and does not display the turnover found in the other substructures. However, it is quite odd that predominantly nucleated galaxies from OPTICS 9 have been assigned to OPTICS 17. The substructure OPTICS 10, one of the lowest-density substructures, also stands out with occupation fractions that are higher than expected for its density. This may be due to the best-fit ellipse for this substructure. Figure A.11 suggests that the representative ellipse for this substructure is too large, driven by a narrow stream of substructure members extending from the main body. This artificially lowers the estimated density and may account for the outlier behaviour of this structure. Overall, based on the ability of ellipses to approximate the substructure regions, most of the current density estimates should be robust, although a comparison of these density estimates with values from other methods (i.e., based on the distance to the fifth-nearest neighbour) is forthcoming.

4.4.2 NSC-galaxy stellar mass relation

The most recent estimates of the NSC-galaxy stellar mass relation in the Virgo Cluster were produced in Spengler et al. (2017, see also Chapter 2), which matched previous results for the high-mass end of the nucleated galaxy population (e.g., Côté et al., 2006; Ferrarese et al., 2006a; Turner et al., 2012). SJ18 quantified a change in the mass relation at lower galaxy masses — although the typical NSC-galaxy mass ratio of ∼0.03% was still valid for the high mass end, a larger ratio was observed at lower masses. Figure 4.6 shows this mass relation for the complete NGVS sample, with previous measurements from Spengler et al. and for the Pilot Programme overlaid for comparison. Overall, there is good agreement among the three samples across the

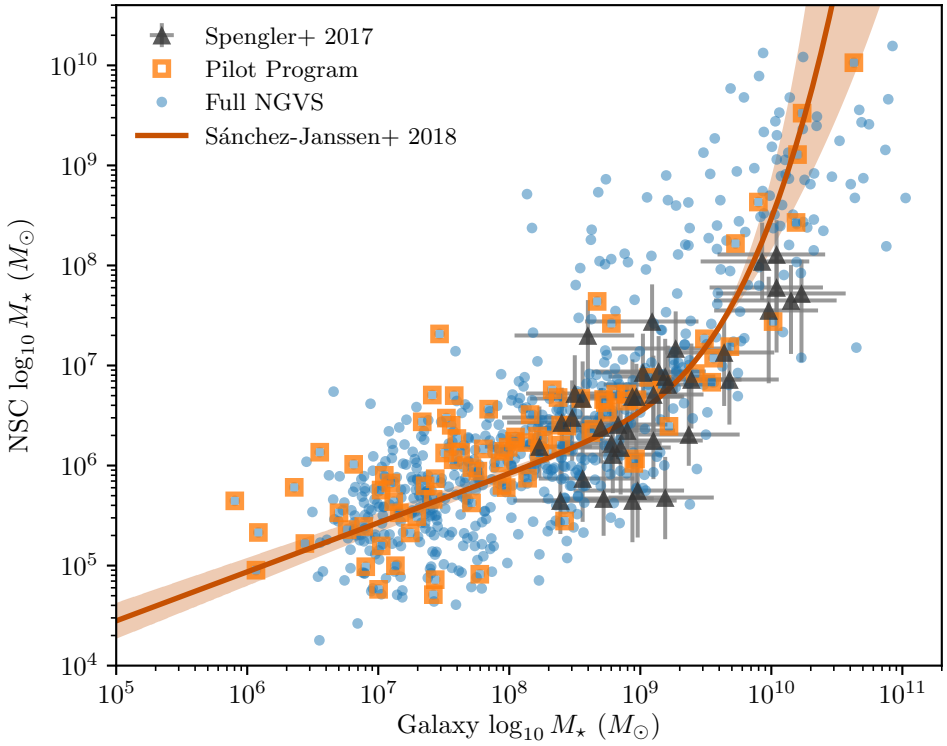

Figure 4.6 Stellar masses of NSCs in Virgo as a function of their host galaxies' stellar masses. Blue points show all objects in NGVS confidently classified as nucleated. Open orange squares show recalculated masses for galaxies included in the pilot program from SJ18, and filled grey triangles show estimates from the 39 nucleated galaxies in the Virgo Redux study (Spengler et al. 2017; see also Chapter 2). The dark orange line and shaded region show the best fit and associated uncertainty determined by SJ18.

full mass range and with the trend derived by SJ18. The complete NGVS sample appears to scatter to preferentially higher NSC masses compared to those measured in the previous Spengler et al. work; however, this is likely due to the challenges in decoupling NSCs from their host galaxies in such bright, complex systems, and especially when using only two-component models of the brightness profile (for more details on this issue, see Chapter 2).

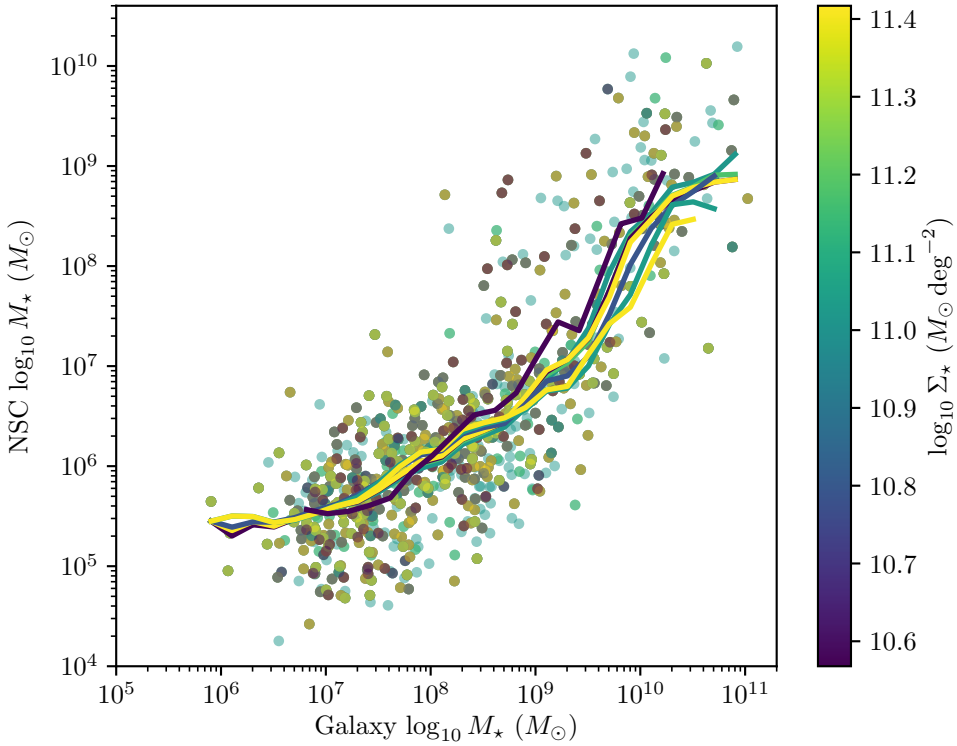

Figure 4.7 NSC-galaxy mass relation within the eight most confidently detected substructures in Virgo, colour-coded by stellar mass surface density of the substructures. Solid lines show the average trend within each substructure. For clarity, $1\,\sigma$ regions of each line have been omitted, but any variations among the lines are well within these regions.

The overall mass relation for Virgo is consistent with previous results, but there is a significant amount of scatter around the general trend. With the substructure classifications from Chapter 3, I can investigate if this scatter is the result of the scaling relation varying with environment. Figure 4.7 shows the NSC-galaxy mass relation again, but for each of the eight substructures from Chapter 2 that are best confirmed by velocities and SBF distances. The same trend persists in the scaling relation, suggesting that the scatter in the mass relation is not a product of the

environmental changes. This may be intrinsic scatter due to the stochastic formation of NSCs, as proposed by SJ18, or due to the simple mass estimation based on a single colour and luminosity (rather than full SED fitting). The scatter may also be a morphological effect, which is driven by environment to some extent. Seth et al. (2008) and Georgiev et al. (2016) noted that NSCs in late-type galaxies are systematically smaller and less massive than NSCs of early-type galaxies at fixed galaxy mass. Unfortunately, the morphological classification of all NGVS galaxies has not been completed for ∼2,500 galaxies, mostly with magnitudes fainter than $g \sim 16$ mag, so this effect cannot be investigated currently.

4.4.3 NSC mass function

With these data, it is possible to create a mass- and volume-limited sample across the entire mass range for which NSCs have been detected. Prior results from SJ18 for the core of Virgo found a Gaussian distribution with a slight high-mass tail. As shown in Figure 4.8, this is broadly consistent with the distribution from the complete NGVS, although the distribution appears more bimodal and the high-mass tail can now be modeled as a separate, smaller Gaussian. Interestingly, a bimodal NSC mass function has also been observed in the Fornax Cluster (Ordenes-Briceño et al., 2018b), although in Fornax the bimodal peaks occur at masses of $10^{5.4}$ and $10^{6.3} M_{\odot}$. When fitting both distributions with a double-Gaussian model, both have a prominent Gaussian centred at $\sim 10^6 M_{\odot}$, although the distribution from the core region is marginally broader and shifted to slightly higher masses. Perhaps NSCs (and their host galaxies) are preferentially more massive in denser environments, producing a variable NSC mass function while maintaining the same NSC-galaxy mass relation.

The mass function throughout different environmental densities is shown in Figure 4.9. Given the rarity of NSCs with masses above $10^8 M_{\odot}$, the secondary higher-mass peak in the mass function is not considered in great detail in this analysis because low number statistics, and corresponding uncertainties on the shape of the mass distribution, make it difficult to draw any meaningful conclusions. Focusing on the larger peak in the distribution at smaller masses, it seems plausible that the denser substructures have slightly broader distributions with peaks centred at higher masses. However, the inset panels in Figure 4.9 reveal that there are no correlations between the shape or position of the mass function and substructure density. Within the uncertainties, the mass functions are consistent across all environments in this

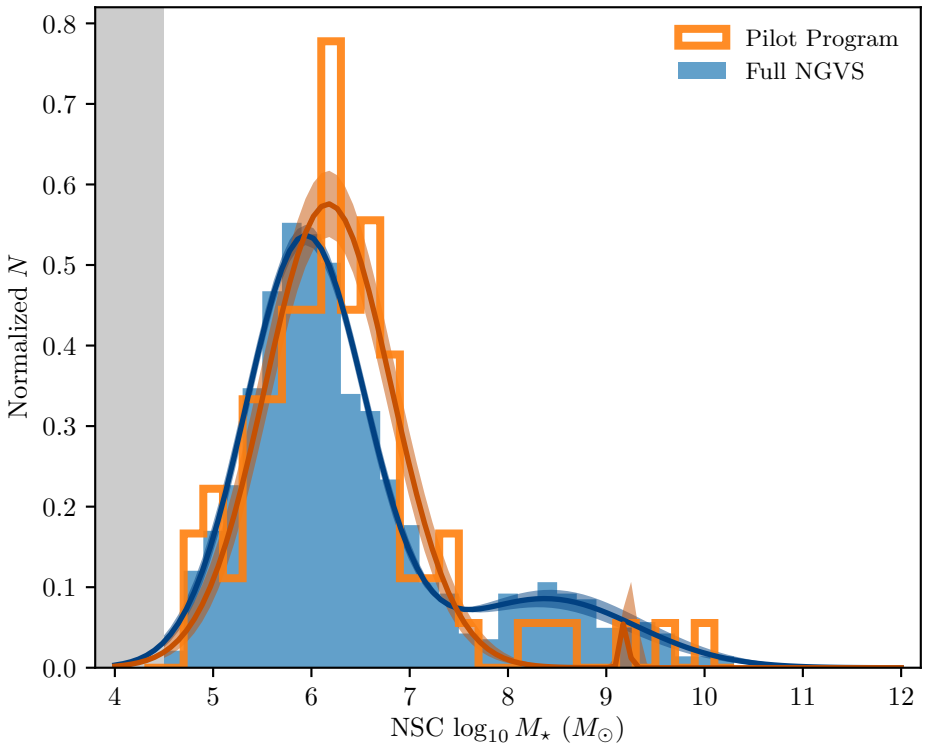

Figure 4.8 Distribution of NSC masses for galaxies within the NGVS pilot region (orange histogram) compared to the distribution from the full NGVS (shaded blue histogram). Each distribution has been fit with a combination of two Gaussian profiles, with the resulting best-fit curves to the pilot sample and full NGVS shown by the orange and blue lines, respectively. Shaded areas around each line indicate the 1σ uncertainty on the fit. Result for the Pilot Programme are consistent with those measured by R. Sánchez-Janssen et al. (2018, submitted).

sample.

4.4.4 Galaxy and NSC colours

Regardless of galaxy mass or morphology, NSCs appear consistently bluer than their hosts in optical colours (e.g., Lotz et al., 2004; Côté et al., 2006; Turner et al., 2012; Spengler et al., 2017; Ordenes-Briceño et al., 2018b, SJ18). This is often attributed to some portion of the NSC stellar population being formed more recently than the rest of the galaxy. The colours of NSCs could be affected by environment — NSCs within galaxies in the densest regions of Virgo likely have spent the longest time in the cluster potential, passively evolving without much recent gas accretion and manifesting as relatively older and redder NSCs. In contrast, NSCs in lower-density environments may have had more recent bursts of star formation and contain a larger fraction of younger, bluer stars as a result.

The NSC-galaxy colour relation is shown for the full NGVS in Figure 4.10 and within each substructure in Figure 4.11. The NSC colours show significant scatter, and overall, NSCs are 0.06 ± 0.13 mag bluer than their hosts, so there is no statistically significant colour difference. It is interesting to note that the reddest galaxies preferentially have relatively bluer NSCs, but bluer galaxies are more likely to have relatively redder NSCs. This may indicate that NSCs, regardless of their host, have a typical colour; although, the colour regions driving these apparent trends are very sparsely populated so this effect may simply be a result of limited sampling. In any case, Figure 4.11 shows that there is no obvious shift in this colour relation with variations in environment density, suggesting that the stellar populations of NSCs and their hosts remain relatively unaffected by the environment.

The relationship between NSC and galaxy colour is often studied, but what about the relationship between colours of nucleated and non-nucleated galaxies? These colours are shown for all galaxies in NGVS brighter than $g = 20$ mag[3] in the colour-magnitude diagram in Figure 4.12. There is a clear trend for galaxies to appear redder at brighter magnitudes. This is thought to be predominantly an effect of higher metallicities — the larger gravitational potentials of brighter, more massive galaxies can better retain enriched gas from stellar winds and supernovae, producing subsequent generations of more metal-rich stars (e.g., Kodama & Arimoto, 1997; Ferreras et al.,

[3]For unbiased results, analysis is limited to the magnitude range populated by both nucleated and non-nucleated systems.

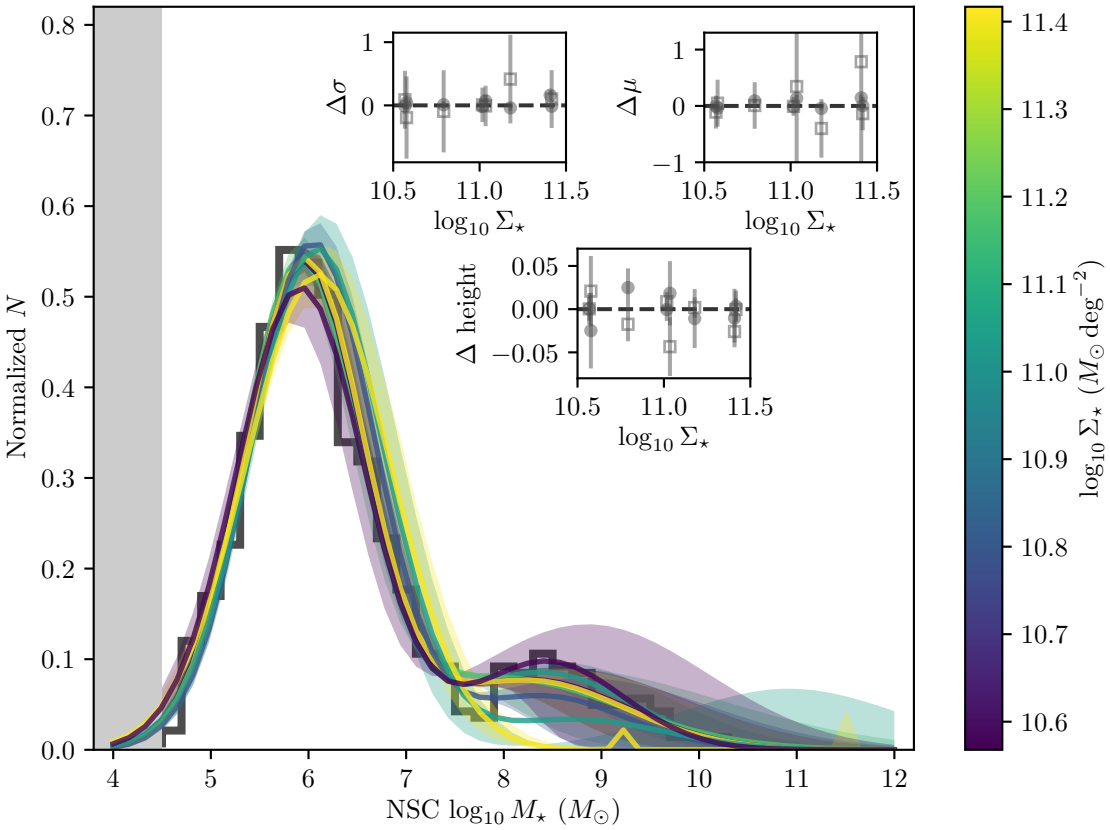

Figure 4.9 Same as Figure 4.8, but for each substructure identified in Virgo and classified according to its stellar mass surface density. For clarity, only the best-fit double Gaussian profile for each substructure is shown, along with $1\,\sigma$ shaded areas. The grey region on the left indicates the mass range below the 10σ detection limit of the NGVS. For reference, the NSC mass function of the full NGVS is shown as the grey histogram. Inset panels show how the free parameters in each Gausian fit deviates from the median values of those parameters as a function of stellar mass surface density. The parameters are width σ (top left inset), mean μ (top right), and the height or normalization (bottom). Filled circles show deviations for the primary Gaussian component (centred at $\log_{10} M_\star \sim 6$), while open squares show the secondary component (centred at $\log_{10} M_\star \sim 8.5$). No clear trends emerge between the Gaussian properties and substructure density.

1999). However, scatter around the mean relation at constant magnitude could be caused by age differences, not only changes in metallicity. Nucleated galaxies tend to be only marginally redder than the non-nucleated population, but, interestingly, the colour differences increase to up to 0.3 mag in the magnitude range $18 \geq g \geq 12$. This also happens to be the regime where NSCs are most prevalent. The same trends and colour differences persist within each substructure, as shown in Figure 4.13. Perhaps the processes responsible for the growth of NSCs within the past few Gyr can also effect the host galaxies to a lesser extent, such as by triggering a small amount of star formation from metal-rich gas and reddening the galaxy. Whatever may be responsible for the colour difference, it is not influenced by environmental changes, as shown in Figure 4.13. The trends within each environment are consistent within the 1 σ uncertainties, and the amplitude of the colour offset in the aforementioned magnitude range remains unchanged.

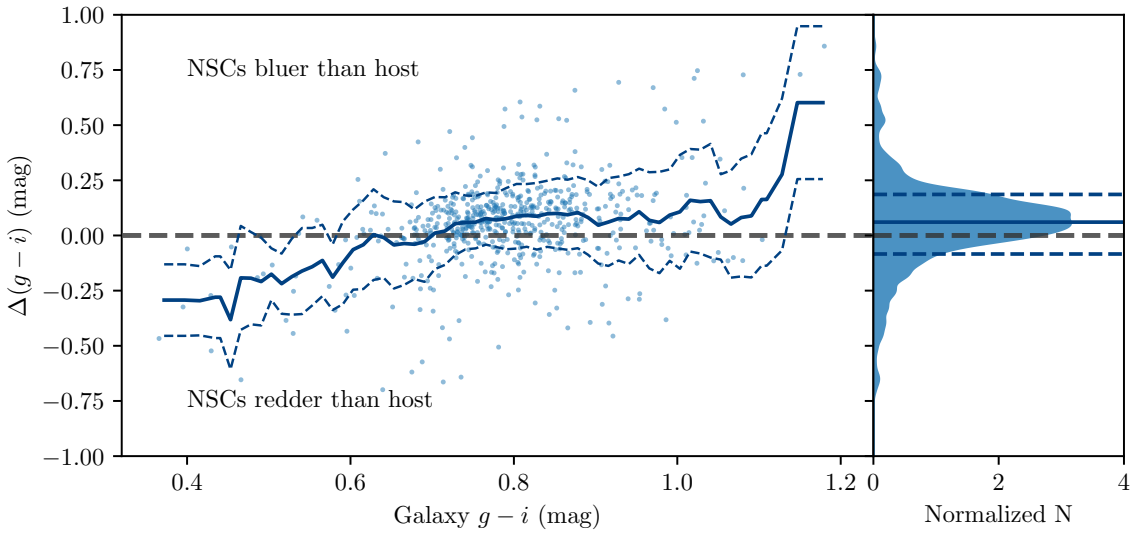

Figure 4.10 *(left panel)* NSC-galaxy colour differences for the full NGVS sample as a function of galaxy colour. The colour difference is (galaxy colour) - (NSC colour), such that objects with bluer NSCs appear above the horizontal grey dashed line, and those with redder NSCs are below this line. The solid blue line shows the average colour difference trend, and dashed lines show the 1σ uncertainty on the average relation. *(right panel)* Data from the left panel collapsed into a normalized distribution of all NSC-galaxy colour differences. As before, the solid line shows the mean colour difference, and dashed lines denote the 1σ range.

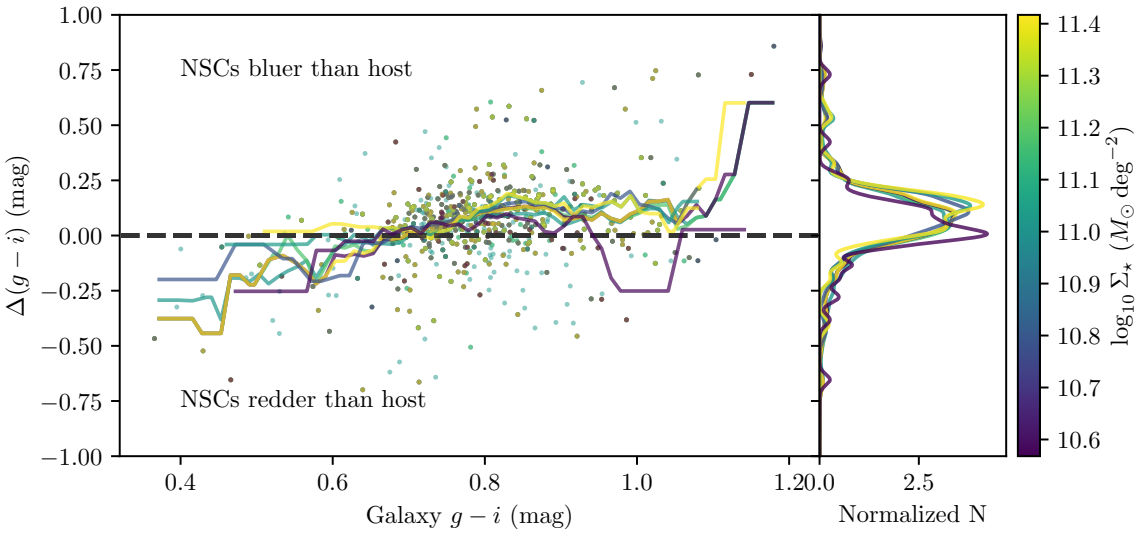

Figure 4.11 Same as Figure 4.10, but separated according to substructure and colour-coded by substructure mass surface density.

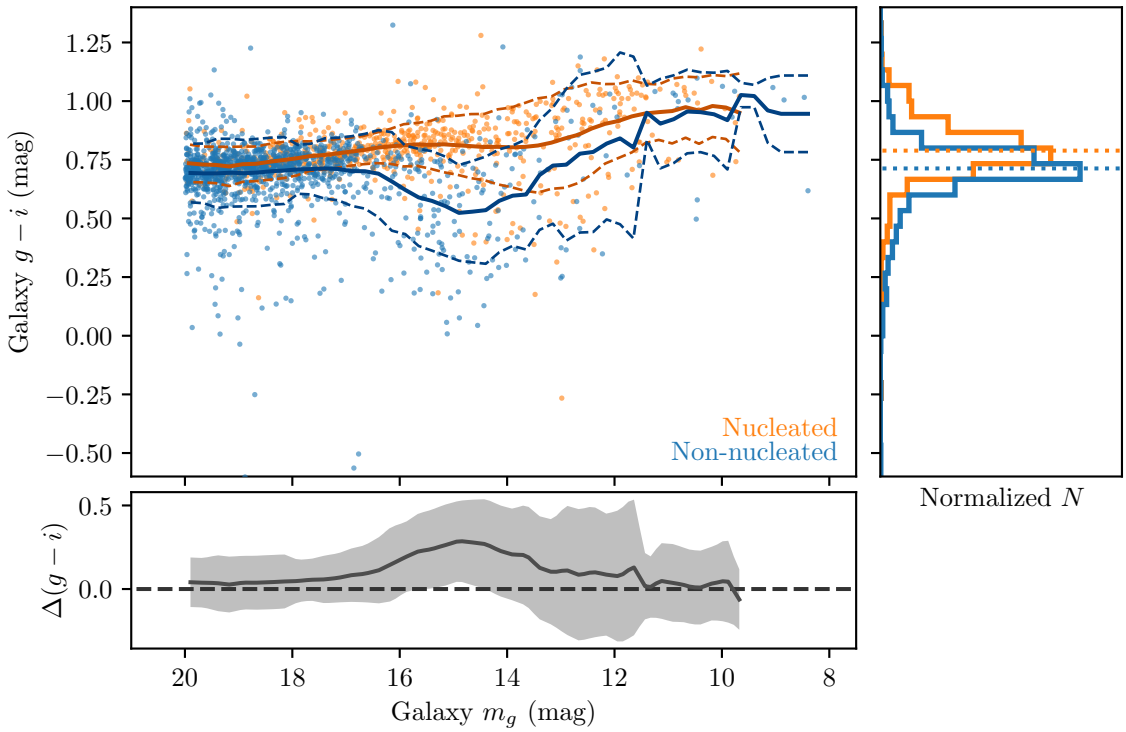

Figure 4.12 Galaxy $g - i$ colour as a function of apparent g-band magnitude for nucleated (orange points) and non-nucleated (blue points) galaxies. Both samples are limited to $m_g < 20$, the magnitude range populated by both nucleated and non-nucleated galaxies. Solid dark orange and dark blue lines show the average colour-magnitude relation for nucleated and non-nucleated galaxies, respectively, estimated using the mean of a sliding bin with a width of 1 mag. Dashed lines show the $1\,\sigma$ spread of each population. *(top right panel)* Normalized colour histograms of each population, following the same colour coding as the previous panel. Dotted lines show the median colour of the two groups, with nucleated galaxies, as a whole, appearing slightly redder than their non-nucleated counterparts. *(bottom panel)* The colour difference between nucleated and non-nucleated galaxies as a function of magnitude, using the average lines from the top left panel. The shaded region shows the $1\,\sigma$ range. Nucleated galaxies are notably redder primarily in the magnitude range $17 \leq m_g \leq 12$, where NSCs are most abundant (see Figure 4.1).

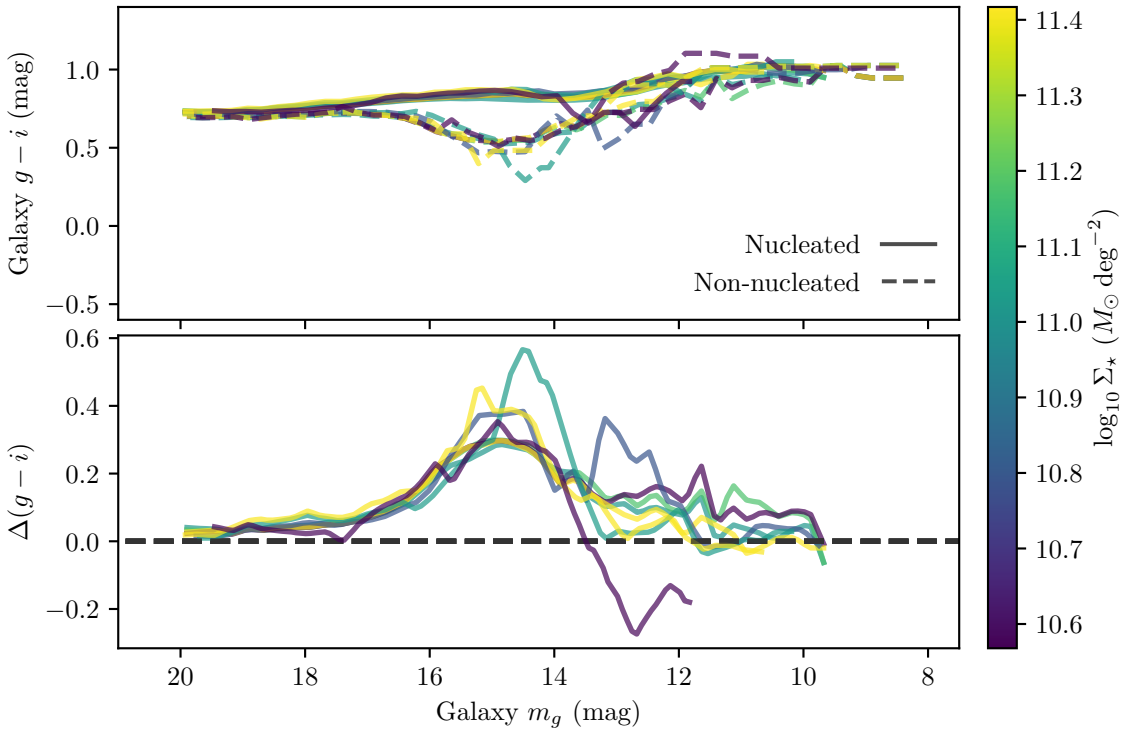

Figure 4.13 *(top panel)* Similar to the bottom left panel of Figure 4.12, but showing the average colour-magnitude relations for nucleated (solid lines) and non-nucleated (dashed lines) galaxies within each substructure. Lines are colour-coded according to substructure stellar mass surface density. *(bottom panel)* Colour differences between the nucleated and non-nucleated samples of each substructure. For clarity, the $1\,\sigma$ uncertainties on each trend have been omitted, as they are larger than the deviations among the lines.

4.4.5 Galaxy structural parameters

Unfortunately, sizes and shapes cannot be reliably estimated for NSCs from these ground-based observations (in which all but the largest NSCs are unresolved). However, structural properties of their host galaxies are available to search for structural variations that may arise due to environment or the presence of an NSC, which can help constrain which mechanism(s) play a role in the existence of NSCs.

Ellipticities

Ellipticity[4] quantifies the roundness of a galaxy with values between zero (completely circular) and one (completely flattened). Estimates of each galaxy's ellipticity are produced both from `ELLIPSE` and GALFIT but in slightly different ways. `ELLIPSE`, as summarized in Chapter 2, fits ellipses to isophotes of constant surface brightness, each with independent values for the free parameters, including ellipticity. The ellipticity used in this analysis is the average from all isophotes. However, there are some exceptions — for some very round galaxies, which causes the position angle to be poorly constrained, the ellipticity of all isophotes must be fixed to a low but non-zero value of 0.05 for the fit to converge. As a result, there is an artificial peak in the ellipticity distributions at this value, rather than having those galaxies more distributed among other low-ellipticity values. In contrast to the `ELLIPSE` procedure, GALFIT fits a single axis ratio b/a for the entire brightness model, which is used to create a representative ellipticity for each galaxy.

Many previous studies of the Virgo and Fornax clusters have determined that nucleated galaxies are rounder than non-nucleated galaxies of comparable mass or luminosity (van den Bergh, 1986; Impey et al., 1988; Ferguson & Sandage, 1989; Ichikawa, 1989; Binggeli & Popescu, 1995; Grant et al., 2005; Lisker et al., 2007; Eigenthaler et al., 2018). Additionally, den Brok et al. (2014) found that, among nucleated galaxies at fixed magnitude, rounder galaxies have brighter NSCs. This was attributed to the lack of rotational support making it easier for gas to fall to the centre of the galaxy, or possibly because of environment — galaxies that have spent a longer time in the cluster potential have become rounder and stripped of some of their mass, increasing the relative luminosity of their NSCs. We now revisit the shapes of nucleated and non-nucleated galaxies in Virgo, both throughout the

[4]Ellipticity e is defined as $1 - b/a$, where a and b are the semi-major and semi-minor axes of an ellipse, respectively

entire cluster as done in the literature, and within the different environments. If the proposed environmental dependence of den Brok et al. (2014) is a factor in the Virgo Cluster, one would expect to see relatively higher proportions of rounder galaxies in denser environments (which should be the earlier structures to form in Virgo).

The ellipticity distributions within substructures can be stochastic and do not always have obvious parametric (i.e., Gaussian) forms. Therefore, I have generated kernel density estimations (KDEs) for all distributions for clarity when comparing among the substructures. This also permits a rudimentary treatment of uncertainty from measurement errors as well as sample size by defining a particular bandwidth for the kernel smoothing. I adopted the bandwidth selection rule from Silverman (1986, p. 45), which determines the ideal bandwidth δ using the equation $\delta = (4/3)^{1/5}\bar{\sigma}n^{1/5}$, where n is the number of galaxies in the sample or substructure and $\bar{\sigma}$ is the mean ellipticity uncertainty of the n galaxies.

Figure 4.14 shows the ellipticity distributions for all nucleated and non-nucleated galaxies in the NGVS. As expected, the nucleated galaxies are clearly more rounded, on average. The figure contains both the KDEs and original histograms of the data to evaluate how well the bandwidth choice represents the original distribution. The overall shapes of the histograms are well-matched by the KDEs, and the peaks at $e = 0.05$ are smoothed to a more reasonable distribution. Based on this result it seems appropriate to apply the KDE approach to the distributions of individual substructures as well. These results are shown in Figure 4.15. The same general trend persists — nucleated galaxies are rounder than non-nucleated galaxies in all environments — but the typical ellipticity values seem independent of environmental density.

Sérsic indices

Just as for ellipticity, similar trends with galaxy concentration as measured by the Séric index n, have been observed. Nucleated galaxies appear more concentrated than non-nucleated galaxies at similar luminosities (Eigenthaler et al., 2018). This may contribute to the increase in NSC occupation fraction in higher density environments because galaxies with higher concentrations should be more likely to survive the tidal interactions that are more common in these environments. In this case, environment does not directly influence the growth of an NSC, but can still contribute to the observed environmental dependence of the NSC occupation fraction — the slope of

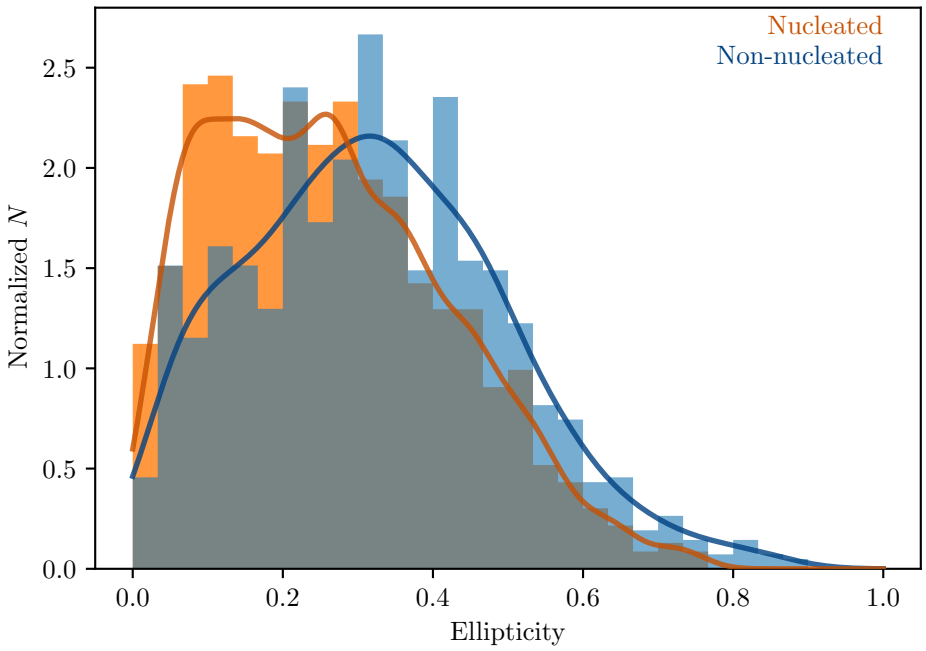

Figure 4.14 Distribution of ellipticities for nucleated (orange) and non-nucleated (blue) galaxies. Normalized histograms show the binned data and lines are the corresponding kernel density estimations (KDEs), with the kernel bandwidth selected according to sample size and uncertainty (full details available in the text). The exceptionally high bin at low ellipticities ($e = 0.05$) is due to `ELLIPSE` requiring a fixed non-zero ellipticity for some very round galaxies for which it could not converge on a fitted value.

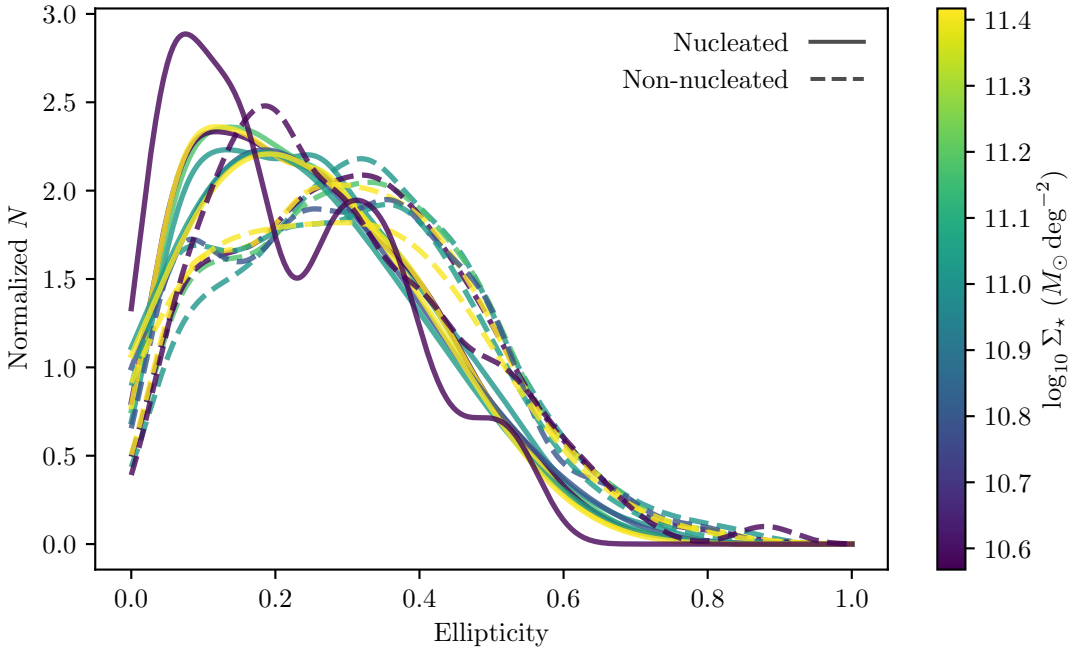

Figure 4.15 Distribution of ellipticities for nucleated (solid lines) and non-nucleated (dashed lines) galaxies within each of the eight best substructures, coloured by stellar mass surface density. The lines are the KDEs for each sample with the bandwidth selected as described in the text.

the distribution of low-n non-nucleated galaxies should steepen as density increases, due to the preferential disruption of those galaxies. If, however, the distributions of n values remain unchanged across the various environments, the observed larger n for nucleated galaxies may be a consequence of the particular formation processes in these galaxies. den Brok et al. (2014) estimate that the observed luminosities of NSCs within galaxies with relatively higher n cannot be generated by GC infall alone, so dissipative processes must play at least a minor role in the formation of NSCs in these systems.

Distributions of n for nucleated and non-nucleated galaxies throughout the full NGVS are shown in Figure 4.16. KDEs have been generated for the sample following the same method used for the ellipticities. As expected, the nucleated galaxy population is shifted to larger n by $\sim$0.5, on average. The same distributions within each substructure are shown in Figure 4.17. The shapes of the nucleated and non-nucleated distributions are effectively identical across all densities, indicating that low-n galaxies are not preferentially being destroyed in higher density environments.

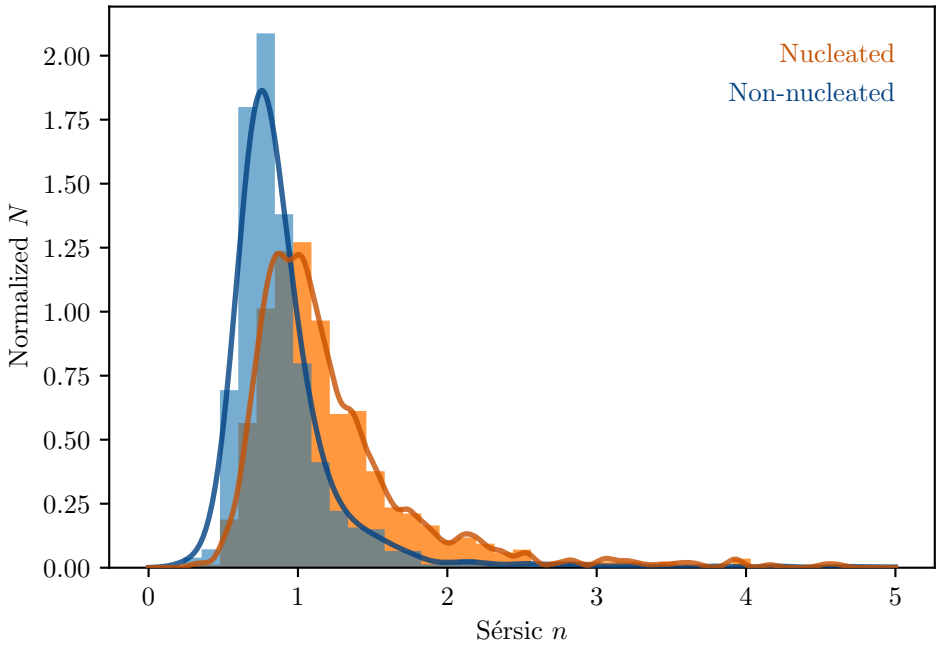

Figure 4.16 Same as Figure 4.14, but for galaxy concentration as measured by the Sérsic index n. Although galaxies in the sample can have values for n up to 10, only $n < 5$ have been shown here to highlight the bulk of the distributions.

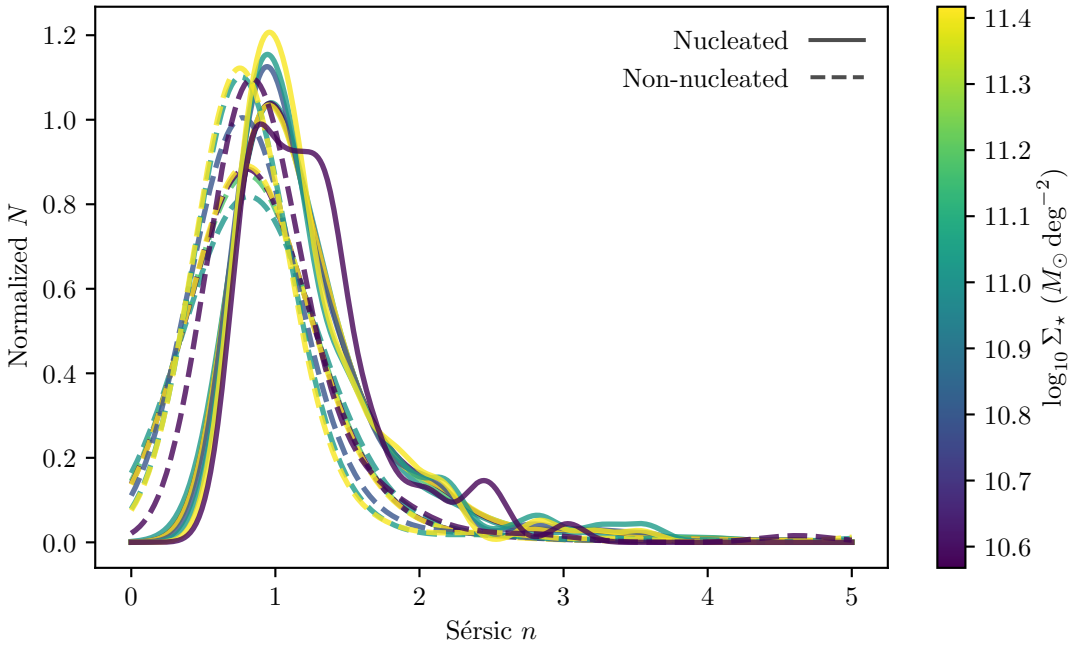

Figure 4.17 Same as Figure 4.15, but for Sérsic index n. Although galaxies in the sample can have values for n up to 10, only $n < 5$ have been shown here to highlight the bulk of the distributions.

4.5 Conclusions and Summary

Using the substructures identified in Chapter 2 and the sample of structural and photometric properties for galaxies throughout the Virgo Cluster, I have investigated the impact of environment on the NSC occupation fraction, the relationship between NSCs and their hosts, and the structural and photometric properties of nucleated and non-nucleated galaxies. The primary results can be summarized as follows:

- A large spread in NSC occupation fraction at similar substructure masses suggests that halo mass is not the sole factor in the presence of NSCs. Instead, there is a pronounced correlation with stellar mass surface density, particularly in galaxies with stellar masses $10^7 \leq M_\star \leq 10^9 M_\odot$.

- NSCs follow a consistent mass function with peaks in the distribution at stellar masses $\sim 10^6$ and $10^{8.5} M_\odot$, regardless of environment. They also maintain the same colours and mass scaling relation with their host galaxies. The scatter in the colours and mass relation may be an inherent scatter due to the stochastic nature of NSC formation, or it may be evidence of a secondary dependence on galaxy morphology, which requires further investigation.

- Nucleated galaxies are $\sim$0.3 mag redder at the 1 σ level in optical bands than their non-nucleated counterparts in the galaxy mass range $10^7 \leq M_\star \leq 10^{10} M_\odot$, where NSCs are most common. This suggests a possible metallicity increase in the stellar populations. This colour offset remains consistent regardless of environment density.

- Nucleated galaxies are rounder and more concentrated, on average, compared to galaxies without NSCs. However, none of these differences show any variation with environment density.

These results indicate that environment density regulates the presence of NSCs without preferentially driving a particular formation mechanism, which would impart an environmental dependence on the properties of NSCs and/or their hosts. This indicates that the environment may be most crucial only in the initial creation of an NSC. Alternatively, the formation avenues of NSCs may be influenced equally by the environment so that no single process is preferred in a particular environment. For example, increased environmental density is correlated with a higher number of GCs

around a galaxy (Peng et al., 2008), aiding the GC infall formation scenario. High density environments are also responsible for increased interaction rates and dense IGM, both of which can add or trap gas in the centres of galaxies, boosting the *in situ* formation scenario (Babul & Rees, 1992; Mihos & Hernquist, 1994).

Given the strong link between NSCs and GCs, it is imperative that future work compares the distribution of these two types of compact stellar systems throughout Virgo. The NGVS includes detections of tens of thousands of GCs throughout the cluster, and a catalogue of photometry for robust GC detections is forthcoming (E. W. Peng et al., in preparation). With this catalogue, it will be possible to study the properties of GC systems associated with even the faintest galaxies in Virgo, shedding light on how GCs contribute to the formation and growth of NSCs across a range of environments and galaxy masses.

Additionally, while this work has taken the first steps into exploring the relationship between the environment and properties of nucleated and non-nucleated galaxies, a more thorough investigation into the role of morphology is required. Currently, a visual classification of all NGVS galaxies is incomplete. But, given the relationship between galaxy morphology and environment, as well as previous results indicating variation in NSC-galaxy scaling relations with morphology and other structural properties (e.g., Seth et al., 2008; den Brok et al., 2014; Georgiev et al., 2016) a rigorous investigation of these trends within NGVS will be most valuable.

Chapter 5

Thesis summary and future steps

In this thesis, I have used broadband UV, optical, and near-IR photometry from the ACSVCS, Virgo Redux and NGVS programmes to explore the photometric and structural properties of NSCs and their host galaxies. These properties are valuable for constraining the masses, ages, and chemical compositions of these objects, particularly for those with complete UV, optical and IR coverage and spaced-based observations with sufficient resolution to resolve the NSCs. The unprecedented sensitivity and spatial coverage of the NGVS has permitted a novel investigation into the relationships among NSCs, their host galaxies, and the surrounding environment, and the implications of these relationships for galaxy evolution.

Most of our knowledge of the stellar populations of NSCs comes from limited samples of spectroscopic observations (Seth et al., 2006; Paudel et al., 2011; Guérou et al., 2015) and studies that focus on late-type galaxies where the low central surface brightness of the host galaxy makes it easier to extract the NSC light (Rossa et al., 2006; Walcher et al., 2006; Carson et al., 2015). The populations of NSCs in early-type galaxies must typically be estimated from limited colours or optical wavelength coverage (e.g., Lotz et al., 2004; Butler & Martínez-Delgado, 2005; Côté et al., 2006), so they can be highly uncertain and prone to age-metallicity degeneracies. Expanding our knowledge of these stellar populations requires broad wavelength coverage for a large, statistically meaningful sample of NSCs — ideally those within early-type galaxies. Chapter 2 addresses this missing sample, providing mass, age and metallicity estimates for 39 NSCs and their early-type hosts using multi-band imaging spanning UV, optical and near-IR wavelengths. The results present a complex picture for NSC formation — the revised mass scaling relation, with roughly a factor of two improvement in mass uncertainties, cannot be replicated in all mass regimes by any single

formation scenario. This reaffirms the idea that NSCs are formed by a stochastic mix of processes. However, NSCs may have different predominant formation mechanisms at different masses. The high resolution imaging in this analysis enabled estimates of NSC structural parameters, revealing that NSCs in brighter galaxies are preferentially flatter in shape. This is consistent with predictions from dissipative formation scenarios, suggesting that these brightest NSCs may form predominantly *in situ* via gas infall. These NSCs are also the oldest and most metal-rich, implying that while they contain an old stellar population (possibly from infalling GCs), they must have experienced substantial metal enrichment from either infalling gas or repeated episodes of star formation. The ages and metallicities from this analysis are more uncertain than the masses, but a comparison with spectroscopically-derived parameters confirms that metallicities, at least, can be reliably measured from broadband photometry with sufficiently broad wavelength coverage. This is encouraging for expanding the sample of NSC population estimates because it indicates that expensive spectroscopic observations are not necessarily essential for meaningful estimates of NSC population properties. These metallicities, when compared to those measured for UCDs, show that at least a subset of the UCD population has metallicities similar to those of NSCs — supporting the idea that tidally stripped nucleated galaxies are the progenitors of these UCDs.

The analysis of Chapter 2 was restricted to NSCs from a particular galaxy morphology, and without consideration for the surrounding environment of the galaxies. Both of these factors could potentially have at least a secondary effect on the formation and growth of NSCs. Containing a diverse range of both late- and early-type galaxies within an area covering the Virgo Cluster out to its virial radius, the NGVS is an ideal dataset to explore the influence of these parameters. Additionally, the characterization of the complex substructure in Virgo can be used to evaluate the success of the ΛCDM model on galaxy cluster-sized spatial scales. However, first the substructures must be identified in an objective, self-consistent way — there is no single established technique from past literature studies, and heterogeneous classifications of substructures may account for some of the potential discrepancy between ΛCDM prediction and observed galaxy clusters (Jauzac et al., 2016; Schwinn et al., 2017, 2018). Chapter 3 introduces a novel algorithm to identify the substructures in Virgo. The performance of this algorithm is tested by applying it to simulated clusters in which the true galaxy distributions are known. The algorithm performs well, recovering virtually all previously-identified substructures in Virgo even when

limited to projected sky coordinates for the initial substructure identification. It also extracts a handful of brand new substructure candidates; velocities and SBF distances for some of these candidates suggest that they are *bona fide* substructures still in the process of incorporating into the Virgo Cluster halo. The tentatively different amounts of substructure in Virgo and simulated clusters suggests that the ΛCDM cosmology may need to be modified; however, it is also plausible that the Virgo Cluster has an anomalous amount of substructure, so an expanded investigation with a larger, representative sample of observed galaxy clusters is essential for a proper test of cosmological paradigms.

With a set of verified substructures detected with the NGVS, it is possible to revisit the outstanding questions from Chapter 2, but now with the ability to explore how NSC properties and scaling relations change throughout the different environments of the Virgo Cluster. Recent results from R. Sánchez-Janssen et al. (2018, submitted) suggested that total halo mass drives the observed variation in NSC occupation fraction among different galaxy clusters and the Local Group. However, this conclusion was based on observations covering only the innermost core regions of the targeted galaxy clusters, which are fairly similar environments in terms of mass density. The analysis in Chapter 4 explores NSC colours, masses, and scaling relations throughout environments spanning a factor of 100 in density, providing a much improved measure of the role of environment. These result clearly indicate that NSCs are more common in higher density environments, but, interestingly, their stellar populations and the properties of their hosts are largely unaffected by changes in environmental density.

The relationships between NSCs and other compact stellar systems (GCs and UCDs) has largely been overlooked in this work, despite their similarities in sizes and colours, and the theorized connections among their methods of formation (see §1.3). The NGVS permits an immediate investigation into how GCs and UCDs compare to NSCs in terms of their stellar populations (based on optical colours) and distributions throughout Virgo. If these systems have similar stellar populations, or match each others' distributions throughout the cluster, that can provide new evidence for the evolutionary connections among these objects. Another pressing goal for this research should be to produce morphological classifications for all Virgo galaxies to look for a morphological dependence on NSC properties in addition to the environmental dependence presented in Chapter 4. Thinking more broadly, the analysis techniques in this thesis can be applied to datasets for other galaxy clusters like Fornax and Coma, which have been or are being surveyed in observing programmes with sensitivities

and coverage comparable to the NGVS (den Brok et al., 2014; Eigenthaler et al., 2018; Ordenes-Briceño et al., 2018a). This is especially valuable for the validation of ΛCDM substructure, which requires a larger sample of observed clusters for a meaningful statistical analysis.

There are also a few additional observations that can be valuable for many of the outstanding questions in the study of NSCs and their environments. One of the most straightforward proposals is a survey of (nucleated) Virgo galaxies with high resolution IR imaging. This will broaden the wavelength coverage for galaxies within the NGVS[1], enabling more robust determinations of stellar population properties comparable to those estimated in Chapter 2. Sufficiently high resolution to resolve the NSCs is crucial for the best separation of the NSC and galaxy light and to expand the study of NSC structural parameters, which can further constrain formation mechanisms. This high resolution imaging is also valuable for dynamical mass estimates, which have not been addressed in this thesis. Images of resolved NSCs at IR wavelengths, where the starlight is least obscured by dust, are most useful for mapping the stellar mass distribution of the NSCs. By combining these IR images with kinematics from long-slit or integral field spectroscopy, it becomes possible to search for any black holes that may co-exist with the NSCs. The upcoming James Webb Space Telescope, with its IR sensitivity and exquisite resolution provided by space-based observations, would be an ideal choice for these IR observations.

IR imaging can leverage the existing data to determine stellar populations for a larger sample of NSCs, but acquiring spectroscopy has many appeals as well. Spectra with high spatial and spectral resolution across optical and IR wavelengths will provide the most detailed estimates of NSC stellar populations via measuring the abundances of specific elements, while simultaneously acquiring the kinematics of NSCs and their hosts. With kinematics of the galaxies, it becomes possible to quantify the behaviour of the $M - \sigma$ relation in relatively unexplored low-mass regimes. Finally, spectroscopic observations, even those with low spatial or spectral resolution, can be used to build up the catalogue of recessional velocities of Virgo galaxies. Although there are presently over 800 velocities measured for NGVS galaxies, very few measurements exist for galaxies fainter than $M_V \sim -15$ mag, which are the most abundant systems in Virgo. With a more complete velocity catalogue, the 3D structure of Virgo can be explored in greater detail, building upon the analysis of Chapter 3

[1]Many NGVS targets, unfortunately, do not currently have IR imaging from Virgo Redux or NGVS-IR.

and providing more robust confirmations of current substructure candidates. IFUs on 8-meter class telescopes, such as GMOS on Gemini or MUSE on VLT, are best suited for probing these faint galaxies because light from the entire field of view (rather than within a narrow slit or fiber as in traditional spectrographs) can be stacked into a single spectrum, maximizing the signal.

The current deep, wide-field observations have already produced exciting developments in the study of NSCs and and their connections to other compact stellar systems. Never before have such expansive, detailed samples existed for such observationally challenging targets. With the advent of the next generation of observatories and instruments, even more discoveries are guaranteed to be on the horizon. Who knows what we will find?

Bibliography

Abolfathi, B., Aguado, D. S., Aguilar, G., Allende Prieto, C., Almeida, A., Ananna, T. T., Anders, F., Anderson, S. F., Andrews, B. H., Anguiano, B., and et al. 2018, Astrophysical Journal, Supplement Series, 235, 42

Allington-Smith, J., Murray, G., Content, R., Dodsworth, G., Davies, R., Miller, B. W., Jorgensen, I., Hook, I., Crampton, D., and Murowinski, R. 2002, Publications of the ASP, 114, 892

Anders, P., Bissantz, N., Fritze-v. Alvensleben, U., and de Grijs, R. 2004, Monthly Notices of the RAS, 347, 196

Ankerst, M., Breunig, M. M., Kriegel, H.-P., and Sander, J. 1999, in in Proceedings of the 1999 ACM SIGMOD International Conference on Management of Data, SIGMOD '99 (New York, NY, USA: ACM), 49–60

Antonini, F., Barausse, E., and Silk, J. 2015, Astrophysical Journal, 812, 72

Antonini, F., Capuzzo-Dolcetta, R., Mastrobuono-Battisti, A., and Merritt, D. 2012, Astrophysical Journal, 750, 111

Babul, A. and Rees, M. J. 1992, Monthly Notices of the RAS, 255, 346

Balcells, M., Graham, A. W., and Peletier, R. F. 2007, Astrophysical Journal, 665, 1084

Barlow, T. A. and Sargent, W. L. W. 1997, Astronomical Journal, 113, 136

Becklin, E. E. and Neugebauer, G. 1968, Astrophysical Journal, 151, 145

Bekki, K. 2007, PASA, 24, 77

— 2015, Astrophysical Journal, Letters to the Editor, 812, L14

Bell, E. F., McIntosh, D. H., Katz, N., and Weinberg, M. D. 2003, Astrophysical Journal, Supplement Series, 149, 289

Bertin, E. 2011, in Astronomical Society of the Pacific Conference Series, Vol. 442, Astronomical Data Analysis Software and Systems XX, ed. I. N. Evans, A. Accomazzi, D. J. Mink, & A. H. Rots, 435

Binggeli, B. and Popescu, C. C. 1995, Astronomy and Astrophysics, 298, 63

Binggeli, B., Popescu, C. C., and Tammann, G. A. 1993, Astronomy and Astrophysics, Supplement Series, 98, 275

Binggeli, B., Sandage, A., and Tammann, G. A. 1985, Astronomical Journal, 90, 1681

Binggeli, B., Tammann, G. A., and Sandage, A. 1987, Astronomical Journal, 94, 251

Bird, C. M. 1994, Astronomical Journal, 107, 1637

Blakeslee, J. P., Ajhar, E. A., and Tonry, J. L. 1999, in Astrophysics and Space Science Library, Vol. 237, Post-Hipparcos Cosmic Candles, ed. A. Heck & F. Caputo, 181

Blakeslee, J. P., Jordán, A., Mei, S., Côté, P., Ferrarese, L., Infante, L., Peng, E. W., Tonry, J. L., and West, M. J. 2009, Astrophysical Journal, 694, 556

Böhringer, H., Briel, U. G., Schwarz, R. A., Voges, W., Hartner, G., and Trümper, J. 1994, Nature, 368, 828

Böker, T., Laine, S., van der Marel, R. P., Sarzi, M., Rix, H.-W., Ho, L. C., and Shields, J. C. 2002, Astronomical Journal, 123, 1389

Böker, T., Sarzi, M., McLaughlin, D. E., van der Marel, R. P., Rix, H.-W., Ho, L. C., and Shields, J. C. 2004, Astronomical Journal, 127, 105

Boselli, A., Voyer, E., Boissier, S., Cucciati, O., Consolandi, G., Cortese, L., Fumagalli, M., Gavazzi, G., Heinis, S., Roehlly, Y., and Toloba, E. 2014, Astronomy and Astrophysics, 570, A69

Boulade, O., Charlot, X., Abbon, P., Aune, S., Borgeaud, P., Carton, P.-H., Carty, M., Da Costa, J., Deschamps, H., Desforge, D., Eppellé, D., Gallais, P., Gosset, L., Granelli, R., Gros, M., de Kat, J., Loiseau, D., Ritou, J.-., Roussé, J. Y., Starzynski, P., Vignal, N., and Vigroux, L. G. 2003, in Proc. SPIE, Vol. 4841, Instrument

Design and Performance for Optical/Infrared Ground-based Telescopes, ed. M. Iye & A. F. M. Moorwood, 72–81

Bourne, M. A. and Power, C. 2016, Monthly Notices of the RAS, 456, L20

Boylan-Kolchin, M., Bullock, J. S., and Kaplinghat, M. 2011, Monthly Notices of the RAS, 415, L40

Bruzual, G. and Charlot, S. 2003, Monthly Notices of the RAS, 344, 1000

Bullock, J. S. 2010, ArXiv e-prints

Butler, D. J. and Martínez-Delgado, D. 2005, Astronomical Journal, 129, 2217

Calzetti, D., Armus, L., Bohlin, R. C., Kinney, A. L., Koornneef, J., and Storchi-Bergmann, T. 2000, Astrophysical Journal, 533, 682

Cantiello, M., Blakeslee, J. P., Ferrarese, L., Côté, P., Roediger, J. C., Raimondo, G., Peng, E. W., Gwyn, S., Durrell, P. R., and Cuillandre, J.-C. 2018, Astrophysical Journal, 856, 126

Caon, N., Capaccioli, M., and D'Onofrio, M. 1993, Monthly Notices of the RAS, 265, 1013

Cappellari, M., McDermid, R. M., Alatalo, K., Blitz, L., Bois, M., Bournaud, F., Bureau, M., Crocker, A. F., Davies, R. L., Davis, T. A., de Zeeuw, P. T., Duc, P.-A., Emsellem, E., Khochfar, S., Krajnović, D., Kuntschner, H., Lablanche, P.-Y., Morganti, R., Naab, T., Oosterloo, T., Sarzi, M., Scott, N., Serra, P., Weijmans, A.-M., and Young, L. M. 2012, Nature, 484, 485

Capuzzo-Dolcetta, R. and Miocchi, P. 2008, Monthly Notices of the RAS, 388, L69

Carollo, C. M., Stiavelli, M., de Zeeuw, P. T., and Mack, J. 1997, Astronomical Journal, 114, 2366

Carollo, C. M., Stiavelli, M., and Mack, J. 1998, Astronomical Journal, 116, 68

Carollo, C. M., Stiavelli, M., Seigar, M., de Zeeuw, P. T., and Dejonghe, H. 2002, Astronomical Journal, 123, 159

Carson, D. J., Barth, A. J., Seth, A. C., den Brok, M., Cappellari, M., Greene, J. E., Ho, L. C., and Neumayer, N. 2015, Astronomical Journal, 149, 170

Chen, Y.-T., Kavelaars, J. J., Gwyn, S., Ferrarese, L., Côté, P., Jordán, A., Suc, V., Cuillandre, J.-C., and Ip, W.-H. 2013, Astrophysical Journal, Letters to the Editor, 775, L8

Chilingarian, I. V. 2009, Monthly Notices of the RAS, 394, 1229

Chilingarian, I. V., Sil'Chenko, O. K., Afanasiev, V. L., and Prugniel, P. 2007, Astronomy Letters, 33, 292

Cleveland, W. S. 1979, Journal of the American Statistical Association, 74, 829

Cole, D. R., Debattista, V. P., Varri, A. L., Hartmann, M., and Seth, A. C. 2016, ArXiv e-prints

Conroy, C. and Gunn, J. E. 2010, Astrophysical Journal, 712, 833

Côté, P., Blakeslee, J. P., Ferrarese, L., Jordán, A., Mei, S., Merritt, D., Milosavljević, M., Peng, E. W., Tonry, J. L., and West, M. J. 2004, Astrophysical Journal, Supplement Series, 153, 223

Côté, P., Piatek, S., Ferrarese, L., Jordán, A., Merritt, D., Peng, E. W., Haşegan, M., Blakeslee, J. P., Mei, S., West, M. J., Milosavljević, M., and Tonry, J. L. 2006, Astrophysical Journal, Supplement Series, 165, 57

Cox, T. J., Dutta, S. N., Di Matteo, T., Hernquist, L., Hopkins, P. F., Robertson, B., and Springel, V. 2006, Astrophysical Journal, 650, 791

Crockett, R. M., Kaviraj, S., Silk, J. I., Whitmore, B. C., O'Connell, R. W., Mutchler, M., Balick, B., Bond, H. E., Calzetti, D., Carollo, C. M., Disney, M. J., Dopita, M. A., Frogel, J. A., Hall, D. N. B., Holtzman, J. A., Kimble, R. A., McCarthy, P. J., Paresce, F., Saha, A., Trauger, J. T., Walker, A. R., Windhorst, R. A., Young, E. T., Jeong, H., and Yi, S. K. 2011, Astrophysical Journal, 727, 115

Davis, M., Efstathiou, G., Frenk, C. S., and White, S. D. M. 1985, Astrophysical Journal, 292, 371

De Looze, I., Baes, M., Zibetti, S., Fritz, J., Cortese, L., Davies, J. I., Verstappen, J., Bendo, G. J., Bianchi, S., Clemens, M., Bomans, D. J., Boselli, A., Corbelli, E., Dariush, A., di Serego Alighieri, S., Fadda, D., Garcia-Appadoo, D. A., Gavazzi, G., Giovanardi, C., Grossi, M., Hughes, T. M., Hunt, L. K., Jones, A. P., Madden, S.,

Pierini, D., Pohlen, M., Sabatini, S., Smith, M. W. L., Vlahakis, C., and Xilouris, E. M. 2010, Astronomy and Astrophysics, 518, L54

de Meulenaer, P., Narbutis, D., Mineikis, T., and Vansevičius, V. 2014, Astronomy and Astrophysics, 569, A4

de Vaucouleurs, G. 1959, Handbuch der Physik, 53, 275

— 1961, Astrophysical Journal, Supplement Series, 6, 213

de Vaucouleurs, G. and Corwin, Jr., H. G. 1986, Astronomical Journal, 92, 722

den Brok, M., Peletier, R. F., Seth, A., Balcells, M., Dominguez, L., Graham, A. W., Carter, D., Erwin, P., Ferguson, H. C., Goudfrooij, P., Guzmán, R., Hoyos, C., Jogee, S., Lucey, J., Phillipps, S., Puzia, T., Valentijn, E., Kleijn, G. V., and Weinzirl, T. 2014, Monthly Notices of the RAS, 445, 2385

di Serego Alighieri, S., Bianchi, S., Pappalardo, C., Zibetti, S., Auld, R., Baes, M., Bendo, G., Corbelli, E., Davies, J. I., Davis, T., De Looze, I., Fritz, J., Gavazzi, G., Giovanardi, C., Grossi, M., Hunt, L. K., Magrini, L., Pierini, D., and Xilouris, E. M. 2013, Astronomy and Astrophysics, 552, A8

Doi, M., Tanaka, M., Fukugita, M., Gunn, J. E., Yasuda, N., Ivezić, Ž., Brinkmann, J., de Haars, E., Kleinman, S. J., Krzesinski, J., and French Leger, R. 2010, Astronomical Journal, 139, 1628

Dressler, A. 1980, Astrophysical Journal, 236, 351

Dressler, A. and Shectman, S. A. 1988, Astronomical Journal, 95, 985

Drinkwater, M. J., Gregg, M. D., Hilker, M., Bekki, K., Couch, W. J., Ferguson, H. C., Jones, J. B., and Phillipps, S. 2003, Nature, 423, 519

Durrell, P. R., Côté, P., Peng, E. W., Blakeslee, J. P., Ferrarese, L., Mihos, J. C., Puzia, T. H., Lançon, A., Liu, C., Zhang, H., Cuillandre, J.-C., McConnachie, A., Jordán, A., Accetta, K., Boissier, S., Boselli, A., Courteau, S., Duc, P.-A., Emsellem, E., Gwyn, S., Mei, S., and Taylor, J. E. 2014, Astrophysical Journal, 794, 103

Eigenthaler, P., Puzia, T. H., Taylor, M. A., Ordenes-Briceño, Y., Muñoz, R. P., Ribbeck, K. X., Alamo-Martínez, K. A., Zhang, H., Ángel, S., Capaccioli, M., Côté, P., Ferrarese, L., Galaz, G., Grebel, E. K., Hempel, M., Hilker, M., Lançon, A., Mieske, S., Miller, B., Paolillo, M., Powalka, M., Richtler, T., Roediger, J., Rong, Y., Sánchez-Janssen, R., and Spengler, C. 2018, Astrophysical Journal, 855, 142

Eisenstein, D. J., Weinberg, D. H., Agol, E., Aihara, H., Allende Prieto, C., Anderson, S. F., Arns, J. A., Aubourg, É., Bailey, S., Balbinot, E., and et al. 2011, Astronomical Journal, 142, 72

Faber, S. M., Phillips, A. C., Kibrick, R. I., Alcott, B., Allen, S. L., Burrous, J., Cantrall, T., Clarke, D., Coil, A. L., Cowley, D. J., Davis, M., Deich, W. T. S., Dietsch, K., Gilmore, D. K., Harper, C. A., Hilyard, D. F., Lewis, J. P., McVeigh, M., Newman, J., Osborne, J., Schiavon, R., Stover, R. J., Tucker, D., Wallace, V., Wei, M., Wirth, G., and Wright, C. A. 2003, Instrument Design and Performance for Optical/Infrared Ground-based Telescopes. Proceedings of the SPIE, 4841, 1657

Fan, X., Narayanan, V. K., Lupton, R. H., Strauss, M. A., Knapp, G. R., Becker, R. H., White, R. L., Pentericci, L., Leggett, S. K., Haiman, Z., Gunn, J. E., Ivezić, Ž., Schneider, D. P., Anderson, S. F., Brinkmann, J., Bahcall, N. A., Connolly, A. J., Csabai, I., Doi, M., Fukugita, M., Geballe, T., Grebel, E. K., Harbeck, D., Hennessy, G., Lamb, D. Q., Miknaitis, G., Munn, J. A., Nichol, R., Okamura, S., Pier, J. R., Prada, F., Richards, G. T., Szalay, A., and York, D. G. 2001, Astronomical Journal, 122, 2833

Fan, Z. and de Grijs, R. 2012, Monthly Notices of the RAS, 424, 2009

— 2014, Astrophysical Journal, Supplement Series, 211, 22

Ferguson, H. C. and Sandage, A. 1989, Astrophysical Journal, Letters to the Editor, 346, L53

Ferrarese, L., Côté, P., Cuillandre, J.-C., Gwyn, S. D. J., Peng, E. W., MacArthur, L. A., Duc, P.-A., Boselli, A., Mei, S., Erben, T., McConnachie, A. W., Durrell, P. R., Mihos, J. C., Jordán, A., Lançon, A., Puzia, T. H., Emsellem, E., Balogh, M. L., Blakeslee, J. P., van Waerbeke, L., Gavazzi, R., Vollmer, B., Kavelaars, J. J., Woods, D., Ball, N. M., Boissier, S., Courteau, S., Ferriere, E., Gavazzi,

G., Hildebrandt, H., Hudelot, P., Huertas-Company, M., Liu, C., McLaughlin, D., Mellier, Y., Milkeraitis, M., Schade, D., Balkowski, C., Bournaud, F., Carlberg, R. G., Chapman, S. C., Hoekstra, H., Peng, C., Sawicki, M., Simard, L., Taylor, J. E., Tully, R. B., van Driel, W., Wilson, C. D., Burdullis, T., Mahoney, B., and Manset, N. 2012, Astrophysical Journal, Supplement Series, 200, 4

Ferrarese, L., Côté, P., Dalla Bontà, E., Peng, E. W., Merritt, D., Jordán, A., Blakeslee, J. P., Haşegan, M., Mei, S., Piatek, S., Tonry, J. L., and West, M. J. 2006a, Astrophysical Journal, Letters to the Editor, 644, L21

Ferrarese, L., Côté, P., Jordán, A., Peng, E. W., Blakeslee, J. P., Piatek, S., Mei, S., Merritt, D., Milosavljević, M., Tonry, J. L., and West, M. J. 2006b, Astrophysical Journal, Supplement Series, 164, 334

Ferrarese, L. and Merritt, D. 2000, Astrophysical Journal, Letters to the Editor, 539, L9

Ferreras, I., Charlot, S., and Silk, J. 1999, Astrophysical Journal, 521, 81

Fioc, M. and Rocca-Volmerange, B. 1997, Astronomy and Astrophysics, 326, 950

— 1999, ArXiv Astrophysics e-prints

Ford, H. C., Bartko, F., Bely, P. Y., Broadhurst, T., Burrows, C. J., Cheng, E. S., Clampin, M., Crocker, J. H., Feldman, P. D., Golimowski, D. A., Hartig, G. F., Illingworth, G., Kimble, R. A., Lesser, M. P., Miley, G., Neff, S. G., Postman, M., Sparks, W. B., Tsvetanov, Z., White, R. L., Sullivan, P., Krebs, C. A., Leviton, D. B., La Jeunesse, T., Burmester, W., Fike, S., Johnson, R., Slusher, R. B., Volmer, P., and Woodruff, R. A. 1998, in Proc. SPIE, Vol. 3356, Space Telescopes and Instruments V, ed. P. Y. Bely & J. B. Breckinridge, 234–248

Foreman-Mackey, D., Hogg, D. W., Lang, D., and Goodman, J. 2013, Publications of the ASP, 125, 306

Ftaclas, C., Fanelli, M. N., and Struble, M. F. 1984, Astrophysical Journal, 282, 19

Gallo, E., Treu, T., Marshall, P. J., Woo, J.-H., Leipski, C., and Antonucci, R. 2010, Astrophysical Journal, 714, 25

Gavazzi, G., Boselli, A., Scodeggio, M., Pierini, D., and Belsole, E. 1999, Monthly Notices of the RAS, 304, 595

Gebhardt, K., Bender, R., Bower, G., Dressler, A., Faber, S. M., Filippenko, A. V., Green, R., Grillmair, C., Ho, L. C., Kormendy, J., Lauer, T. R., Magorrian, J., Pinkney, J., Richstone, D., and Tremaine, S. 2000, Astrophysical Journal, Letters to the Editor, 539, L13

Geha, M., Guhathakurta, P., and van der Marel, R. P. 2002, Astronomical Journal, 124, 3073

Genel, S., Vogelsberger, M., Springel, V., Sijacki, D., Nelson, D., Snyder, G., Rodriguez-Gomez, V., Torrey, P., and Hernquist, L. 2014, Monthly Notices of the RAS, 445, 175

Georgiev, I. Y. and Böker, T. 2014, Monthly Notices of the RAS, 441, 3570

Georgiev, I. Y., Böker, T., Leigh, N., Lützgendorf, N., and Neumayer, N. 2016, Monthly Notices of the RAS, 457, 2122

Georgiev, I. Y., Goudfrooij, P., and Puzia, T. H. 2012, Monthly Notices of the RAS, 420, 1317

Ghez, A. M., Salim, S., Weinberg, N. N., Lu, J. R., Do, T., Dunn, J. K., Matthews, K., Morris, M. R., Yelda, S., Becklin, E. E., Kremenek, T., Milosavljevic, M., and Naiman, J. 2008, Astrophysical Journal, 689, 1044

Glass, L., Ferrarese, L., Côté, P., Jordán, A., Peng, E., Blakeslee, J. P., Chen, C.-W., Infante, L., Mei, S., Tonry, J. L., and West, M. J. 2011, Astrophysical Journal, 726, 31

Gnedin, O. Y., Ostriker, J. P., and Tremaine, S. 2014, Astrophysical Journal, 785, 71

Goerdt, T., Moore, B., Kazantzidis, S., Kaufmann, T., Macciò, A. V., and Stadel, J. 2008, Monthly Notices of the RAS, 385, 2136

Goudfrooij, P. and Kruijssen, J. M. D. 2014, Astrophysical Journal, 780, 43

Graham, A. W. 2012, Monthly Notices of the RAS, 422, 1586

Graham, A. W. and Driver, S. P. 2005, PASA, 22, 118

Grant, N. I., Kuipers, J. A., and Phillipps, S. 2005, Monthly Notices of the RAS, 363, 1019

Graves, G. J. and Schiavon, R. P. 2008, Astrophysical Journal, Supplement Series, 177, 446

Greene, J. E. 2012, Nature Communications, 3, 1304

Guérou, A., Emsellem, E., McDermid, R. M., Côté, P., Ferrarese, L., Blakeslee, J. P., Durrell, P. R., MacArthur, L. A., Peng, E. W., Cuillandre, J.-C., and Gwyn, S. 2015, Astrophysical Journal, 804, 70

Guillard, N., Emsellem, E., and Renaud, F. 2016, Monthly Notices of the RAS, 461, 3620

Gunn, J. E., Carr, M., Rockosi, C., Sekiguchi, M., Berry, K., Elms, B., de Haas, E., Ivezić, Ž., Knapp, G., Lupton, R., Pauls, G., Simcoe, R., Hirsch, R., Sanford, D., Wang, S., York, D., Harris, F., Annis, J., Bartozek, L., Boroski, W., Bakken, J., Haldeman, M., Kent, S., Holm, S., Holmgren, D., Petravick, D., Prosapio, A., Rechenmacher, R., Doi, M., Fukugita, M., Shimasaku, K., Okada, N., Hull, C., Siegmund, W., Mannery, E., Blouke, M., Heidtman, D., Schneider, D., Lucinio, R., and Brinkman, J. 1998, Astronomical Journal, 116, 3040

Gunn, J. E., Siegmund, W. A., Mannery, E. J., Owen, R. E., Hull, C. L., Leger, R. F., Carey, L. N., Knapp, G. R., York, D. G., Boroski, W. N., Kent, S. M., Lupton, R. H., Rockosi, C. M., Evans, M. L., Waddell, P., Anderson, J. E., Annis, J., Barentine, J. C., Bartoszek, L. M., Bastian, S., Bracker, S. B., Brewington, H. J., Briegel, C. I., Brinkmann, J., Brown, Y. J., Carr, M. A., Czarapata, P. C., Drennan, C. C., Dombeck, T., Federwitz, G. R., Gillespie, B. A., Gonzales, C., Hansen, S. U., Harvanek, M., Hayes, J., Jordan, W., Kinney, E., Klaene, M., Kleinman, S. J., Kron, R. G., Kresinski, J., Lee, G., Limmongkol, S., Lindenmeyer, C. W., Long, D. C., Loomis, C. L., McGehee, P. M., Mantsch, P. M., Neilsen, Jr., E. H., Neswold, R. M., Newman, P. R., Nitta, A., Peoples, Jr., J., Pier, J. R., Prieto, P. S., Prosapio, A., Rivetta, C., Schneider, D. P., Snedden, S., and Wang, S.-i. 2006, Astronomical Journal, 131, 2332

Gwyn, S. D. J. 2008, Publications of the ASP, 120, 212

Hartmann, M., Debattista, V. P., Seth, A., Cappellari, M., and Quinn, T. R. 2011, Monthly Notices of the RAS, 418, 2697

Häussler, B., McIntosh, D. H., Barden, M., Bell, E. F., Rix, H.-W., Borch, A., Beckwith, S. V. W., Caldwell, J. A. R., Heymans, C., Jahnke, K., Jogee, S., Koposov, S. E., Meisenheimer, K., Sánchez, S. F., Somerville, R. S., Wisotzki, L., and Wolf, C. 2007, Astrophysical Journal, Supplement Series, 172, 615

Hempel, M., Hilker, M., Kissler-Patig, M., Puzia, T. H., Minniti, D., and Goudfrooij, P. 2003, Astronomy and Astrophysics, 405, 487

Hook, I. M., Jørgensen, I., Allington-Smith, J. R., Davies, R. L., Metcalfe, N., Murowinski, R. G., and Crampton, D. 2004, Publications of the ASP, 116, 425

Hubble, E. 1926, Contributions from the Mount Wilson Observatory / Carnegie Institution of Washington, 324, 1

Hubble, E. and Humason, M. L. 1931, Astrophysical Journal, 74, 43

Ichikawa, S.-I. 1989, Astronomical Journal, 97, 1600

Impey, C., Bothun, G., and Malin, D. 1988, Astrophysical Journal, 330, 634

Janz, J., Laurikainen, E., Lisker, T., Salo, H., Peletier, R. F., Niemi, S.-M., den Brok, M., Toloba, E., Falcón-Barroso, J., Boselli, A., and Hensler, G. 2012, Astrophysical Journal, Letters to the Editor, 745, L24

Janz, J. and Lisker, T. 2008, Astrophysical Journal, Letters to the Editor, 689, L25

— 2009, Astrophysical Journal, Letters to the Editor, 696, L102

Janz, J., Norris, M. A., Forbes, D. A., Huxor, A., Romanowsky, A. J., Frank, M. J., Escudero, C. G., Faifer, F. R., Forte, J. C., Kannappan, S. J., Maraston, C., Brodie, J. P., Strader, J., and Thompson, B. R. 2016, Monthly Notices of the RAS, 456, 617

Jauzac, M., Eckert, D., Schwinn, J., Harvey, D., Baugh, C. M., Robertson, A., Bose, S., Massey, R., Owers, M., Ebeling, H., Shan, H. Y., Jullo, E., Kneib, J.-P., Richard, J., Atek, H., Clément, B., Egami, E., Israel, H., Knowles, K., Limousin, M., Natarajan, P., Rexroth, M., Taylor, P., and Tchernin, C. 2016, Monthly Notices of the RAS, 463, 3876

Jedrzejewski, R. I. 1987, Monthly Notices of the RAS, 226, 747

Jordán, A., Blakeslee, J. P., Peng, E. W., Mei, S., Côté, P., Ferrarese, L., Tonry, J. L., Merritt, D., Milosavljević, M., and West, M. J. 2004a, Astrophysical Journal, Supplement Series, 154, 509

Jordán, A., Côté, P., West, M. J., Marzke, R. O., Minniti, D., and Rejkuba, M. 2004b, Astronomical Journal, 127, 24

Kannappan, S. J. and Gawiser, E. 2007, Astrophysical Journal, Letters to the Editor, 657, L5

Karachentsev, I. D. and Nasonova, O. G. 2010, Monthly Notices of the RAS, 405, 1075

Karachentsev, I. D., Tully, R. B., Wu, P.-F., Shaya, E. J., and Dolphin, A. E. 2014, Astrophysical Journal, 782, 4

Kaviraj, S., Crockett, R. M., Whitmore, B. C., Silk, J., O'Connell, R. W., Windhorst, R. A., Mutchler, M., Rejkuba, M., Yi, S., Frogel, J. A., and Calzetti, D. 2012, Monthly Notices of the RAS, 422, L96

Kaviraj, S., Rey, S.-C., Rich, R. M., Yoon, S.-J., and Yi, S. K. 2007a, Monthly Notices of the RAS, 381, L74

Kaviraj, S., Schawinski, K., Devriendt, J. E. G., Ferreras, I., Khochfar, S., Yoon, S.-J., Yi, S. K., Deharveng, J.-M., Boselli, A., Barlow, T., Conrow, T., Forster, K., Friedman, P. G., Martin, D. C., Morrissey, P., Neff, S., Schiminovich, D., Seibert, M., Small, T., Wyder, T., Bianchi, L., Donas, J., Heckman, T., Lee, Y.-W., Madore, B., Milliard, B., Rich, R. M., and Szalay, A. 2007b, Astrophysical Journal, Supplement Series, 173, 619

Kim, S., Rey, S.-C., Jerjen, H., Lisker, T., Sung, E.-C., Lee, Y., Chung, J., Pak, M., Yi, W., and Lee, W. 2014, Astrophysical Journal, Supplement Series, 215, 22

King, A. 2003, Astrophysical Journal, Letters to the Editor, 596, L27

King, I. R. 1966, Astronomical Journal, 71, 64

Klypin, A., Kravtsov, A. V., Valenzuela, O., and Prada, F. 1999, Astrophysical Journal, 522, 82

Kodama, T. and Arimoto, N. 1997, Astronomy and Astrophysics, 320, 41

Koleva, M., Prugniel, P., de Rijcke, S., and Zeilinger, W. W. 2011, Monthly Notices of the RAS, 417, 1643

Kormendy, J. and Richstone, D. 1995, Annual Review of Astronomy and Astrophysics, 33, 581

Kourkchi, E. and Tully, R. B. 2017, Astrophysical Journal, 843, 16

Kuntschner, H. 2004, Astronomy and Astrophysics, 426, 737

Lange, R., Moffett, A. J., Driver, S. P., Robotham, A. S. G., Lagos, C. d. P., Kelvin, L. S., Conselice, C., Margalef-Bentabol, B., Alpaslan, M., Baldry, I., Bland-Hawthorn, J., Bremer, M., Brough, S., Cluver, M., Colless, M., Davies, L. J. M., Häußler, B., Holwerda, B. W., Hopkins, A. M., Kafle, P. R., Kennedy, R., Liske, J., Phillipps, S., Popescu, C. C., Taylor, E. N., Tuffs, R., van Kampen, E., and Wright, A. H. 2016, Monthly Notices of the RAS, 462, 1470

Leigh, N., Böker, T., and Knigge, C. 2012, Monthly Notices of the RAS, 424, 2130

Li, A. and Draine, B. T. 2001, Astrophysical Journal, 554, 778

Li, Z., Han, Z., and Zhang, F. 2007, Astronomy and Astrophysics, 464, 853

Lisker, T., Grebel, E. K., Binggeli, B., and Glatt, K. 2007, Astrophysical Journal, 660, 1186

Lisker, T., Janz, J., Hensler, G., Kim, S., Rey, S.-C., Weinmann, S., Mastropietro, C., Hielscher, O., Paudel, S., and Kotulla, R. 2009, Astrophysical Journal, Letters to the Editor, 706, L124

Liu, C., Peng, E. W., Côté, P., Ferrarese, L., Jordán, A., Mihos, J. C., Zhang, H.-X., Muñoz, R. P., Puzia, T. H., Lançon, A., Gwyn, S., Cuillandre, J.-C., Blakeslee, J. P., Boselli, A., Durrell, P. R., Duc, P.-A., Guhathakurta, P., MacArthur, L. A., Mei, S., Sánchez-Janssen, R., and Xu, H. 2015, Astrophysical Journal, 812, 34

Liu, Y., Ho, L. C., and Peng, E. 2016, Astrophysical Journal, Letters to the Editor, 829, L26

Lotz, J. M., Miller, B. W., and Ferguson, H. C. 2004, Astrophysical Journal, 613, 262

Lotz, J. M., Telford, R., Ferguson, H. C., Miller, B. W., Stiavelli, M., and Mack, J. 2001, Astrophysical Journal, 552, 572

Ma, X., Hopkins, P. F., Faucher-Giguère, C.-A., Zolman, N., Muratov, A. L., Kereš, D., and Quataert, E. 2016, Monthly Notices of the RAS, 456, 16

Magorrian, J., Tremaine, S., Richstone, D., Bender, R., Bower, G., Dressler, A., Faber, S. M., Gebhardt, K., Green, R., Grillmair, C., Kormendy, J., and Lauer, T. 1998, Astronomical Journal, 115, 2285

Mahajan, S., Drinkwater, M. J., Driver, S., Kelvin, L. S., Hopkins, A. M., Baldry, I., Phillipps, S., Bland-Hawthorn, J., Brough, S., Loveday, J., Penny, S. J., and Robotham, A. S. G. 2015, Monthly Notices of the RAS, 446, 2967

Maraston, C. 2005, Monthly Notices of the RAS, 362, 799

McConnachie, A. W. 2012, Astronomical Journal, 144, 4

McConnell, N. J. and Ma, C.-P. 2013, Astrophysical Journal, 764, 184

McDermid, R. M., Alatalo, K., Blitz, L., Bournaud, F., Bureau, M., Cappellari, M., Crocker, A. F., Davies, R. L., Davis, T. A., de Zeeuw, P. T., Duc, P.-A., Emsellem, E., Khochfar, S., Krajnović, D., Kuntschner, H., Morganti, R., Naab, T., Oosterloo, T., Sarzi, M., Scott, N., Serra, P., Weijmans, A.-M., and Young, L. M. 2015, Monthly Notices of the RAS, 448, 3484

McLaughlin, D. E. 1999, Astrophysical Journal, Letters to the Editor, 512, L9

McLaughlin, D. E., King, A. R., and Nayakshin, S. 2006, Astrophysical Journal, Letters to the Editor, 650, L37

McQuillin, R. C. and McLaughlin, D. E. 2012, Monthly Notices of the RAS, 423, 2162

Mei, S., Blakeslee, J. P., Côté, P., Tonry, J. L., West, M. J., Ferrarese, L., Jordán, A., Peng, E. W., Anthony, A., and Merritt, D. 2007, Astrophysical Journal, 655, 144

Mendel, J. T., Simard, L., Palmer, M., Ellison, S. L., and Patton, D. R. 2014, Astrophysical Journal, Supplement Series, 210, 3

Mentz, J. J., La Barbera, F., Peletier, R. F., Falcón-Barroso, J., Lisker, T., van de Ven, G., Loubser, S. I., Hilker, M., Sánchez-Janssen, R., Napolitano, N., Cantiello, M., Capaccioli, M., Norris, M., Paolillo, M., Smith, R., Beasley, M. A., Lyubenova, M., Munoz, R., and Puzia, T. 2016, Monthly Notices of the RAS, 463, 2819

Mieske, S., Frank, M. J., Baumgardt, H., Lützgendorf, N., Neumayer, N., and Hilker, M. 2013, Astronomy and Astrophysics, 558, A14

Mieske, S., Hilker, M., Jordán, A., Infante, L., Kissler-Patig, M., Rejkuba, M., Richtler, T., Côté, P., Baumgardt, H., West, M. J., Ferrarese, L., and Peng, E. W. 2008, Astronomy and Astrophysics, 487, 921

Mihos, J. C. and Hernquist, L. 1994, Astrophysical Journal, Letters to the Editor, 437, L47

Milne, E. A. 1928, The Observatory, 51, 88

Milosavljević, M. 2004, Astrophysical Journal, Letters to the Editor, 605, L13

Misgeld, I. and Hilker, M. 2011, Monthly Notices of the RAS, 414, 3699

Muñoz, R. P., Eigenthaler, P., Puzia, T. H., Taylor, M. A., Ordenes-Briceño, Y., Alamo-Martínez, K., Ribbeck, K. X., Ángel, S., Capaccioli, M., Côté, P., Ferrarese, L., Galaz, G., Hempel, M., Hilker, M., Jordán, A., Lançon, A., Mieske, S., Paolillo, M., Richtler, T., Sánchez-Janssen, R., and Zhang, H. 2015, Astrophysical Journal, Letters to the Editor, 813, L15

Muñoz, R. P., Puzia, T. H., Lançon, A., Peng, E. W., Côté, P., Ferrarese, L., Blakeslee, J. P., Mei, S., Cuillandre, J.-C., Hudelot, P., Courteau, S., Duc, P.-A., Balogh, M. L., Boselli, A., Bournaud, F., Carlberg, R. G., Chapman, S. C., Durrell, P., Eigenthaler, P., Emsellem, E., Gavazzi, G., Gwyn, S., Huertas-Company, M., Ilbert, O., Jordán, A., Läsker, R., Licitra, R., Liu, C., MacArthur, L., McConnachie, A., McCracken, H. J., Mellier, Y., Peng, C. Y., Raichoor, A., Taylor, M. A., Tonry, J. L., Tully, R. B., and Zhang, H. 2014, Astrophysical Journal, Supplement Series, 210, 4

Muzzin, A., Marchesini, D., van Dokkum, P. G., Labbé, I., Kriek, M., and Franx, M. 2009, Astrophysical Journal, 701, 1839

Naab, T., Khochfar, S., and Burkert, A. 2006, Astrophysical Journal, Letters to the Editor, 636, L81

Nayakshin, S., Wilkinson, M. I., and King, A. 2009, Monthly Notices of the RAS, 398, L54

Neumayer, N. and Walcher, C. J. 2012, Advances in Astronomy, 2012, 709038

Norris, M. A., Kannappan, S. J., Forbes, D. A., Romanowsky, A. J., Brodie, J. P., Faifer, F. R., Huxor, A., Maraston, C., Moffett, A. J., Penny, S. J., Pota, V., Smith-Castelli, A., Strader, J., Bradley, D., Eckert, K. D., Fohring, D., McBride, J., Stark, D. V., and Vaduvescu, O. 2014, Monthly Notices of the RAS, 443, 1151

Oh, K. S. and Lin, D. N. C. 2000, Astrophysical Journal, 543, 620

Ordenes-Briceño, Y., Eigenthaler, P., Taylor, M. A., Puzia, T. H., Alamo-Martínez, K., Ribbeck, K. X., Muñoz, R. P., Zhang, H., Grebel, E. K., Ángel, S., Côté, P., Ferrarese, L., Hilker, M., Lançon, A., Mieske, S., Miller, B. W., Rong, Y., and Sánchez-Janssen, R. 2018a, Astrophysical Journal, 859, 52

Ordenes-Briceño, Y., Puzia, T. H., Eigenthaler, P., Taylor, M. A., Muñoz, R. P., Zhang, H., Alamo-Martínez, K., Ribbeck, K. X., Grebel, E. K., Ángel, S., Côté, P., Ferrarese, L., Hilker, M., Lançon, A., Mieske, S., Miller, B. W., Rong, Y., and Sánchez-Janssen, R. 2018b, Astrophysical Journal, 860, 4

Paturel, G. 1979, Astronomy and Astrophysics, 71, 106

Paudel, S., Duc, P.-A., Côté, P., Cuillandre, J.-C., Ferrarese, L., Ferriere, E., Gwyn, S. D. J., Mihos, J. C., Vollmer, B., Balogh, M. L., Carlberg, R. G., Boissier, S., Boselli, A., Durrell, P. R., Emsellem, E., MacArthur, L. A., Mei, S., Michel-Dansac, L., and van Driel, W. 2013, Astrophysical Journal, 767, 133

Paudel, S., Lisker, T., and Kuntschner, H. 2011, Monthly Notices of the RAS, 413, 1764

Peng, C. Y., Ho, L. C., Impey, C. D., and Rix, H.-W. 2002, Astronomical Journal, 124, 266

— 2010, Astronomical Journal, 139, 2097

Peng, E. W., Jordán, A., Côté, P., Takamiya, M., West, M. J., Blakeslee, J. P., Chen, C.-W., Ferrarese, L., Mei, S., Tonry, J. L., and West, A. A. 2008, Astrophysical Journal, 681, 197

Pfeffer, J. and Baumgardt, H. 2013, Monthly Notices of the RAS, 433, 1997

Pfeffer, J., Griffen, B. F., Baumgardt, H., and Hilker, M. 2014, Monthly Notices of the RAS, 444, 3670

Phillips, A. C., Illingworth, G. D., MacKenty, J. W., and Franx, M. 1996, Astronomical Journal, 111, 1566

Planck Collaboration, Ade, P. A. R., Aghanim, N., Arnaud, M., Ashdown, M., Aumont, J., Baccigalupi, C., Banday, A. J., Barreiro, R. B., Bartlett, J. G., and et al. 2016, Astronomy and Astrophysics, 594, A13

Powalka, M., Lançon, A., Puzia, T. H., Peng, E. W., Liu, C., Muñoz, R. P., Blakeslee, J. P., Côté, P., Ferrarese, L., Roediger, J., Sánchez-Janssen, R., Zhang, H., Durrell, P. R., Cuillandre, J.-C., Duc, P.-A., Guhathakurta, P., Gwyn, S. D. J., Hudelot, P., Mei, S., and Toloba, E. 2016, Astrophysical Journal, Supplement Series, 227, 12

Puget, P., Stadler, E., Doyon, R., Gigan, P., Thibault, S., Luppino, G., Barrick, G., Benedict, T., Forveille, T., Rambold, W., Thomas, J., Vermeulen, T., Ward, J., Beuzit, J.-L., Feautrier, P., Magnard, Y., Mella, G., Preis, O., Vallee, P., Wang, S.-y., Lin, C.-J., Hall, D. N., and Hodapp, K. W. 2004, in Proc. SPIE, Vol. 5492, Ground-based Instrumentation for Astronomy, ed. A. F. M. Moorwood & M. Iye, 978–987

Puzia, T. H., Kissler-Patig, M., Thomas, D., Maraston, C., Saglia, R. P., Bender, R., Goudfrooij, P., and Hempel, M. 2005, Astronomy and Astrophysics, 439, 997

Puzia, T. H., Zepf, S. E., Kissler-Patig, M., Hilker, M., Minniti, D., and Goudfrooij, P. 2002, Astronomy and Astrophysics, 391, 453

Reaves, G. 1962, Publications of the ASP, 74, 392

— 1983, Astrophysical Journal, Supplement Series, 53, 375

Roediger, J. C., Ferrarese, L., Côté, P., MacArthur, L. A., Sánchez-Janssen, R., Blakeslee, J. P., Peng, E. W., Liu, C., Munoz, R., Cuillandre, J.-C., Gwyn, S., Mei, S., Boissier, S., Boselli, A., Cantiello, M., Courteau, S., Duc, P.-A., Lançon, A., Mihos, J. C., Puzia, T. H., Taylor, J. E., Durrell, P. R., Toloba, E., Guhathakurta, P., and Zhang, H. 2017, Astrophysical Journal, 836, 120

Rossa, J., van der Marel, R. P., Böker, T., Gerssen, J., Ho, L. C., Rix, H.-W., Shields, J. C., and Walcher, C.-J. 2006, Astronomical Journal, 132, 1074

Saglia, R. P., Opitsch, M., Erwin, P., Thomas, J., Beifiori, A., Fabricius, M., Mazzalay, X., Nowak, N., Rusli, S. P., and Bender, R. 2016, Astrophysical Journal, 818, 47

Salim, S., Rich, R. M., Charlot, S., Brinchmann, J., Johnson, B. D., Schiminovich, D., Seibert, M., Mallery, R., Heckman, T. M., Forster, K., Friedman, P. G., Martin, D. C., Morrissey, P., Neff, S. G., Small, T., Wyder, T. K., Bianchi, L., Donas, J., Lee, Y.-W., Madore, B. F., Milliard, B., Szalay, A. S., Welsh, B. Y., and Yi, S. K. 2007, Astrophysical Journal, Supplement Series, 173, 267

Schawinski, K., Urry, C. M., Simmons, B. D., Fortson, L., Kaviraj, S., Keel, W. C., Lintott, C. J., Masters, K. L., Nichol, R. C., Sarzi, M., Skibba, R., Treister, E., Willett, K. W., Wong, O. I., and Yi, S. K. 2014, Monthly Notices of the RAS, 440, 889

Schiavon, R. P. 2007, Astrophysical Journal, Supplement Series, 171, 146

Schindler, S., Binggeli, B., and Böhringer, H. 1999, Astronomy and Astrophysics, 343, 420

Schinnerer, E., Böker, T., Meier, D. S., and Calzetti, D. 2008, Astrophysical Journal, Letters to the Editor, 684, L21

Schlafly, E. F. and Finkbeiner, D. P. 2011, Astrophysical Journal, 737, 103

Schödel, R., Eckart, A., Alexander, T., Merritt, D., Genzel, R., Sternberg, A., Meyer, L., Kul, F., Moultaka, J., Ott, T., and Straubmeier, C. 2007, Astronomy and Astrophysics, 469, 125

Scholz, F. W. and Stephens, M. A. 1987, Journal of the American Statistical Association, 82, 918

Schweizer, F. 1979, Astrophysical Journal, 233, 23

Schwinn, J., Baugh, C. M., Jauzac, M., Bartelmann, M., and Eckert, D. 2018, ArXiv e-prints

Schwinn, J., Jauzac, M., Baugh, C. M., Bartelmann, M., Eckert, D., Harvey, D., Natarajan, P., and Massey, R. 2017, Monthly Notices of the RAS, 467, 2913

Scott, N. and Graham, A. W. 2013, Astrophysical Journal, 763, 76

Searle, L. and Zinn, R. 1978, Astrophysical Journal, 225, 357

Sersic, J. L. 1968, Atlas de Galaxias Australes

Seth, A., Agüeros, M., Lee, D., and Basu-Zych, A. 2008, Astrophysical Journal, 678, 116

Seth, A. C., Dalcanton, J. J., Hodge, P. W., and Debattista, V. P. 2006, Astronomical Journal, 132, 2539

Seth, A. C., van den Bosch, R., Mieske, S., Baumgardt, H., Brok, M. D., Strader, J., Neumayer, N., Chilingarian, I., Hilker, M., McDermid, R., Spitler, L., Brodie, J., Frank, M. J., and Walsh, J. L. 2014, Nature, 513, 398

Shapley, H. and Ames, A. 1929a, Harvard College Observatory Bulletin, 865, 1

— 1929b, Harvard College Observatory Bulletin, 866, 20

— 1929c, Harvard College Observatory Bulletin, 868, 3

— 1929d, Harvard College Observatory Bulletin, 869, 22

Sheinis, A. I., Bolte, M., Epps, H. W., Kibrick, R. I., Miller, J. S., Radovan, M. V., Bigelow, B. C., and Sutin, B. M. 2002, Publications of the ASP, 114, 851

Silverman, B. W. 1986, Density Estimation for Statistics and Data Analysis (London; New York: Chapman and Hall)

Simon, J. D. and Geha, M. 2007, Astrophysical Journal, 670, 313

Solanes, J. M., Sanchis, T., Salvador-Solé, E., Giovanelli, R., and Haynes, M. P. 2002, Astronomical Journal, 124, 2440

Spengler, C., Côté, P., Roediger, J., Ferrarese, L., Sánchez-Janssen, R., Toloba, E., Liu, Y., Guhathakurta, P., Cuillandre, J.-C., Gwyn, S., Zirm, A., Muñoz, R., Puzia, T., Lançon, A., Peng, E. W., Mei, S., and Powalka, M. 2017, Astrophysical Journal, 849, 55

Stetson, P. B. 1987, Publications of the ASP, 99, 191

Stetson, P. B. 1993, in IAU Colloq. 136: Stellar Photometry - Current Techniques and Future Developments, ed. C. J. Butler & I. Elliott, Vol. 136, 291

Taylor, E. N., Hopkins, A. M., Baldry, I. K., Brown, M. J. I., Driver, S. P., Kelvin, L. S., Hill, D. T., Robotham, A. S. G., Bland-Hawthorn, J., Jones, D. H., Sharp, R. G., Thomas, D., Liske, J., Loveday, J., Norberg, P., Peacock, J. A., Bamford, S. P., Brough, S., Colless, M., Cameron, E., Conselice, C. J., Croom, S. M., Frenk, C. S., Gunawardhana, M., Kuijken, K., Nichol, R. C., Parkinson, H. R., Phillipps, S., Pimbblet, K. A., Popescu, C. C., Prescott, M., Sutherland, W. J., Tuffs, R. J., van Kampen, E., and Wijesinghe, D. 2011, Monthly Notices of the RAS, 418, 1587

Terrazas, B. A., Bell, E. F., Henriques, B. M. B., White, S. D. M., Cattaneo, A., and Woo, J. 2016, Astrophysical Journal, Letters to the Editor, 830, L12

Thomas, D., Maraston, C., and Bender, R. 2003, Monthly Notices of the RAS, 339, 897

Thompson, R. I. 1994, in Proc. SPIE, Vol. 2209, Space Optics 1994: Earth Observation and Astronomy, ed. M. G. Cerutti-Maori & P. Roussel, 319–330

Toloba, E., Li, B., Guhathakurta, P., Peng, E. W., Ferrarese, L., Côté, P., Emsellem, E., Gwyn, S., Zhang, H., Boselli, A., Cuillandre, J.-C., Jordan, A., and Liu, C. 2016, Astrophysical Journal, 822, 51

Tonry, J. and Schneider, D. P. 1988, Astronomical Journal, 96, 807

Tonry, J. L. 1991, Astrophysical Journal, Letters to the Editor, 373, L1

Trager, S. C., Faber, S. M., Worthey, G., and González, J. J. 2000, Astronomical Journal, 119, 1645

Tremaine, S., Gebhardt, K., Bender, R., Bower, G., Dressler, A., Faber, S. M., Filippenko, A. V., Green, R., Grillmair, C., Ho, L. C., Kormendy, J., Lauer, T. R.,

Magorrian, J., Pinkney, J., and Richstone, D. 2002, Astrophysical Journal, 574, 740

Tremaine, S. D., Ostriker, J. P., and Spitzer, Jr., L. 1975, Astrophysical Journal, 196, 407

Tsatsi, A., Mastrobuono-Battisti, A., van de Ven, G., Perets, H. B., Bianchini, P., and Neumayer, N. 2017, Monthly Notices of the RAS, 464, 3720

Turner, M. L., Côté, P., Ferrarese, L., Jordán, A., Blakeslee, J. P., Mei, S., Peng, E. W., and West, M. J. 2012, Astrophysical Journal, Supplement Series, 203, 5

Urban, O., Werner, N., Simionescu, A., Allen, S. W., and Böhringer, H. 2011, Monthly Notices of the RAS, 414, 2101

van den Bergh, S. 1986, Astronomical Journal, 91, 271

van den Bosch, R. C. E. 2016, Astrophysical Journal, 831, 134

Vazdekis, A. 1999, Astrophysical Journal, 513, 224

Vogelsberger, M., Genel, S., Springel, V., Torrey, P., Sijacki, D., Xu, D., Snyder, G., Bird, S., Nelson, D., and Hernquist, L. 2014a, Nature, 509, 177

Vogelsberger, M., Genel, S., Springel, V., Torrey, P., Sijacki, D., Xu, D., Snyder, G., Nelson, D., and Hernquist, L. 2014b, Monthly Notices of the RAS, 444, 1518

Volonteri, M. 2010, Astronomy and Astrophysics Reviews, 18, 279

Walcher, C. J., Böker, T., Charlot, S., Ho, L. C., Rix, H.-W., Rossa, J., Shields, J. C., and van der Marel, R. P. 2006, Astrophysical Journal, 649, 692

Walcher, C. J., van der Marel, R. P., McLaughlin, D., Rix, H.-W., Böker, T., Häring, N., Ho, L. C., Sarzi, M., and Shields, J. C. 2005, Astrophysical Journal, 618, 237

Wehner, E. H. and Harris, W. E. 2006, Astrophysical Journal, Letters to the Editor, 644, L17

Weiss, A., Salaris, M., Ferguson, J. W., and Alexander, D. R. 2006, ArXiv Astrophysics e-prints

West, M. J. and Blakeslee, J. P. 2000, Astrophysical Journal, Letters to the Editor, 543, L27

White, S. D. M. and Rees, M. J. 1978, Monthly Notices of the RAS, 183, 341

Worthey, G., Faber, S. M., Gonzalez, J. J., and Burstein, D. 1994, Astrophysical Journal, Supplement Series, 94, 687

Yamada, Y., Arimoto, N., Vazdekis, A., and Peletier, R. F. 2006, Astrophysical Journal, 637, 200

Yi, S. K., Yoon, S.-J., Kaviraj, S., Deharveng, J.-M., Rich, R. M., Salim, S., Boselli, A., Lee, Y.-W., Ree, C. H., Sohn, Y.-J., Rey, S.-C., Lee, J.-W., Rhee, J., Bianchi, L., Byun, Y.-I., Donas, J., Friedman, P. G., Heckman, T. M., Jelinsky, P., Madore, B. F., Malina, R., Martin, D. C., Milliard, B., Morrissey, P., Neff, S., Schiminovich, D., Siegmund, O., Small, T., Szalay, A. S., Jee, M. J., Kim, S.-W., Barlow, T., Forster, K., Welsh, B., and Wyder, T. K. 2005, Astrophysical Journal, Letters to the Editor, 619, L111

Zhang, H.-X., Peng, E. W., Côté, P., Liu, C., Ferrarese, L., Cuillandre, J.-C., Caldwell, N., Gwyn, S. D. J., Jordán, A., Lançon, A., Li, B., Muñoz, R. P., Puzia, T. H., Bekki, K., Blakeslee, J. P., Boselli, A., Drinkwater, M. J., Duc, P.-A., Durrell, P., Emsellem, E., Firth, P., and Sánchez-Janssen, R. 2015, Astrophysical Journal, 802, 30

Appendix

Appendix A

Virgo substructures identified with OPTICS

In this section we include detailed supplementary figures for Chapter 3, showing each substructure extracted from OPTICS. Figures for each substructure display the positions of each member within the entire NGVS sample. Additional panels show histograms of any measured recessional velocities or SBF distances for the substructure members, when available, as well as the mass distribution. Corresponding histograms of all measured velocities, SBF distances, and galaxy stellar masses are shown for comparison. Note that these substructures are colour-matched to the substructures shown in Figure 3.8 — for example, the OPTICS substructure matched to Virgo A is highlighted in green here in the Appendix, as well as in earlier the dendrogram and reachability plot.

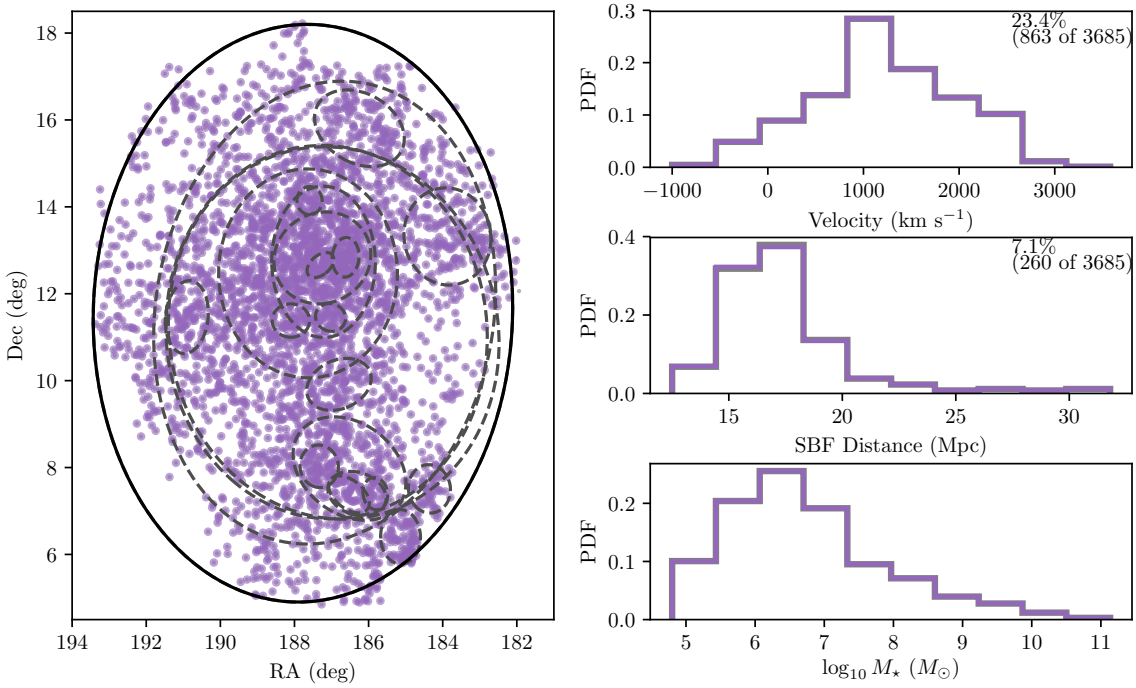

Figure A.1 OPTICS 0, a parent structure consisting of the entire dataset.

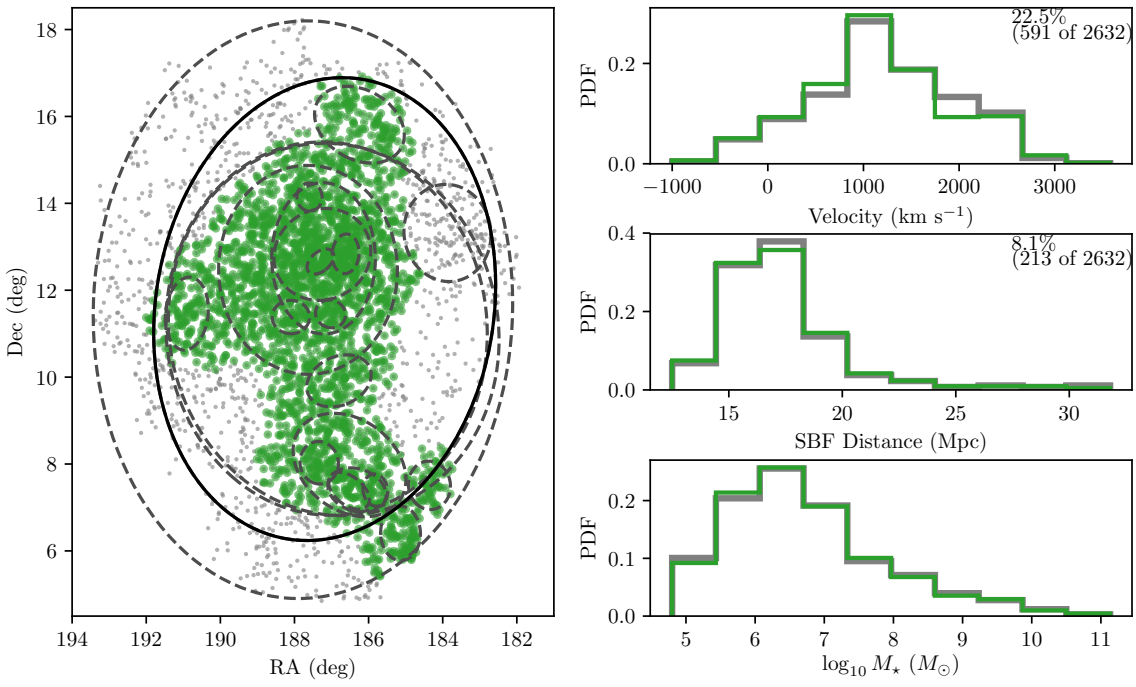

Figure A.2 Sky maps and velocity, distance, and mass distributions for OPTICS 1.

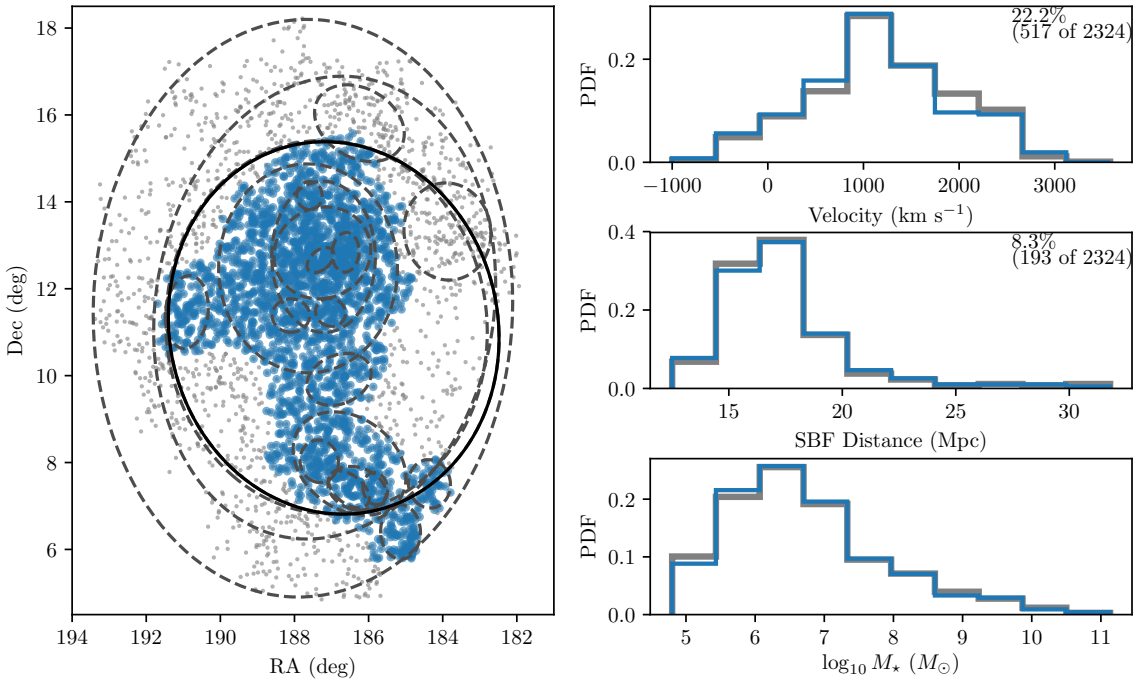

Figure A.3 Sky maps and velocity, distance, and mass distributions for OPTICS 2.

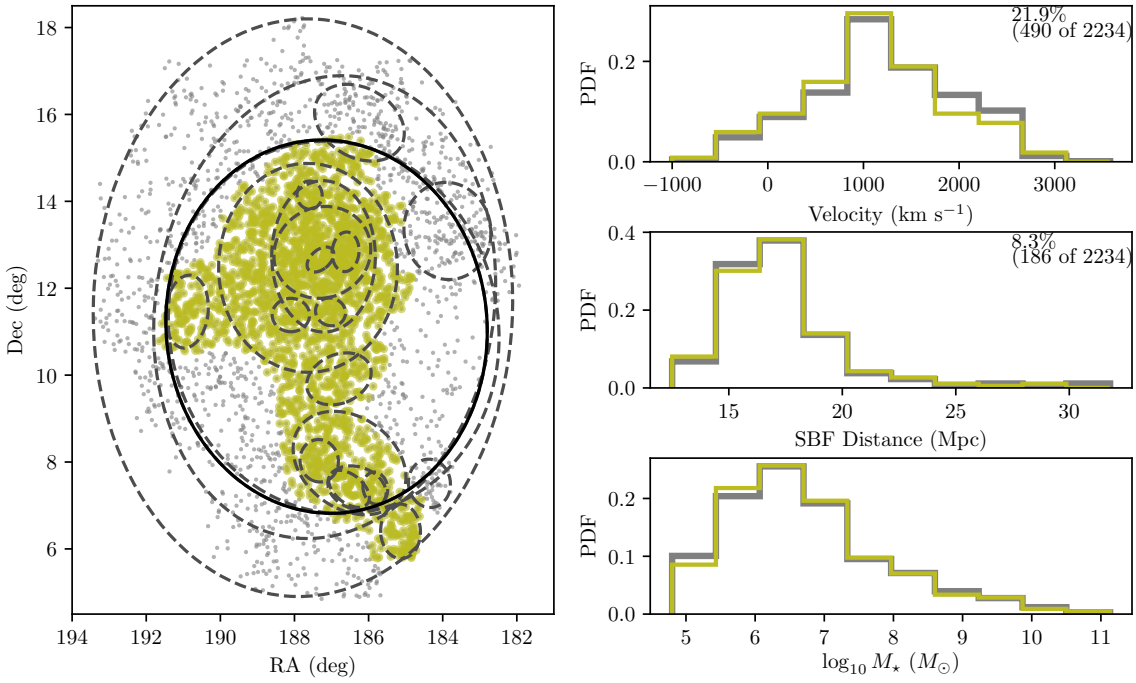

Figure A.4 Sky maps and velocity, distance, and mass distributions for OPTICS 3.

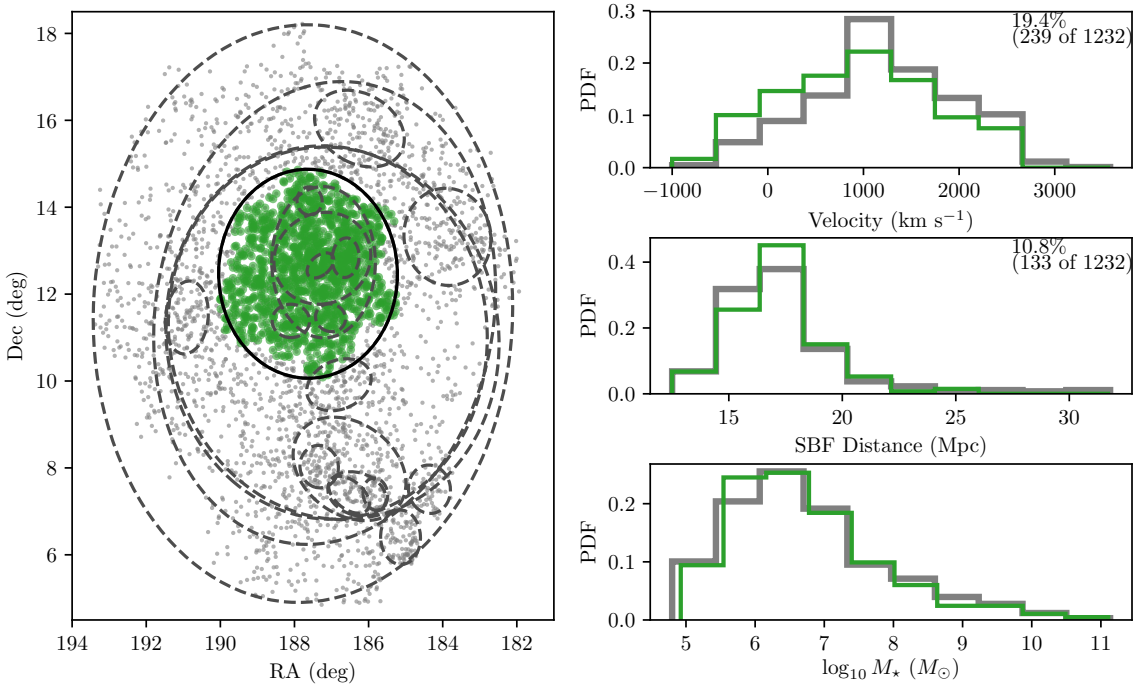

Figure A.5 Sky maps and velocity, distance, and mass distributions for OPTICS 4, roughly corresponding to Virgo A.

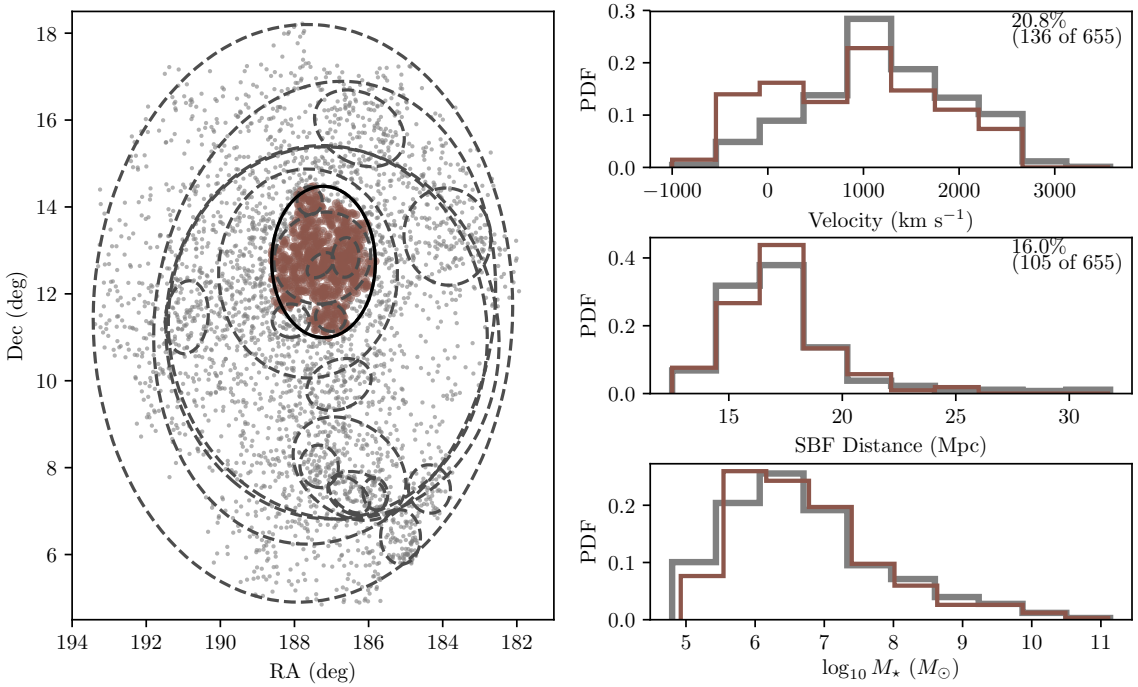

Figure A.6 Sky maps and velocity, distance, and mass distributions for OPTICS 5.

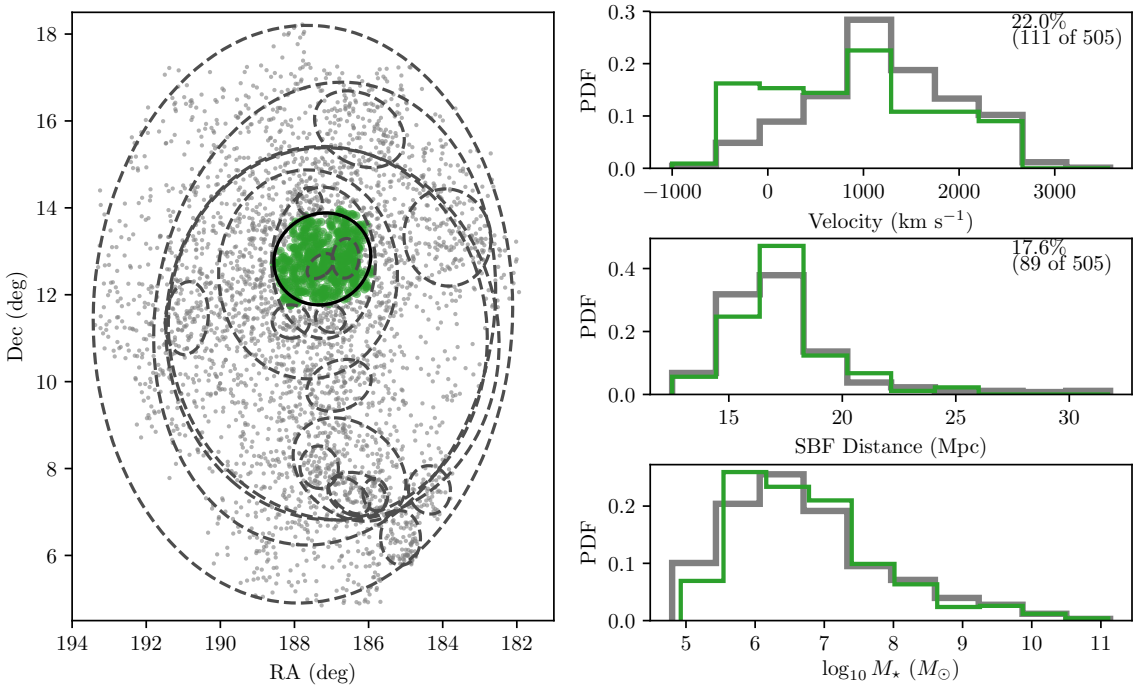

Figure A.7 Sky maps and velocity, distance, and mass distributions for OPTICS 6.

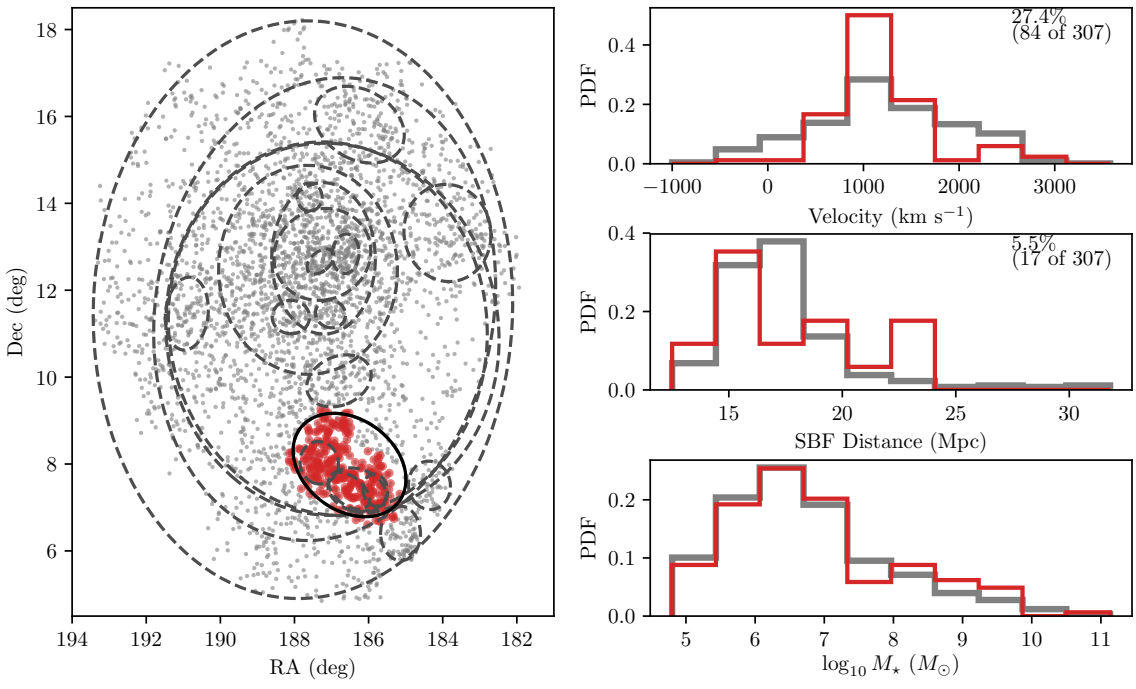

Figure A.8 Sky maps and velocity, distance, and mass distributions for OPTICS 7.

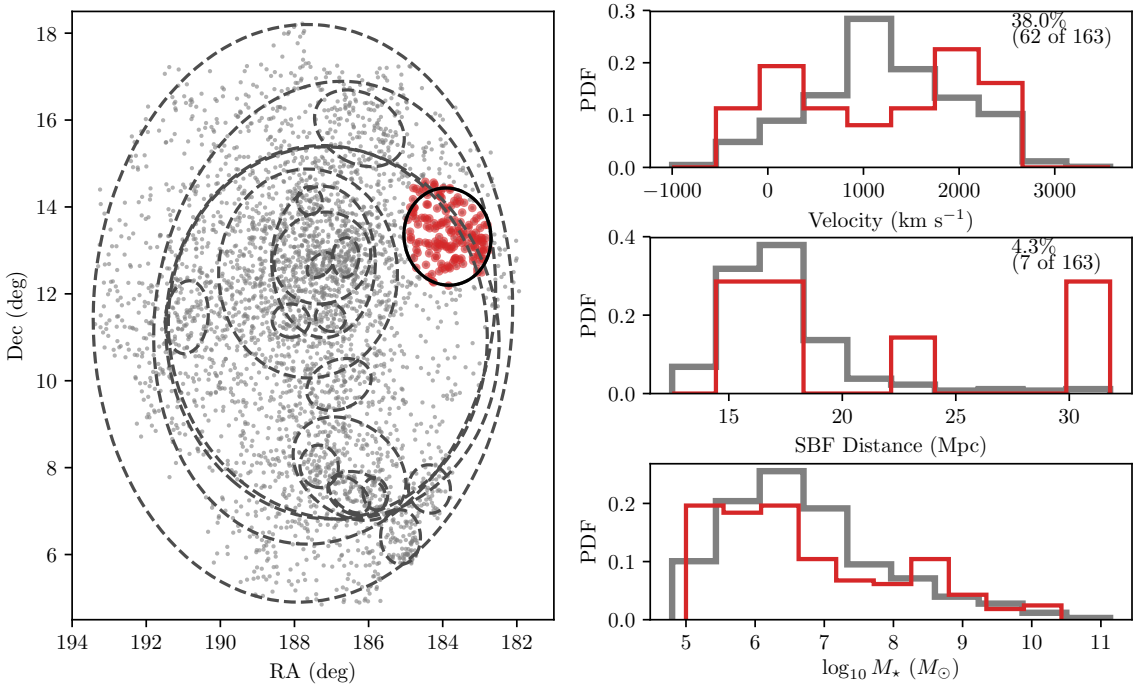

Figure A.9 Sky maps and velocity, distance, and mass distributions for OPTICS 8, a superposition of the LVC and M cloud. Note the bimodal velocity distribution for this substructure which can also be less strongly seen in the distance distribution.

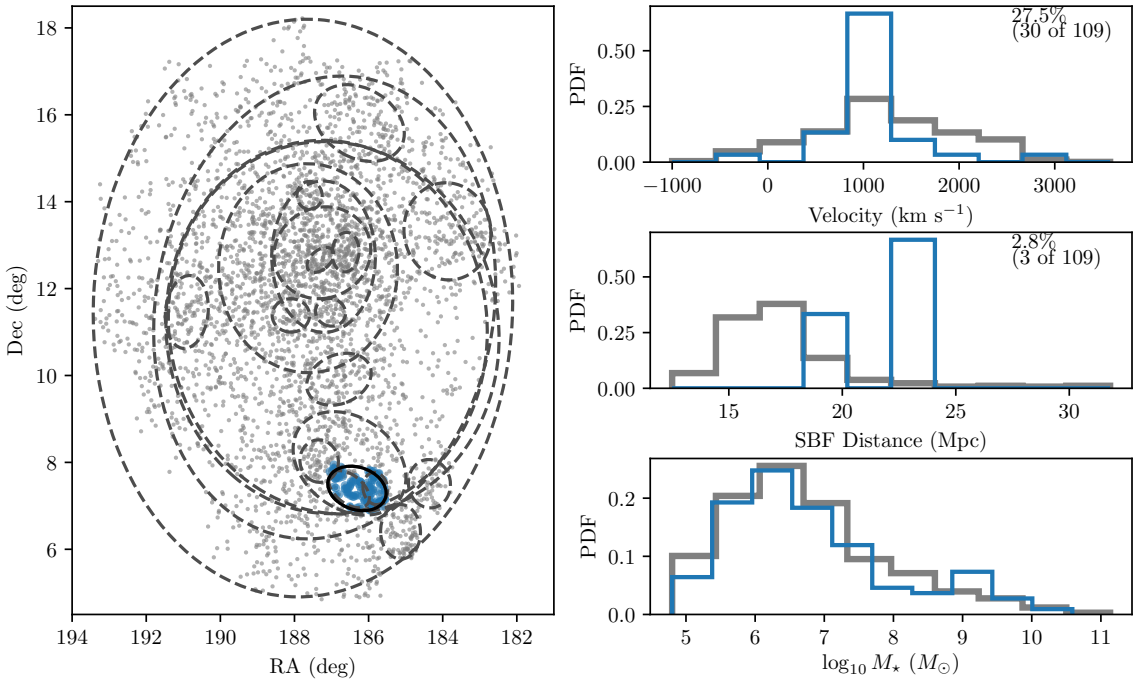

Figure A.10 Sky maps and velocity, distance, and mass distributions for OPTICS 9, corresponding to the W′ cloud.

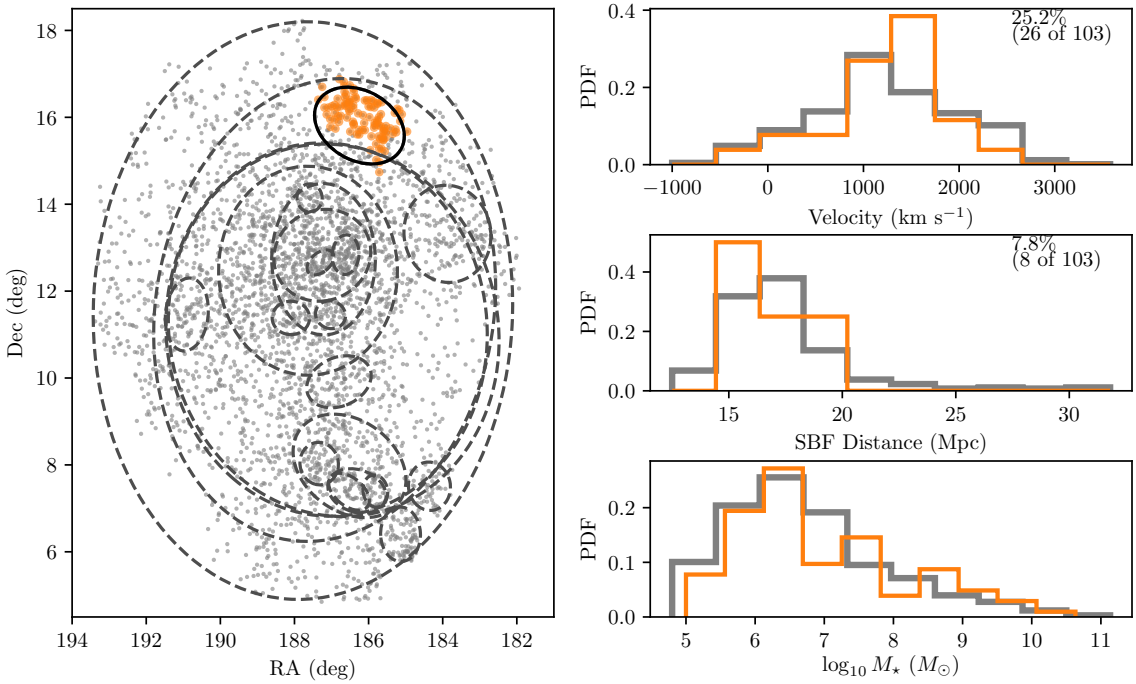

Figure A.11 Sky maps and velocity, distance, and mass distributions for OPTICS 10, a group around M100 which is one of the promising new candidates from this study.

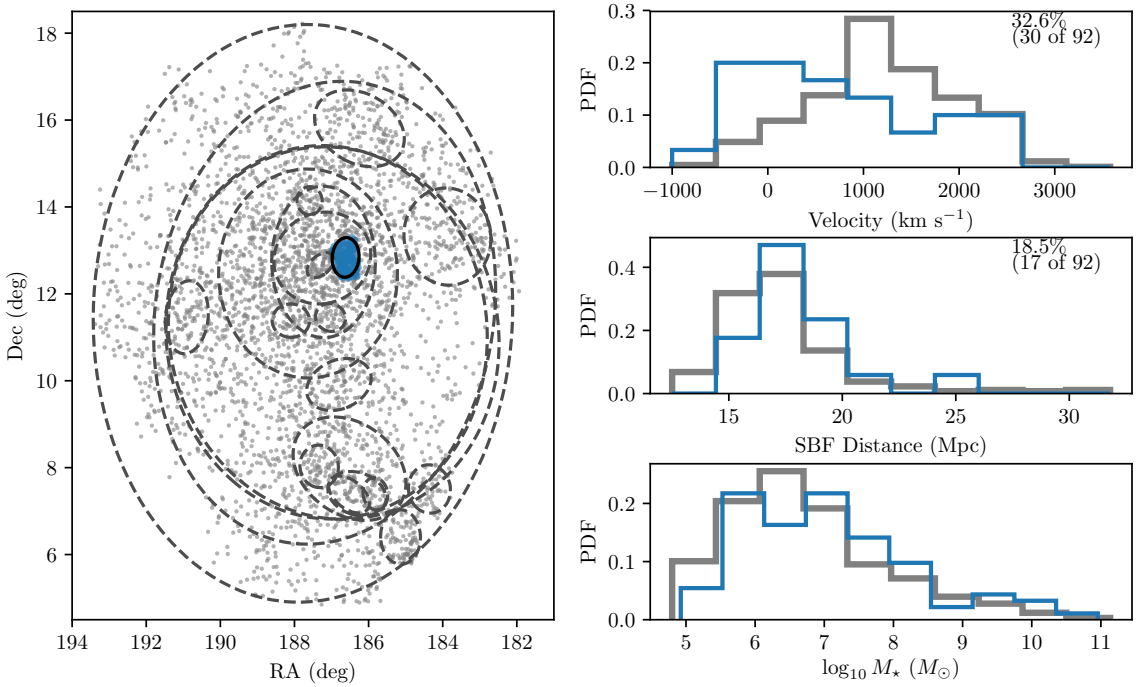

Figure A.12 Sky maps and velocity, distance, and mass distributions for OPTICS 11.

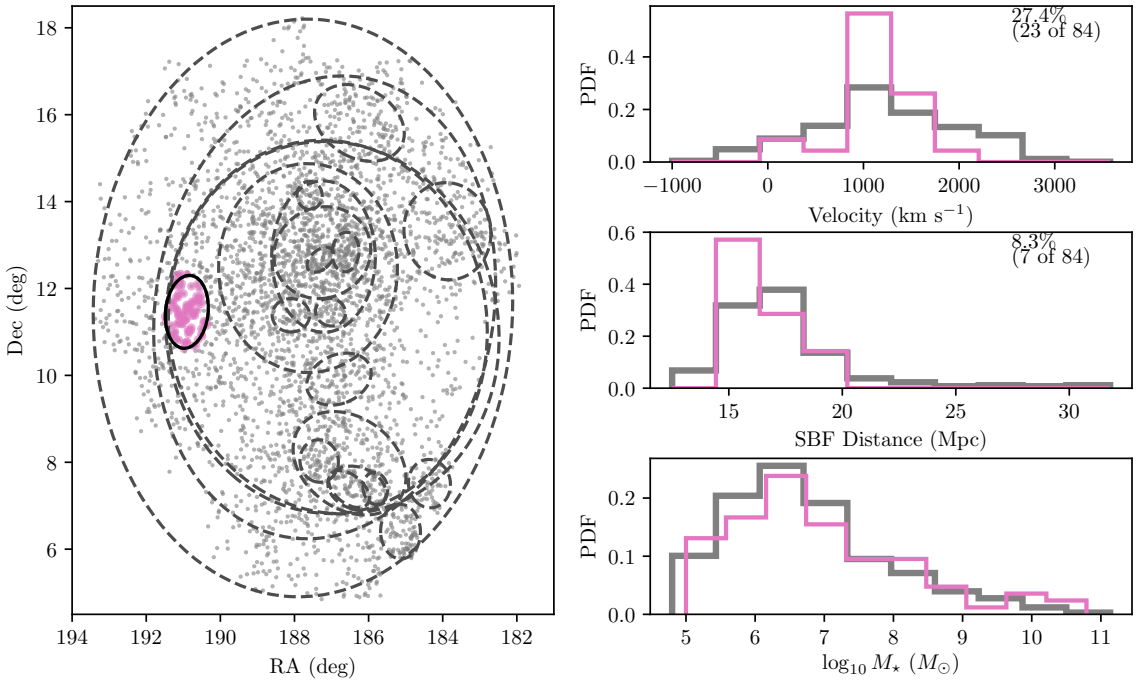

Figure A.13 Sky maps and velocity, distance, and mass distributions for OPTICS 12, corresponding to Virgo C.

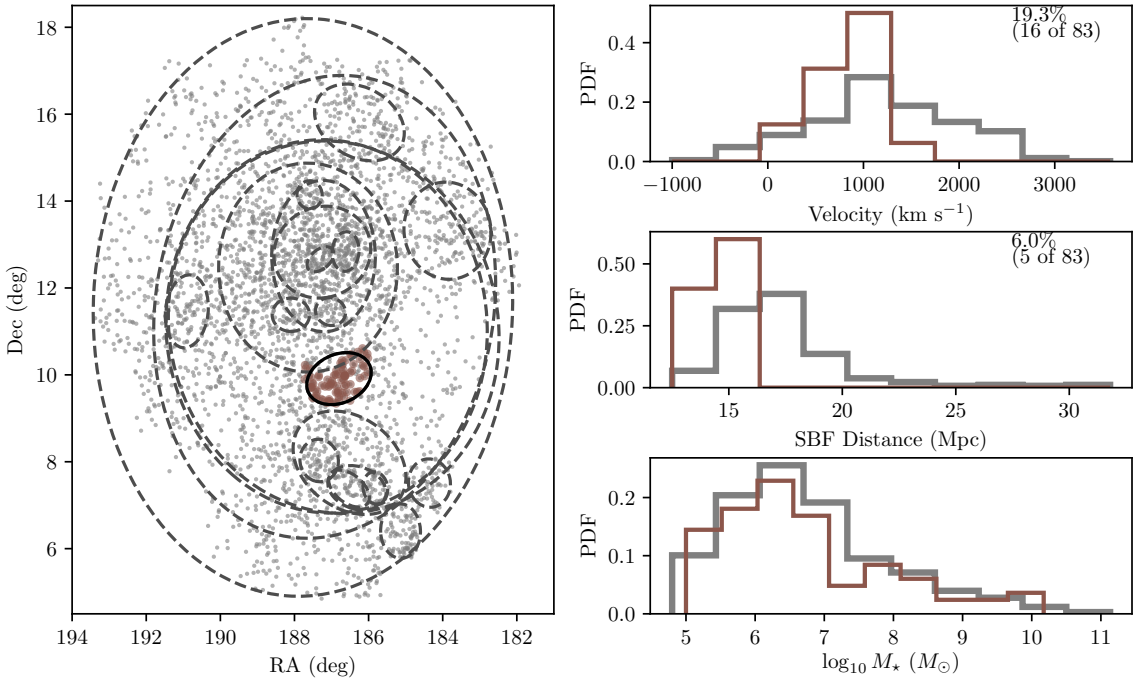

Figure A.14 Sky maps and velocity, distance, and mass distributions for OPTICS 13, another of the new candidates that appears to be a *bona fide* structure.

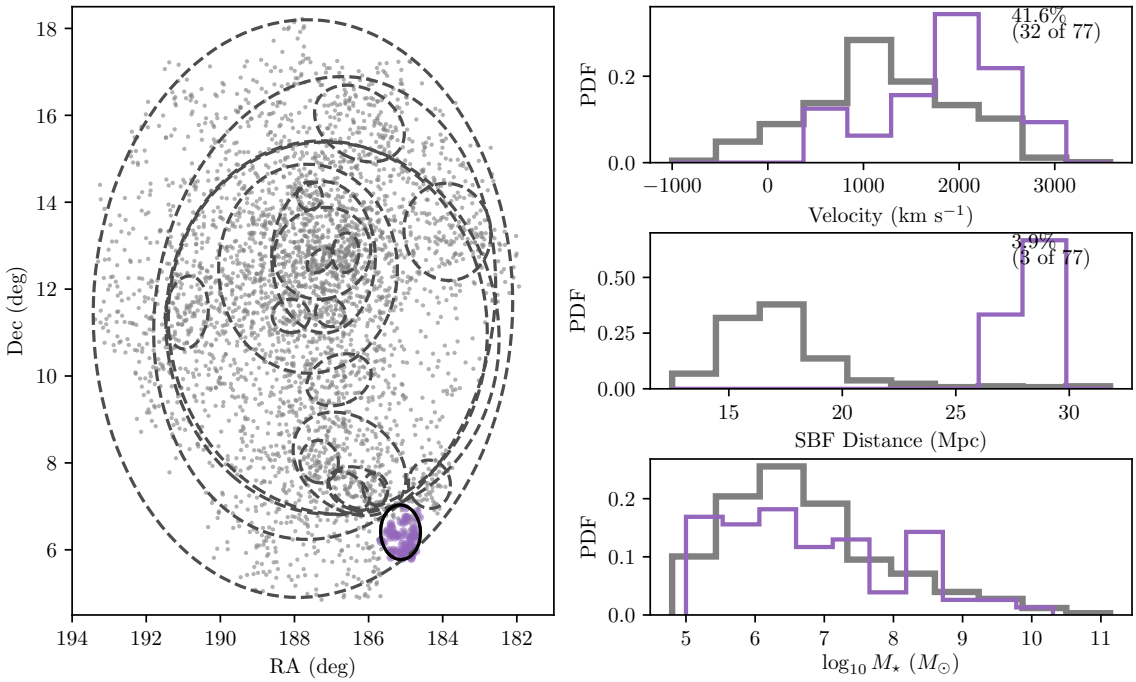

Figure A.15 Sky maps and velocity, distance, and mass distributions for OPTICS 14, corresponding to the W cloud.

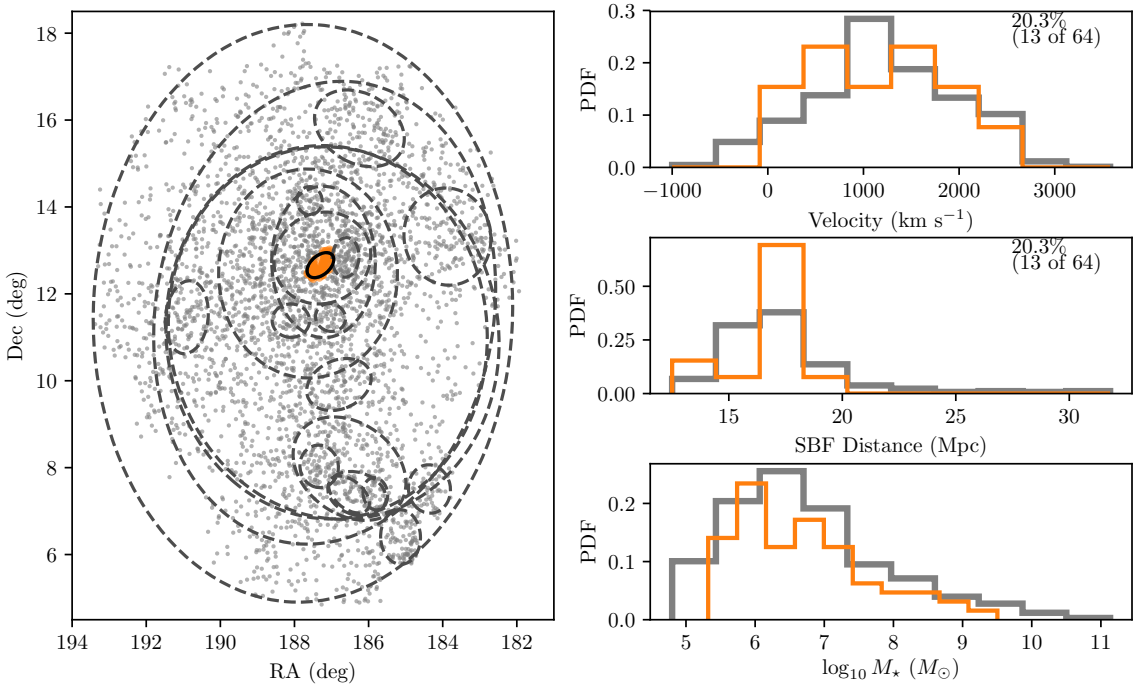

Figure A.16 Sky maps and velocity, distance, and mass distributions for OPTICS 15.

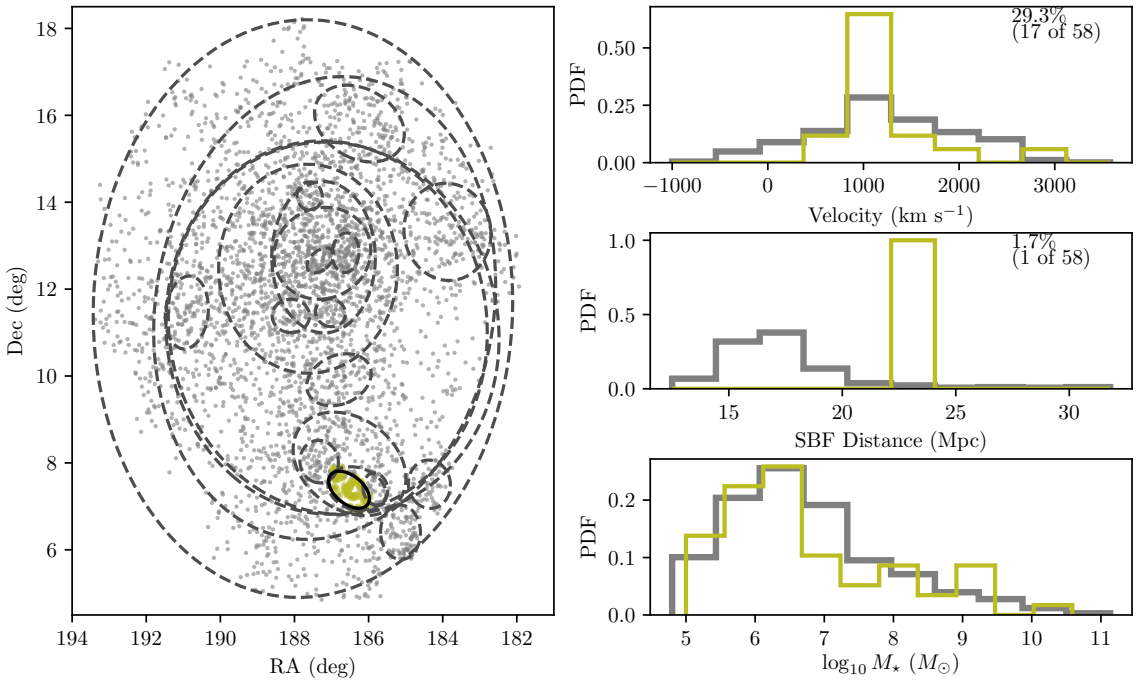

Figure A.17 Sky maps and velocity, distance, and mass distributions for OPTICS 16.

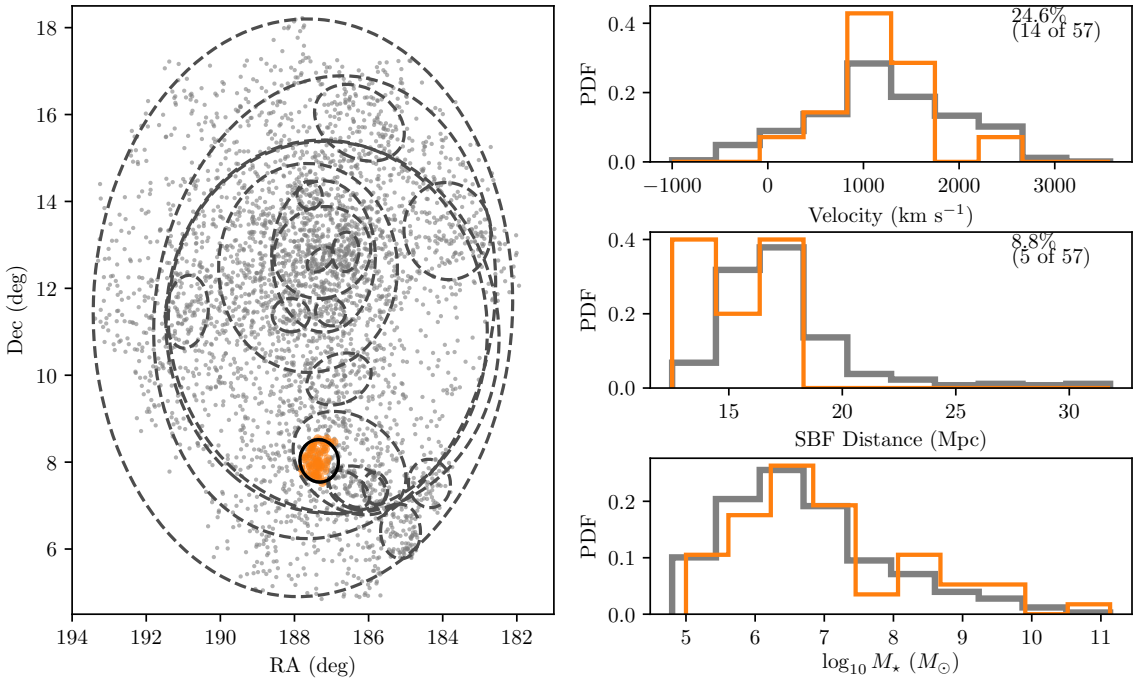

Figure A.18 Sky maps and velocity, distance, and mass distributions for OPTICS 17, roughly consistent with Virgo B.

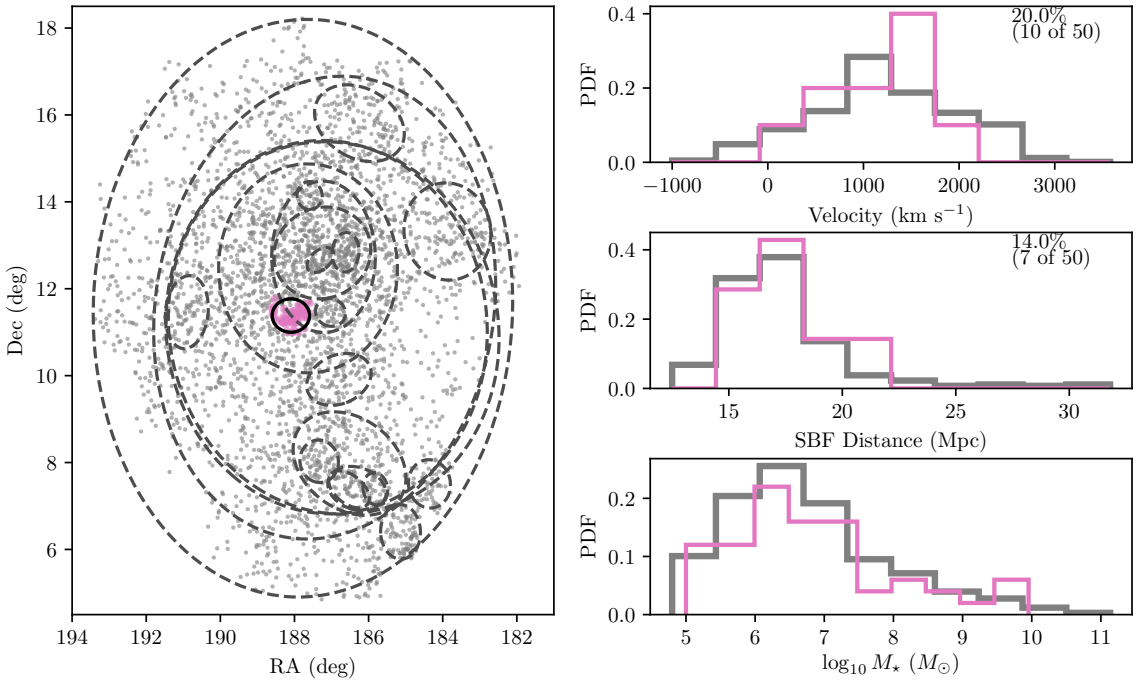

Figure A.19 Sky maps and velocity, distance, and mass distributions for OPTICS 18.

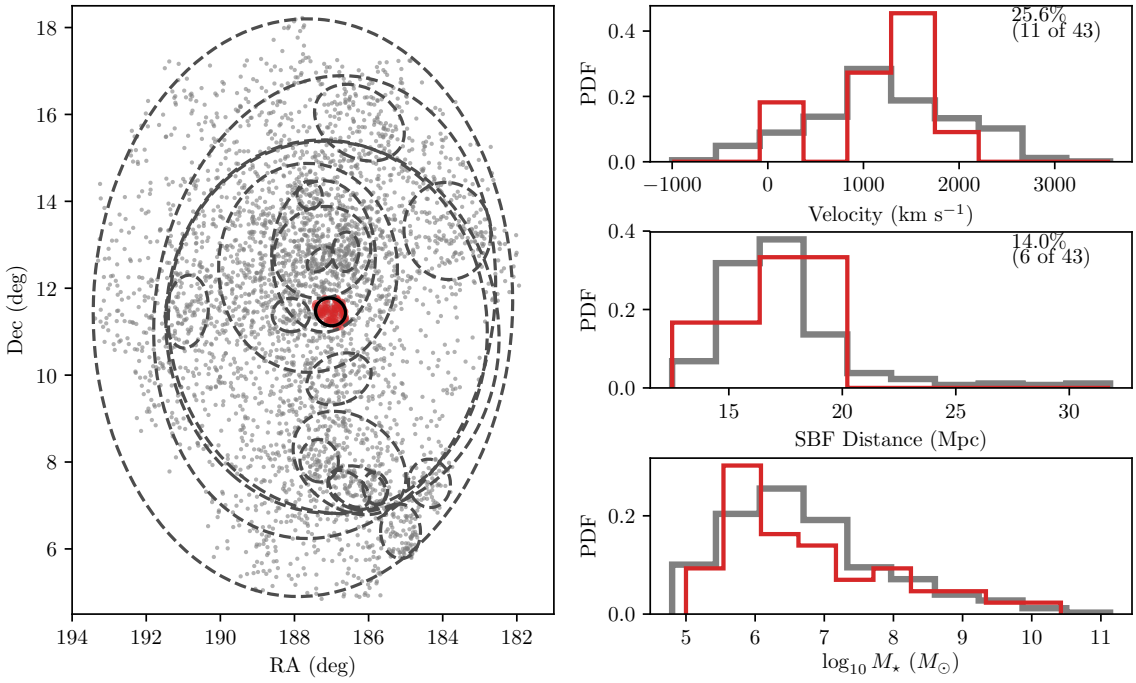

Figure A.20 Sky maps and velocity, distance, and mass distributions for OPTICS 19.

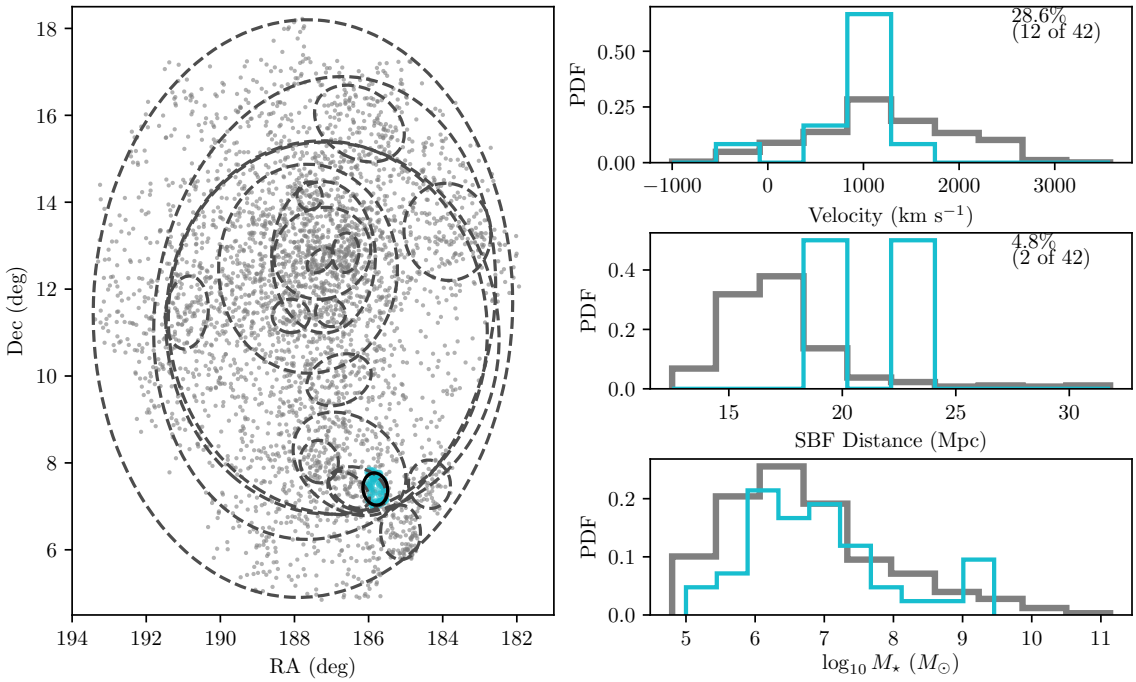

Figure A.21 Sky maps and velocity, distance, and mass distributions for OPTICS 20.

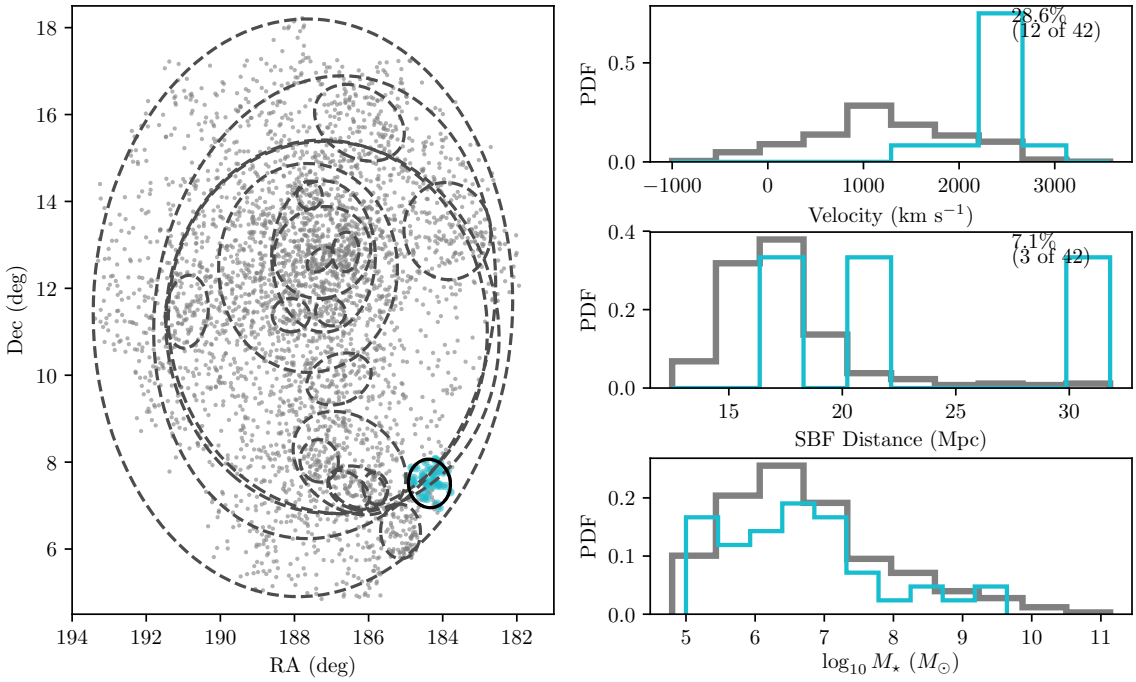

Figure A.22 Sky maps and velocity, distance, and mass distributions for OPTICS 21, a potential new extension to the W cloud.

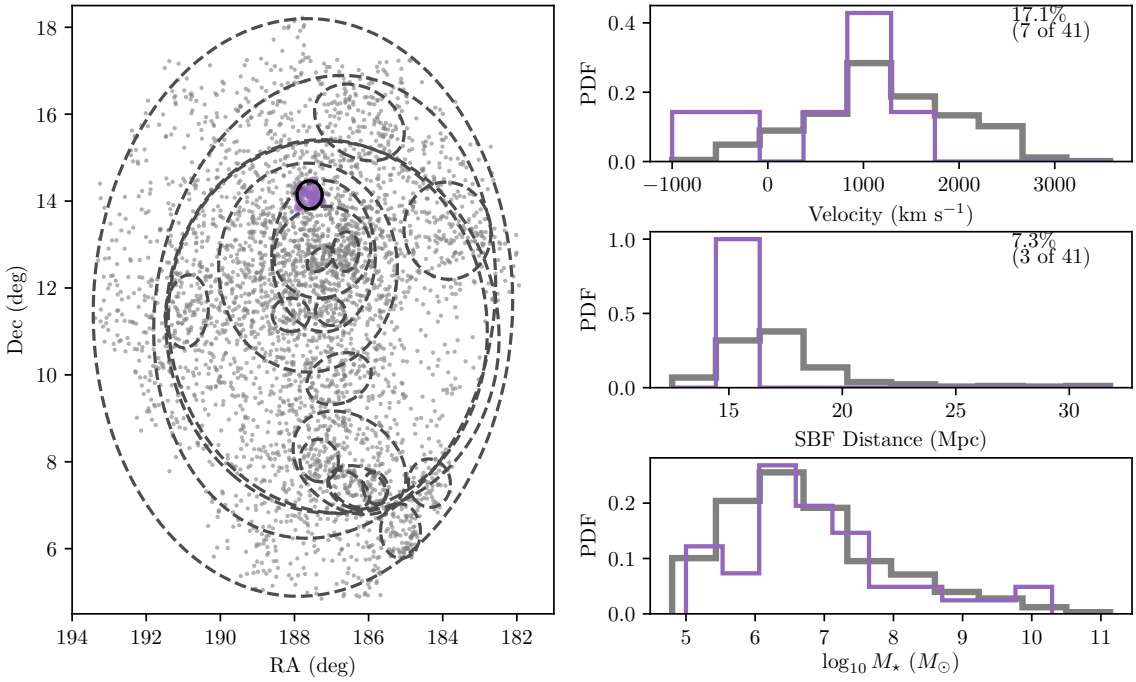

Figure A.23 Sky maps and velocity, distance, and mass distributions for OPTICS 22.